Investigation of non-cooperative target recognition of small and slow moving air targets in modern air defence surveillance radar

Børge Torvik

A dissertation submitted in partial fulfillment

of the requirements for the degree of

Doctor of Philosophy

of

University College London.

Department of Electronic and Electrical Engineering

University College London

December 12, 2016

I, Børge Torvik, confirm that the work presented in this thesis is my own. Where information has been derived from other sources, I confirm that this has been indicated in the work.

Abstract

This thesis covers research in the field of non-cooperative target recognition given the limitations of modern air defence surveillance radars. The potential presence of low observable manned or unmanned targets within the vast surveillance volume demand highly sensitive systems. This may again introduce unwanted detections of single birds of comparable radar cross section, previously avoided by use of wide clutter rejection filters and sensitivity time control. The demand for methods effectively separating between birds and slow moving manmade targets is evident.

The research questions addressed are connected to identification of characteristic features of birds and manmade targets of comparable size. Ultimately the goal has been to find methods that can utilize such features to effectively distinguish between the classes. In contrast to the vast majority of non-cooperative target recognition publications, this thesis includes non-rigid targets covering a range of dielectric properties and targets falling in the resonant and Rayleigh scattering regions. These factors combined with insufficient spatial resolution for classification require alternative approaches such as utilization of periodic RCS modulation, micro-Doppler- and polarimetric signatures.

Signatures of birds and UAVs are investigated through electromagnetic prediction and radar measurements. A flexible and fully polarimetric radar capable of simultaneous operation in both L- and S-band is developed for collection of relevant signatures. Inspired by the use of polarimetric radar for classification of precipitation covered in the weather radar literature, focus has been on using similar methods to recognize signatures of rotors, propellers and bird wings. Novel micro-Doppler signatures combining polarimetric information from this sensor is found to hold

information about the orientation of such target parts. This information combined with several other features is evaluated for classification. The benefit from involving polarimetric measurements is especially investigated, and is found to be highly valuable when information provided by other methods is limited.

Acknowledgements

I would like to thank my supervisors Professor Hugh Griffiths and Professor Karl Woodbridge for support and guidance through all these years. Many thanks also to Karl Erik Olsen for encouragement, inspiration and organizing the funding provided by the Royal Norwegian Air Force and Norwegian Defence Research Establishment (FFI). I would also like to thank my colleagues at FFI Terje Johnsen, Øystein Lie-Svendsen, Jonas Myhre Cristiansen, Idar Nordheim-Næss and Erlend Finden for fruitful discussions and support during trials.

I am deeply indebted to my wife Gunn Mari and daughters Ida Helene and Kristine. Thank you for your endless patience, understanding and support throughout this journey.

Finally, I would like to thank the people in the radar group at UCL for welcoming me and making my research stay with you such a joy.

Contents

1 Introduction **39**

1.1 Overview 39

1.2 Motivation of work 40

1.3 Long range air defence surveillance radars 42

1.4 Target recognition 45

1.5 Research questions and methods 50

1.6 Novel contributions 52

1.7 Publications 53

1.8 Thesis outline 54

2 Research Context **57**

2.1 Detection and classification of birds 58

2.1.1 The first years of bird detection and classification attempts . 58

2.1.2 Bird RCS predictions 61

2.1.3 Contribution from bird body parts to overall RCS 63

2.1.4 RCS measurements 65

2.1.5 Motion pattern 65

2.1.6 Amplitude modulation of backscattered waveform 67

2.1.7 Doppler and μ-Doppler Signatures 70

2.1.8 Analysis of μ-Doppler signatures of non-rigid targets 73

2.1.9 Polarimetric signatures 74

2.1.10 Existing bird classification routines 79

2.1.11 Resonance effects in echoes from birds 80

2.1.12 Classification based on spatial resolution 80
2.2 Classification of small man-made targets 81
2.2.1 Small man-made targets 81
2.2.2 Methods for classification of small man-made targets 82
2.2.3 Amplitude modulation based methods 83
2.2.4 μ-Doppler methods 87
2.2.5 Polarimetric methods 88
2.2.6 Resonance effects and target impulse response matching . . 92
2.3 Summary 94

3 Birds and UAVs as radar targets 97
3.1 Wave propagation 97
3.2 Target materials 98
3.2.1 Reflection coefficient 99
3.2.2 Wavenumber in general lossy medium 100
3.2.3 Wavenumber in lossless medium 101
3.2.4 Wavenumber in good conductor 101
3.2.5 Example of lossless and lossy materials 101
3.3 Scattering regimes 102
3.3.1 Rayleigh region 103
3.3.2 Resonance region 104
3.4 Scattering from small airborne targets 104
3.4.1 The prolate spheroid bird model 104
3.4.2 Bird size in wavelengths 105
3.4.3 Internal reflections and resonances 107
3.4.4 Small man-made airborne targets 108
3.5 Polarization 109
3.5.1 Polarization scattering matrix 109
3.5.2 FSA and BSA convention 110
3.5.3 Differential RCS 110
3.5.4 Linear depolarization ratio 111

3.5.5 Differential phase . . . 112
3.6 Spectral analysis . . . 115
3.6.1 Velocity resolution . . . 115
3.6.2 μ-Doppler signatures . . . 116
3.6.3 Apparent μ-Doppler signature . . . 117
3.7 Summary . . . 118

4 Electromagnetic prediction **121**
4.1 Electromagnetic prediction code . . . 121
4.2 Simulation overview . . . 122
4.3 Predictions on avian target models . . . 123
4.3.1 Prolate spheroid models . . . 124
4.3.2 3D bird models . . . 127
4.3.3 Parameters for classification . . . 135
4.4 Man-made aerial targets . . . 141
4.4.1 Dihedral, trihedral and wire scatterers . . . 141
4.4.2 RCS prediction of rotors and propellers . . . 143
4.4.3 Classification of UAVs as UAVs . . . 146
4.5 Precision of electromagnetic predictions . . . 148
4.6 Summary . . . 149

5 Initial measurements **153**
5.1 Measurements . . . 153
5.1.1 K-band . . . 153
5.1.2 Network analyzer at 1 GHz and 4 GHz . . . 155
5.1.3 X-band . . . 155
5.2 Signal processing . . . 157
5.3 Results . . . 157
5.3.1 K-band measurements . . . 157
5.3.2 Network analyzer measurements at 1 and 4 GHz . . . 158
5.3.3 X-band measurements . . . 161

5.4 Summary 167

6 Hardware development of BirdRAD 169

6.1 Required capabilities 169

6.2 System specifications 171

6.2.1 Bandwidth 172

6.2.2 Detection range 172

6.2.3 Pulse repetition frequency 174

6.3 Hardware implementation 178

6.3.1 Pulse- and waveforms 178

6.3.2 Transmitter and Receiver 180

6.3.3 Digitization 182

6.3.4 System control 182

6.4 Pan-tilt unit and camera 183

6.5 System test and characterization 184

6.5.1 Example: ISAR-imaging 185

6.5.2 Stability 186

6.6 System calibration 187

6.6.1 Absolute RCS calibration 187

6.6.2 Field calibration of polarimetric channels 188

6.6.3 Characterization of antennas 189

6.7 Summary 190

7 BirdRAD measurements 191

7.1 Measurement overview 191

7.2 Measurement setup 192

7.3 Targets 193

7.3.1 Birds 194

7.3.2 UAVs 194

7.3.3 Bird measurements 195

7.3.4 UAV measurements 196

7.4 Database 197
7.5 Summary 199

8 Signal processing **201**
8.1 Overview 201
8.2 Demodulation and compression 203
8.2.1 Demodulation 203
8.2.2 Pulse compression 204
8.3 Target signature formation 205
8.3.1 Detection 205
8.3.2 Target time signal reconstruction 206
8.4 Spectral estimation 209
8.4.1 The periodogram 209
8.4.2 Velocity resolution 210
8.4.3 Extraction of measures associated with micro-motion 210
8.5 Extraction of features for classification 212
8.5.1 Spectral features 212
8.5.2 Time domain features 214
8.5.3 Quefrency domain features 214
8.5.4 Polarimetric processing 215
8.5.5 Feature extraction recap 221
8.6 Feature selection 223
8.6.1 Exhaustive search 224
8.6.2 Sequential search 224
8.6.3 Selected approach 225
8.7 Classification 227
8.7.1 Classifier 227
8.7.2 Cross validation 227
8.8 Summary 228

9 BirdRAD measurement results **229**

9.1 Target class characteristics 229

9.1.1 Time domain characteristics 230

9.1.2 Non-polarimetric μ-Doppler features 234

9.1.3 Polarimetric μ-Doppler features 239

9.1.4 Target characteristics summarized 246

9.2 Feature statistics 247

9.2.1 Non-polarimetric features 248

9.2.2 Polarimetric features 248

9.3 Feature selection 252

9.3.1 Single polarized features 253

9.3.2 Polarimetric features 255

9.3.3 Combination of all available features 258

9.3.4 Impact of introducing polarimetric features 260

9.4 Classification results 261

9.4.1 Two classes: *Bird* or *UAV* 262

9.4.2 Three classes: *Bird*, *UAV* or *Unknown* 264

9.4.3 Four classes: *A-D* 265

9.4.4 Comparison of frequency bands 267

9.4.5 Inclusion of radial velocity 269

9.5 Potential sources of error 271

9.6 Summary 272

10 Conclusions and future work **275**

10.1 Summary of scope 275

10.2 Summary of findings 277

10.3 Summary of achievements 279

10.4 Further work 280

Appendices **283**

A BirdRAD hardware **283**

A.1 Transmitter 283

A.2 Receiver 284

A.3 Signal timing 286

B New prolate spheriod model **289**

Bibliography **290**

List of Figures

1.1 Beam pointing in azimuth as function of physical antenna face pointing direction. The beam is scanned forward and backward to maximize time on target in azimuth bearing 180°. The figure is inspired by an unclassified presentation of SAMPSON by BAE Systems. 44

1.2 Suggested adaptation of recognition of biological and meteorological scatterers in blue to well established NATO recognition levels in gray. 48

1.3 Rough illustration of NCTR techniques and their suitability as function of bandwidth, carrier frequency and time available on target. . . 50

2.1 Measured and predicted bird RCS values. Dots represent S-band values from [1]. Note that no values above 2 kg is found. Blue, red and black lines show rough estimations of expected RCS values of birds represented as spheres with reflection coefficient as of water in L-band, S-band and K-band respectively. 66

3.1 Reflection geometry 99

3.2 Reflection coefficient for three different materials. 102

3.3 RCS of a conductive sphere showing three scattering regimes adapted from [2]. Note the logarithmic scale on both axes. 103

3.4 Measured and estimated weight for prolate spheroid and different semi-major to semi-minor ratios m. 106

3.5 Size of prolate spheroid measured in wavelengths along the path of HH- and VV-polarized creeping waves. The prolate spheroid with $m = 3.5$ is illuminated broadside. 107

3.6 Reflection and transmission in different human tissues. Normal incidence. Separate plots for ”bird wings” and ”average bird” based on data from [3]. All other data from [4]. 108

3.7 Estimated differential phase shift from dihedral as function of dielectric constant and illumination angle θ. 113

3.8 Paths of traveling wave for horizontal and vertical polarization adapted from [5]. 114

3.9 Spread in Doppler cells in L- and S-band from different bird species. 60% of the bird wing length is assumed to contribute with a wing opening angle of 120°. CPI is kept at 35% of the time of a wing beat interval and elevation angle is 5°. 116

4.1 Simulation coordinate system 123

4.2 3D models of prolate spheroids with different semi-major to semi-minor axis ratios m 124

4.3 Predicted RCS for HH-polarization σ_{hh} and differential RCS σ_{dr} for prolate spheroid model with c=18 cm and a=b=5.14 cm. 125

4.4 Differential phase δ_{vh} for prolate spheroid model with c=18 cm and a=b=5.14. 126

4.5 3D gannet models created in the Rhinoceros software [6]. 128

4.6 3D models of birds made in the Rhinoceros software. 129

4.7 RCS comparison of prolate spheroid, bird body without wings and bird with wings in level position. Predictions done with FDTD code. 130

4.8 RCS of gannets modeled by different materials. Models 60% of full size and with wings level. All results from predictions by the FDTD code. 131

4.9 Histograms showing RCS of bird model and horizontally oriented bird wing. All models scaled to 60% of full gannet size. Evaluated over azimuth angles $\theta = 0 - 180^{\circ}$. All results from predictions by the FDTD code. 132

4.10 RCS [dBsm] of horizontally oriented gannet wing. Model 60% of full size. Predictions by FDTD code. 133

4.11 RCS of gannet wings of different sizes. All results from predictions with the FDTD code. 134

4.12 σ_{dr} predictions made with the FDTD code of gannet and gannet wing. Model 60% of full size 135

4.13 RCS and σ_{dr} predictions made with the FDTD code of gannet wing across L- and S-band. Model 60% of full size 136

4.14 Differential phase δ_{vh} of gannet with wings and body alone of different sizes for frequencies $f_c \in [1.2, 3.4]$GHz. All results from predictions with the FDTD code 138

4.15 Comparison of σ_{hh} and σ_{vv} for bird with wings 45° up and 45° down relative to model with horizontally oriented wings. Predictions from FDTD code 139

4.16 Differential RCS σ_{dr} as function of wavelength to size ratio at selected illumination angles θ 141

4.17 Dihedral and trihedral. Each side 10 cm. 142

4.18 Differential phase of dihedral corner reflector of 10x10 cm plates made in aluminum 142

4.19 Differential phase of trihedral corner reflector of 10x10 cm plates made in aluminum 143

4.20 3D model of DJI phantom II propeller. Maximum length 22.8 cm, width 2.4 cm and height 1.0 cm. 144

4.21 Prediction of RCS [dBsm] of DJI phantom II 22.8 cm rotor blade. FDTD prediction code. 145

4.22 Kestrel 2000 main rotor blade 146

4.23 RCS of full size Kestrel 2000 main rotor blade, down scaled version to 20% of full size and full sized box model in L- and S-band at different polarizations 147

5.1 K-HC1 hardware 154
5.2 The two targets measured with network analyzer. 155
5.3 The gannets were tracked by a Ku-band system and video well synchronized with the radar data was recorded. 156
5.4 Spectrogram of Mallard duck and Kestrel UAV measured in K-band 158
5.5 Measurements of UAV helicopter at 1 GHz with different polarizations. 159
5.6 Measurements of UAV helicopter at 4 GHz with different polarisations. 160
5.7 Power spectral density of returns from DJI Phantom II rotor blades of different materials at HH-polarization and $f_c = 4$ GHz. 161
5.8 Micro-Doppler signature of flying gannet at different aspect angles. Capital letters indicating position of wings (U=up, M=middle, D=down) 163
5.9 Upper left panel shows measured σ_{vv} of wings, body alone and entire bird as function of aspect angle. The lower left shows ratios between wings and body/entire bird. The upper right panel shows simulated σ_{vv} difference between bird with wings in upper and lower position compared to level wings. Lower right panel shows simulated ratios between σ_{vv} of wings and bird body. Dielectric parameters similar to human skin used in simulations. 164

6.1 BirdRAD antennas, pan-tilt device and video camera. 170
6.2 Calculated detection ranges for BirdRAD using parameters in Table 6.1. 173
6.3 PRF_{bf} [Hz] for sampling every blade flash as function of rotor/propeller blade length L and RPM. 176

6.4 $PRF_{\Delta f_d}$ [Hz] for sampling Doppler shift generated by blade tip velocity as function of rotor/propeller blade length L and RPM. 177

6.5 The BirdRAD system. 178

6.6 BirdRAD system hardware layout. Components in blue indicate L-band, red S-band and green components are common to both frequencies. 179

6.7 BirdRAD control signals. 183

6.8 HH-polarization impulse responses with pulse compression with theoretical LFM pulse in blue and measured frequency response with ripple compensation approach in red. 185

6.9 ISAR images of a Boeing 737-800 formed from HH-channel in S-band with and without ripple reduction applied. 186

6.10 Stability measurements collected over 10 minutes. 187

6.11 Calibration balloon with a diameter of 1.13 m. 188

6.12 Characterization of antenna in anechoic chamber 189

7.1 BirdRAD at Smøla April 2015. 192

7.2 BirdRAD at Ydersbotn April 2016. 192

7.3 Three sea eagles during data collection. 193

7.4 Four of the man-made targets measured with BirdRAD. 195

7.5 Bird aspect angles. 196

7.6 GPS tracks of quadcopter Ravn and fixed wing Multiplex Easystar II. 197

7.7 Distribution of orientation angles of UAVs relative to radar during data collection. 198

7.8 Range and velocities of targets covered in the database. 199

8.1 Software packages developed for processing of BirdRAD data. Both real and simulated data can be used as input to the processing chain. 202

8.2 Different processing steps for signature extraction in the form of screenshots from the processing software. The target is a flapping gannet measured with PicoSAR in X-band. 205

8.3 Velocity resolution for selected dwell times τ_d of 5, 10, 20, 40, 100, 150, 250 and 700 ms. 210

8.4 Spectrogram of flapping sea eagle. σ_{hh} in S-band. τ_d=150 ms. Colours indicate uncalibrated power values. Epoch: 2015-04-25 14:00:44.000. 211

8.5 Feature extraction from time domain signal $\sigma(t)$. 222

8.6 Time consumption for exhaustive search with increasing number of features included. 224

8.7 Feature selection procedure 226

9.1 RCS of crow with flapping wings illuminated at $\theta \approx 140°$. Epoch: 2016-04-13 12:43:07.658. 230

9.2 RCS in S-band of soaring sea eagle seen broadside ($\theta \approx 270°$). Epoch 2015-04-25 14:00:04.000. 232

9.3 RCS of Ravn UAV flying towards the radar ($\theta = -2°$). All relevant polarizations and both frequency bands. Epoch: 2016-04-13 08:11:59.583. 233

9.4 RCS of Multiplex EasyStar flying towards the radar ($\theta = -105°$). Epoch: 2016-04-13 08:36:34.718. 234

9.5 Simultaneous μ-Doppler signatures of flapping crow in L- and S-band. The colour indicates SNR. A threshold of 13.8 dB is applied. CPI τ_d=150 ms. Epoch: 2016-04-13 12:43:07.658. 235

9.6 σ_{hh} time-frequency signature of soaring sea eagle in S-band. The colour indicates SNR. A threshold of 13.8 dB is applied. CPI τ_d=150 ms. Epoch: 2015-04-25 14:00:04.000. 237

9.7 Spectrogram of Ravn UAV in L- and S-band. The colour indicates SNR. A threshold of 13.8 dB is applied. CPI τ_d=150 ms. Note that the velocity axis differ from the other figures. Epoch: 2016-04-13 08:11:59.583. 238

9.8 Spectrogram of Multiplex Easystar model aircraft in L- and S-band. The colour indicates SNR. A threshold of 13.8 dB is applied. CPI τ_d=150 ms. Epoch: 2016-04-13 08:36:34.718. 239

9.9 Spectrogram of differential RCS σ_{dr} for flapping crow. $\tau_d = 150\ ms$. Epoch: 2016-04-13 12:43:07.658 240

9.10 Spectrogram of linear polarization ratio δ for flapping crow. $\tau_d = 150\ ms$. Epoch: 2016-04-13 12:43:07.658. 241

9.11 Spectrogram of co-polarized phase difference δ_{vh}. for flapping crow. $\tau_d = 150\ ms$. Epoch: 2016-04-13 12:43:07.658. 242

9.12 Spectrogram of maximum ψ [°] in polarization synthesis for flapping crow. $\tau_d = 150\ ms$. Epoch: 2016-04-13 12:43:07.658. 243

9.13 Spectrogram of linear depolarization ratio δ and differential co-polarization ratio σ_{dr} for soaring sea eagle in S-band. $\tau_d = 150\ ms$. Epoch 2015-04-25 14:00:04.000. 244

9.14 Spectrogram of maximum δ and σ_{dr} for soaring sea eagle $\tau_d = 150\ ms$. Epoch 2015-04-25 14:00:04.000. 245

9.15 Spectrogram of σ_{dr} Ravn UAV with dwell time $\tau_d = 3$ ms. Epoch: 2016-04-13 08:11:59.583. 245

9.16 Spectrogram of σ_{dr} Multiplex Easystar UAV with dwell time $\tau_d = 150ms$. Epoch: 2016-04-13 08:36:34.718. 246

9.17 Spectrogram of co-polarimetric phase difference δ_{vh}. Multiplex Easystar UAV with dwell time $\tau_d = 150$ ms. Epoch: 2016-04-13 08:36:34.718. 247

9.18 B_{hh} shown as function of Δv_{hh} for all classes available in each band. Data from all BirdRAD collections in the database. Dwell time $\tau_d = 150$ ms. 248

9.19 σ_{dr} based on BirdRAD measurements of fixed wing UAV and flapping seagull. Body/fuselage and rotational parts in solid and dashed lines respectively. Values calculated from spectrograms formed with dwell time $\tau_d = 150$ ms. 249

9.20 δ_{vh} for all bird bodies and fixed wing UAVs in the database. Dwell time $\tau_d = 150$ ms. 251

9.21 BirdRAD measurements. H vs. $\bar{\alpha}$ for all classes. Dwell time $\tau_d =$ 5 ms. 252

9.22 Comparison of classification performance based on single polarized features at two polarizations and in two frequency bands. 255

9.23 Comparison of classification performance based on polarimetric features alone extracted from L- and S-band. 257

9.24 Results of forward sequential search among polarimetric features in Table 8.2. 258

9.25 Comparison of classification performance based on single polarized parameters along and combination of single polarized and polarimetric features. 260

9.26 True positives and false positives in binary classification problem. By adjusting the threshold indicated by the solid black line, the true positive and false negative rate change. 262

9.27 ROC curves for UAV as positive class in the two-class problem. . . 263

9.28 Alternative ROC curve indicating performance of classifier as function of the probability of declaring a class rather than labeling the target *unknown*. 265

9.29 Classification performance in four-class problem in L-band. 266

9.30 Classification performance in four-class problem in S-band. 266

9.31 P_{cc} for classification with $P_m < 0.1$ and $\tau_d = 5$ ms in different frequency bands. Blue line denote HH-features alone, red shows the combination of HH-features and polarimetric parameters and yellow show the performance where radial velocity is included in addition. 270

A.1 Timings of BirdRAD during one full PRI for all four channels . . . 287

List of Tables

1.1 Example of classification tree, adapted from [7], based on definitions presented in NATO AAP-6 Glossary of Terms and Definitions [8]. 47

2.1 Differential RCS, differential phase and cross-correlation coefficient of hydro meteors, refractive index gradients and biota. Values collected from [9–14], all measured in S-band. Rows with multiple values means different values found in the literature. 76

5.1 WBF classification score as function of SNR and aspect angle ©2014 IEEE 166

6.1 BirdRAD parameters used for detection range calculation. 174
6.2 Predefined waveforms for the BirdRAD system. 180
6.3 Phase corrections. 190

7.1 Duration of high quality signatures in the database. 198

8.1 Non-polarimetric features tested for classification. 222
8.2 Polarimetric features tested for classification. 223

9.1 Targets selected for visualization of target characteristics. 230
9.2 Selected horizontal co-polarized features among candidates found in Table 8.1. Feature selection A according to Figure 8.7. 253
9.3 Selected vertical co-polarized features among candidates found in Table 8.1. Feature selection B according to Figure 8.7. 254

9.4 Selected polarimetric features among candidates found in Table 8.2. Feature selection C according to Figure 8.7. 256
9.5 Final selection of features for classification. Combination of polarimetric and HH-polarized features. Feature selection D according to Figure 8.7. 258
9.6 Final selection of features for classification. Combination of polarimetric and VV-polarized features. Feature selection E according to Figure 8.7. 259
9.7 AUC for two-class problem in L- and S-band. Areas are presented for HH-single polarized features and the combination of all selected HH-single polarized and polarimetric features at three dwell times τ_d. 263
9.8 AUC for the two-class problem based on individual L- and S-band measurement and both combined. Areas are presented for HH single polarized features and combination of all selected HH single polarized and polarimetric features at three dwell times τ_d. 267
9.9 Confusion matrix of true positive rates for separation between birds and UAVs based on both HH single polarized features alone with $P_m < 0.1$ and $\tau_d = 5\ ms$. 268
9.10 Confusion matrix of true positive rates for separation between birds and UAVs based on both HH single polarized and polarimetric features with $P_m < 0.1$. $\tau_d = 5\ ms$. 269
9.11 Confusion matrix of true positive rates for separation between birds and UAVs based on radial velocity in addition to automatic selected features with $P_m < 0.1$ and $\tau_d = 5\ ms$. 269

A.1 Components in L-band transmitter 283
A.2 Components in S-band transmitter 284
A.3 Components in L-band receiver channels 284
A.4 Components in LNA unit 284
A.5 Components in S-band receiver channels 285
A.6 Other central BirdRAD components 285

Glossary of Terms

ABF	Adaptive beam forming
ACC	Antenna centered coordinate system
ADC	Analog to digital conversion
ADR	Air defence radars
ADS-B	Automatic dependent surveillance - broadcast
AESA	Active electronically steerable antenna
AOK	Adaptive optimal kernel transform
AM	Amplitude modulation
ATR	Automatic target recognition
AUC	Area under curve
AWG	Arbitrary waveform generator
BAM	Bird activity modulation
BSA	Backscatter alignment
CPI	Coherent processing interval
CW	Continuous wave
CWT	Continuous wavelet transform
DAC	Digital to analog converter
DBF	Digital beam forming
DDC	Digital down conversion
DFT	Discrete Fourier transform
EIRP	Equivalent isotropically radiated power
EM	Electromagnetic
ESM	Electronic support measures

FAA	Federal aviation administration
FDTD	Finite difference time domain
FFI	Forsvarets forskningsinstitutt (Norwegian Defence Research Establishment)
FFT	Fast Fourier transform
FIR	Finite impulse response
FPGA	Field programmable gate array
FMCW	Frequency modulated continuous wave
FSA	Forward scattering alignment
GPS	Global positioning system
GUI	Graphical user interface
HRRP	High-resolution range profile
IDFT	Inverse discrete Fourier transform
IF	Intermediate frequency
IFF	Identification, friend or foe
IFFT	Inverse fast Fourier transform
INS	Inertial navigation system
ISAR	Inverse synthetic aperture radar
IRT	Inverse radon transform
JEM	Jet engine modulation
K-NN	K-nearest neighborhood (classifier)
LDR	Linear depolarization ratio
LFM	Linear frequency modulation
LNA	Low noise amplifier
LO	Local oscillator
LOS	Line of sight
LVTTL	Low voltage transistor-transistor logic
MFA	Multifunction array
MFR	Multifunction radar
MTI	Moving target indication

MTRC	Motion through resolution cells
NCTR	Non-cooperative target recognition
PA	Power amplifier
PCA	Principal component analysis
PDF	Probability density function
PEC	Perfect electric conductor
PESA	Passive electronically steerable antenna
POL-SAR	Polarimetric SAR
POL-ISAR	Polarimetric ISAR
PRF	Pulse repetition frequency
PRI	Pulse repetition interval
PSM	Polarization scattering matrix
PSD	Power spectral density
PWF	Polarimetric whitening filter
RCS	Radar cross section
RF	Radio frequency
ROC	Receiver operating characteristic
RDI	Range Doppler image
RPM	Revolutions per minute
RTI	Range time intensity
SAR	Synthetic aperture radar
SNR	Signal to noise ratio
SPWV	Smoothed pseudo Wigner-Ville transform
STC	Sensitivity time control
STFT	Short time Fourier transform
SVC	Support vector classifier
SVD	Singular value decomposition
SUAV	Small unmanned aerial vehicle
TBM	Theatre ballistic missile
TRM	Transmit receive module

TWT	Traveling wave tube
UAV	Unmanned aerial vehicle
VPA	Virtual polarization adaptation
WBF	Wing beat frequency

List of Symbols

All symbols are defined in the main body of the text. The general ones are also listed here.

Symbol	Meaning
a	Semi-minor axis
A	Anisotropy
A_e	Effective antenna area
B	Bandwidth
B_{dr}	Differential body to total power ratio
B_{hh}, B_{vv}	Body to total power ratio for HH- and VV-polarization
B_{IF}	IF bandwidth
c	Speed of light
C_p	Circumference of bird (around chest)
$dBsm$	Decibel square meter
E	Electrical field
$\hat{f}$	Normalized frequency
f_c	Center frequency
f_d	Doppler frequency
f_{fl}	Rotor flash rate
f_{0hh}, f_{0vv}	Fundamental frequency from spectral analysis of $\|\sigma\|$ for HH- and VV-polarization
f_{prf}	Pulse repetition frequency
f_{rot}	Rotational frequency

f_s	Sampling frequency
G	Antenna gain
H	Entropy
IF	Intermediate frequency
K	Target vector
K_{dp}	Specific differential phase
k	Real wavenumber
L	Length/target size
L_{body}	Length of bird body
L_{tail}	Length of bird tail
L_{tot}	Total bird length
m	Prolate spheroid semi-major to semi-minor axis ratio
m_1, m_2	First and second order spectral moments
$m3_{hh}$, $m3_{vv}$	Spectral moment of third order - skewness for HH- and VV-polarization
$m4_{hh}$, $m4_{vv}$	Spectral moment of fourth order - kurtosis for HH- and VV-polarization
M_{hh}, M_{vv}	Maximum to mean RCS ratio for HH- and VV-polarization
N	Number of rotor blades
n	Pulse number / slow time variable
P_{avg}	Average power
P_{cc}	Probability of correct classification
P_d	Probability of declaration
P_{FA}	Probability of false alarm
P_k	Pseudo probability
p_b	Polynomial representing body in spectrogram
p_t	Polynomial representing target in RTI
q_{0hh}, q_{0vv}	Flash rate extracted from cepstral analysis of $\lvert\sigma\rvert$ for HH- and VV-polarization

q_{0rhh}, q_{0rvv}	Flash rate extracted from cepstral analysis of $\Re(\sigma)$ for HH- and VV-polarization
R_{dc}	Range-Doppler coupling
R_a	Range to center of sample window
R_0	Quantized R_a
rpm	Rotor/propeller rotations per minute
R_b	Inner blind range
R_t	Range to scatterer
R_{max}	Maximum detection range
R_u	Unambiguous range
S	Complex scattering matrix
S_{dr}	Mean frequency of σ_{dr}
S_δ	Depolarization mean frequency measure
S_{hh}, S_{vv}	Mean frequency corresponding to m_1 for HH- and VV-polarization
S_{min}	Minimum signal power required for detection
S_{rel}	Relative scattering matrix
$S_{T,R}$	Stokes vector transmit and receive
s_{if}	IF signal
s_r	Received signal
T	Transmission coefficient, coherency matrix
T_s	Interval associated with range window δR
T_S	Sampling interval
T_p	Pulse duration
t_f	Fast time variable
v_c	Velocity cutoff in clutter rejection filter
v_{max}	Maximum rotor blade tip velocity
v_{tip}	Rotor tip velocity
W_p	Weight of plucked bird
W_t	Total bird weight

Z	Reflectivity
Z_{dr}	Differential reflectivity
α	Real part of propagation constant
$\bar{\alpha}$	Polarimetric eigenvector parameter
β	Imaginary part of propagation constant
$\|\beta\|$	Cross-polarized correlation coefficient
$\angle\beta$	Cross-polarized phase difference
γ	Complex wavenumber
γ_c	Chirp rate
Γ	Reflection coefficient
Δf_d	Frequency resolution
Δv_r	Velocity resolution
Δv_{hh}, Δv_{vv}	Velocity span corresponding to m_2 for *hh*- and *vv*-polarization
$\Delta(n)$	Range difference between pulses
δ	Linear depolarzation ratio
δ_{vh}	Co-polar differential phase
η	Impedance
ε	Permittivity
$\|\varepsilon\|$	Cross-polarized correlation coefficient
$\angle\varepsilon$	Cross-polarized phase difference
λ	Wavelength
μ	Permeability
$\|\rho\|$	Co-polarized correlation coefficient
ρ_{hv}	Co-polar cross correlation coefficient
ρ_p	Average density of plucked birds
σ_{hh}, σ_{vv}, σ_{hv}, σ_{vh}	RCS at *hh*,*vv*,*hv* and *vh*-polarization
σ_{dr}	Co-polarimetric differential RCS
σ_{rt}	RCS for transmitted and received polarization t and r respectively

σ	Electric conductivity
τ_d	Dwell time
τ_{bf}	Time between rotor blade flash
τ_p	Pulse length
τ_{PRI}	Pulse repetition interval
τ_w	Window length
Φ_{dp}	Differential phase
$\hat{\phi}_{rt}$	Doppler spectrum compensated for translational velocity
χ	Ellipticity angle polarization synthesis
Ψ	Inclination angle polarization synthesis
ω	Angular frequency
ω_{rot}	Rotation rate

Chapter 1

Introduction

1.1 Overview

Since the very first radars were introduced more than two generations ago, radar has constantly evolved towards what we today refer to as modern radar. These are systems that in their most advanced form are capable of simultaneously solving multiple tasks such as surveillance, tracking and classification. The main reasons for the improved performance in current systems over older ones are associated with increased sensitivity and resolution, the first allowing for improved detection, and the latter for enhanced classification. Flexibility is another feature that clearly distinguishes newer systems from their predecessors. Modern antenna technology enables adaptive beam steering, while arbitrary waveform generators allows for adaptation of waveform properties from one pulse to the next. Systems with these capabilities are often referred to as adaptive. Such adaptivity is typically required in multifunction radars, where a large number of tasks are to be carried out in a short time. The potential lack of resources requires optimization of time allocated to each task.

One important trend, in addition to adaptivity, is the development of more cognitive systems, commonly referred to as cognitive radar [15]. The demand for both adaptivity and more intelligent resource management arise from the increased sensitivity and number of tasks in multifunction radar systems. Today even what are considered to be adaptive systems are often based on strict rules and thereby

deterministic, however, inspiration from biology is taken to develop future radars in the direction of cognitive systems. The topic of this thesis is non-cooperative target recognition (NCTR) of small and slow moving air targets within the limits of modern/near future air defense surveillance radar systems. The ideas presented are linked to this trend towards more adaptive and cognitive radars, as some rough target classification is considered to be essential in development of future high-performance multifunction air defence radar (ADR) systems.

1.2 Motivation of work

Modern ADRs are, as already pointed out, becoming more sensitive than their predecessors [16], which is believed to be a necessity for detection of low signature targets at far range. Development in analog to digital converters and the introduction of digitization at antenna element level gives increased dynamic range [17] and reduced need for sensitivity time control (STC). In addition, ultra stable waveform generation and local oscillators (LO), allow for enhanced signal processing and detection of small slow moving targets even in dense ground clutter [18]. A consequence of this is a significantly increased number of detections of moving objects, not necessarily targets of interest, which will initiate tracks and thereby require radar resources. In particular, these new targets are slow moving ones at ranges traditionally dominated by the STC or previously filtered out due to wider ground clutter rejection region.

Since the early years of surveillance radar, flocks of birds have been detected. According to Flock [19], many fighter aircraft have been scrambled through the years to identify suspicious echoes originating from bird flocks. With increased sensitivity in modern systems, it is expected that larger single birds can be detected at significant distances as well. As a result, these can represent a potential problem for radars of this class. Reports on modern high-performance multifunction radars in clutter rich environment, like the UK ARTIST technology demonstrator [18] already points in this direction. In the context of resource management, hundreds or thousands of bird tracks will take time away from other important tasks. If these

challenges are not resolved in early stages of target acquisition, the radar's signal processor might be overwhelmed, and thereby prevent detection of potential threats. Following increased sensitivity in radar systems, the need for quick verification of target class rapidly emerges. Distinguishing between biological scatterers and man-made objects is in this context a key capability to maintain radar performance. However, it must be emphasized that this is demanding as the time available for such verification is generally significantly limited.

Beyond preventing saturation of the signal processor, recognition capability is important in order to discriminate between large single birds and unmanned aerial vehicles (UAVs). This is a virtually unachievable task in traditional surveillance radars, as both size and trajectory of the two target classes might be quite similar. Without some advanced classification capability, UAVs that mimic bird behavior, ultimately flying like birds with flapping wings [20], are easily mistaken for birds. In other cases, detection and recognition of birds might be of great interest to avoid collision with aircraft. As the number of both potential bird/UAV misinterpretations and bird collision situations are lower than the number of bird tracks, it will be possible to allocate more time for these tasks. In all cases, the need for fast and reliable classification algorithms arise. Classification based on track kinematics has been suggested and should not be underestimated, however, indications are strong that more advanced classification methods are needed to provide higher confidence in classification [18].

Although modern air defence surveillance systems allow for more target recognition functionality than their predecessors, it must be emphasized that these systems are not optimal for implementation of classification methods. Systems with higher carrier frequency and wider bandwidth, would generally be a better choice if NCTR was the primary task. However, the challenge in this thesis is finding optimal methods within typical limitations found in air defense surveillance systems.

1.3 Long range air defence surveillance radars

Air defence surveillance radar or *early warning radar* are terms frequently used throughout this thesis. These are traditionally military ground based, mono-static, single polarized and powerful systems with the primary task of detecting enemy targets at ranges far beyond the horizon. Historically these systems have operated in L- and S-band, 1-2 GHz and 2-4 GHz respectively, to reduce attenuation through atmosphere and precipitation. Long detection ranges are important to detect potential threats, like enemy manned or unmanned aircraft, cruise missiles or even tactical ballistic missiles (TBM) in sufficient time to respond with the appropriate resources. Nevertheless, surveillance at short and medium range, requiring ground and weather clutter mitigation, have been important tasks. Secondarily, radars of this class have often been used for controlling own air forces and supporting civilian air traffic control when needed. Within this thesis the terms are not strictly limited to the traditional perception, but equally well used in a somewhat wider meaning covering of a modern or future ground based multifunction radar.

Traditionally transmitters in air defence surveillance systems have, due to the high power required, been thermionic tube-type transmitters. This includes high-power oscillators, such as magnetrons or high-power amplifiers such as traveling-wave tubes (TWT) or multi cavity klystrons [21]. Either way each radar consists of one single component responsible for the high power radio frequency (RF) output. This signal has commonly been transmitted by mechanically rotating reflector-antennas. However, in advanced ship and fighter aircraft radar systems, passive electronically steerable antennas (PESA) have dominated the last decades. These are systems making use of one central tube-type amplifier, but passive phase shifters are used for controlling the phase of the signal to ideally each of several elements in an array antenna. Beam steering can this way be done in one or two dimensions depending on system requirements. A combination of passive electronic elevation steering and azimuth scan has been and still is commonly used in several operational systems.

In recent years, solid state transmitters have become more common in modern

early warning radars. In such systems the large central tube-type transmitter is replaced by numerous transistor based transmit/receive modules (TRMs) behind the elements in the antenna front face [22]. These systems are known as active electronically steered/scanned antennas (AESAs). Although digitization of each antenna element is rarely seen in larger systems, the trend is towards less elements in the sub-arrays combining elements before digitization. The main advantages of AESA technology on the transmit side include more flexible and adaptive antenna beam control, lower sidelobe level, more efficient transmit power generation [22] and improved fault-tolerance, also referred to as graceful degradation. On the receive side, the main advantages result from the possibility of implementing multiple receive channels through digitization of elements or sub-arrays of elements, and by that digital beam forming (DBF). This way radars can be designed to provide adaptive beam forming (ABF), highly desirable to counteract the effect of jamming. In addition this architecture allows for increased dynamic range and thus increased sensitivity in the receiver, parallel signal processing of simultaneous receive beams in real time enhancing search and track capabilities and multi function arrays (MFA) [22]. Introduction of AESA and DBF technology in air defence surveillance radars may, by increased efficiency and flexibility, provide the ability to solve tasks far beyond traditional detection at long distances.

Mechanically rotating antennas with additional electronic azimuth beam steering, are in many systems considered to be a good cost benefit solution compared to several static array faces for full azimuth coverage. Further discussion is limited to such rotating systems. Electronic beam steering in these systems gives the ability to compensate for the antenna rotation by pointing the beam in a different direction than the physical antenna pointing direction. Typically this can be used to increase time on target compared to traditional rotating systems, by allowing for forward and backward azimuth scanning of the beam, see Figure 1.1. In this example, inspired by a presentation of the SAMPSON radar by BAE Systems, maximal time on target is achieved at the bearing of 180°given a maximum of boresight scan angle of $\pm 60°$.

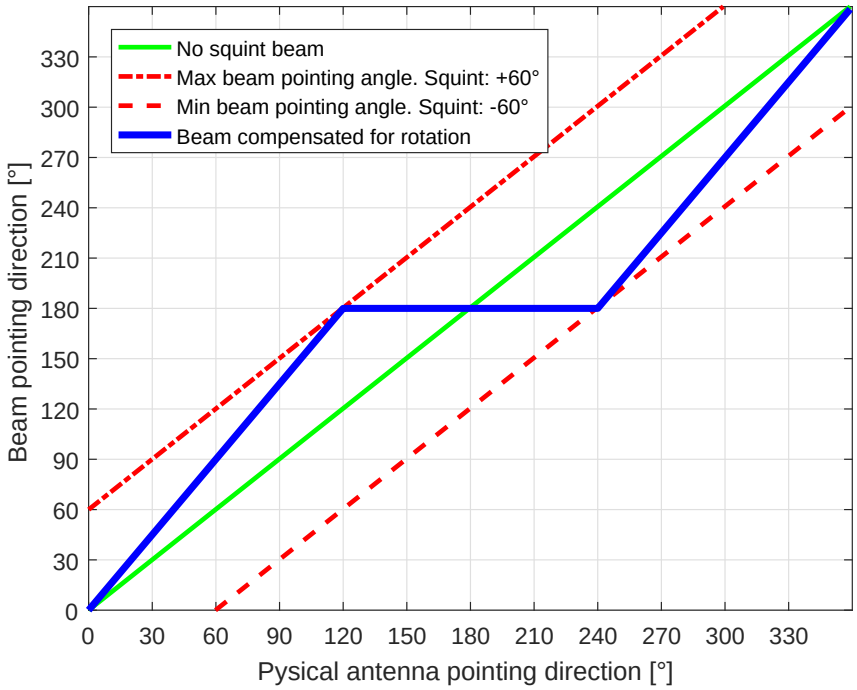

Figure 1.1: Beam pointing in azimuth as function of physical antenna face pointing direction. The beam is scanned forward and backward to maximize time on target in azimuth bearing 180°. The figure is inspired by an unclassified presentation of SAMPSON by BAE Systems.

Time is generally a critical resource in surveillance radars, responsible for searching a vast volume at high update rates and the dwell time at each target is normally short. At the same time, dwell time is an important factor for classification methods relying on velocity resolution, see Chapter 8.4.2 for details. A quick investigation of what dwell times are achievable in different systems is useful. Given a typical 360° rotation period of 12 seconds, identical to 5 revolutions per minute (RPM), and a beam width of 1.5° in both azimuth and elevation, a 2D radar will limit the time the target is in the beam to $\frac{1.5^\circ}{360^\circ} \times 12s = 50$ ms. The same maximum dwell time is achieved in DBF systems, by broadening the transmit beam and performing the elevation scan digitally in the receiver. Alternatively, a PESA system may also achieve identical time on the target by putting the beam at the target and omit any elevation scan. It is worth emphasizing that the latter solution comes at the expense of coverage during that particular scan. Such prioritization of resources is dealt with in the field of resource management, and is further complicated by the introduction of azimuth scan and increasing number of simultaneous tasks. With a

linear elevation pencil beam scan over 20° (not necessarily realistic in long range mode) the dwell time is reduced to $\frac{1.5^\circ}{360^\circ} \times \frac{1.5^\circ}{20^\circ} \times 12s = 3.75$ ms. This means that this is the dwell available when searching the entire volume without any prioritization of any sectors. Including the ability to counteract the antenna rotation, thus prioritizing one look direction, a significant increase in dwell time can be achieved. In the most flexible case, still with the same beam width and rotation constraints, but with additional flexible azimuth scan up to $\pm 60^\circ$ off boresight a time on target equal to $\frac{120^\circ}{360^\circ} \times 12s = 4$ s can be achieved. This rather extreme example require that all resources are put into the task of investigating one single target during the scan.

The effective time available for processing is dependent on range due to the pulse travel time. For a target at 150 km this constitutes 1 ms. As this is subtracted from the beam dwell times, with a rotation rate of 5 RPM one is left with a few milliseconds in a traditional PESA 3D ADR, tens of milliseconds in a 2D or 3D radar with flexible elevation scan and up to seconds in a full flexible 2D radar, all with the same rotation rate and antenna beam widths. Increasing the rotation rate, would be difficult in older radars, however, modern radar may solve different tasks on subsequent scans. By increasing the scan rate to 15 RPM, the task could be divided into three. One scan could be reserved for detection of long range targets with no elevation scan. The next could be left for short range detection with elevation scan, while the last could be used for instance for classification purposes. Still an update rate of 12 seconds can be achieved for long range detections, while $\frac{120^\circ}{360^\circ} \times \frac{60^\circ}{15^\circ} = \frac{4}{3}$ s minus pulse travel time of continuous data collection can be achieved if a flexible elevation and $\pm 60^\circ$azimuth scan is utilized.

1.4 Target recognition

Radar has for decades been a key sensor for detection and location of targets in large volumes, regardless of weather and light conditions. However, the need for distinguishing between targets, and essentially between hostile and friendly ones, has traditionally been solved with additional devices such as identification friend or foe (IFF) systems or to some extent highly trained radar operators [7]. Recognition

based on electronic support measures (ESM) based recognition utilize pulses emitted from the target, and are assessed not to fall under the NCTR umbrella and are therefore not covered in this thesis.

Automated classification based solely on information from radar has proven challenging, however, progress in several areas has been made during the recent years [7]. The field is commonly subdivided into two large groups, namely automatic target recognition (ATR) and non-cooperative target recognition (NCTR). The first mainly dealing with classification of ground targets from an air- or space-borne platform. NCTR covers classification of air targets from a ground or airborne platform. As indicated in the thesis title, methods applicable to ground based radars are covered in the following. NCTR capabilities in such radars are traditionally found in dedicated tracking radars operating at higher frequency, often in X-band and above, and especially as part of weapon systems [23]. However, some classification functionality is found in large modern naval multifunction radars.

The terminology within the field of classification is highly ambiguous, however, NATO AAP-6 Glossary of Terms and Definitions [8] provides a conceptual framework, which will be used throughout this thesis. This document defines concepts forming the basis of a classification tree, clarifying the different levels of classification listed in Table 1.1. As can be seen, the target is through the classification process divided into more and more precise sub-groups, however, there are no absolute boundaries between the different levels of classification. The idea behind this table is to illustrate that widely used terms are reserved for specified levels of classification in NATO terminology, although this may not always be adhered to in the literature.

Target recognition of man-made air targets in custom made radar systems might be considered to be a well established field. The TIRA system operated by Fraunhofer FHR near Bonn in Germany is an example of a radar highly adapted to the task of space object classification. The large bandwidth and high carrier frequency in this system, combined with smooth movement of space objects have resulted in inverse synthetic aperture radar (ISAR) images providing recognition at

Recognition level	Meaning	Example
Detection	Distinguish targets from clutter, interference and noise	Target or not target
Classification	Giving the target a meta-class	Aircraft, tracked vehicle, ship, bird etc.
Recognition	Giving the target a class	Fighter aircraft, tank, destroyer, goose
Identification	Giving the target a sub-class	F-16, Leopard 2, Type 45, Canada goose
Characterization	Finding the class variant	F-16A, Leopard 2A5, Type 45 Batch 1
Fingerprinting	Finding more technical precise analysis	F-16A with AIM-120 AMRAAM, Type 45 Batch 1 with Aster 15 missiles

Table 1.1: Example of classification tree, adapted from [7], based on definitions presented in NATO AAP-6 Glossary of Terms and Definitions [8].

the level of identification and even characterization in Table 1.1. Implementation of such functionality into less specialized systems with other primary tasks, such as air defense surveillance and multi function radars, is on the other hand more challenging. This field is assessed to be more immature. This applies in particular to classification of airborne biological scatterers as birds, insects and bats in surveillance systems. Figure 1.2 shows an example of a classification tree for man-made air targets based on [8] to the left in gray, and a suggested expansion for biological and meteorological scatterers in blue. This figure does not purport to be complete, but illustrates that targets with clearly different functions, defined as target classes by NATO [8], not necessarily are separable with radar. Recognition by radar makes more easily use of other features than function. The level above ”Recognition” in Figure 1.2 is typically divided into containers of targets more easily distinguishable by radar. Throughout this thesis separation between birds and UAVs is the focus. According to Figure 1.2 the term *classification* is then the most correct to use.

Time on target, bandwidth and carrier frequency are considered three key factors for NCTR. In short, as air defence radars traditionally score low on all these it might sound challenging to aim for classification of small targets in such systems. One of the key differences between implementing NCTR in a custom made system

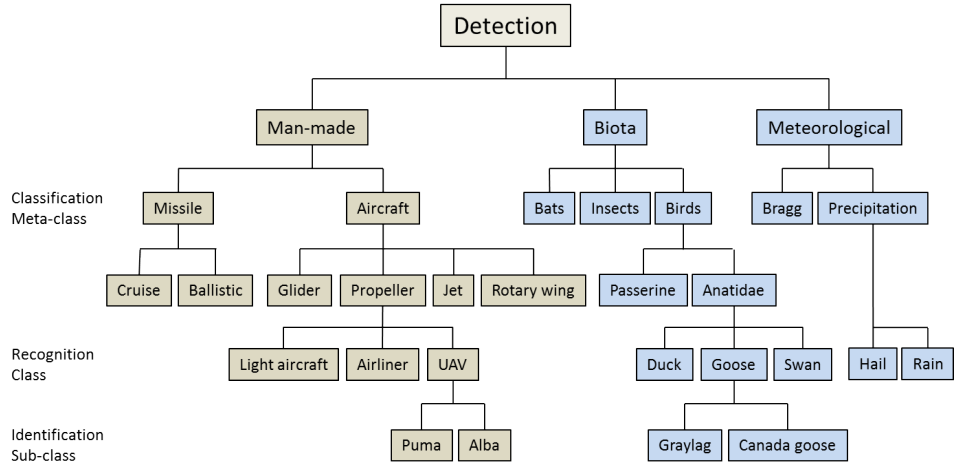

Figure 1.2: Suggested adaptation of recognition of biological and meteorological scatterers in blue to well established NATO recognition levels in gray.

and doing the same in a continuously rotating air defence radar system is as already introduced, the time available for recognition. Although tracking radars as part of weapon systems may have limited time available, the coherent time on target is normally much longer than that available within one scan of a surveillance radar. The bandwidth needed to resolve bird sized targets is unachievable due to frequency allocation, and the low carrier frequency leads to small targets falling in the resonance and even Rayleigh scattering regions.

Figure 1.3 gives a rough impression of some available NCTR techniques and their suitability as function of three basic system properties: time, bandwidth and carrier frequency. The different methods are covered in detail in Chapter 2. It must be emphasized that the suitability of these methods is dependent on properties of both the radar system itself and the object observed, thus the figure must be considered as a rough guide only. The black box in the middle illustrates system properties available in a modern surveillance system. As discussed, modern radars may allow for forward/back-scan to increase dwell time, on which several classic NCTR techniques depend to achieve the required Doppler/velocity-resolution. Especially, the combination of low carrier frequencies and limited coherent processing time (CPI) is bad for velocity resolution. This has typically an effect in micro-Doppler (μ-Doppler) analysis and on cross-range resolution in imaging techniques. This is

roughly illustrated by the blue striped boxes marked *ISAR* and *Micro-Doppler* in the figure, having little volume in common with the radar system. Further on, the available bandwidth, for achieving range resolution, is lower at typical surveillance radar frequencies compared to X-band and above. This is indicated by the location of the *HRR*- and *ISAR*- blocks in the figure. In sum these disadvantages, due to constraints on time available and lower frequencies, lead to reduced recognition capabilities associated with the methods utilizing spatial resolution. Jet engine modulation (JEM) is a technique for fingerprinting of jet engines by determination of the number of blades on the different compressor or turbine stages. This technique has reduced capability at lower frequencies, as penetration into the engine decreases [23]. The *JEM* box is thus found in the lower right corner of the figure.

Recording of multiple polarizations are normally not included in modern air defence radars. On the other hand, there is no physical reason not to. As a polarimetric system requires roughly twice the hardware of a single polarization system, it is all down to a cost benefit analysis. If the usefulness can be documented, air defence radars will be polarimetric in the future. Therefore polarimetric signatures are included and indicated by the yellow volume. These are independent of the system properties on the axes. By extending this volume along the time and bandwidth axis, spectral and spatial information could be obtained as well. Although the information content in polarimetric variables may be limited, it will be available under the constraints on time, carrier frequency and bandwidth, as long as the system allows for multiple polarizations. This makes polarimetric features especially interesting for classification in air defence systems.

Traditional NCTR techniques are covered in more detail in Chapter 2. From Figure 1.3 we understand that the required bandwidth for resolving small airborne targets is not available in frequency bands normally preferred for air surveillance radars. This mean that methods relying on spatial resolution, such as HRRP and ISAR techniques, are excluded as potential candidates for classification in this context. The low capability of low frequencies to penetrate into small jet-engines leads to exclusion of traditional JEM-techniques as well. The methods covered in the

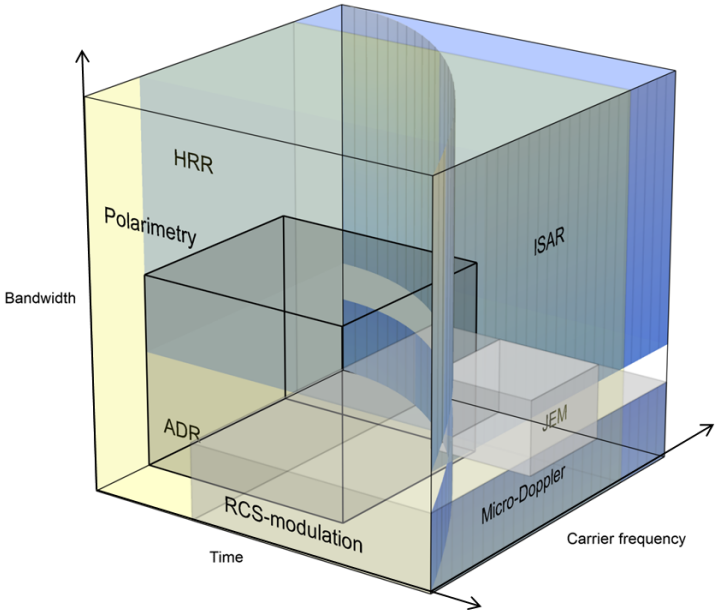

Figure 1.3: Rough illustration of NCTR techniques and their suitability as function of bandwidth, carrier frequency and time available on target.

remainder of the thesis are therefore reduced to methods utilizing:

1. Periodic radar cross section (RCS) modulations
2. μ-Doppler signatures
3. Polarimetric signatures

1.5 Research questions and methods

This thesis focuses on the feasibility of distinguishing between birds and slow moving UAVs of comparable size. The problem is related to the challenges of designing an effective classification routine within the limitations of modern air defense surveillance radars. This includes, evaluating the detectability of such targets, recognizing the challenges of classifying them in such systems, ideally finding characteristic features in radar signatures usable for separation requiring short dwell times and ultimately suggesting an effective classification scheme.

This problem can be subdivided into two closely related research questions:

1. Given the target behaviour and signatures observable with modern or future

air defence surveillance radar in search mode, what is the optimum approach to effectively reduce the number of tracks initiated by birds?

2. Given the target behaviour and signatures observable with modern or future air defence surveillance radar in classification mode, what is the optimum approach to effectively distinguish between large birds, and slow moving UAVs of similar size?

The main difference between the two tasks is related to the time available on the target. The ultimate outcome of the work would be to find methods that classify birds as birds within the dwell time available when the entire search volume is scanned without prioritization, and thereby finding a solution to question number one. This would remove the major factor limiting the achievable quality of surface and slow air pictures in the naval domain today, as well as significantly enhance the quality of air force air picture in coastal areas. This is naturally considered to represent a demanding task. Question number two allow more time to be spent on each target, as this task is believed to be requested less frequently. Therefore a greater variety of potential techniques may be applied. Whereas dwell times available in search mode are of the order of milliseconds, the time on target may now in extreme cases reach seconds. However, the limitations given by surveillance radar properties still makes this a tough challenge.

The problem of biological scatterers in the air is not limited to birds, but to insects and bats as well. The reason for narrowing the scope of this thesis to only involve birds is related to what is believed to be the main future operational challenges for air defence radars provided by biological scatterers in Norway. Since the major part of the surveillance volume of interest is above ocean, coastal areas and close to arctic climate, the presence of insects is considered to be small. The presence of large sea birds, geese and ducks is on the other hand believed to be substantial. In addition the ground velocity of birds is more comparable to small manmade targets. The further delimitation to include only large birds, typically heavier than roughly 0.5 kg, is related to the fact that these are the most easily detectable birds, the largest hazard to air traffic, and also the most challenging to

distinguish from manmade objects.

The influence from sea- and ground-clutter is dependent on the environment, the target's position and radial velocity, the radar's spatial resolution and the velocity resolution achieved as function of carrier frequency and dwell time. Although such interference is likely to be a limiting factor in detecting small and slow moving targets in dense clutter, this is largely disregarded in this study. The problems addressed are connected to classification of already detected targets.

The presented research questions are addressed by analysis of simulations and radar measurements. One important aspect is to understand the scattering mechanisms of both birds and UAVs. Central in this context are the RCS and polarimetric signatures of bird wings, aircraft propellers and helicopter rotors, which is expected to be essential in several classification schemes. Bird and aircraft materials are therefore of interest. Less conductive materials on the target surface may lead to potentially substantial reflections from the target's interior. In this context electromagnetic predictions have proven valuable. For measurements in the relevant frequency bands, highly flexible radar hardware, custom made for the task is developed.

1.6 Novel contributions

The main novel aspects of this work are considered to be:

- Electromagnetic prediction of three dimensional bird models falling in the resonance scattering region with relevant dielectric constant is presented. A special focus is put on the contribution from bird wings to the total RCS depending on polarization, wing orientation and aspect angle.

- Measurements of single wild birds with correlated video recordings and analysis of contribution from bird wings to the total RCS depending on aspect angle in several frequency bands have been performed. Comparison of simultaneously collected L- and S-band signatures of wild birds and UAVs of comparable size is previously not found in the literature.

- Simulations and measurements showing the significance of polarization and dielectric properties on the detectability of bird wings, small UAV rotors and propellers falling in the Rayleigh region.

- Determination of apparent orientation angle of bird wings, rotors and propellers in polarimetric μ-Doppler signatures. The combination of polarimetric parameters and μ-Doppler signatures for this purpose is considered novel.

- Evaluation of polarimetric and non-polarimetric features for separation between birds and UAVs of similar size in modern air defence radar. Methods significantly contributing to classification given both short and long dwell times available are identified.

1.7 Publications

Results connected to research covered by this thesis have so far been presented in the form of one journal article, five conference papers, as well as contributions to two specialist meetings, one book chapter and one NATO task group final report. The latter contribution is due to my participation in the NATO RTO task group SET-180 *Analysis and Recognition of Radar Signatures for Non-Cooperative Identification of Unmanned Aerial Vehicles*.

The following publications and contributions have resulted from the work in this thesis:

- Børge Torvik, Karl Erik Olsen, and Hugh D. Griffiths. Classification of birds and UAVs based on radar polarimetry. IEEE Geoscience and Remote Sensing Letters, Vol. 13 No. 9 pages 1305-1309, Sept 2016.

- Matt Ritchie, Francesco Fioranelli, Hugh D. Griffiths, and Børge Torvik. Monostatic and bistatic radar measurements of birds and micro-drone. 2016 IEEE Radar Conference, pages 1-5, Philadelphia, USA, May 2016.

- Børge Torvik. Measurements of flying birds. Contribution to chapter 4 in NATO STO-TR-SET-180 Final report, NATO RESTRICTED, 2015.

- Børge Torvik. Future NCTR capabilities in air defence radar. Presentation given at Vectors in Radar Technology, London, UK, Nov 2015.

- Børge Torvik and Tor Berger. Target classification challenges in modern long range air defence radar. In NATO STO-MP-SET-228 Radar imaging for target identification, 2015.

- Matt Ritchie, Francesco Fioranelli, Hugh D. Griffiths, and Børge Torvik. Micro-drone RCS analysis. IEEE Radar Conference, pages 452-456, Johannesburg, South Africa, 2015

- Børge Torvik, Karl Erik Olsen, and Hugh D. Griffiths. X-band measurements of radar signatures of large sea birds. In International Radar Conference, 2014, pages 1-6, Lille, France, Oct 2014.

- Børge Torvik, Atle Knapskog, Oystein Lie-Svendsen, Karl Erik Olsen, and Hugh D. Griffiths. Amplitude modulation on echoes from large birds. Proceedings of the 11th European Radar Conference (EuRAD), 2014, pages 177-180, Rome, Italy, Oct 2014.

- Karl Erik Olsen, Terje Johnsen, Oystein Lie-Svendsen, and Børge Torvik. Micro-Doppler signatures of helicopter rotor blades. Chapter 7 in the book *Radar Micro-Doppler signature: processing and applications* [24], pages 187-227, 2014.

- Børge Torvik, Karl Erik Olsen, and Hugh D. Griffiths. K-band radar signature analysis of a flying mallard duck. Proc. 14 th International Radar Symposium (IRS), 2013, volume 2, pages 584-591, Dresden, Germany, 2013.

1.8 Thesis outline

This thesis is divided into ten chapters which detail the aspects of performing classification of small targets in the context of modern air defence radar. Chapter 1 gives an introduction to the topic and presents the research problem, aims of work and highlights the contributions resulting from the study. The next chapter, Chapter 2,

provides an overview of the research context in the form of a literature review. This chapter covers the existing literature on detection and classification of birds, as well as classic NCTR techniques for classification of man-made targets. In this latter part an extra focus is put on publications covering methods considered relevant for classification of bird sized man-made targets.

Theoretical considerations on birds and small UAVs as long range air defence radar targets are presented in Chapter 3. This chapter covers basic electromagnetic scattering theory relevant to mono-static radar, focusing on the reflected fields as a function of target material, its size and the polarization of the illuminating electrical field. Chapter 4 presents results of electromagnetic predictions. This chapter is roughly divided in two, where the first part covers predictions of avian targets, whereas the last one deals with small man-made aerial targets. Theory presented in the previous chapter is investigated in simulations and forms the basis for hypotheses to be further explored. Features expected to be useful in context of classification are identified.

Documentation of initial measurements and results is included in Chapter 5. This chapter aims at showing measurements and considerations forming the basis for further development of hardware and signal processing. Work in the initial phase was connected to detection of bird wings, rotors and propeller in different frequency bands and this is reflected in the chapter. This gave experience for further development of my own radar BirdRAD for investigation of the research questions in relevant frequency bands. A high level description of this experimental system is found in Chapter 6. Here the focus is on system specifications, implementation and calibration. More details on electronic components included in the final design can be found in Appendix A. Chapter 7 deals with the signal processing applied to the recorded BirdRAD data all the way from demodulation and compression to signature analysis, feature extraction, feature selection and classification.

Chapter 8 gives an overview of the radar measurements performed with BirdRAD. This chapter describes the measurement campaigns, the targets involved and the database of signatures resulting from the campaigns. The results from mea-

surements and processing are provided in Chapter 9. Results from analysis of time domain signatures, frequency domain signatures, as well as polarimetric signatures are presented. Special attention is given to feature selection. Finally, results from classification is presented. Classification performance as function of dwell time is investigated for separation both between birds and man-made targets, and in the somewhat more challenging case for distinguishing between the four classes of flapping birds, soaring birds, UAVs with conductive propellers and UAVs with non-conductive propellers.

The thesis is rounded off by final conclusions in Chapter 10. This chapter draws final conclusions of the research and discusses potential future work on the topic.

Chapter 2

Research Context

This chapter focuses on publications relevant to the problem of radar based target recognition of small air targets in lower frequency bands. Literature covering scattering characteristics and radar signatures of small man-made targets and birds is in particular central, however, topics such as scattering caused by insects, precipitation and atmospheric refractive index gradients are also covered. The material is subdivided into two main sections. The first covers literature highlighting detection and classification of birds, whereas the second part is a review of literature on classification of man-made targets. This latter part is focusing on methods relevant for recognizing UAVs of sizes comparable to large birds. To cover the research in these areas, contributions from several research communities have been evaluated. Scientists from different disciplines, like radar engineering, meteorology, entomology and ornithology, have approached challenges connected to small radar targets differently and their findings are published in a large variety of literature.

One problem, which has engaged many scientists through the years, is the mystery of radar echoes from apparently clear atmosphere. Explanations have varied, often depending on the author's professional background. Contributions have come from a variety of disciplines, and proposed explanations have included the presence of local precipitation, atmospheric refraction gradients, insects, and birds. The consensus today is that all these physical phenomena may contribute to clear air echoes. This suggests that evaluating contributions in the literature from several professional disciplines provides the best starting point for moving forward with the

small target classification problem.

2.1 Detection and classification of birds

During the last 60 years, radar has been an important instrument for both ornithologists and entomologists in their studies of birds and insects [1]. This has resulted in numerous articles on detection and classification of birds, insects and even bats. This section of the research context chapter focuses on publications concerning birds. Initially a historical description of the topic is given, followed by a review of papers discussing birds as radar targets and different methods suggested for bird classification. The methods covered are mainly based on analysis of RCS, motion pattern, amplitude modulation of target echo, μ-Doppler signatures and polarimetric dependencies.

2.1.1 The first years of bird detection and classification attempts

Flock and Green [25] give an overview of the first years of detection and classification of birds with radar. According to them the very first observations of birds with radar were done by Page using a VHF radar at 200 MHz on the U.S.S. New York near Puerto Rico in 1939. However, this information was described in an, at the time classified, Naval Research Laboratory report and not published in the open literature until 1956 in [26]. According to the same source Page reported that a boatswain's bird, identified by binoculars, was followed out to a distance of 11,000 yards ($\approx$ 10 km). Interestingly, he describes fading of the echo, and that this was correlated with the bird's wing beating. This is a phenomenon covered in more detail in Chapter 2.1.6 on amplitude modulation.

The first discussions on bird detections reported in the open literature was published by Brooks [27] in March 1945, who wrote that his ornithologist friend serving as a naval officer during World War II told him that "*on numerous occasions the radar equipment in use on his vessel has detected the presence of good-sized birds, albatrosses, man-o'-war birds, etc., at distances as great as five or six thousand yards*". Brooks, who at the time was employed at West Virginia University, also described his plans to investigate detection of birds further. However, no more re-

ports on the topic written by him has been found. The paper of Lack and Varley [28] followed up with a report in October the same year, describing early observations of birds with radar during the war. They refer to secret reports on detections of gannets flying singly above sea in 1941. From these articles there is reason to believe that detections of birds were commonly done during World War II, however, they were not necessarily identified as such.

The importance of echoes from birds as a cause of clutter in surveillance radars may have been underestimated over the years. However, the topic was recognized by Bonham and Blake [26] in 1956, who discovered numerous unexplained echoes they believed originated from birds during measurement campaigns at sea. These were referred to as *phantoms* by radar operators, as these were echoes from apparently clear sky. Other commonly used and appropriate names of the phenomena are *ghosts* and *point angels*. Over the years there has been discussion on what the sources of these phenomena might be. The tendency has been that meteorologists claim it to be weather, entomologist insects and ornithologists birds. One explanation to this might be the different properties of the radars being used. Radars adapted to detecting a specific type of targets, may perform poorly in detecting other kind of objects. According to Skolnik [29], birds are probably the most common source of these phenomena. However, the prevailing opinion today is that apparent clear atmosphere echoes can be caused by a variety of scatterers, ranging from precipitation and refraction index gradients to insects and birds [14].

The idea that the presence of birds may complicate detection of man-made radar targets is not new. However, in contrast to the single bird problem addressed in this thesis the focus has mainly been on bird flocks. These can reach large RCS values, and be detected and tracked in various types of radar systems. According to Flock and Green [25], the RCS of birds flocks, for instance of geese or cranes, can reach values larger than large jet aircraft. However, the same authors claim that RCS and radial speeds may usually be more comparable to light aircraft and helicopters. Further they argue that widely used techniques such as STC and moving target indication (MTI) tuned to suppress land clutter and bird echoes (also considered

to be clutter) easily can conceal targets of interest as well. Even though this was claimed back in 1974, similar techniques are still widely used in long range air surveillance systems in use today.

In his book *Radar Ornithology* [30], Eastwood illuminates the suitability of radar as an instrument for ornithologists. This book was published in 1967 and is the only book to date covering the topic of radar ornithology. Eastwood presents the principles of radar, presumably intended for the typical ornithologist reader, focusing on possibilities and limitations of radar for solving ornithological research questions. The book also covers the topic of bird migration thoroughly. Study of bird migration has been one of the main applications of radar in ornithology. The introduction of radar was in this context a revolution for monitoring bird movements at high altitude and long distances, regardless of weather both during day and in particular at night. Vaughn [1] published in 1985 a thorough review of the main publications covering radar ornithology and entomology. This article gives an overview of the historical development on several important aspects connected to detection and classification of birds.

The publication rate of bird-radar related publications has varied through the years. The 1960s and 1970s seems to have been productive with respect to research in the field. After some quiet decades the topic appears to have gained some popularity in recent years. In connection with recent research within the area of aeroecology, embracing the domains of atmospheric science, earth science, ecology, geography, computational biology, and engineering there has been renewed interest in using radar for ornithological research [31]. The weather radar community connected to the American NEXRAD meteorological radar system has been especially active publishing on the topic in recent years. Although this is an advanced system tailored to monitor weather, the impression is that several of the publications in the field are based on data from systems not especially modern nor advanced. Typically systems are old and discarded military radars, or commercially available products based on primitive maritime navigation radars. This may be sufficient as long as positioning of the birds is central, however, for extraction of signatures for

classification generally more advanced equipment is required.

Another important topic beyond radar ornithology is, and has been for years, the hazard of bird-aircraft collision. Several articles have been published on the topic, and will be presented in the following thematic presentation. In 2000 the Federal aviation administration (FAA) in the USA started a research program to develop a bird radar system from existing FAA radars. After seven years the research was terminated with no result [32]. This indicates that a reliable bird detection system with a sufficiently low false alarm rate is difficult to implement in traditional systems with mechanically rotating single polarized systems. In this context the question of bird classification is essential in order to keep false alarm rate low, and to distinguish between the harmful large birds and the less hazardous small ones. One of the questions to be addressed in this thesis is if system properties found in modern air defense radar systems, such as the possibility for increased time on target, can help classification.

Although detection of birds was reported just after World War II, systematic tracking of birds was not commonly done until 1957-1958 [25]. Continuous tracking and gathering data of flying birds paved the way for bird signature extraction. However, before presenting the suggested classification methods, a closer look at bird RCS and detectability is required.

2.1.2 Bird RCS predictions

Understanding what RCS can be expected from birds and their individual body parts is important to understand their radar signatures, and the potential for using these in classification. In 1985 Vaughn [1] pointed out that "*At present it appears impossible to describe σ for birds and insects in detail*". Since then, the access to RCS prediction codes and processing power has increased dramatically. Yet, no description of RCS prediction of birds beyond use of simple geometric shapes and point targets has been found. Challenges connected to RCS prediction of birds discussed in the literature, are mainly related to the ratio between target size and radar wavelength, as birds tend to fall in either the Rayleigh, resonance or optics scattering region depending on bird size and wavelength in use. Other factors are

non spherical body shapes causing aspect and polarization dependencies, movement of the non-rigid body including wing beating, head turning and breathing, as well as various scattering properties across the bird body. The result from these processes is RCS values fluctuating with time and bird behavior.

The earlier mentioned paper by Lack and Varley [28] reported that "*single birds may give echoes not much smaller than those from metal spheres of comparable size*". Schaefer [33] discusses RCS and polarization dependencies of birds at radar frequencies in detail. The lack of modern RCS prediction software left Schaefer with two idealized body shapes, a sphere and a prolate spheroid bird model. The volume of these shapes corresponded to them being filled with water with a weight equivalent to that of the bird. In his discussion of the sphere model, he suggests S-band as the preferred frequency band for bird detectability. This assumption is based on the alleged minimal absorption in bird materials at these frequencies, and that contributions from internal resonance within the body of small birds may be large and add constructively to specular reflections and creeping waves. This would then result in a large total RCS compared to measurements at other frequencies. These claims are also based on the assumptions of spherical shaped birds and having the size of a goldcrest. This bird size was chosen to show the increased visibility of the smallest bird in Europe and by that substantiate the increased detectability of birds in general. This claim appears weakly founded, firstly because the biological tissues covered in the online database [4] show monotonically increasing absorption with increasing frequency. Secondly, because resonant effects in real birds is difficult to predict, as these depend on radar wavelength, bird size, shape, fat percentage and orientation. Interference between specular, creeping and internal waves may easily end up destructive.

Schaefer claimed in the same paper that a prolate spheroid, an ellipsoid of revolution about the long axis, is a better bird scattering model than the sphere. He suggested the major- to minor-axis ratio of 2:1, based on measurements of nine different bird species. The suggestion of this simple shape reflects his opinion that contributions from wings, neck and head is more or less negligible in lower radar

frequency bands. This is of importance as bird wings may be associated with micro motion usable in Doppler analysis if the backscattered power is high enough.

2.1.3 Contribution from bird body parts to overall RCS

An evaluation of the contribution from wings and other body parts to the overall echo is important to better understand the underlying physical processes causing characteristic signatures in bird data, as well as for evaluating the suitability for different classification methods. Schaefer investigated this theoretically and presented in [33] electromagnetic properties of different materials found in birds estimated for S-band frequencies. These are mostly estimations based on measurements of human tissue. However, birds were dissected to find the weight distribution between different body parts. Based on this Schaefer concluded that due to the rather small variations of dielectric constants between different body parts, one average value of $\varepsilon = \varepsilon' + j\varepsilon'' = 44 - j14$ was an acceptable approximation for the entire body. Note that this applies to S-band. Schaefer refers to an unpublished measurement of the complex dielectric constant of bird feathers in S- and X-band. This was carried out by Coultas and Houghton in 1959, and Schaefer states their findings to be $\varepsilon = 1.25 - j0$ which is rather close to the value of air, and therefore that the plumage may be disregarded as a contributor to the total echo. This view is supported by the experimental results presented by Edwards and Houghton [34], where a dead rook was measured with the same result both with and without feathers. The plumage was also measured alone to a RCS value of -43 dBsm.

The importance of wings as radar reflectors has received some attention. Schaefer reported that the contribution from bones in bird wings and legs can be neglected as scatterers. Nevertheless, he allows for the possibility of a small contribution from the wing stubs with high water content, but concludes that bird echoes arise predominantly from the thorax, abdomen and pulled-in thighs.

Some experimental results also points in the same direction. Blacksmith and Mack [35] presented RCS measurements of living ducks and chickens, and stated that "*spreading or folding the wings had a negligible effect on the results.*" These measurements were done with vertical polarization at 400 MHz, and large variance

in the data was attributed to the variation of head and neck position between measurements. The lack of influence on the RCS measurements by spreading the bird's wings may be due to the wings being in an orthogonal position with respect to the E-field. Blacksmith and Mack did not provide a detailed description of their experiment. However, they seem to have struggled considerably with birds sabotaging the experiments and describe the problems of measuring living birds very well. In despair of birds not sitting still for RCS measurements, they conclude by referring to the cookbook *Joy of Cooking* for suggestions on how to best make use of agitated birds.

Furthermore, Edwards and Houghton claimed [34] that "*These outspread wing views of the bird [...] differed from the broadside measurements [wings closed] by less than 5 percent*". This has by several, like [30] and [33], been interpreted to mean that wings do not contribute significantly to the overall RCS of birds. However, there are several aspects that undermine the basis for such a conclusion in the paper. The fact that Edwards and Houghton measured RCS of dead birds, contributes to questioning of the findings. According to Vaughn [1], the RCS of such birds will differ from living ones. He explains this by claiming that "*the geometry of the free liquid (i.e. blood plasma) in any animal changes immediately after death: It flows to the lowest part of the body.*" This is claimed to be significant for RCS measurements of wings, as the vascular liquid in these will flow into the bird's body. The interstitial and inter cellular liquid will on the other hand, according to Vaughn, "*stay in place and slowly evaporate*".

Edward and Houghton's measurements were done with the wings spread at back and belly views only, and compared to broadside. The geometry in their experiment is described rather poorly, so how the wings actually coincided with the E-field during measurements is uncertain. Polarization is believed to be an important factor when evaluating bird RCS at low frequencies. Vaughn [1] in fact argues that the wings may contribute substantially to the overall RCS, and that the geometry of the wings and polarization is of great importance.

Green and Balsley [36] presented a spectrogram of a flying Canada goose in

1974, which indicate that the wings in parts of the wing flapping sequence return more power than the body. These data was collected at an azimuth angle of 45°. Data showing contribution from wings is later presented in several other papers like [37] and my own papers [38–40]. In such spectrograms the contributions from the moving wings can be isolated as their Doppler shifts differ from the main body in parts of the wing flapping sequence.

2.1.4 RCS measurements

RCS measurements have been done of different bird species and at different frequencies. Large variance in the results is seen, which may partially be explained by variable experiment quality. The already cited article by Vaughn [1] includes a figure of "[...] *virtually all bird and insects measurements reported prior to 1984*" in his paper. These are measurements in UHF-, S-, C- and X-band, without specification of polarization and bird orientation, and is partially reproduced in Figure 2.1. As he points out himself in a foot note, he missed the L-band experiments of a goose and two ducks by Mack et al. from 1979 [41]. This paper reports on controlled measurements of living birds at VV- and HH-polarization covering 180° in azimuth angle at 5° intervals. It is obvious from this paper that measurements of living birds in a controlled environment is challenging and introduces uncertainty due to the bird's exact orientation. In addition the birds were often sitting, with the wings folded and the neck only partly outstretched during the measurements. This is a position of the body rather different from the natural during flight, and must be considered to be of less practical importance. The report clearly shows larger RCS of the bird seen from the side compared to from the front or tail. Generally larger RCS with horizontal polarization is seen. No measurements of RCS of birds were found for the period from 1985 until today. It is also worth noting that only values for birds less than 2 kg are found.

2.1.5 Motion pattern

The air speed of migrating birds is claimed to be a good aid to distinguish between avian and non avian air targets. According to Schaefer [33] the main problem is to

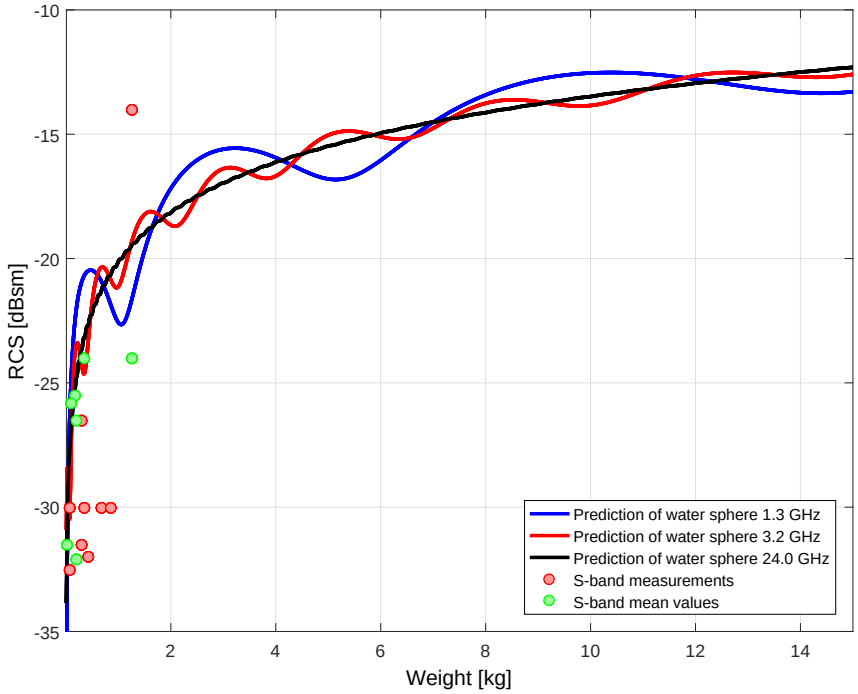

Figure 2.1: Measured and predicted bird RCS values. Dots represent S-band values from [1]. Note that no values above 2 kg is found. Blue, red and black lines show rough estimations of expected RCS values of birds represented as spheres with reflection coefficient as of water in L-band, S-band and K-band respectively.

measure it properly, as only the ground speed can be derived from radar measurements. The findings of Emlen in his study of migrating sparrows with accurate wind information at different heights [42] is in contrast to this. His results showed that the air speed was highly variable. In fact the birds were speeding up in head winds and slowing down in tail winds, making the ground speed more constant. The adjustments in air speed was determined to be 2/3 of what the wind induced changes to ground speed would have been if flying at constant air speed. One explanation might be that birds use visual references when controlling flying speed. The wind speed compensation is best documented in head wind, and in this case the reason is believed to be to reduce the power expenditure by minimizing the flight time in head wind [43].

Moon published in 2002 an article [43] on flying behaviour based on measurements of 72 different bird species gathered after 1980. One of his histograms shows a mean air speed of 14.4 m/s across all species, and the existence of species regularly reaching air speeds above 20 m/s. Moon highlights that a bird's air velocity

generally increases with increasing weight, decreasing wing size, increasing flying altitude, during migration and naturally when chasing or being chased. All birds tend to fly somewhat slower than their maximum speed during regular flight. Moon also presents data on flying altitude of birds. According to him 50% of birds in Europe fly below 700 meters, and 90% fly below 2000 m. However, Moon refers to identification of a flock of 30 swans at an altitude of 8200 m above the Hebrides and a bird-aircraft collision at 11.300 meters above West Africa indicating that birds can fly surprisingly high. In his article published later the same year [16], Moon concludes that there is considerable overlap between bird tracks and those of man-made targets. On the basis of these two articles, the two most relevant on the subject, the requirement for methods based on other discriminants is conspicuous. However, track and context based methods may give important inputs in the classification process. This is shown in the work of Mohajerin et al. [44]. They showed good track based classification performance on simulated UAV tracks merged with real aircraft and bird tracks.

2.1.6 Amplitude modulation of backscattered waveform

As mentioned in Chapter 2.1.1, Page was probably the first to describe bird detections, described fading of the echo amplitude which was correlated with the bird's wing beating. One of the first papers showing amplitude modulation was published by LaGrone et al. [45] in 1964, showing a RCS calibrated bird signature of a Turkey buzzard with oscillating RCS level. Utilization of this effect of temporal fluctuation of RCS is thoroughly described by Houghton and Blackwell [46], and is in this paper referred to as Bird Activity Modulation (BAM). These modulations can according to them originate from wings, head turning or rapid aspect changes. As discussed in Chapter 2.1.3, Schaefer published a thorough paper on bird signatures [33] where he presents his doubts about wings causing the amplitude modulation alone. This is an interesting question, and it is quite possible that the modulation is caused by several processes. The modulation index or modulation depth, known from amplitude modulation techniques in communication technology, is a value describing the extent of the modulation and gives an impression of how strong the fluctuations

in amplitude are. By inspection of figures presented in [46], a modulation index of 25-40% seems typical. Interference between different scatterers may lead to fluctuation due to small changes in orientation dependent on bird size compared to wavelength in use. An example of this can be is found in my own paper [40], where fluctuations uncorrelated with the wing beat frequency are found in measurements of gannets in X-band.

The amplitude modulation technique for bird recognition makes use of the potential oscillating amplitude of echoes from birds to extract the wing beat frequency (WBF). A coherent radar is not required, however, the amplitude modulations will naturally also be present in bird signatures containing Doppler information. In 1960 Greenewalt [47] substantiated that wing beating of birds and insects in general can be described as a mechanical oscillator with resonance frequency equal to the WBF, based on high speed camera studies of a ruby-throated hummingbird. The thorough work of Perslew [48] shows the complex kinematics of avian wing movement under different flying conditions. His results show that wing beat kinematics vary with cruise speed.

The relationships between wing length and WBF, and between bird mass and WBF is discussed in [49] and [50] for 80 bird species, and the WBF of a selection of 41 species was verified and tabulated by Houghton and Blackwell [46] in 1972. They suggested that BAM waveforms could be used to classify an object as a flying animal, and how they combined with other information such as speed, regional location, abundance and seasonal distribution of species, could be used to classify bird species. It was suggested that this could be done by determination of the fundamental frequency component in the signal and comparison with known wing beat frequencies. The paper explains the theory based on measurements of single birds, however, they claim that good results can be achieved with a low number of birds within the resolution cell as well. This view is also supported by Flock [51]. He emphasizes that the amplitude modulations on the returned signal are not sinusoidal in general, as both fundamental and harmonic frequencies may be present. He suggested that the harmonic components may add information and contribute to

identification of signatures from single birds. However, with several birds within the resolution cell only the fundamental frequency component is supposedly of use.

The ability to identify bird species based on WBF requires constant and separable values from other species during flight. According to Emlen [42], who studied RCS, WBF, length of flapping periods and length of pause periods and air speed of flying birds, found that the WBF was one of the most constant measures. However, he found a slightly increasing flap rate with increasing air speed. Bruderer [52], also investigated this and found that the WBF varied up to $\pm 15\%$ for migrating birds and up to $\pm 30\%$ for three species in nonmigratory flight. Regarding flap and pause periods, [42] concluded that variability of these measures for passerines was so high that their value in "*fine-scale partitioning of passerine signature types*" is questionable.

The presence of wing beat modulation on data from birds tracked by radar is essential if this method shall contribute to bird classification. However, publications such as [53] by Ireland and Williams in 1974 suggest that this may not always be the case. In their report 40% of the tracks of birds over Bermuda were categorized as having *irregular* (in contrast to *bursting* and *continuous*) amplitude modulation, meaning that no clear fundamental frequency component could be found. The reasons for this could be that a flock was being tracked, low signal to noise ratio (SNR), the bird was soaring, the target was not a bird, or the aspect angle led to a poor amplitude modulation signature. Ireland and Williams segmented their data into four groups depending on heading of the bird's flight. The percentage of tracks with no amplitude modulation identifiable as wing beating varies across these groups, and may be influenced by aspect angle variances. However, there is not enough information in the article to conclude on this. Vaughn [1] also claims that the amplitude modulation at the wing beat rate is highly dependent on aspect angle.

The physical cause of the amplitude modulation has been discussed. Schaefer claimed [3] that the major reason, along with small contributions from wings and aspect angle changes, was due to rhythmic expansion and contraction of the bird's pectoral muscle, flexing and bending of the rib cage, and enlarging and contracting

of the abdominal cavity. On his prolate spheroid bird model, this would give constant length of the major axis, however, the minor axis would oscillate in length. These variation could according to him lead to constructive and destructive interference of the creeping wave (he assumed the bird to be in the resonance region) explaining the RCS variations. According to Schaefer a change in the minor axis of 10% is enough. Vaughn [1] disagrees with this, as he points to the wings as a main source of contribution. The fact that the wing forearm of many species is close in length to a half-wave or full-wave dipole antenna at commonly used radar frequencies, is central in his argumentation for the amplitude modulation originating from the wings.

The amplitude modulation method for bird classification is independent of carrier frequency. The modulation of the backscattered waveform is caused by temporal variation in target RCS, and the radar's ability to determine this accurately is dependent on the frequency resolution given by the observation period of the signal. This is unlike the velocity resolution required in μ-Doppler analysis where the wavelength is a key parameter. A disadvantage of this method when evaluated for implementation in an air defense surveillance system, is the long observation time required to achieve this resolution. A resolution of one Hz, to determine the WBF normally in the range 3.6-9.6 Hz [46], would require one second of target observation. This is technically achievable in a modern surveillance system, however, it might come at the expense of other tasks. A well designed resource management system would be required to allocate the resource to such a task, without severely reducing the quality of the performance of other tasks.

2.1.7 Doppler and μ-Doppler Signatures

A target moving relative to a radar induces a frequency shift, or Doppler shift f_d, of the backscattered echo relative to the transmitted carrier frequency f_c. Any additional rotational motion to the translational velocity of a rigid target can be defined as *micro motion*, which causes micro-Doppler (μ-Doppler) shifts. According to Chen's book *The Micro-Doppler effect in radar* [54] such movement can be rotating propellers of a fixed wing aircraft, rotating rotors of a helicopter, rotating antennas,

flapping wings of a bird, swinging arms and legs of a moving person etc. In general Doppler signatures of birds give information on radial velocity, variable velocity of wing segments and wing beat rate [36]. This information can be extracted from the time-dependent Doppler spectrum as it contains information on both range rates and amplitude variation. Towards the end of his book Chen gives a superficial review of some of the earlier publications on μ-Doppler signatures of birds and proposes a kinematic model for simulation of the μ-Doppler shifts from a flying bird. This is a model built up of ellipsoids. One ellipsoid constitute the body, whereas the wings are composed of three ellipsoids connected in the joints. Such a model can be used to roughly predict the appearance of the μ-Doppler signature. However, as each body part is inaccurately modeled with respect to shape and material, and any interaction between body parts are disregarded, it can never give a precise prediction of the full μ-Doppler signature. On the other hand, combining exact electromagnetic prediction of three dimensional bird models with realistic movement is challenging and may not be worth the effort.

Vaughn [1] gives a thorough review of the earlier work on the topic. The most important articles from the early years of Doppler signature extraction from bird measurements are found in [36, 51, 55]. Green was according to [51] the first to publish Doppler signatures of birds. This work, done with a simple CW radar, was published in [56][1]. The report *A preliminary investigation of bird classification by Doppler radar* written for NASA by Martinson in 1973 [55] covers the concept of bird signatures in Doppler spectra. Based on X-band Doppler measurements of small and large birds, he emphasized the need of frequency resolution and the maximum CPI limited by the wing beat frequency. In reality he points at the relationship between velocity resolution, wavelength and integration time available when using Fourier based spectral estimation methods. Even in X-band, he claims that signatures only from the largest birds, the ones with the lowest WBF, will be useful. To ensure suitable velocity resolution for adequate signature extraction he suggests that increasing the carrier frequency is required. This is relevant as this thesis deals with

[1] report inaccessible

surveillance radars in L- and S-band.

In their paper from 1972, Green and Balsley [36] present different analysis techniques for Doppler signatures. This is the *sonogram*, *the time dependent spectral analysis* (spectrogram), *time-averaged power spectrum*, *the audio technique* and the *audio-visual technique*. The audio techniques were based on Doppler frequency shifts falling in the audio range (typically down converted from RF by homodyning), and that the human ear and brain are excellent at recognizing sounds. This technique has later been widely used in military equipment for manual classification of humans, vehicles and tanks etc by radar. The use of this technique is described in [57]. The time dependent spectral analysis, hereafter referred to as a spectrogram, was according to the authors considered to be very promising, but also seen as complex at the time. In [36] the first spectrogram of birds, a Canadian goose, was presented. This is the first strong indication found that shows that the wings may be important contributors to the overall RCS.

In his paper from 1976, Flock [19] points out the value of Doppler signatures in addition to the amplitude signatures more commonly used at the time. He stated that "*[. . .] the combination of amplitude and Doppler spectra or signatures is potentially more useful than one type alone*". Exactly how, he does not write.

As discussed in Chapter 2.1.6 there are several articles dealing with the relationship between WBF and bird dimensions. Vaughn [1] found that an increase in wing length of a factor of ten, only increases the maximum Doppler bandwidth about 60%. This is due to the decreasing WBF with increasing wing length, resulting in a partial compensation of the maximum Doppler shift. There are also reports on use of the spectral width for classification of birds in weather radars. Gauthreaux et al. [58] shows that the width of the spectrum from birds is different from insects. This is based on data of birds flocks and swarms of insects, and not studies of single individuals. The width of the spectrum referred to is therefore considered to be influenced by the variation of an individual bird's radial movement and not the spectrum width caused by flapping wings alone.

2.1.8 Analysis of μ-Doppler signatures of non-rigid targets

No specific literature on utilization of attributes from bird μ-Doppler signatures has been found. However, examples of such for human gait analysis has been documented in the book *The Micro-Doppler Effect in Radar* by Chen [54]. Humans are examples of non-rigid targets. These are targets where the distance between scatterers is not constant during motion. According to Chen biological non-rigid targets can be modeled as jointly connected segments, and their motion can be treated as the motion of multiple smaller rigid bodies. Although human radar signatures are not central in this thesis, the methods applied for analysis of such targets may be relevant for classification of birds.

Biological motion contains large amounts of information to which the human visual system is highly sensitive. Troje [59] refers to several studies claiming to determine gender, recognize emotions and even identify individual persons from human gait. It is worth emphasizing that these are based on analysis of visual observations rather than μ-Doppler signatures. The latter task is according to Chen still challenging [54]. He briefly covers methods providing statistical decomposed components like principle component analysis (PCA) and singular value decomposition (SVD). However, the uncorrelated or independent components resulting from these techniques are according to Chen not necessarily associated with μ-Doppler signatures from individual body parts. In fact he underlines that such signatures are often correlated and dependent, as movement of body parts often are synchronized. In the case of small targets de Wit et al. show in [60] that features extracted with SVD applied to X-band spectrograms of small targets correspond well with physical features like target velocity, spectrum periodicity, and spectrum width. This might be connected to the inner structure of μ-Doppler signatures of targets like birds and UAVs being less complex than human motion. In [61] Raj et al. show that a lot of information can be extracted from the envelope of the time-frequency signature of the human gait. This implies that such rather simple methods for feature extraction in time-frequency representations may be good enough when dealing with small targets.

Target classification by μ-Doppler has also been exploited in the acoustic domain. Balleri et al. [62] describe classification of a person undertaking different actions, and different actions performed by different persons by use of an acoustic sensor. In this article the performance of combinations of three different feature extraction methods, PCA, Cepstrum, and MEL Cepstrum, and two different classifiers are evaluated. These are the Naïve Bayesian and the K-nearest neighborhood (K-NN) classifiers. The best results were found when combining PCA and the Naïve Bayesian classifier.

2.1.9 Polarimetric signatures

Using polarimetric signatures has been suggested as a means to distinguish birds from insects, precipitation, ground clutter and scattering due to refractive index gradients in the atmosphere. The major part of publications on this topic originate from the meteorological radar community, where in recent years polarimetric variables have commonly been used to distinguish between different kinds of precipitation in S-band. Beyond this, detection and classification of birds and insects has been, although in a small number, covered regularly in the radar meteorology literature since the 1990s. The publications largely focus on the challenge of distinguishing biota from precipitation, for the purpose of preventing birds and insects influencing Doppler frequency measurements for wind speed calculations. The magnitude of traditional single polarized reflectivity (RCS per unit volume) is important, however, experimental utilization of polarimetric variables for classification of scatterers is documented. Suggested methods include use of differential reflectivity, from now on referred to as differential RCS σ_{dr}, co-polarized cross-correlation coefficient ρ_{hv} and differential phase between orthogonal linear polarizations Φ_{dp}. Description of these variables are given in Chapter 3.

The basis for investigating these parameters in weather radar is the assumption of radar scatterers falling in the Rayleigh scattering region. These can based on scattering from small targets, for instance rain drops, be used to estimate its shape and size as explained in Chapter 3.5. The basis for expanding this theory to larger targets like birds is generally not well founded in the publications in the area. This

is a topic addressed later in this thesis.

Although polarization effects are described in earlier papers, the first publication on characterization of biota and weather by polarization dependencies was written by Mueller [63] in 1983. He describes how differential polarization based on orthogonal linear polarization measurements can be used to distinguish between insect-, bird- and meteorological echoes. In data from the CHILL radar[2], he found aspect independent mean differential RCS values for insects of 0.9 dB. Later Mueller and Larkin [64] found differential RCS up to 7 dB and aspect dependencies in measurement of insects migrating with the wind, clearly differing from the first findings of Mueller. This was later confirmed by measurements done by Zrnic and Ryzhkov [14], finding σ_{dr} around 2-10 dB for insects. This deviation from Mueller's findings is explained by the insects in Mueller's data being passive tracers of the wind, and thus randomly oriented. The values of σ_{dr} are assumed to be linked to the length to width ratio of the target body and explained with Rayleigh theory. A prolate spheroid is a commonly used model for both birds and insects in this context. According to [1] major-axis to minor-axis ratios of 2:1 to 3:1 are typical for birds, while ratios from 1:1 to 10:1 can be found for insects. This taken into account, the span in insect σ_{dr} measurements is not surprising. Actively migrating insects would be more co-oriented, and recent data on the topic tends to show differential RCS values for insects in the range from 4-10 dB [12,65,66]. Mueller and Larkin later suggested [64] the use of this effect to distinguish between insects as passive tracers and or active migrants.

Mueller also measured birds in his experiment. These were classified as birds by use of a telescope and a spotlight, however, the actual bird species is not mentioned in the article. The equivalent mean σ_{dr} value for a flock of birds, estimated to be 20 - 50 individuals in Mueller's measurements [63] was 3 dB. These were collected over azimuth angles between $0-360^{\circ}$, and tended to be more aspect dependent than the insects. The highest differential RCS values were found for broadside views, as Mueller expected according to the prolate spheroid scattering model

[2] S-band according to [64]

assumed. However, he found considerably lower σ_{dr} when illuminating the birds from behind compared to from the front. This difference was not expected and could not be explained by the same model.

Zrnic and Ryzhkov also presented σ_{dr} values from flocks of songbirds in their two thorough articles [14] and [10]. They found values in the range from -1 to 3 dB in their experiment, assumed to be values from all azimuth aspect angles, however, this is not clearly stated in the articles. The findings are considered to be somewhat lower than those of Mueller [63]. More measurements of σ_{dr} are presented in Table 2.1. The variance in reported σ_{dr} measurements is high. The main reason is believed to be differences between species, birds not being prolate spheroids, potential resonance effects, and orientation of the birds during measurements.

	Hydro meteors	Ground clutter	Insects	Birds
σ_{dr} [dB]	$-$1-5	0	2-10	$-$1-3
			4-9	2-5
			5-10	$-$5-10
$\Phi_{dp}[^\circ]$	~ 0	0-360	5-40	70-100
				70
			60-100	$-$90-90
ρ_{hv}	> 0.8	< 0.7	0.3-0.4	0.5
				< 0.8

Table 2.1: Differential RCS, differential phase and cross-correlation coefficient of hydro meteors, refractive index gradients and biota. Values collected from [9–14], all measured in S-band. Rows with multiple values means different values found in the literature.

The co-polar differential phase Φ_{dp} has contributions from both a backscatter and a propagation component when measuring volume clutter. In observations of biological scatterers in such clutter, Zrnic and Ryzhkov [14] found that the backscatter component dominates. If this is true in large weather radar resolution cells, it is certainly valid in smaller cells provided in modern air defence systems. However, the influence on Φ_{dp} from transmission through precipitation between the radar and the target might be a possibility. More details on this topic can be found in Chapter 3.5.5. Claims that measurements of Φ_{dp} can contribute to the classification of bird are presented by several authors. Zrnic and Ryzhkov presents in [14] Φ_{dp} measure-

ments of birds between 70°and 100°[3] and insects in the range between 5°and 40°. According to the authors these phases clearly differs from the differential phase of rain, which is expected to be close to 0°. Zhang et al. [13] presents differential phase measurement of birds and insects in the same frequency band. The values presented for birds is rather constant at an average value of 70°, while the same values for insects is around 30°. Bachmann and Zrnic found differential phase values of insects almost 30° higher than previously reported by Zrnic and Ryzhkov [14] and Zhang et al [13] as values from $60° - 100°$ were found. The values were taken from spectral density plots, so contributions from scatterers of different velocity were filtered out in contrast to earlier reports. It should be noted that these values are measured in S-band, and are according to theory presented in Chapter 3.5 expected to be sensitive to target size and orientation. The eagerness to find constant values of Φ_{dp} for birds is in light of this a bit odd. However, Zrnic and Ryzhkov [10, 14] conclude that insects and birds can be distinguished between by use of σ_{dr} and Φ_{dp}. Figure 2 in [14] shows good separation between the classes based on these two variables. Whereas σ_{dr} has a certain ability to distinguish birds from insects, Φ_{dp} is due to significantly higher values for birds, claimed to be an even better feature for separating between the two classes.

The co-polar correlation coefficient ρ_{hv} is also claimed to contribute to classification of birds and insects as this value tends to be lower for insects than for birds, [10, 67]. The same parameters can also be used to distinguish between biological scatterers and precipitation, which hold values close to one. Although differential RCS for birds and precipitation may reach the same values, the differential phase and differential correlation coefficient may differ more clearly.

Radar meteorologists use irregularities in the refractive index of air, wind plumes and echoes from small insects to measure wind fields. However, active fliers like birds and larger insects may contaminate such measurements, as suggested by Bachmann and Zrnic [12]. They showed that polarimetric spectral analysis can contribute to derivation of usable wind speed measurements in data with presence

[3] from the poorly printed Figure 3c

of birds. In their analysis birds and insects are clearly separated by differences in Doppler shift. This article is the first on differential polarimetric variables for classification of biota to introduce velocity resolution.

The measurements described so far in this chapter on polarimetric variables are all gathered with meteorological systems with poor range resolution operating in S-band. The large resolution cells will presumably rarely contain individual birds. The presented polarimetric variables are therefore to be interpreted as average values in both time and space. Moreover, in general there are too few measurements where the target aspect angle, class and species are determined with external observations. Compared to the long target observation intervals required for the amplitude modulation and μ-Doppler methods, polarimetric information can be obtained extremely rapidly. However, combining methods for example by performing polarimetric spectral analysis on isolated targets in range, potentially as part of μ-Doppler analysis, may give useful information to the classification process.

A few papers covering polarimetric μ-Doppler simulations and measurements of human gait are published. In [68, 69] Tahmoush and Silvious show spectrograms of differential phases measured in Ka-band. Their hypothesis is that scattering from dihedral scatterers like elbows and knees can be identified due to characterizing differential phase values close to -180°. Simulations of polarimetric radar signatures for human walking at 2 GHz were presented by Park et al. in [70]. They claim that cross polarized signatures will emphasize movements of legs and arms due to their at times tilted geometry with respect to the orientation of the linear polarizations in use. Results of polarimetry of wind turbine measurements are covered in the papers of Fioranelli et al. [71] and Krasnov and Yarovoy [72]. Both show spectrograms of co- and cross-polarized returns from wind farms, in S- and X-band and S-band respectively. The latter publication show results of the Huynen decomposition applied to the data. However, beyond claiming that the results are interesting for further studies of mitigation of wind farm clutter, there is little information on how the polarimetric information will be utilized.

2.1.10 Existing bird classification routines

Schuur et al. presented in [67] an algorithm for hydrometeor identification by use use of polarimetric weather radar in S-band. The method can be optimized for differentiating between meteorological and non-meteorological scatterers, or for distinguishing different categories of meteorological echo. The routine makes use of reflectivity Z, differential RCS σ_{dr}, cross-correlation coefficient ρ_{hv} and two texture parameters $SD(Z)$ and $SD(\Phi_{dp})$ derived from σ_{dr} and Φ_{dp} respectively. $SD(Z)$ is obtained by subtracting a range averaged version of Z from its original values and calculating the standard deviation on the result. Such texture parameters characterize small scale variations and are frequently used to separate between meteorological and non-meteorological echoes [73]. Membership function parameters for the three classes, *ground clutter/anomalous propagation*, *biological scatterers* and *meteorological scatterers* are presented. The magnitude of the reflectivity Z gives a rough indication of class membership as precipitation tends to return less power than scatterers in the other two classes. High positive σ_{dr} ($>$ 4 dB according to Figure 2 in the article) unambiguously indicates biological scatterers. Negative σ_{dr} on the other hand, indicates ground clutter or anomalous propagation conditions. In between there is a region of overlap of σ_{dr} values from around 0 dB to 4 dB. Echoes are classified as originating from precipitation if $\rho_{hv} > 0.85$ and from biota if $\rho_{hv} < 0.5$. One interesting statement in the paper is that echoes from man-made objects as well as turbidity have ρ_{hv} close to one. All in all overlaps are found between the membership functions for all targets, however, the authors claim their combination is efficient for classification.

Zaugg et al. published a thorough article [74] on automatic classification of birds utilizing temporal patterns produced by birds with flapping wings based on vertically polarized X-band data from a tracking radar. Mean values and standard deviations of spectral coefficients for each frequency component resulting from a continuous wavelet transform (CWT), along with the total backscattered power level were used in a support vector classifier (SVC). Pre-processing with several normalization steps and use of SVC leads to a rather unclear physical origin to the

classification. However, the method relies on the time varying spectral content of the returned signal from flapping wings. The classification routine was trained to discriminate between two classes, namely *birds* and *other*. The results show that classification between birds and other targets (insects and clutter) with this method is possible. The area under curve (AUC) values, which is the area under the receiver operation curve (ROC) can be interpreted as an average performance of the classifier. These AUC values are found to be between 0.88 and 0.99 in the different data sets, which are considered good results.

2.1.11 Resonance effects in echoes from birds

Melnikov et al. [11] reported in 2012 on resonance effects in echoes from birds in S-band. The findings were done in data from the WSR-88D weather surveillance radars operated by the U.S. National weather service. They argue that relatively small frequency shifts of 5-10% change radar reflectivity/RCS by several decibels. A mean differential RCS of +6 dB at a frequency difference of 290 MHz is found in measurements of large bird flocks. Their results are explained by theory for the resonance region where the RCS oscillates with respect to the ratio between bird circumference and wavelength. Simulations of reflectivity for water filled spheres and spheroids with different orientations are presented for two different frequency spacings. These simulations show variation in reflectivity of values ranging from -15 dB to +20 dB between the two frequencies as function of sphere/spheroid dimension and orientation. Also Wilson [9] shows simulations of reflectivity at different frequencies of simple geometrical shapes in the resonant scattering region. These simulations show how the reflectivity differences between different frequency bands vary with target size.

2.1.12 Classification based on spatial resolution

ISAR imaging of birds has been suggested for classification of birds by Zhu et al. [75,76]. Such methods require both fine range and cross-range resolution, typically more than ten resolution cells in each dimension. A bandwidth in the order of several GHz and a wavelength in the millimeter band is required, which is far from

achievable in a typical air defense surveillance radar. Such methods are therefore considered irrelevant in the context of this thesis. The papers of Zhu et al. do not show real data, however, simulations for 94 GHz are presented.

2.2 Classification of small man-made targets

The requirement to recognize friendly forces in the battle space is and has been central throughout history. Since the beginning of World War II this challenge has been met with cooperative systems, such as identification, friend or foe (IFF). These systems have proven highly useful, however, they lack the capability to identify hostile targets or friendly units with malfunctioning equipment. Development of increasingly sophisticated radars has, in addition to implementation of more advanced interrogating systems, led to an increasing extent of signature based non-cooperative classification methods.

Although there are several civilian applications for radar based classification methods, the largest customer and user of such technology is the military. This has traditionally led to some secrecy regarding methods and their performance, and has further resulted in much classified literature on the topic. Nevertheless, the topic of NCTR embraces several widely known techniques, of which several are considered to be well established in the literature. Due to the large interest in automatic classification systems, this has been and will be an active research field for many years. This chapter focuses on the the methods most relevant for classification of small man-made targets in an air defence surveillance system.

2.2.1 Small man-made targets

Before moving on, an explanation of the term *small man-made target* is required. In this thesis such a target is defined as a slow moving aircraft with a physical size comparable to large birds, in other words having a maximum size in any dimension less than around two meters. Due to its small size such an air vehicle will be unmanned, however, the low velocity excludes missiles of any kind. UAVs can be subdivided into different classes pending on weight, maximum endurance, maximum altitude, wing loading and engine type [77]. Using a definition based on

platform weight, a UAV with a mass less than 5 kg is referred to as a *micro UAV*, whereas a weight between 5-50 kg is defined to be in the *light UAV* class. The size limitations mentioned above naturally means that these two classes cover the targets of interest. Terms such as small UAV (SUAV) and miniature UAV are also often used for aircraft of this size.

2.2.2 Methods for classification of small man-made targets

The paper of Harmanny and de Wit from 2012 [78] describes the potential of using μ-Doppler signatures for classification of small UAVs, including simulation and measurements of miniature helicopters and multi-copters. In [79] they followed up with a new paper showing good results on discriminating between small UAVs and birds using spectral and cepstral analysis in a dedicated X-band system. More details on cepstral analysis can be found in Chapter 8.5.3. In the previously covered article from the same year [60] they focus on feature extraction from spectrograms by use of SVD. The same authors contribute to the publication of Molchanov et al. [80], where different μ-Doppler signature based classifiers for separation between different micro UAVs are presented. A bird class is also included, achieving a correct classification score of 97%. It is worth emphasizing that all measurements were done in X-band and by continuously gathering data of the target, quite differently from a long range surveillance radar. The evaluated methods are all based on μ-Doppler signature extraction from short time Fourier transform STFT based spectrograms. The already mentioned methods SVD and PCA are used to decompose the micro motion and express the signatures in terms of its eigenvectors. The classifiers compared are linear support vector machine (SVM), nonlinear SVM and a Naïve Bayes classifier. The results are very similar, 94.91%, 95.39% and 93.6% respectively. Rosenbach and Schiller discuss in Chapter 6 of [7] the performance of different classifiers. They refer to an experiment performed at Fraunhofer FHR where the efficiency of nine different classifiers classifying aircraft in ISAR images were compared. The differences between methods were minimal. In fact, the authors conclude that the question of implementation complexity is the most important when choosing a classifier. On the other hand they emphasize the importance of

finding robust features taht describe the targets effectively. Seen in light of this, the described paper of Molchanov et al. shows similar results as all classifiers perform almost equally well. The article does not describe the features and their physical origin very well. Methods similar to classic image recognition techniques are applied to time-frequency data, and the output evaluated. Throughout this thesis the attention will be on finding good features rather than considering specific classifiers.

Although few publications are found on classification of UAVs specifically relevant to air defence radar, classic NCTR publications are considered a good base for finding methods to classify UAVs despite differences in airframe size and materials in use. In the remainder of this thesis publications of NCTR techniques suggested for classification of manned aircraft are included.

2.2.3 Amplitude modulation based methods

Amplitude modulation of radar echoes has been used for classification of aircraft, in particular helicopters. UAVs can take the form of small helicopters or multicopters with several rotors, and helicopter classification methods are therefore considered relevant for the topic of this thesis. Both Tait [23] and Chen [54] describe helicopter classification in their books. Although several of the suggested techniques make use of μ-Doppler shifts, they are here grouped under amplitude modulation methods as they all rely on the periodic amplitude modulation of echoes backscattered from rotating rotor blades.

In the optics scattering region rotor blades can be approximated by flat plates illuminated and rotating in a plane [23]. A maximum, a powerful reflection referred to as a *flash*, is seen when the direction of illumination is close to orthogonal to the blade. Since the backscattered power from the blades is concentrated in time, the blade flashes are most easily detected in the time domain [57]. The feature used for classification is in this case the main rotor flash frequency, and if the rear rotor is detected its flash frequency can be exploited as well. In the latter case the gear exchange ratio, which in most cases is constant, can be estimated. This technique does not necessarily require a coherent radar as long as the blade parity (odd/even) can be determined. In this case this has to be found by the presence of amplitude

variation between successive flashes for odd numbers of blades. The amplitude will vary due to the different RCS of approaching and receding blades caused by the shape of the blades. Such differences are considered to be undetectable of small rotor blades for low frequency, see Chapter 4.4.2.2. The assumption of echoes in the optics scattering region does not hold in these cases. Pulse-Doppler radars can on the other hand determine if a blade is approaching or receding from the sign of the Doppler shift and are naturally the preferred choice. Such radars also enable the use of Doppler processing techniques.

Rotander et al. suggested in [81] to use the ratio between the blade length and number of main rotor blades, the *L/N*-quotient, for classification of helicopters. The main idea behind the *L/N*-quotient technique is to measure the time between blade flashes τ_{bf} in the time domain, and extract the maximum blade tip velocity $\vec{v}_{max}$ from the Doppler spectrum. These two parameters is related through the following equations with three unknowns, the rotation rate f_{rot}, blade length L and the number of blades N.

$$2\pi f_{rot} L = \omega_{rot} L = v_{max} \tag{2.1}$$

$$2\pi f_{rot} N = \omega_{rot} N = \frac{1}{\tau_{bf}} \tag{2.2}$$

This implies that both L and N cannot be found. However, the ratio L/N can. As long as the number of blades are even, one approaching and one receding blade will be orthogonal to the radar at the same time. In the case of an odd number of blades, these occurrences will not happen simultaneously and result in twice the number of reflections. This means that N in Equation 2.2 should be replaced with $2N$ in the case of an odd number of blades. The usefulness of the *L/N* parameter obviously depends on how well it separates between helicopter types. A figure showing *L/N*-quotients for 15 different helicopters in the article, suggests that the method theoretically has potential to distinguish between several helicopter classes. The practical efficiency of the technique relies on what quotients can be expected

for helicopters not included, and on how accurately τ_{bf} and $\vec{v}_{max}$ can be measured under operational conditions with moderate to low SNR. Although not specified in the article, an assumption of the rotor rotating such that $\vec{\omega}_{rot}$ is in the plane orthogonal to the line of sight is made. Rotation out of this plane will not affect the time between blade flashes, however, the measured maximum tip velocity will decrease. In practice this is only significant when the helicopter is illuminated from considerable elevation angles. However, if such angles are not compensated for, the *L/N*-quotient will be influenced and its usefulness for classification degraded.

Yoon et al. [82] suggested a method that estimates the number of blades N unambiguously. This method is based on evaluation of the Doppler shift from the blade tip by time-frequency analysis. In addition to rotors with odd and even number of blades having distinct patterns with regards to timings of broadside reflections and sign of Doppler shifts, the authors suggested that N could be found by counting the of number of sinusoids in the spectrogram originating from the blade tips. Measurements of model helicopters were shown to support their theory. In their data they were able to track the blade tips over time, and the number of sinusoids were shown to match the number of blades. An implementation of such a method into a practical system is considered to be challenging. Generally, based on my experience with reflections from rotor blades, blade tips have significantly aspect dependent RCS and a high SNR is required to exploit these reflections for classification.

Cilliers and Nel suggested a technique [83] to estimate the number of rotor blades based on the utilization of echoes from blade tips as well. This method builds on time-frequency analysis, compensation for translational velocity and finally a tomographic imaging of the blades by an inverse radon transform (IRT). The rotation rate $\vec{\omega}_{rot}$ of the rotor is found by searching for the value $|\omega_{rot}|$ giving the best focused image. The blade length is calculated from this value and the Doppler shift of the blade tip.

For time domain rotor amplitude modulation analysis it is important that at least one complete pulse detects the rotor flash, so the required pulse repetition

frequency (PRF) is actually dependent on the duration of the flash [23]. This is generally required to be high for Doppler based techniques, however, its value is dependent on the wavelength in use. Lower frequency is therefore an advantage in this context. UAV helicopters are more or less down scaled helicopters and essentially work as full sized ones. The main differences are smaller size, larger angular velocity of rotors and in some cases less reflective materials in rotor blades are found.

Propeller driven aircraft may produce μ-Doppler signatures useful for classification. The situation is similar to that of helicopters, however, the rotational velocity of the rotor $\vec{\omega}_{rot}$ is now under normal conditions closer to the horizontal plane, making signatures generally more azimuth angle dependent. As for most large helicopters, full size propeller driven aircraft often have jet turbine engines rather than piston engines. This allows for the application of possibly more robust JEM based methods for classification. For smaller UAVs, one can not rely on JEM methods as piston and electrical engines are prevalent.

JEM is a method for classification of jet engines. This is done by estimating the number of blades on the different compressor and turbine stages associated with jet aircraft, turbine driven helicopter and turboprop aircraft. The method exploits the interaction between the engine's moving parts and the radar signal [23]. This limits the usable aspect angles to those where the radar pulse can penetrate into the engine duct either from the front or the back and return back to the radar without too much loss. The choice of carrier frequency is important in order to have echoes backscattered from several compressor or turbine stages to improve classification. In S-band and lower, equivalent to frequencies below approximately 4 GHz, penetration beyond the first compressor or turbine blade stage is more difficult than at higher frequencies [84]. In an air defense surveillance system, typically operating at these lower frequencies, single stage classification of jet engines is achievable. This reduces the method's capability compared to classification based on multiple stages, as the strength of multi-stage classification is in the unique combinations of blade counts on different stages. The mentioned penetration is valid for full sized

engines, but the performance of JEM techniques for classification of smaller UAV engines is unknown. However, it is reasonable to expect it to be rather limited and the method is therefore not covered in more detail in this thesis.

2.2.4 μ-Doppler methods

μ-Doppler signature analysis has been found useful in several radar applications, including classification of space, air, and ground targets. Examples of the utilization may be determination of vehicle class based on measurement of engine vibrations or classification of human behaviour by gait analysis. The book *The Micro-Doppler Effect in Radar* by Chen [54] covers μ-Doppler effects of both rigid and non-rigid bodies. The differences between these two classes is highly relevant when trying to distinguish between birds and small aircraft. A rigid target is an object where the distances between distinguishable scatterers remain constant during motion [85]. Birds naturally therefore belong to the non-rigid body class, whereas aircraft are mainly considered rigid.

One of the early articles on the topic was written by Chen in 2000 [86], covering the effect from micro-motion of vibrating and rotating scatterers in radar signatures. In this paper he emphasizes the usefulness of the time-frequency transform for μ-Doppler analysis. Examples of μ-Doppler effect from vibrating objects, and rotating structures like helicopter blades and antennas is given. Although μ-Doppler signatures may be extracted directly from isolated range cells, or even from continuous wave (CW) data without range resolution, the technique is often applied in conjunction with HRR-profiles or 2D radar imaging techniques. Increasing the spatial resolution in one or two dimensions improve the ability to extract signatures from individual moving scatterers on the target. The article of Clemente et al. [87] gives an overview of the development of μ-Doppler techniques applied to radar imaging, ultrasound and through the wall radar. Extraction of μ-Doppler signatures from ground targets in real SAR images was according to them first shown by Sparr and Krane [88]. They describe μ-Doppler signatures originating from two corner reflectors oscillating with an amplitude of millimeters in AN/APY-6 SAR images. Sinusoidal phase modulation with time in agreement with ground truth

measurements were found after application of high resolution time-frequency analysis methods, such as smoothed pseudo Wigner-Ville (SPWV) and adaptive optimal kernel (AOK) transformations.

Another more relevant technique to air defence surveillance radars is the ISAR imaging method. Whereas SAR-images of the ground are formed by precise knowledge of the movement of a mobile radar, ISAR images are formed of moving targets from a stationary or moving platform. Although any movement of the radar could be compensated for by accurate navigation solutions, the relative movement between radar and any air, sea and ground target is generally not known accurately enough to form well focused images. This means that both translational and rotational motions of a target have to be estimated from the radar data itself. A presentation of μ-Doppler based methods for classification of both rigid and non-rigid targets in ISAR can be found in the article of Chen et al. [85]. Here they show examples of isolating μ-Doppler signatures from wheels of driving cars, and rotors from flying helicopters.

During the last decade, the interest seems to have shifted from extracting μ-Doppler signatures from ISAR-images to actually compensating for the movement and obtain focused images [87]. An example of this is given in the article of Zhu et al. [76] where a focusing technique for ISAR-images of birds with flapping wings is presented. This paper is covered in Chapter 2.1.12. Techniques for focusing unfocused images due to micro-motion is considered to be out of the scope of this thesis.

2.2.5 Polarimetric methods

The first works within the field of radar polarimetry were done by Sinclair and Kennaugh at Ohio State University in the late 1940s [89]. Their contribution was mainly on establishing the essential theoretical basis for exploitation of polarization. According to Giuli [90] great interest for the techniques was shown from industry and universities in the 1950s and 1960s. During these years development of instrumentation and measurement techniques were in focus. The same author claims that the topic was shown less attention for some years following this period. The rea-

sons were mainly connected to the complexity of the not fully understood polarization phenomenon, and the increased complication and cost of doubling the number of channels in dual polarization radars. Moreover, understanding polarimetric responses of distributed targets requires extensive and expensive measurements and may have seemed daunting at the time. Due to both technological and theoretical advances during the 1970s, in particular with the PhD thesis *Phenomenological theory of radar targets* [91] by Huynen, the interest in the topic increased again. In this work nine parameters, later known as the Huynen parameters, are presented. Each of them is claimed to contain real physical target information. In the same thesis Huynen presented his *Target decomposition theorem*, later known as *Huynen's Target Decomposition Theorem*. This work was an important contribution to the field of polarimetric target classification and an important basis for other decomposition techniques, such as the $H/A/\bar{\alpha}$ covered individually later in this chapter.

Backscatter from precipitation can be seen as the sum of contributions from a large number of (close to) spherical scatterers, which under ideal conditions and without multipath between hydrometeors, results in a scattering matrix as that of a sphere [90]. A circular polarized wave interacting with the precipitation therefore results in a backscattered wave with the opposite rotation sense. An attenuation of 10 - 35 dB of weather clutter is achievable by choosing the opposite polarization. As long as the target does not scatter like a sphere, detection in precipitation is enhanced this way. While some regard weather as clutter, others consider it the target. In the field of radar meteorology radar polarimetry has been given much attention. According to Giuli [90] important contributions to this field were given in the 1970's. Several of the publications mentioned in Chapter 2.1 deal with data from the NEXRAD system operated by the National Weather Service in the USA, which now is upgraded with dual-polarimetric capabilities [92]. This enables the discrimination between different classes of echo, such as ground clutter and anomalous propagation, biological scatterers (including insects and birds), dry snow, wet snow, stratiform rain, convective rain, and rain/hail mixture [93].

Polarimetry has also been suggested for use in target recognition, both in the

context of NCTR and ATR. As the echo from any target may be influenced by the polarization of the transmitted radar pulse, such change in polarization between transmitted and received pulses will contain some information about the target. The topic of polarimetry in NCTR is briefly covered by Skolnik [94]. He considers the use of polarimetry in this context to be disappointing, as the effectiveness to perform classification of complex targets according to him has proven low. He points out four different possible explanations to this. The first one is possible influence on the polarization of the signal due to multipath from clutter. Secondly he suggests the signal leakage between orthogonal polarization channels often is too large. Thirdly, alternating polarization states of subsequent pulses leads to inaccuracy if the target move between pulses. The last problem is that of multiple unresolved scatterers within range cells contribute with individual specific polarizations, however, the composite echo has polarization different from each individual scatterer. Giuli covers polarization of man-made targets in [90], where he as well highlights the problem of low spatial resolution. His suggestion is to use higher resolution, advantageously bi-dimensional (range and cross-range), in combination with shorter dwell times. The reduced resolution limits the number of scattering centers and the aspect angle dependency of the signature. Short-term measurements increase the possibility to isolate highly polarized target returns in cases were the polarization rapidly changes with time. Quite interestingly, Giuli also discusses the use of polarization to attenuate unwanted contributions from chaff and jamming.

Polarization diversity techniques to increase radar performance in terms of target detection, disturbance suppression and target identification have been suggested. Such techniques involves adjusting the polarization state of the transmitting and receiving antenna to maximize the signal to interference level. This can be done as long one has knowledge of the target and interference scattering matrices. In 1981 Poelman suggested the virtual polarization adaptation (VPA) technique [95], which is a method that adaptively optimizes the transmit and receive polarization states. This adaptation is done virtually as it is achieved by signal processing and not physically in the antenna. By knowledge of the scattering matrix of a target, calculation

of the received power for any combination of transmit and receive antenna is possible [96]. This process is referred to as polarization synthesis and is well explained and demonstrated to increase classification in SAR images [96]. More details on polarization synthesis is found in Chapter 8.5.4.1.

The effect of resolution and polarization on target classification in SAR images is documented by Novak et al. [97]. They found that the classification score improved with increasing resolution, and by use of dual polarization compared to single polarization images. The improvement by use of multiple polarizations was due to image enhancement, and not due to extraction of features from the scattering matrices itself.

In the field of remote sensing, polarimetric SAR has become a popular tool. In particular instantaneously measured HH, HV, VH and VV data, referred to as fully polarimetric or quadrature polarization data [98], has received much attention since sensors such as the phased array type L-band SAR (PALSAR), Radarsat-2, and TerraSAR-X became operational [99]. Such measurements are achieved through simultaneous transmission of two encoded orthogonal signals in orthogonally polarized pulses as for example in [100]. The benefit is increased precision in the scattering matrix, especially the relative phases, compared to the *pseudo-scattering matrix* achieved by alternating polarization. The main application of polarimetric SAR imagery is terrain classification. A large number of polarimetric indicators are suggested for classification of vegetation etc. Lardeux et al. suggested a classification algorithm including 54 variables [99]. The NATO publication *Direct and inverse methods in polarimetric radar* [101] by Boerner et al., is a thorough description of historic and current use of radar polarimetry until 1992, including a chapter on polarimetric synthetic aperture (POL-SAR) and inverse SAR (POL-ISAR).

Tait [23] briefly covers the topic of polarization in the field of NCTR. His coverage is limited to describe scattering matrices of simple geometrical objects, and points to the fact that the basis of using polarization in NCTR is to decide the geometrical shape of the scatterer from its scattering matrix. Chamberlain et al. [102] describe compact range measurements of five commercial aircraft models with po-

larimetric radar, where they utilize equivalent theory. Features for target classification of these models are found by parametrization of the polarimetric information in the backscattered wave by *ellipse fitting*. The features extracted are amplitude A, ellipticity ε and tilt angle τ. These are shown to have a strong relationship with the geometrical structure of the aircraft, and demonstrated to provide classification capability. Martorella et al. [103] presented similar techniques in ISAR images, however, cross range position was added as a classification feature. Classification results were presented on simulated target models only. This work was followed by an article by some of the same authors in [104]. Here they describe a classification method for fully polarimetric ISAR images, where the geometrical information in the image is ignored and only the polarimetric features of a selection of scatterers are used. This was done to make the classification robust to the image projection, which normally is a complicating factor in ISAR NCTR algorithms. The suggested approach included the use of the Pol-CLEAN algorithm described in [105] for extraction of polarimetric scattering features from a selection of bright scatterers in the image, followed by a Cameron's decomposition and a Neural network classifier. Cameron's decomposition is a method of decomposing a target's polarimetric response into simpler responses from known objects based on its scattering matrix. Several decomposition techniques are proposed of which several are described by Mott in [106] and thoroughly reviewed by Cloude and Pottier in [107]. The only purpose of applying the ISAR imaging step in [105] is to isolate polarimetric signatures prior to classification. The classification algorithms were in this case validated with simple geometrical shapes on a turn table. In 2011 Martorella et al. published an article [108] on a polarimetric model matching method for target recognition by means of polarimetric ISAR images. The idea behind this is to generate 3D point scatterer models with polarimetric information, which in turn can be compared with features extracted from scattering centers in 2D ISAR images.

2.2.6 Resonance effects and target impulse response matching

In the resonance scattering region target dimensions are comparable to the wavelength in use. This is explained in Chapter 3.3. Under this scattering regime the

backscattered power is dependent on the wavelength, as resonances at certain frequencies due to surface wave scattering effects called creeping waves occur. This effect has been proposed to be utilized in target recognition techniques, typically by using a number of carefully selected frequencies and evaluate the returns of these. According to Ksienski et al. [109] the use of long wavelengths compared to the size of the target provides information about the overall dimension, shape and material composition. Higher frequencies on the other hand characterize the fine scale details of the target. For this reason the authors point to the suitability of the Rayleigh and the lower resonant region for classification. Lin and Ksienski [110] used frequencies ranging from 2-25 MHz for recognition of fighter aircraft, thus operating in the transition between the Rayleigh and resonant region. They used features consisting of amplitude, polarization and phase at different wavelengths for classification and found that only two frequencies were required for high reliability of correct classification. As commented by Skolnik [94] these techniques have a good theoretical basis, however, the problem is the low frequency required to recognize full sized man-made targets like aircraft and ships.

Using transfer function poles for classification has also been suggested [111, 112]. This was based on the earlier findings that scattered signal from targets, when illuminated with a Dirac like pulse, consist of the early time and late time signals [113]. The latter part can be expressed by poles in the s-plane [114]. Lazarakos [115] wrote his master thesis on the topic, and gives a review of available techniques for determining the position of such poles. Classification of simple geometric shapes like wires was demonstrated, however, recognition of more complex targets were tested with a negative result. Dudley [114] highlights the practical limitations of detecting creeping waves beyond the first creeping wave around the target when noise is introduced to the system. According to him this limits the utilization of creeping wave resonance to be of little practical interest for target classification.

The E- and K-pulses are pulses designed to cancel the poles induced by complex natural resonances [116]. This requires that the targets' natural resonances are known, and that each target is illuminated by an adapted pulse in order to be rec-

ognized. This approach is somewhat similar to methods suggested by Gjessing in his book *Target adaptive matched illumination RADAR* [117], however, his techniques does not exploit natural resonances due to surface waves. Gjessing's main idea is to match the illuminated wave in frequency (and/or polarization) to the target to maximize the backscattered power. In principle this means transmitting only the frequencies that result in constructive interference of echoes. This of course requires *a priori* knowledge of the target's impulse response, which can be quite complex and aspect angle dependent for large targets at high frequencies. On the other hand, when the target is detected, it is classified at the same time. This is naturally not completely true as the adapted waveform will not be orthogonal to all other targets. To be able to evaluate the interference between scatterers on large targets, Gjessing suggested using the combination of two real wave numbers k in a synthetic ΔK channel. It is worth noting that since the illuminating waves are launched at higher radio frequencies and the ΔK channel is formed by signal processing, no resonance due to surface wave effects is expected. As Gjessing et al. [118] later point out this processing technique is associated with cross terms which have to be compensated for by averaging in range or frequency to extract the wanted ΔK response.

2.3 Summary

In this chapter literature considered relevant to the research problem has been presented and discussed. This has included literature on detection and classification of birds by radar, as well as classic NCTR techniques found applicable to classification of small man-made targets. The size of the targets of interest makes Rayleigh and resonant scattering important. However, the vast majority of classification methods covered in the literature assumes scattering in the optics region. An effort has therefore been made to balance the "classic" NCTR literature with low frequency theory. Publications covering classification of birds and man-made targets have been treated separately. For each target class classification based on periodic RCS modulation-, μ-Doppler- and polarimetric signatures are covered in detail. In addition several other less well-known methods with relevance to the research problem have been

presented.

The problem of separating between birds and UAVs in air defence radar systems has not previously been covered specifically in the literature. Publication on classification of each of the classes separately is however found. Whereas recognition of UAVs is a relatively new topic, classification of birds by radar is covered in papers dating back to World war II. With exception of papers covering amplitude modulation based classification of birds and birds in weather radar, the vast majority of these publications cover higher carrier frequencies than normally found in air defence radar systems. In this context, this thesis is different by focusing on what is achievable at L- and S-band frequencies. In particular, μ-Doppler signatures have not been found to be previously covered at these frequencies. Simultaneous operation in both bands or comparison of classification results between them is another topic to be addressed in this thesis not found in the literature.

The most important topic missing in the literature considered is related to classification in search radars. Most studies have been carried out with tracking radars or systems otherwise achieving long observation times. One key objective in this thesis is to investigate the consequences of reducing dwell time in terms of classification. This is important for implementation in air defence radars, where dwell times may be significantly limited. In the hunt for useful features for classification requiring short observation times, polarimetric parameters covered in the meteorological radar literature are interesting. Weather radar measurements presented suffer from poor range resolution and in situ observations. By combining better controlled experiments, significantly improved range resolution and ideas from the remote sensing community, this thesis aims to contribute with more polarimetric parameters of single birds of known species and aspect angle.

From this chapter the conclusion is that the research questions formulated in Chapter 1.5 have not previously been addressed in the literature. The methods found to be most relevant for the small target classification problem, and thus taken further for closer investigation, are connected to amplitude modulation of echoes, μ-Doppler and polarimetric signatures.

Chapter 3

Birds and UAVs as radar targets

This chapter presents theoretical considerations on birds and small UAVs as long range air defence radar targets. In particular scattering mechanisms relevant to classification of such targets in L- and S-band are covered. In addition to their small physical size, these are characterized by being electrically small and composed of a wide range of materials. Whereas classic NCTR techniques often assume large targets with conductive surfaces many times the wavelength in size, this chapter covers scattering mechanisms of targets being smaller or comparable to the wavelength and having arbitrary dielectric properties.

3.1 Wave propagation

Reflection of electromagnetic (EM) waves is essential for all use of radar. Maxwell's equations are a set of fundamental laws describing all electromagnetic behavior [2], including interaction of transmitted radar pulses with any target. The wave equations for electric and magnetic fields can be derived from these and form the basis for the theory presented in this chapter. The derivation can be found in many text books on the subject e.g. [119, 120] and is not included here. However, the solution is utilized and factors like target material, size and shape are evaluated in the context of target classification.

EM-waves have the property of storing energy. The capacity is dependent on the medium they travel through and determined by this material's permittivity ε and permeability μ [2]. In free space these quantities have the values $\varepsilon_0 = 8.85 \times 10^{-12}$

F/m and $\mu_0 = 4\pi \times 10^{-7}$ H/m respectively. Materials are commonly characterized by generally complex values relative to these as ε_r and μ_r. However, in many practical settings involving non-magnetic materials, the relative permeability is real and equal to that of free space such that $\mu_r = 1$. This is considered to be a good approximation for all targets of interest in this thesis.

The time domain solution of the mentioned wave equation for the electrical field component of the wave traveling in the positive z-direction can according to [119] be expressed as

$$E(z,t) = E^+ e^{-\gamma z} e^{j\omega t} = E e^{-\alpha z} e^{j(\omega t - \beta z)} \tag{3.1}$$

Here t denotes time, z the distance along the direction of propagation and ω the angular frequency. $\gamma = \alpha + j\beta$ is the complex propagation constant, where the real part α is associated with losses and is observed to attenuate the wave with positive distance. The imaginary part β is on the other hand seen to influence the phase of the wave. As will be covered in Chapter 3.2, this propagation constant is again determined by the dielectric properties of the material, which is particularly important when investigating the targets covered in this thesis.

3.2 Target materials

Different material properties may be a distinct characteristic that separate small airborne targets from larger ones. The surface of a conventional full sized aircraft largely consists of conductive materials like aluminum, small UAVs may be made substantially of thermoplastics, fiberglass and carbon fiber reinforced polymer, while birds naturally consist of different layers of biological tissue. These materials have all different dielectric properties leading to variations in reflectivity and transmission into the target body.

Materials allowing for penetration into to the target interior are particularly challenging for classification techniques utilizing spatial resolution like radar range profiles or images. Although SAR/ISAR images of large conductive aircraft differ from optical images in certain ways, the similarity is expected to be significantly

less when reflections from the inside of a target contributes to the image. Spatial resolution based techniques are not covered in this thesis, however, evaluation of RCS of bird wings, rotors and propellers of different materials is considered essential to understand the potential for classification. Thorough descriptions on the topic are found in *Radar Cross Section* by Knott et. al. [2], *Microwave engineering* by Pozar [119] and in particular *RF/Microwave Interaction with Biological Tissues* by Vorst et al. [121]. This section gives a short summary of the most important basics and their importance for small target classification.

3.2.1 Reflection coefficient

Reflections of EM waves from a target occur as the wave travels from a medium with impedance η_1 into another medium with different impedance η_2, see Figure 3.1. Here θ_1 and θ_2 are the reflection and transmission angles formed with the surface normal respectively. One part of the wave is generally reflected off the boundary, whereas the other part is transmitted into the new medium. The field strengths of these two parts are given by the reflection coefficient $\Gamma = \frac{E^r}{E^i}$ and transmission coefficient $T = \frac{E^t}{E^i}$ [119]. Here E^i, E^r and E^t is the electric field incident on the boundary, reflected off the boundary and penetrated into the new medium respectively.

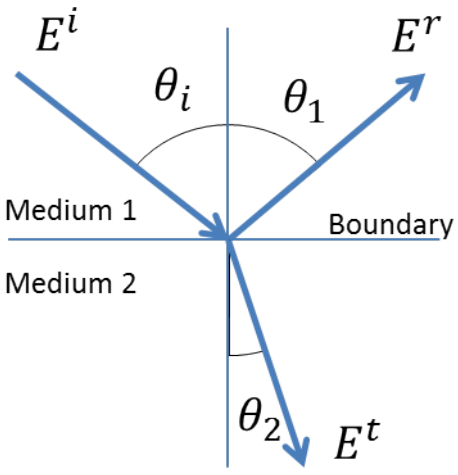

Figure 3.1: Reflection geometry

For oblique incidence, Γ and T are dependent on incidence angle and polariza-

tion. If we define the plane of incidence as the plane containing both the normal to the interface between the materials and the direction of propagation, we can decompose the incoming electrical field into components parallel or orthogonal to the incidence plane. In remote sensing parallel and orthogonal polarization are commonly referred to as vertical and horizontal respectively, where the orthogonal component thus coincides with the Earth's surface. This is the definition used in the remainder of this document. According to [120] horizontal and vertical components of the reflection coefficient can then be expressed

$$\Gamma_h = \frac{\eta_2 \cos(\theta_1) - \eta_1 \cos(\theta_2)}{\eta_2 \cos(\theta_1) + \eta_1 \cos(\theta_2)} \tag{3.2}$$

$$\Gamma_v = \frac{\eta_2 \cos(\theta_2) - \eta_1 \cos(\theta_1)}{\eta_2 \cos(\theta_2) + \eta_1 \cos(\theta_1)} \tag{3.3}$$

The impedance of a medium is according to [119] given by

$$\eta = \frac{j\omega\mu}{\gamma} \tag{3.4}$$

where ω specifies the angular frequency and γ is the potentially complex wavenumber in the medium already introduced in section 3.1 as the propagation constant. This latter quantity is calculated differently depending on the material's conductive properties. Materials are frequently grouped into three classes of *lossless media*, general *lossy media* and *good conductors*.

3.2.2 Wavenumber in general lossy medium

In a general lossy dielectric, relevant to for instance biological tissue, γ is according to [119] derived from Maxwell's equations under the constraints of being in the far field and in a linear, isotropic and homogeneous medium as

$$\gamma = \alpha + j\beta = j\omega\sqrt{\mu\varepsilon}\sqrt{1 - j\frac{\sigma}{\omega\varepsilon}} \tag{3.5}$$

In general ε may be complex depending on the susceptibility of the material. However, it is common to replace ε with the real part of the permittivity ε' and let σ

represent the total effective losses $\sigma_{tot} = \omega\varepsilon'' + \sigma$. The reason for this is that the ohmic losses induced by σ are inseparable from losses due to dielectric damping $\omega\varepsilon''$ during high frequency measurements. Another maybe even more popular approach is to use the real permittivity and loss tangent $tan\ \delta = \frac{\omega\varepsilon''+\sigma}{\omega\varepsilon'}$. In this case according to [119] the wavenumber is

$$\gamma = j\omega\sqrt{\mu\varepsilon}\sqrt{1 - j\frac{\sigma}{\omega\varepsilon}} = j\omega\sqrt{\mu\varepsilon'(1 - jtan\,\delta)}. \tag{3.6}$$

3.2.3 Wavenumber in lossless medium

In free space and lossless dielectric media the electrical conductivity σ and the displacement current due to damping of vibrating dipoles is zero. In this case Equation 3.5 is simplified to the real wavenumber k [119]

$$k = \beta = \omega\sqrt{\varepsilon\mu} = \frac{\omega}{v_p} = \frac{2\pi}{\lambda} \tag{3.7}$$

where v_p is the phase velocity and λ is the wavelength in the medium .

3.2.4 Wavenumber in good conductor

In the case of good conductors, like most metals, the conductive current is much larger than Maxwell's displacement current, which means $\sigma \gg \omega\varepsilon$ or in terms of complex permittivity $\varepsilon'' \gg \varepsilon'$ [119], and the displacement current $j\omega\varepsilon$ can be disregarded. The complex propagation constant can in this situation be written

$$\gamma = (1 + j)\sqrt{\frac{\omega\mu\sigma}{2}} \tag{3.8}$$

3.2.5 Example of lossless and lossy materials

Figure 3.2 exemplifies the reflection coefficients according to Equation 3.2 and 3.3 for horizontal and vertical polarized electrical fields when transmitted through air into three relevant materials as function of incidence angle θ_1. These materials are thermoplastic with $\varepsilon_r = 2.2$, bird average dielectric constant proposed by Schaefer in [33] $\varepsilon_r = 44 - j14$ and human muscle $\varepsilon_r = 25 - j14$. The values given are

approximate and valid for L- and S-band frequencies. One interesting observation

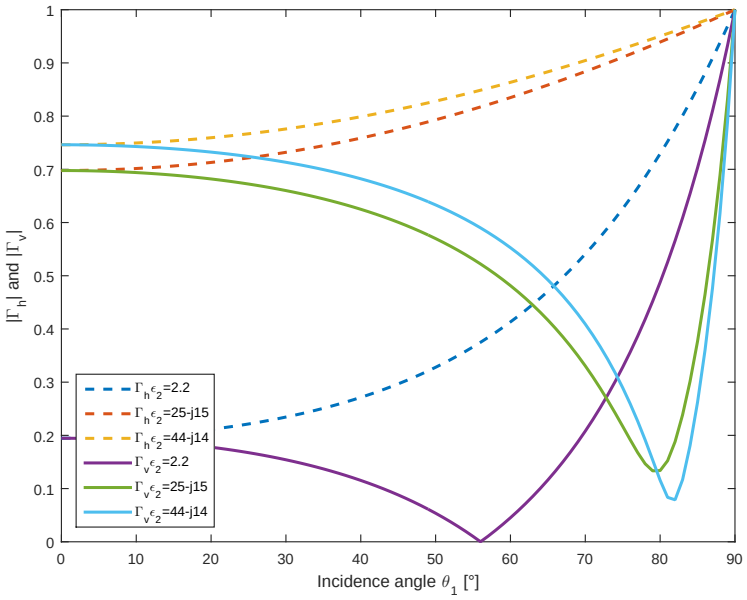

Figure 3.2: Reflection coefficient for three different materials.

from Figure 3.2 is the differences between horizontal and vertical polarizations in cases where the $\theta_1 > 0$. The characteristic minimum seen for vertical polarization is associated with the Brewster angle, where maximum power is transferred into the materials. Note that reflected power is proportional to Γ^2 and that the scattered power is generally not directed back in the direction of the transmitter for incidence angles $\theta_1 > 0$.

3.3 Scattering regimes

Several scattering mechanisms are in general contributing to the RCS of targets depending on their sizes measured in wavelengths. The scattering is commonly divided into three different regions dependent on target size L to wavelength λ ratio L/λ [2]. Each region is dominated by different scattering mechanisms. The best known example showing these effects is reflection from a perfect electric conductive (PEC) sphere. The different regions of scattering are shown in Figure 3.3, as the Rayleigh, resonance and optics region. More details are found in textbooks like *Radar Cross Section* [2] or *Principles of Modern Radar: Basic Principles* [21]. Although the majority of publications in the field of NCTR assume high frequency

approximations, this is less relevant when the wavelength is long and targets are small. To understand the scattering mechanisms of small targets in air defence frequency bands the Rayleigh and resonance regions have to be investigated closer.

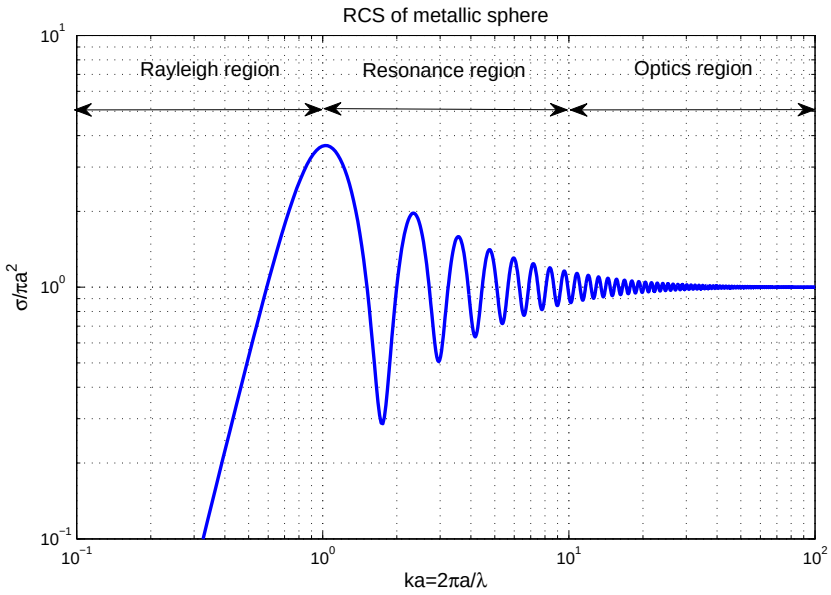

Figure 3.3: RCS of a conductive sphere showing three scattering regimes adapted from [2]. Note the logarithmic scale on both axes.

3.3.1 Rayleigh region

Figure 3.3 shows the RCS normalized with respect to the projected area of the sphere ($\sigma = \pi a^2$) as function of the circumference in wavelengths ka, where a is the radius and k is the real wavenumber. There is no abrupt value of ka for general targets where transition from one zone to the other takes place, however, the Rayleigh region is often taken to be valid for $ka < 1$ and the transition from resonance- to the optics region is normally set to $ka > 10$. For scattering in the Rayleigh region, where target range extent $L \ll \lambda$, there is insignificant variation in the E-field across the target at a fixed time. All target parts experience the same electrical field, which is comparable to a static field incident on the target. However, now the field varies with time [2]. This field pulls charges in opposite ends and induces a dipole moment defined as charge density times separation distance [2]. The strength of this dipole moment is dependent on the size and orientation of the incident field [21]. In this

scattering region the overall target shape is important, whereas target details are of no interest. These assumptions are used to explain the principle of differential RCS later on.

3.3.2 Resonance region

In the resonance region the target size is comparable to the wavelength, which naturally leads to phase differences in the incident electrical field across the target. Scattering in this region consists of both scattering mechanisms normally found in the optics region and surface wave effects were the electric field sticks to the surface and scatters non-locally with respect to the location of illumination. Surface waves occurs in the form of traveling, edge or creeping waves. Backscatter appears as the wave radiates from discontinuities further down the target body, or as in the creeping wave case when the energy reappears on the illuminated face after one or multiple circuits around the target [21, p.226]. Scattering in the resonance region is more dependent on target parts than in the Rayleigh case. However, the overall shape of the target is still the most important, whereas contribution from smaller details remain insignificant.

3.4 Scattering from small airborne targets

Understanding the main scattering mechanisms is considered important in the hunt for useful classification features. In long range radar bands birds and lightweight UAVs tend to scatter in the resonance regions, whereas target parts easily end up in the Rayleigh region. This affects the extractable signatures, potentially in such a way that classification is possible. This section deals with the characteristics of scattering from targets of these classes in the relevant frequency bands.

3.4.1 The prolate spheroid bird model

As mentioned in Chapter 2.1, in 1968 [33] prolate spheroids were suggested as models for birds to support RCS prediction. This must be seen in light of the lack of computational power and need for analytical approximations at the time. On the other hand, although having access to powerful computer tools introduced in Chapter 4, simple models may still be useful to explain the basis for classification theory.

The large wavelength to target size ratio points in the direction of a simple model, as target details are not expected to contribute significantly to the overall RCS. If we initially for the sake of simplicity accept such a model, there are several useful observations that can be made regarding aspect angle and polarization dependencies of the scattered field. However, first the proportion of the model has to be decided on.

The prolate spheroid assumption builds on the relationship between lengths of the three semi axes being $c > b = a$. The semi-major to semi-minor axis ratio $m = \frac{c}{a}$ has to be found. The paper of Hamershock et. al. [122] presents measurements of 12 plucked bird species. By using measured circumferences in this paper to estimate the semi-minor axes, the semi-major axis length that spans the volume of the bird, calculated from the given bird mass and average density, can be found. The model include the bird's head, but not tail feathers. Based on these calculations, which can be found in Appendix B, the semi-major to semi-minor axis ratio is suggested to be $m = 3.5$. The same appendix also show the derivation of Equation 3.9, which is an approximate relationship between plucked bird mass W_p and size under the assumption of a prolate spheroid shaped body.

$$W_p = 1.25\,\pi\,m\,a^3 \tag{3.9}$$

By using Equation 3.9 the ratio m that estimates the measured bird mass the best can be found. Figure 3.4 shows the prediction of W_p for $m = 2$ used in [33] and the suggested $m = 3.5$ in addition to the actual measured masses in [122]. It is worth emphasizing that the *domestic chicken* stands out regarding density and length to diameter ratio compared to wild species.

3.4.2 Bird size in wavelengths

Radars in L- and S-band have different abilities to detect the smallest birds. By still accepting the prolate spheroid model for a while, a rough estimation of bird size measured in wavelengths can be made. In Chapter 3.3 the sphere circumference was used to define the scattering regions. The paths of creeping waves around a

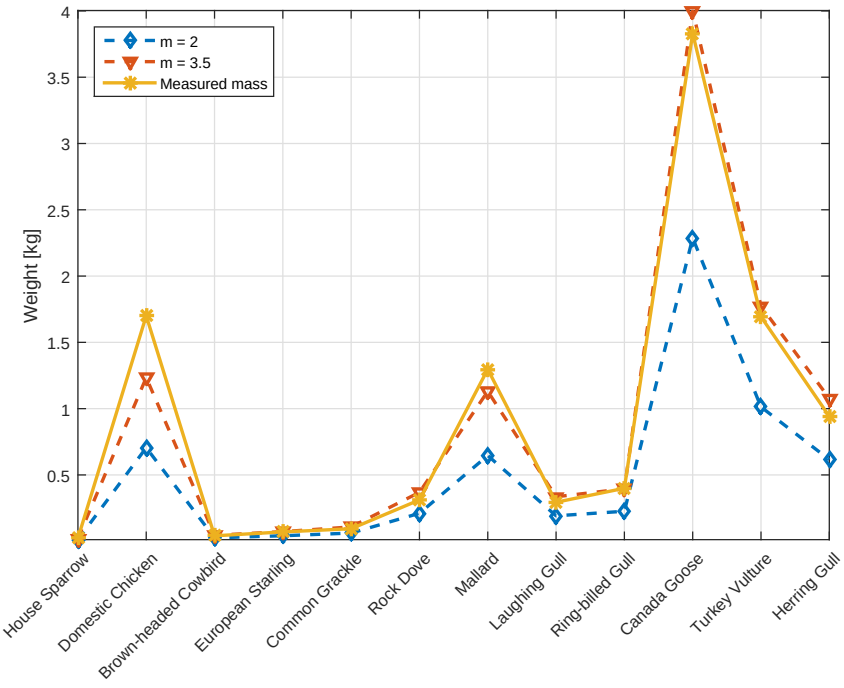

Figure 3.4: Measured and estimated weight for prolate spheroid and different semi-major to semi-minor ratios m.

prolate sphere will be different for different polarizations. This will be explained in more detail in Chapter 3.5.5 on differential polarization. If the semi-major axis c is now in the horizontal plane, the maximum difference in path length between HH- and VV-polarization will occur at broadside illumination. Here these coincide with the longest and shortest circumferences of the spheroid respectively.

If we stick to the criterion for the Rayleigh region being where the circumference is less than one wavelength, Figure 3.5(a) shows that in L-band birds weighing less than $\sim$ 50g, corresponding to a starling in size, fall into the Rayleigh region for any polarization. This also applies to birds of mass less than $\sim$ 5 g for S-band, which in Norway excludes all bird species but the goldcrest. It must be emphasized that these are rough estimations.

For small targets like birds and small UAVs at L- and S-band, contribution from surface waves can be expected. In particular the creeping wave effect is interesting. Due to the possibility of creeping waves refracting into the dielectric bird body, its damping is expected to be larger than an equivalent on a perfectly conducting material. Schaefer [3] found the attenuation of this on dielectric bodies representative of

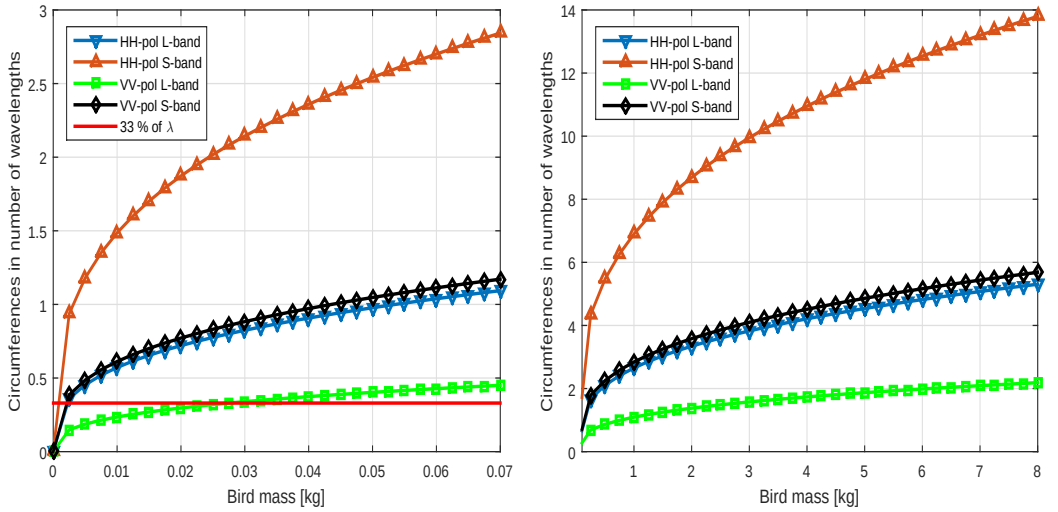

(a) Zoom in on 0 - 0.1 kg (b) Overview 0.1 - 8 kg

Figure 3.5: Size of prolate spheroid measured in wavelengths along the path of HH- and VV-polarized creeping waves. The prolate spheroid with $m = 3.5$ is illuminated broadside.

birds to be roughly equal to the reflection coefficient Γ. Schaefer emphasized that the first revolution of the creeping wave is the one of real significance. If we look at typical values for Γ in figure 3.6(a), we can expect the creeping wave to die out at roughly 60% of the time compared to on a PEC surface. Based on this assumption birds heavier than 8 kg will barely enter the optics region for both polarizations in S-band. Although such simple evaluations are inaccurate as birds are not shaped as prolate spheroids, they indicate that birds of the size relevant to this thesis (≥ 0.5)kg may be treated as falling in the resonant scattering region both for L- and S-band radars. Only the largest birds like swans may fall in the optics region in S-band.

3.4.3 Internal reflections and resonances

Resonances due to internal reflections between layers of tissue are possible dependent on the differences in impedance of the media and the attenuation of the wave inside it. Figure 3.6(a) shows the square of the reflection coefficient, corresponding to power reflected, in the transition from air to different human tissues at orthogonal incidence. The reflected power decreases slightly with increasing frequency for all the materials. Figure 3.6(b) shows how the power decrease with range into different media relative to the incident wave. The relative power level is plotted for both L-

and S-band frequencies for each material, and clearly shows that the attenuation increases with frequency. The data presented is calculated from information available in the database [4] discussed in [123–125]. Potential resonances would depend on interference between waves with the wavelength $\lambda = \frac{2\pi}{\beta}$ in the actual medium, where β is the imaginary part of the complex wave number γ presented in Chapter 3.1. Although it is quite possible that internal resonances can occur where the impedance differences, material thickness and wavelength is right, it's considered unachievable to predict this for all bird species, frequencies and aspect angles. It is also expected that such internal reflections will be considerably attenuated compared to the part reflected off the surface.

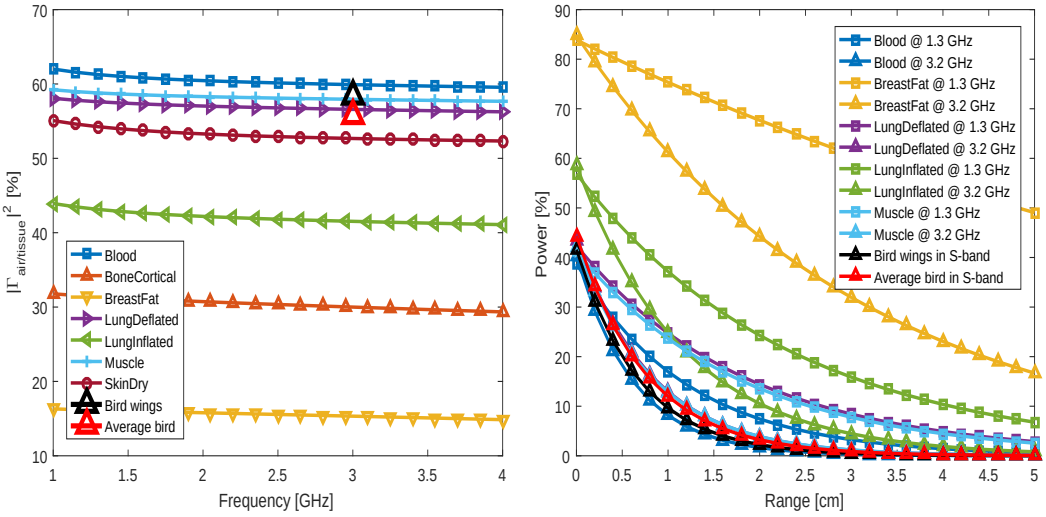

(a) Reflected power from transition between air and different biological tissues.

(b) Transmission into and attenuation in biological tissue. Power relative to incident field.

Figure 3.6: Reflection and transmission in different human tissues. Normal incidence. Separate plots for "bird wings" and "average bird" based on data from [3]. All other data from [4].

3.4.4 Small man-made airborne targets

Small UAVs are more difficult than birds to describe generally. Large variations in shape, position of moving parts and composition of material are found across the classes. For bird sized targets the fuselage surface is, if present, commonly made of a variety of plastics and foams. Although the dielectric properties of such materials vary they are generally found to be more or less transparent in L - and S-band. A

table of different relevant materials can be found in Appendix 5 in [119]. Materials reinforced by carbon fibers are generally much more reflective. The scattered fields are dependent on the number of plies of weave and how the incident field is aligned with the fibers inside the material [126]. The complexity of such material structure is out of the scope of this thesis and the problem is simplified so that plastic, fiberglass and foams are treated as transparent and carbon fiber reinforced materials are regarded as PEC. The latter assumption is based on measurements presented in [126].

In general much of the contributions to the RCS from the target body/fuselage is believed to originate from internal parts, such as wires, batteries, engines etc. A general UAV model is therefore considered unachievable. However, a higher degree of reflections from dihedrals or trihedrals is expected compared to those from birds. Propellers and rotors are normally either made of plastics or carbon fiber reinforced polymer, and therefore represent widely different scattering properties. Whereas the plastic propellers and rotors are expected to be almost undetectable, their carbon fiber counterparts will be highly reflective.

3.5 Polarization

The backscattered E-field from a target is dependent on several factors such as target size to wavelength ratio, aspect angle, shape, spatial distribution of scatterers and material. Another important factor is the target's sensitivity to EM wave polarization. This section is a brief introduction to this vast topic and highlights the effects expected in Rayleigh and resonance scattering regions relevant to the topic of this thesis. For a more thorough description, the reader is referred to textbooks like *Remote Sensing with Polarimetric Radar* by Mott [106] or *Microwave Radar and Radiometric Remote Sensing* by Ulaby et. al. [120].

3.5.1 Polarization scattering matrix

Full utilization of the polarimetric information is obtained when the so called polarization scattering matrix $\mathbf{S}$ is available. According to [127] this can, in the case of a horizontal - vertical basis, be expressed as

$$\mathbf{S} = \begin{bmatrix} |S_{hh}|\, e^{j\phi_{hh}} & |S_{hv}|\, e^{j\phi_{hv}} \\ |S_{vh}|\, e^{j\phi_{vh}} & |S_{vv}|\, e^{j\phi_{vv}} \end{bmatrix} \tag{3.10}$$

$$\mathbf{S} = e^{j\phi_{hh}} \begin{bmatrix} |S_{hh}| & |S_{hv}|\, e^{j(\phi_{hv}-\phi_{hh})} \\ |S_{hv}|\, e^{j(\phi_{hv}-\phi_{hh})} & |S_{vv}|\, e^{j(\phi_{vv}-\phi_{hh})} \end{bmatrix} = e^{j\phi_{hh}}\, \mathbf{S}_{rel} \tag{3.11}$$

This matrix consists of four amplitudes and four phases. However, due to reciprocity in the monostatic case, $S_{hv} = S_{vh}$, and the matrix can be reduced to three amplitudes and two relative phases [127]. The third phase term ϕ_{hh} is in this context not considered to characterize the target in any way besides giving information on the range to the target. The matrix $\mathbf{S}_{rel}$ in Equation 3.11 holds information on the target and forms the basis for the field of polarimetry. The goal is to investigate if $\mathbf{S}_{rel}$ can reveal information useful for classification.

3.5.2 FSA and BSA convention

Two different conventions for describing the scattering matrix $\mathbf{S}$ are commonly used in the literature. In contrast to the forward scattering alignment (FSA) convention, where the orientation of the horizontal and vertical components of the electrical field is always defined according to the direction of wave propagation, the backscatter alignment (BSA) coordinates are always defined with respect to the radar antenna. Being consistent to one definition is important, as the horizontal component is defined in the opposite direction in the two frameworks. The BSA convention is used throughout this thesis.

3.5.3 Differential RCS

Differential RCS σ_{dr} was introduced in Chapter 2.1 as a measure potentially useful for classification of birds as birds. For scattering in the Rayleigh domain σ_{dr} is believed to hold information on the orientation of a target or most likely its parts about the radar line of sight. This is due to the induced dipole moments discussed in Chapter 3.3.1. The phenomenon is covered in the weather radar literature, as this measure is useful for classification of precipitation. The differential RCS can

according to [9] be defined as

$$\sigma_{dr} = 10\log_{10}(\frac{\sigma_{hh}}{\sigma_{vv}}) \tag{3.12}$$

Here $\sigma_{rt} = S_{rt}^2$ with subscripts t and r denoting transmitted and received polarization respectively. As discussed, larger bird bodies will not fall in the Rayleigh region, however, bird wings and UAV rotors and propellers may do.

The strength of the backscattered E-field was in Chapter 3.3.1 described as being dependent on the dipole moment induced, which again is dependent on the target size and alignment with the incident field. From this theory we deduce that illumination of elongated objects will result in polarization dependent RCS, which forms the basis of the hypothesis that bird wings, UAV wings, conductive rotors and propellers can be identified by the differential RCS σ_{dr}.

According to [127] the monostatic scattering matrix for a dipole is dependent on its orientation θ relative to the illuminating E-field about the radar line of sight as:

$$\mathbf{S}_{dipole} = \begin{bmatrix} cos^2(\theta) & \frac{1}{2}sin(2\theta) \\ \frac{1}{2}sin(2\theta) & sin^2(\theta) \end{bmatrix} \tag{3.13}$$

If the characteristic target parts acts as dipoles, Equation 3.13 indicates that polarimetric data can be used to estimate the apparent orientation of such parts around the radar line of sight.

3.5.4 Linear depolarization ratio

The linear depolarization ratio (LDR) is another incoherent parameter extracted directly from $\mathbf{S}_{rel}$. An advantage of incoherent variables is that they are only dependent on magnitudes of the elements in the scattering matrix, which in turn means reduced hardware requirements compared to a fully polarimetric system. The LDR is here denoted δ and expressed

$$\delta = 10\log_{10}(\frac{\sigma_{vh}}{\sigma_{hh}}) \tag{3.14}$$

The logarithm of δ and σ_{dr} is applied for convenience when dealing with potentially small numbers and were not applied in the actual processing as will be described in Chapter 8.5.4. The LDR is a measure of the portion of power depolarized when transmitting horizontally polarized pulses. This can thus be interpreted as holding information on the degree of polarization. However, the main reason for including the parameter here is that it might reveal information about the apparent orientation of dipole like scatterers around the radar line of sight as discussed in previous sections. Equation 3.13 reveals for example that a bird wing orientation $\theta = 45^\circ$ would yield a $\delta = 0$ dB.

3.5.5 Differential phase

Differences in phase between linearly co-polarized channels may occur in both resonance and optics scattering regions. According to high frequency scattering theory an ideal double or even bounce scatterer will result in a differential phase shift $\delta_{vh} = 180^\circ$. A dihedral is a corner reflector associated with double bounce reflections. In [128] Cloude gives an equation for estimation of scattering from such a reflector with arbitrary dielectric properties. Figure 3.7 is an exemplification based on this expression and shows that the opening angle providing 180° phase shift is limited for lossless media and that values different from 180°can be expected for lossy material. Dielectric constants used here are similar to that of some kinds of thermoplastics ($\varepsilon_r = 2.2$) shown in blue, muscle tissue ($\varepsilon_r = 25 - j15$) in red and a PEC material in yellow.

In practical conditions multiple scattering centers may contribute to the total polarization signature, and the degree of polarization is reduced. In such partial polarized cases the differential phase angle may have a variety of values and the average values are used.

For birds and small UAVs in L- and S-band, pure optics region scattering is generally not expected. Normally targets in these classes fall in the resonance region and a contribution from surface waves adds to the opticslike scattering effect and complicates the picture. In this region contributions from differential polarimetric phase shifts may origin from both opticslike scattering and surface waves.

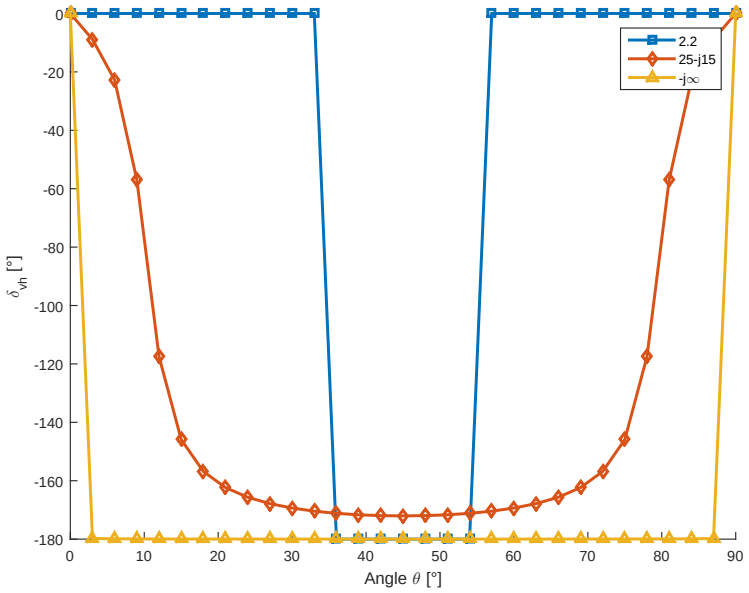

Figure 3.7: Estimated differential phase shift from dihedral as function of dielectric constant and illumination angle θ.

Figure 3.5 showed that the circumference measured in wavelengths is dependent on polarization. This requires some explanation. As discussed in Chapter 3.3.2, surface waves are denoted traveling waves or creeping waves dependent on if it is present on the illuminated side of an object or on the shadow side respectively. According to Knott et. al. [2], a traveling wave can be launched only when the incident E-field has components in the incidence plane both orthogonal and parallel to the surface. If we imagine an horizontal electric field incident on a sphere, this means that a surface wave can only be excited in the regions of the sphere on the outer left and outer right relative to the line of sight, and the traveling path of the wave will a be geodesic along the equator. Correspondingly, a vertically polarized field will launch creeping waves at the poles of the sphere and creep around the geodesic path along the longitude in the continuation of the line of sight. However, due to the spheroidal geometry the vertical and horizontal paths will be equally long. In the case of a prolate spheroid illuminated broadside with the incident wave polarized along the longest axis, the creeping wave will according to Schaefer [3] follow the longest circumference. Correspondingly, a wave polarized orthogonal to the longest axis will follow the circular circumference. Under this assumption, creeping waves with different polarization will experience different traveling distances around the

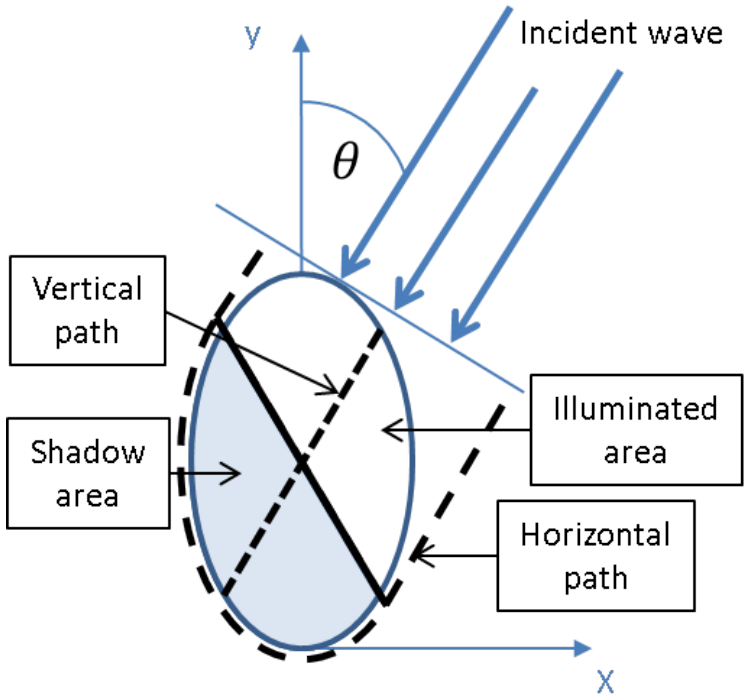

Figure 3.8: Paths of traveling wave for horizontal and vertical polarization adapted from [5].

target. This may be a source of significant differences in measured RCS and phase values between polarizations in the direction of the radar receiver.

Moffat presented in [5] an analytical approximation to the RCS of a PEC prolate spheroid for both parallel and orthogonal polarizations. This accounts for the specular reflection on the illuminated face of the spheroid, as well as the creeping waves going around it. The equations are not reproduced here due to their complexity. Figure 3.8 shows the different propagation paths for horizontal and vertical polarization. For the prolate spheroids illuminated in the *xy*-plane the propagation paths will be identical for illumination angles $\theta = 0°$ and $\theta = 180°$. However, for all other angles there will be a difference in length. This difference can in the case of linear polarization be measured by the differential phase between vertical and horizontal channels, naturally with ambiguities for $n\lambda$. According to [14] this measure can be expressed as

$$\Phi_{dp} = \delta_{vh} + 2\int K_{dp}(r)dr \tag{3.15}$$

where $\delta_{vh} = arg(S_{vv}S_{hh}^{*})$ is the backscatter differential phase and K_{dp} is the specific differential phase, which takes the cumulative phase development through the propagation medium into account. In precipitation the specific differential phase prevails and δ can only be "*significant for large oriented hydrometeors, such as hailstones, aggregates, or drops containing ice cores*" [14]. Measurements of Φ_{dp} are widely used to gauge rainfall in the Rayleigh region under the assumption $\delta_{vh} \approx 0$. The motivation for evaluating this measure for classification purposes of birds is connected to the theory of surface waves traveling along different paths depending on polarization. In this case the assumption is that δ_{vh} will prevail and be used for classification. It should be emphasized that this requires insignificant precipitation between the target and the radar.

3.6 Spectral analysis

Resolving target scatterers in velocity is considered useful both to estimate the degree of micro-motion associated with the target and to extract clean polarimetric signatures of target parts. In the case of small UAVs and birds the most important parts are in this context propellers, rotors and bird wings. Without any velocity resolution the signatures of these will be inseparable from the fuselage/body and frequently dominated by its signature due to potentially large differences in RCS.

3.6.1 Velocity resolution

Spectral analysis techniques used to achieve this are associated with limitations in resolution, which will be described in Chapter 8.4. Let us for now accept that the radial velocity resolution Δv_r can be expressed as

$$\Delta v_r = \frac{\lambda \, \Delta f_d}{2} = \frac{\lambda}{2 \, \tau_d} \tag{3.16}$$

where Δf_d is the Doppler frequency resolution and τ_d equals the coherent processing interval CPI or dwell time. As will be covered later, the spectral estimation techniques to be used requires the spectrum to be stationary, in practice having constant mean and variance. The Doppler spectrum, for example associated with bird wings, is typically nonstationary and the maximum duration of τ_d must be carefully

selected to comply with this requirement.

3.6.2 μ-Doppler signatures

μ-Doppler signatures are suggested to visualize target characteristics in this thesis. Such joint time-frequency representations rely on distinguishing between scatterers based on differences in time and radial velocity. To achieve this a certain velocity and time resolution is required. Limitations in τ_d additional to those already described for stationarity arise as high time resolution is required in short time Fourier transform (STFT)-based methods.

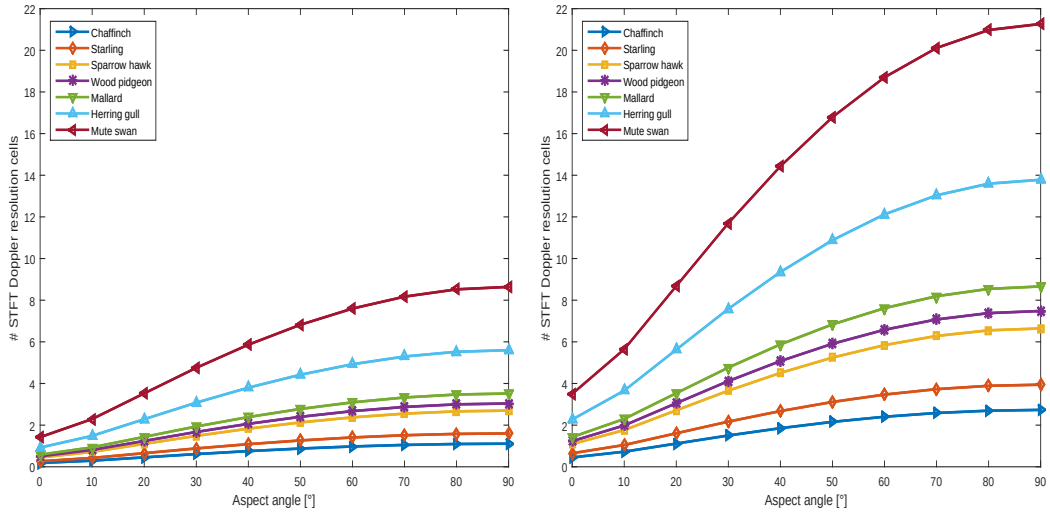

(a) Doppler cell spread L-band (b) Doppler cell spread S-band

Figure 3.9: Spread in Doppler cells in L- and S-band from different bird species. 60% of the bird wing length is assumed to contribute with a wing opening angle of 120°. CPI is kept at 35% of the time of a wing beat interval and elevation angle is 5°.

Figure 3.9 shows rough estimations of the number of Doppler resolution cells different birds can be expected to occupy as function of aspect angle and frequency band. The figure is meant to give an impression of how effective STFT-based μ-Doppler processing may be under relevant limitations. The aspect angles covered correspond to the bird seen from the front at 0° to broadside at 90°. The wing beat frequencies and the wing length are consistent with values for the actual bird species found in [46]. 60% of the bird wing length is assumed to contribute to the backscattered signature. The decreasing wing flapping frequency with increasing

wing length, leads to a partial compensation of wing tip velocity. The CPI is kept at 35% of one wing beat cycle, leading to a longer effective CPI for large birds.

In general the number of occupied Doppler cells is low for both L- and S-band. Sweeping and twisting movement of the wings are disregarded, although such movements would increase the Doppler bandwidth at front and rear aspects. However, the elevation angle of 5° induced can be seen to give similar effect. Figure 3.9 shows the potential challenge of establishing a traditional spectrogram based on a classic STFT algorithm, especially in L-band. High resolution joint time-frequency transforms can contribute to increase both time and frequency resolution, however, as time-frequency representation is not suggested for automatic classification in this thesis this possibility is not investigated in detail.

3.6.3 Apparent μ-Doppler signature

Amplitude modulations of echoes from birds and rotors/propellers are suggested for use in classification. Such modulations may be mistaken for Doppler shifts in the spectrogram when the modulation is of short duration compared to the CPI. This effect is not found to be covered in the μ-Doppler literature, most likely because these techniques usually are applied to high frequency data with significant Doppler shifts and where the relative contribution from any amplitude modulation is low. However, in cases where the Doppler shifts are low, for instance comparable to the theoretical Doppler resolution, contribution from an impulse-like amplitude modulation may in practice dominate the phase modulated signal.

The spectral content of an impulse like modulation is dependent on its shape and duration in the time domain and independent of carrier frequency unlike the phase modulated μ-Doppler signal. The bandwidth of for example a Gaussian shaped impulse is roughly the inverse of its duration. One characteristic of this signal is that it is symmetric in the frequency domain, but that may apply to a helicopter type UAV with even number of blades as well. In the case of a rotor blade flash, a significant bandwidth possibly comparable to the Doppler shift associated with reflections off the blade can be observed at lower carrier frequencies. Doppler shifts of bird wings are significantly lower, so modulations of much longer duration

may cause comparable bandwidths.

Contributions from amplitude modulations are not considered a major problem in the context of separating between birds and UAVs. Frequency domain signatures are believed to hold valuable information for classification whether they are caused by amplitude or phase modulations. The important thing is to be aware that amplitude modulations may affect Doppler signatures when an interpretation of the physical cause is made.

3.7 Summary

A large majority of the publications on NCTR techniques assume scattering in the optics region. Investigations presented in this chapter have revealed that birds and UAVs of comparable size mostly fall in the resonance scattering region in the relevant air defence radar frequency bands. Studies of dielectric properties of birds have shown that the electric field is significantly attenuated inside the body and little reflection from the bird's interior is to be expected. For UAVs a larger portion of less conductive materials compared to full size aircraft is expected. This may result in significant echoes from internal parts as wires, engines and batteries.

Spatial- and velocity resolution are often significantly limited in relevant radars due to frequency allocation challenges, and the combination of low carrier frequency and short dwell times respectively. Additionally, marginal Doppler shifts due to low carrier frequency and impulse like amplitude modulation may cause difficulties in distinguishing between frequency components caused by amplitude and phase modulations. With this in mind, the possibility to separate between birds and man-made targets based traditional NCTR techniques alone does not look promising. However, there exist other parameters potentially more interpretable under such conditions.

One suggestion is including polarimetric parameters that take advantage of scattering in the low frequency regions. Although the targets as a whole generally are found in the resonance region, target parts like bird wings, UAV wings, propellers and rotors may not. If these parts fall in the Rayleigh region as anticipated,

they will act as dipole like scatterers. The differential RCS σ_{dr} of such scatterer is dependent on its alignment with the induced E-field around the line of sight. As the overall target shape is more important than individual target details in this scattering region, the potential of extracting a clean polarimetric signature from flapping bird wings, rotors and propellers by separation in velocity is considered to be high.

The differential phase δ_{vh} is an example of a parameter utilizing scattering in the resonance region. Initial studies presented in this chapter have shown that propagation paths for creeping waves around a simple bird model are different depending on the incident polarization. This parameter is easiest to interpret around frontal, rear and broadside illumination. At other aspects the parameter is dependent on the bird size to wavelength ratio L/λ. Questions still remaining are connected to the influence of wings and how well it separates between target classes, as there might be scattering mechanisms present for man-made targets providing δ_{vh} similar to that of birds.

The next chapter makes use of more advanced models and methods for investigation of the usefulness of these parameters.

Chapter 4

Electromagnetic prediction

This chapter presents the results of electromagnetic prediction of relevant targets and target parts. Topics covered include evaluation of RCS, verification of bird models, comparison of materials, detectability of target parts as well as investigation of aspect angle, frequency and polarization dependencies for several targets. A special attention is given to scattering mechanisms forming the basis for classification based on polarimetric variables such as differential RCS and phase introduced in Chapter 3.

4.1 Electromagnetic prediction code

The interaction between EM-waves and physical objects can be predicted by electromagnetic modeling techniques solving Maxwell's equations on three dimensional models. In order to evaluate RCS and polarimetric signatures of targets and target parts, a finite difference time domain (FDTD) prediction code was used. The implementation was done in *Fortran 90* by my colleague Dr. Øystein Lie-Svendsen. It must be emphasized that the development of the code is the work of him, and my use of it has been in accordance with his instruction manual. This code requires homogeneous targets, which is considered acceptable as internal target structures are generally unknown. The version of the code used for the presented predictions supports dispersive media, which is believed to increase the realism of predictions for biological tissues.

The FDTD method integrates Maxwell's curl-equations in the time-domain.

The scattering target is modeled as a volume with electric permittivity and magnetic permeability potentially specified for every grid point. Scattering takes place as EM waves encounter regions with different impedance, as described in Chapter 3.1. The volume enclosing the scattering object is limited to be small as the method is computationally demanding. At the outer boundary of the volume a layer of perfectly matched impedance is implemented to prevent reflection from the boundary. In use, a plane wave of finite extent is launched towards the scattering object, and the electric and magnetic fields are integrated forward in time until they have vanished. The RCS values presented in this thesis, are obtained by Fourier transformation of the time-domain fields on a surface enclosing the object, and then performing a near to far field transformation of these frequency domain fields. This way bi-static, as well as mono-static, values are calculated in the process. RCS can be calculated at many frequencies simultaneously by choosing a narrow, and hence broadband, incident plane wave. Being a volume method, FDTD is well suited to model scattering from dielectric bodies, in which case radiation penetrates into the body. The method is formally valid at all frequencies, but is best suited at lower frequencies. For numerical stability and accuracy, the grid spacing must be 1/10 of a wavelength or smaller. If thin volumes are modeled, like bird wings, the grid spacing must be fine enough to handle this as a volume. The computation time required to calculate the RCS for frequencies up to 3.7 GHz of a bird with a body length of 45 cm was approximately 26 hours. This time was required for calculation of one polarization alone at the 37 aspect angles presented at a HP workstation PC from 2013. More details on the FDTD-method can be found in [129].

4.2 Simulation overview

Signatures of bird wings, rotors and propellers play key roles in several methods relevant for recognition. Evaluation of the RCS of these parts in the actual frequency bands is crucial when exploring the methods' suitability for classification. Electromagnetic predictions of such components are presented in the following sections. The FDTD code was used on 3D models made in *Rhinoceros* [6] for frequencies

ranging from 1.2 - 3.4 GHz. The models were converted to a readable format of raw triangles with a grid resolution of $\lambda_s/20$ where λ_s is the wavelength associated with the highest required frequency component (S-band). In cases where the shape of the model required finer resolution, for instance for long thin UAV rotor blades, the resolution was increased to avoid holes in the model. Due to excessive time consumption the predictions were done in the *xy*-plane only. Figure 4.1 shows the simulation geometry. Mono-static fields were predicted for azimuth angles θ ranging from 0° to 180° with a resolution of 5° for all models, except the dihedral and trihedral. These were covered for θ between 0° and 90° with the same resolution of 5°. The angle θ indicated as yaw-angle in all relevant figures is the angle formed between the direction of illumination and the *x*-axis. A yaw angle of 0° therefore means illumination from the front, 90° along the negative *y*-axis, whereas 180° corresponds to illumination from the rear.

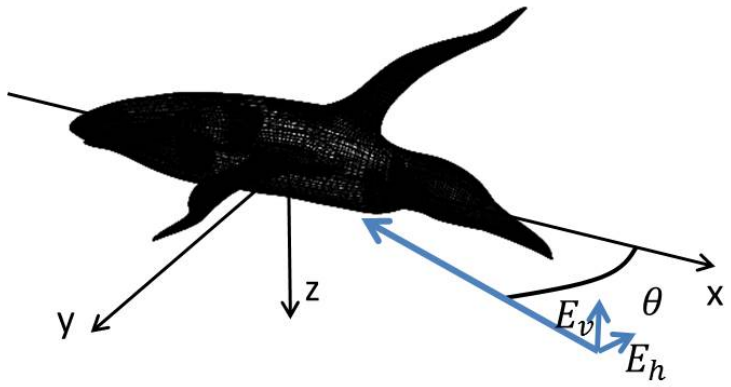

Figure 4.1: Simulation coordinate system

Computations were done twice for each aspect angle, one for vertically and one for horizontally polarized incident field denoted (E_v) along the *z*-axis and (E_h) in the *xy*-plane in Figure 4.1 respectively. For each polarization, the magnitude and phase of co- and cross-polarized components were evaluated.

4.3 Predictions on avian target models

Detectability and signatures of birds and bird parts are central to the research question covered in this thesis. This section covers predictions of prolate spheres as bird models and 3D models of a bird wing and a bird body without wings and with wings

in different positions. Simulations were done for models of different materials and size.

4.3.1 Prolate spheroid models

The prolate spheroid is, as discussed, suggested as a model for prediction of bird RCS, and understanding the scattering mechanisms present on such a simple target may prove valuable for understanding the scattering from birds in general. The monostatic scattered fields from homogeneous prolate spheroids of different sizes and axis ratios were investigated. Figure 4.2 shows two of the models used.

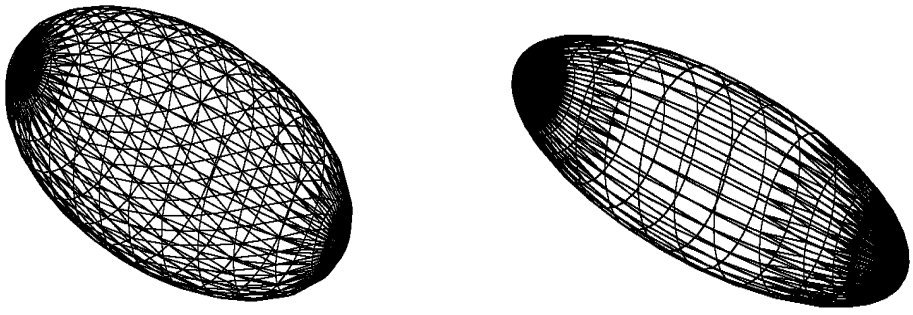

(a) m=2 (b) m=3.5

Figure 4.2: 3D models of prolate spheroids with different semi-major to semi-minor axis ratios m

Figure 4.3 shows the predicted σ_{hh} and σ_{dr} of a prolate spheroid with c = 18 cm and $a = b$ = 5.14 cm, which corresponds to a *Black backed gull* in size. The simulation geometry is as described above with the semi-major axis c coinciding with the x-axis. In Figure 4.3(a) significant variation in σ_{hh} is found across both yaw angle θ and frequency. Not surprisingly the maximum of almost -10 dBsm is found at broadside incidence. From considerations presented in Chapter 3.4.2 objects of this size are found in the resonance region in the investigated frequency band. This means that both opticslike scattering and traveling waves contributes to the total scattered fields. The effect of creeping waves, discussed in Chapter 3.5.5,

is found as frequency dependent variations of RCS across the figure. At broadside, where the contribution from specular scattering is large, this effect is significantly less. For illumination closer to the ends, the specular reflection is less and the frequency dependent effects of constructive and destructive interference between waves propagating in opposite direction around the target are prominent.

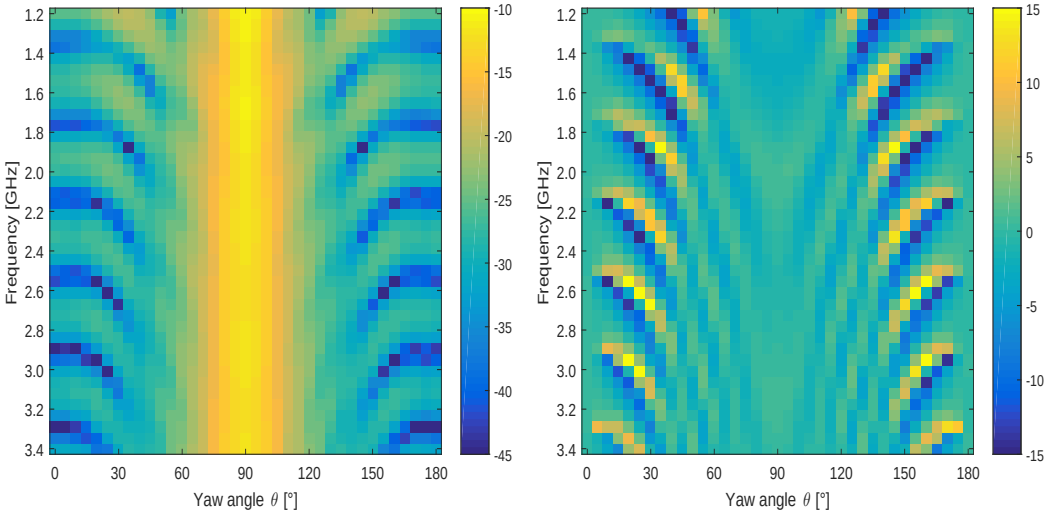

(a) σ_{hh} (b) σ_{dr}

Figure 4.3: Predicted RCS for HH-polarization σ_{hh} and differential RCS σ_{dr} for prolate spheroid model with c=18 cm and a=b=5.14 cm.

Figure 4.3(b) shows σ_{dr} for the same object. Seen from the front ($\theta = 0°$) and the rear ($\theta = 180°$) values are found to be 0 dB. At these incidence angles there are no difference in dimensions of parts responsible for specular contributions nor in the propagation path for creeping waves launched at different polarizations. In regions of yaw angles ranging roughly from 10° - 70° and correspondingly 110° - 170° the contribution from creeping waves and interference of these are prominent. At these incidence angles contributions from specular reflections are small and differences in propagation paths of the creeping waves caused by different polarizations are generally present. Variations in values of more than 30 dB is observed for small variations in frequency. At broadside illumination the projected area contributing to the specular reflection is larger and dominates over the creeping wave effect. However, the contribution from creeping waves are not completely negligible as variations of around 3 dB are found across the frequencies.

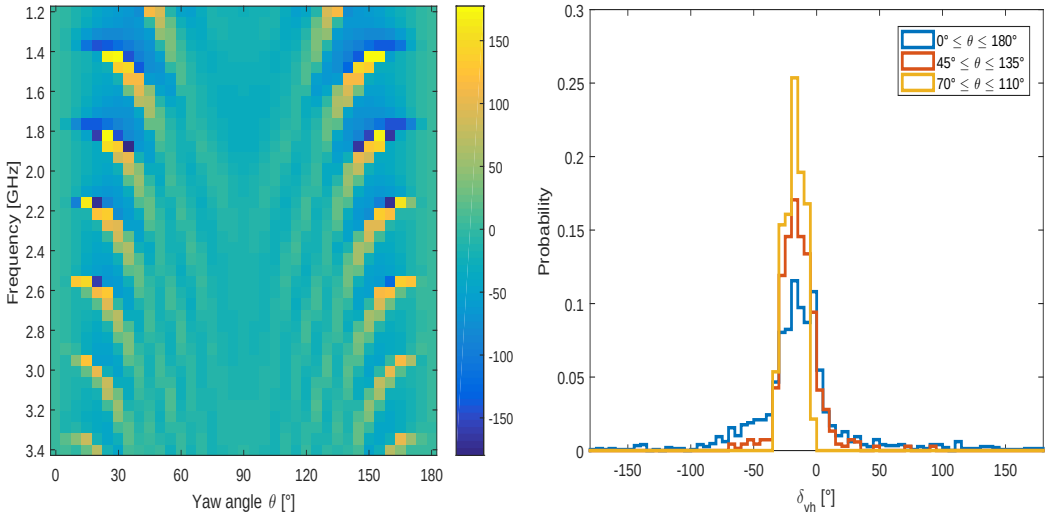

(a) δ_{vh} (b) Histogram of δ_{vh} over all f_c

Figure 4.4: Differential phase δ_{vh} for prolate spheroid model with c=18 cm and a=b=5.14.

Figure 4.4 presents the differential phase δ_{vh} for the same prolate spheroid. Figure 4.4(a) shows δ_{vh} across the same azimuth angles and frequencies. δ_{vh} close to 0° at front and rear views is seen for the same reasons σ_{dr} was observed close to 0 dB in Figure 4.3(a). The rotational symmetry around the line of sight at these illumination angles makes the propagation path length of creeping waves identically long for all incident polarizations and therefore no phase differences occur. For more oblique incidence angles, still for the same reasons as explained for σ_{dr}, the propagation paths of vertical and horizontal polarized waves travel different paths around the object and phase shifts between polarizations are observed. In the case of broadside illumination the scattered field is dominated by the specular reflection, however, the different geodesics of horizontally and vertically polarized waves contribute to a generally negative phase difference. The statistics of δ_{vh} as function of yaw angle θ in selected intervals is found in Figure 4.4(b). The blue line shows the distribution of δ_{vh} over all frequencies and all yaw angles θ in the simulation. Significant peak frequencies are found in the intervals $-20^\circ \leq \delta_{vh} \leq -15^\circ$ and $-5^\circ \leq \delta_{vh} \leq 0^\circ$. As the yaw angle intervals are reduced, as indicated by red and yellow lines, the frequency in the interval $-5^\circ \leq \delta_{vh} \leq 0^\circ$ is reduced significantly since the values close to 0° are mainly associated with front and rear aspect views.

In conclusion, electromagnetic simulation of bird sized prolate spheroids has confirmed that resonant scattering effects are to be expected of bird sized targets. The RCS values varies significantly with aspect angle, frequency and polarization. High absolute values of σ_{dr} are particularly prominent for yaw angles in the intervals $10^\circ \leq \theta \leq 70^\circ$ and $110^\circ \leq \theta \leq 170^\circ$. However, since resonant scattering is observed in this interval σ_{dr} is not suitable for classification as suggested for scatterers like bird wings and UAV propellers and rotors in the Rayleigh region. Separation of such scatterers from the fuselage or bird body in velocity is beneficial for ensuring interpretable signatures. Slightly negative values of δ_{vh} around broadside illumination is on the other hand interesting for classification. A central question is if this is measurable in real life data and separable for example from the expected δ_{vh} values around 0° for odd bounce scatterers. Before testing this on measured data, more realistic bird models must be evaluated.

4.3.2 3D bird models

A bird model was made with help from my colleague Atle Knapskog. This was done in the 3D modeling software Rhinoceros [6] and consisted of a total of five models. One full size gannet body alone, a single gannet wing, and three versions of body and wings in three different positions, namely wings in level position, 45° up and 45° down. Figure 4.5(a) and 4.5(b) shows the single wing and bird body with level wings respectively. The wings were modeled as to best represent the parts with the assumed most muscular parts, see Figure 4.6(b). Bird feathers have been found to provide a negligible contribution to the RCS in both S- and X-band [33, 34], and only plucked birds are therefore considered in the following. All models were in addition to a full size version produced in down scaled versions 60% and 20% of original size for investigation of size dependencies.

4.3.2.1 Model comparison

Although prolate spheroids may have visible similarities to birds there is one obvious problem, namely the lack of wings. With the possibility of predicting the backscattered fields from 3D models, comparisons between a prolate spheroid and

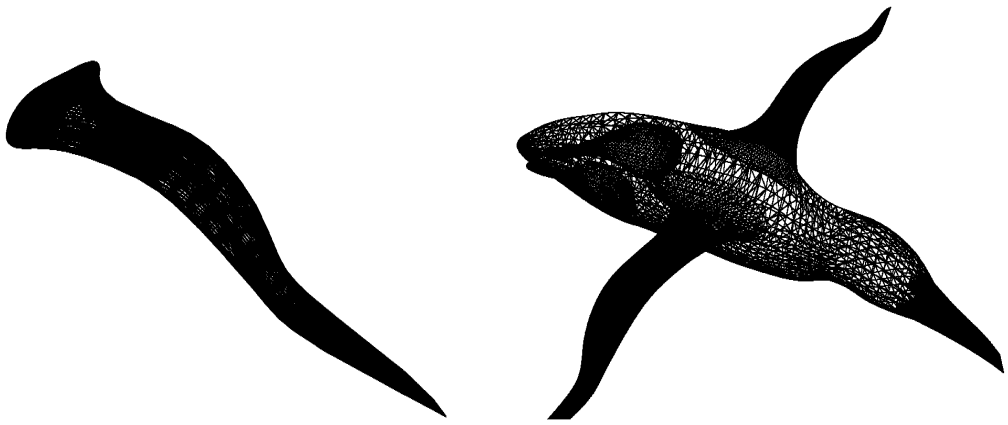

(a) Gannet wing (b) Gannet with level wings

Figure 4.5: 3D gannet models created in the Rhinoceros software [6].

more detailed gannet models with and without wings, shown in Figure 4.5 and Figure 4.6, were performed with the FDTD code. The gannet model used has a body length (beak to tail without feathers) of 46 cm corresponding to 60% of a full size gannet, or a full size black-backed gull. The prolate spheroid was modeled as similar as possible to the bird's body with a semi-major to semi-minor axis $m = 3.5$, resulting in c=18 cm and a=b=5,14 cm. All models were modeled with dielectric properties similar to human muscle.

The results are shown in Figure 4.7. In L-band the prolate spheroid model, seen in Figure 4.7(a) and 4.7(b), is found to be an acceptable overall model for rough estimation of σ_{hh} and σ_{vv} as long as the wings are excluded from the model. However, as level wings are added, the match is reduced. A reasonable compliance is found between models at illumination in the range $40^\circ \leq \theta \leq 140^\circ$. Illumination from the front and rear gives on the other hand a poor match. At least this applies to σ_{hh}. For σ_{vv} the difference is far less. S-band predictions, found in Figure 4.7(c) and 4.7(d) are evidently more sensitive to aspect angle changes. This is to be expected as contribution from target details, and thus decorrelation effects, increase with increasing size to wavelength ratio. As in L-band increased values of σ_{hh} are found at frontal and posterior illumination.

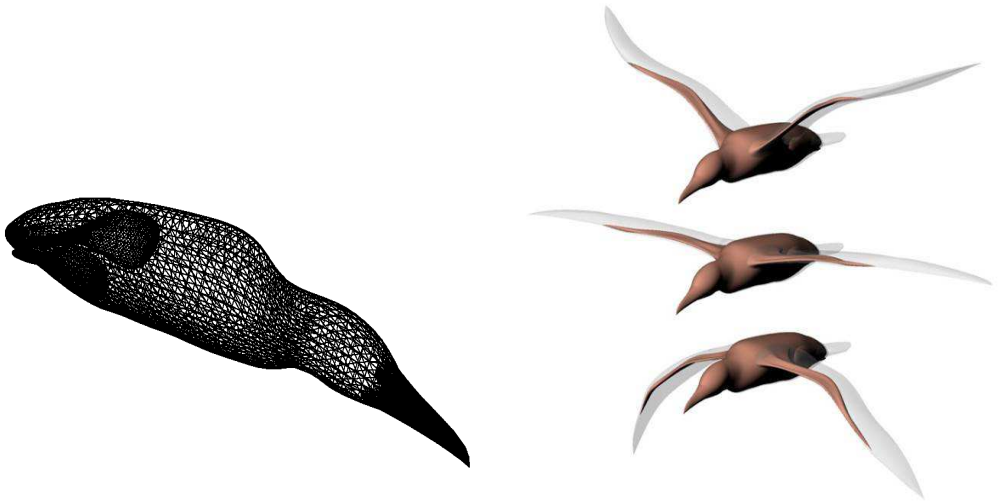

(a) Gannet body without wings

(b) Models of a gannet with three different wing positions. Only the most muscular parts in dark color is modeled

Figure 4.6: 3D models of birds made in the Rhinoceros software.

Generally we may conclude that prolate spheroids have limited validity for RCS prediction of bird models of this size in L- and S-band. The most important finding so far is the significant increase in σ_{hh} for illumination from the front and rear in both frequency bands. This is believed to be due to significant contributions from the horizontally oriented wings, and is the first indication that wings and their orientation relative to the incident polarization is important.

4.3.2.2 RCS of birds and the effect of materials

As already mentioned, birds consist of different materials with distinctive dielectric properties. The prediction code used is limited to handling homogeneous models, and a compromise had to be made for the dielectric constant to be used. Schaefer [3] found an average dielectric constant for birds, where different organs with the associated dielectric constants contributed to the average by its weight percentage. This constant is given for S-band only and not used here. Figure 3.6 showed that these coincide well with human muscle and blood properties. Therefore human tissues, for which good data from [4] covering all the relevant frequency bands is available, was considered to be a good approximation in this case.

Figure 4.8 shows the effect of using dielectric constants for three different ma-

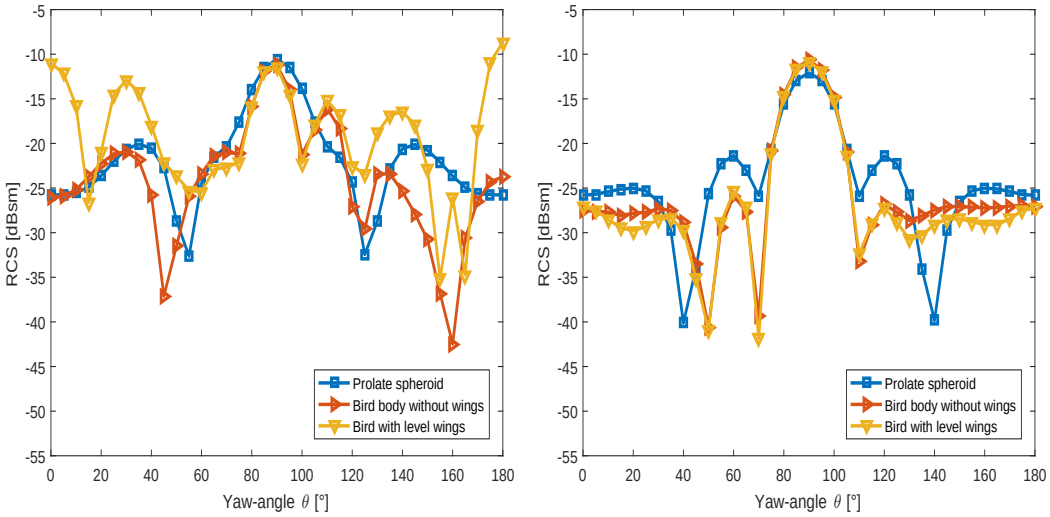

(a) σ_{hh} @ 1.3 GHz (b) σ_{vv} @ 1.3 GHz

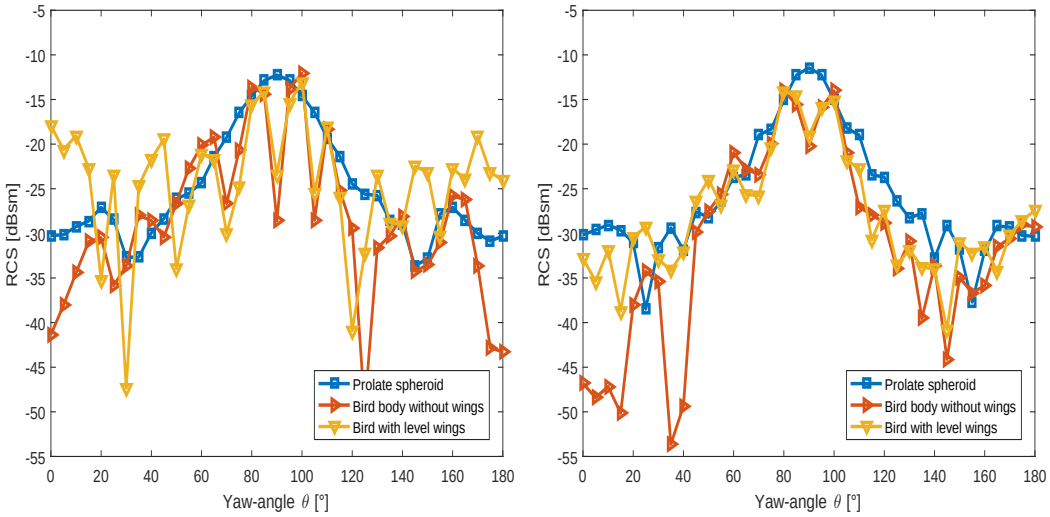

(c) σ_{hh} @ 3.25 GHz (d) σ_{vv} @ 3.25 GHz

Figure 4.7: RCS comparison of prolate spheroid, bird body without wings and bird with wings in level position. Predictions done with FDTD code.

terials on the gannet model scaled to 60% of full size and with its wings level. In general the model treated as perfect electric conductor (PEC), represented by blue lines, gives the largest RCS. This is not unexpected as the reflection coefficient equals one for a such material. However, at certain aspect angles the model with muscle tissue, shown in red, has larger RCS. This is seen at 1.3 GHz close to front and rear aspects. The reasons for this are complex and probably connected to phenomena associated with internal reflections as the wave may penetrate into thinner parts of the muscular bird model and resonate. At other illumination angles this

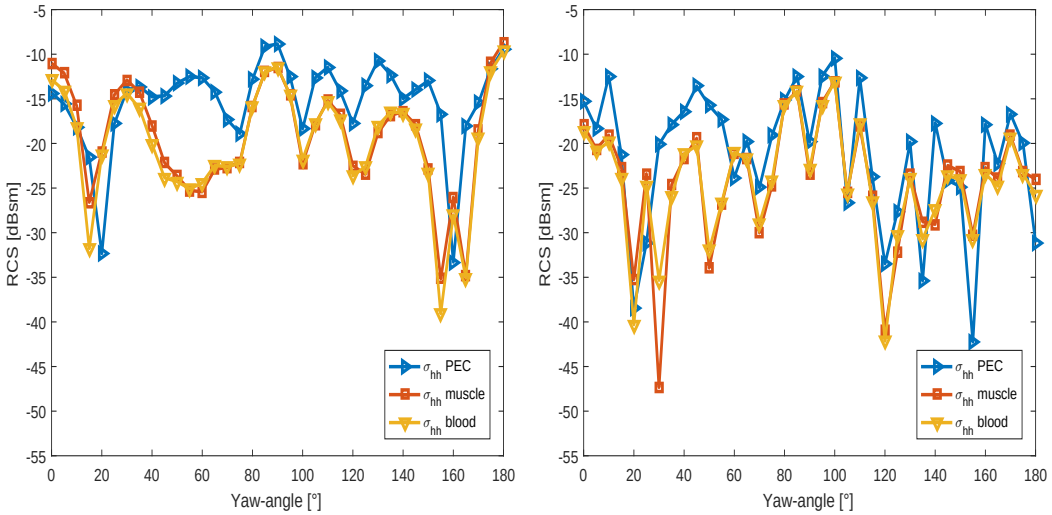

(a) σ_{hh} @ 1.3 GHz (b) σ_{hh} @ 3.25 GHz

Figure 4.8: RCS of gannets modeled by different materials. Models 60% of full size and with wings level. All results from predictions by the FDTD code.

model has more than 10 dB lower RCS compared to the PEC model, however, generally the difference is less in both frequency bands. The similarity between blood, represented by yellow lines, and muscle tissue are generally very high. This indicates that only small errors are introduced by inaccuracies in the dielectric constant.

4.3.2.3 RCS of birds and wings of muscle tissue

Figure 4.9 shows histograms of predicted σ_{hh} and σ_{vv} values for a the gannet model of muscle tissue and a horizontally oriented wing in both L- and S-band. The bird model was scaled to 60% of full scale and having level wings. Azimuth angles in the range 0° to 180° were included. The largest RCS values for the entire bird are found for σ_{hh} at 1.3 GHz, see Figure 4.9(a). Values of σ_{hh} span from -40 dBsm to -10 dBsm for the entire model in this frequency band. The maximum values of σ_{hh} in S-band are found to be slightly lower in the histogram in Figure 4.9(b). RCS at HH-polarization are largely found to be higher than σ_{vv}, and in Figure 4.9(a) the distribution of σ_{hh} is seen to be shifted two bins to the right compared to that of σ_{vv}. This is believed to be connected to the horizontal extent of the model and the presence of horizontally oriented scatterers in the Rayleigh region. Particularly interesting is the distribution of σ_{hh} for the horizontally oriented wing. This is found

between the two mentioned distributions, meaning that the RCS of one wing aligned with the incident E-field is larger than σ_{vv} of the entire bird and only roughly 5 dB less than σ_{hh} of the entire bird on average. The same tendency is found in L-band. This means that contribution from wings are of importance and this is covered in more detail under the topic of differential RCS later in this chapter. Another inter-

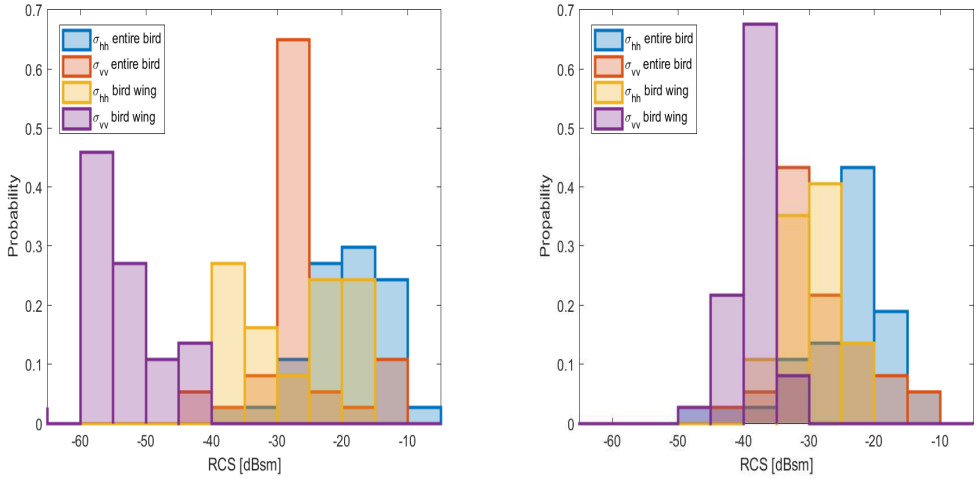

(a) L-band - 1.3 GHz (b) S-band - 3.25 GHz

Figure 4.9: Histograms showing RCS of bird model and horizontally oriented bird wing. All models scaled to 60% of full gannet size. Evaluated over azimuth angles $\theta = 0 - 180°$. All results from predictions by the FDTD code.

esting observation is the significantly lower span in RCS values in S-band compared to L-band. This is especially evident for the wing, and is believed to be caused by dipole-like scattering in the Rayleigh region. The distribution of σ_{vv} for the horizontally oriented wing in L-band is so low that it in practice is undetectable at ranges of interest.

4.3.2.4 Bird wings as radar reflectors

Since signatures and RCS of bird wings have proved to be of great interest for classification, a closer look at their RCS and contribution to the overall target signature is required. Figure 4.10 shows the predicted RCS and differential RCS of a gannet wing in level position scaled to 60% of full size. Variations is seen across azimuth angle and frequency for both σ_{hh} and σ_{vv}, as seen in Figure 4.10(a) and Figure 4.10(b). Illumination from the front and rear aspect generally lead to the least vari-

ations with frequency. This is an indication that the Rayleigh scattering hypothesis holds at these aspects. Illumination along the longest wing axis generally lead to more fluctuation, probably caused by scattering in the resonance region along this dimension. Generally lower RCS values are found for illumination along this axis compared to from front and rear, however, this varies with frequency and wing size. RCS values of wings are actually found less aspect angle dependent than might be expected. Absolute values of σ_{vv} are generally very low, especially at lower frequencies, and the detectability is considered low at this polarization.

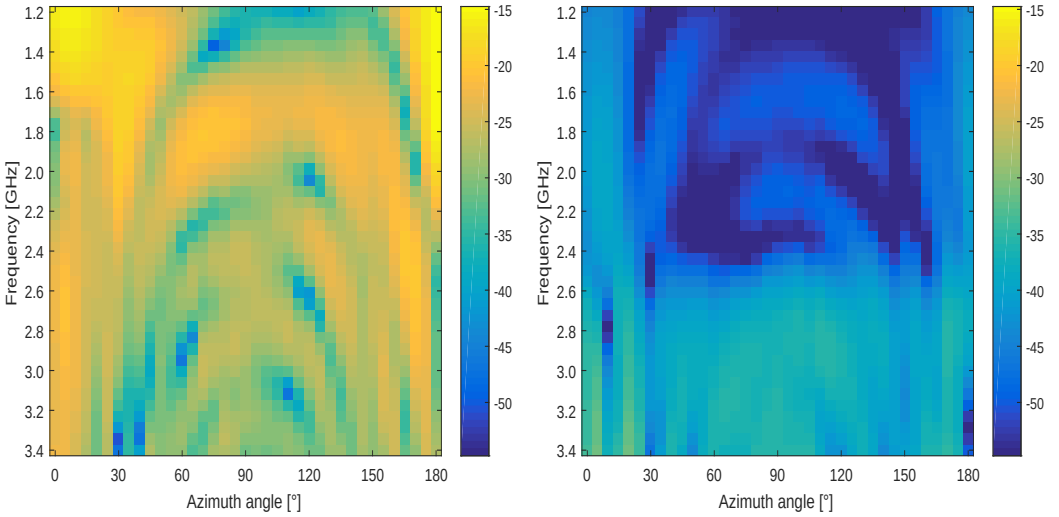

(a) σ_{hh} of gannet wing

(b) σ_{vv} of gannet wing

Figure 4.10: RCS [dBsm] of horizontally oriented gannet wing. Model 60% of full size. Predictions by FDTD code.

Although evaluation of scattering properties over a range of frequencies is equivalent to varying the size of a non-dispersive target model at a fixed frequency, predictions of a gannet wing model of different sizes were performed. This was scaled to sizes of 20%, 60% and 100% of a full size gannet wing. This corresponds to wing lengths (muscular parts only) of 9 cm, 27 cm and 45 cm respectively. These sizes are meant to represent wings of small, medium and large birds. Circumferences of the wing cross sections are roughly 10%, 40% and 60% of the wavelength in air for L-band, and 30%, 100% and 170% of the wavelength in S-band. The extent of the wings along the direction of illumination varies with aspect angle, and is essential to what scattering mechanism is experienced. From the front and

rear the assumption of Rayleigh scattering is considered to hold in both frequency bands. For yaw-angles around 90° the extent is much longer, and scattering in the resonance region may be expected.

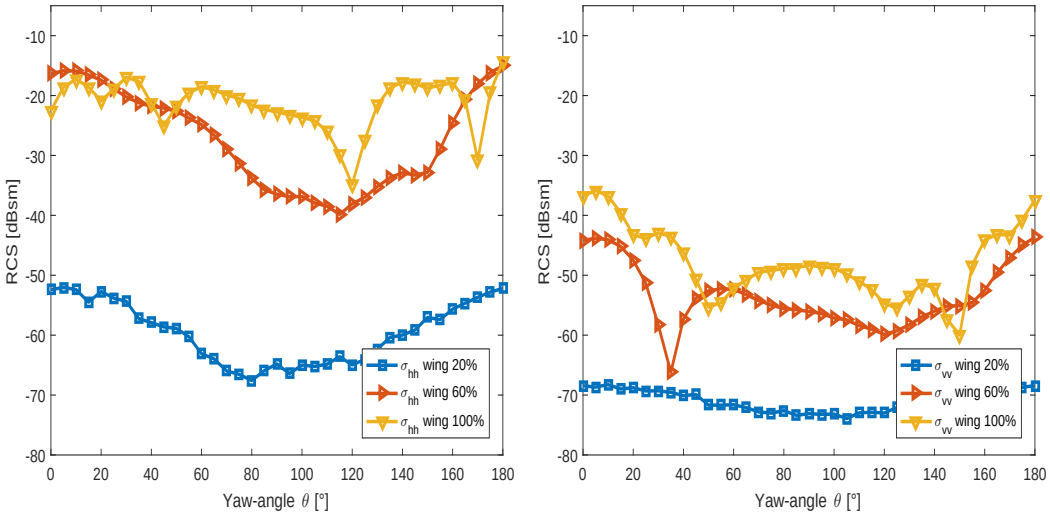

(a) σ_{hh} @ 1.3 GHz (b) σ_{vv} @ 1.3 GHz

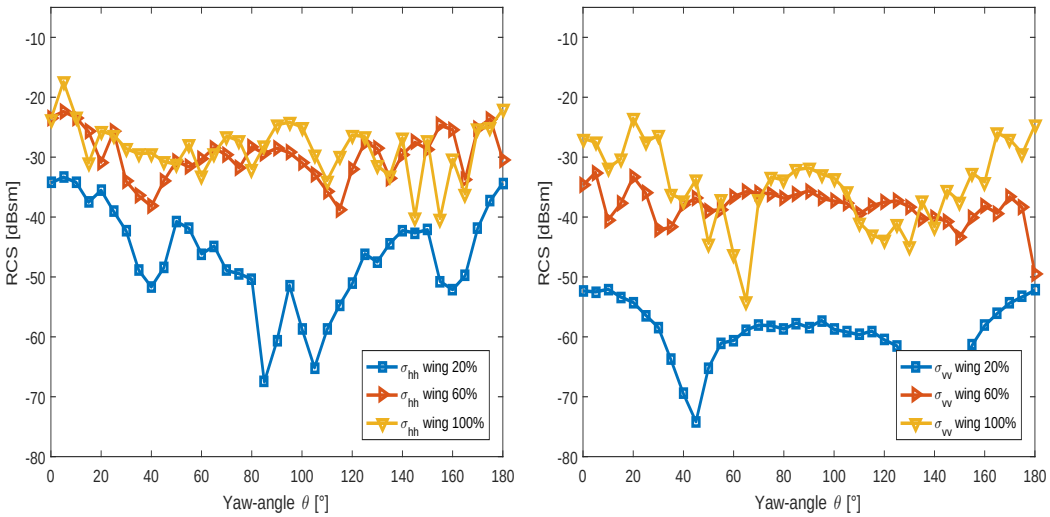

(c) σ_{hh} @ 3.25 GHz (d) σ_{vv} @ 3.25 GHz

Figure 4.11: RCS of gannet wings of different sizes. All results from predictions with the FDTD code.

Figure 4.11 shows the results of the predictions for σ_{hh} and σ_{vv} of bird wings of varying size in L- and S-band. The general finding is that RCS increases with increasing size. In particular reflections from the smallest wing model are low for both polarizations and frequencies. Differences between models at 60% and 100% of full size are far less. σ_{vv} is significantly lower than σ_{hh} in L-band. The same

tendency is found for S-band, however, the difference is much less at this frequency. This difference is an essential part of the motivation for investigating polarimetric parameters further, as the usefulness may increase with decreasing frequency.

4.3.3 Parameters for classification

The reason for investigating RCS and polarimetric variables of birds and bird wings has been to evaluate the suitability for classification. In this section theoretical evaluations of the performance of different classification approaches at L- and S-band are presented.

4.3.3.1 Differential polarization σ_{dr}

An essential requirement from the theory leading up to suggesting σ_{dr} from bird wings as a robust classification feature is that they act as Rayleigh scatterers. As introduced in Chapter 3.5.3, bird bodies will not fall in the Rayleigh region, however, bird wings may do, at least when they are seen from the front and rear. The challenge is that targets in this region are associated with low RCS. If this is too low, the reflections from wings will not be detected in the radar receiver. This is the basis for the claim that the upper Rayleigh region is ideal for extraction of σ_{dr} signatures of bird wings and similar structures.

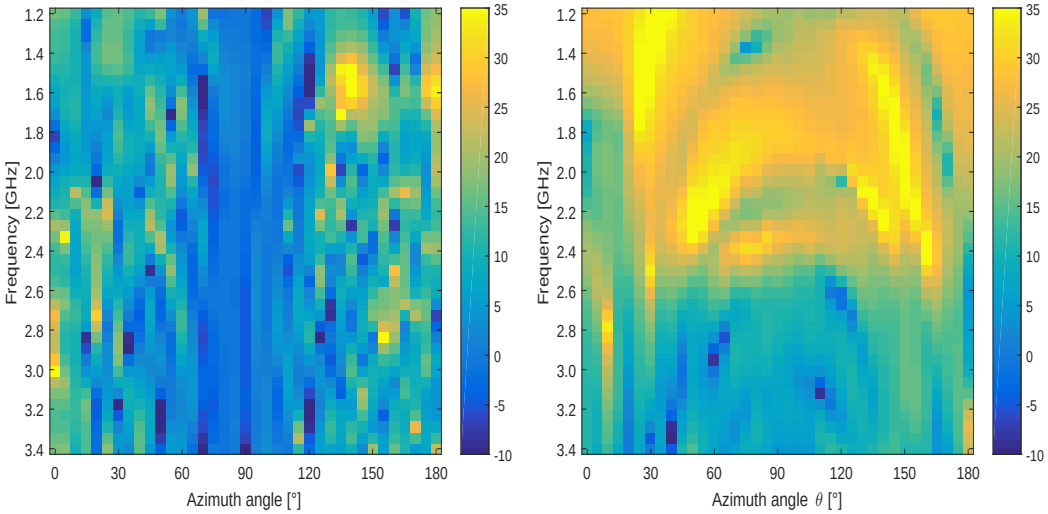

(a) σ_{dr} of entire gannet with level wings

(b) σ_{dr} of level gannet wing alone

Figure 4.12: σ_{dr} predictions made with the FDTD code of gannet and gannet wing. Model 60% of full size

Figure 4.12 shows σ_{dr} for an entire bird with wings level in the left panel and a wing alone in the right. In Figure 4.12(a) a majority of positive values are found. Especially from frontal and posterior views. This is believed to be caused by the horizontal position of the wings. In Figure 4.12(b) less fluctuations are seen. The values are generally higher, in particular at lower frequencies. This is caused by low σ_{vv} at these frequencies, and means that the values must be considered somewhat less accurate due to prediction accuracy. At higher frequencies relatively little fluctuation of values around 5 - 15 dB is found across aspect angles.

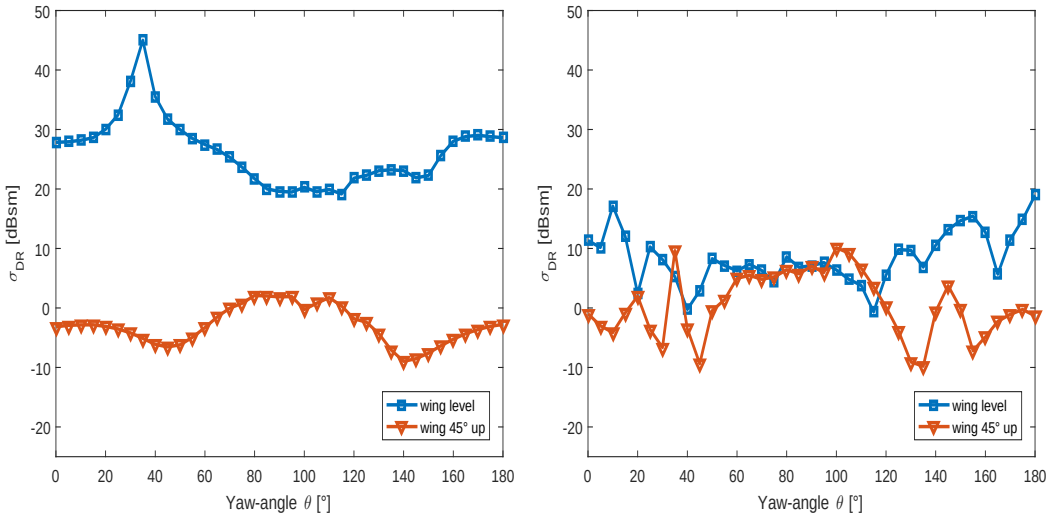

(a) σ_{dr} @ 1.3 GHz (b) σ_{dr} @ 3.25 GHz

Figure 4.13: RCS and σ_{dr} predictions made with the FDTD code of gannet wing across L- and S-band. Model 60% of full size

Figure 4.13(a) and Figure 4.13(b) shows results from prediction of σ_{dr} for the same wing oriented horizontally shown in blue, and 45° up marked by red lines. Values for L- and S-band are shown in the two figures respectively. For the wing in the 45° up position σ_{dr} is low at both frequencies. For the horizontally oriented wing, there are large differences in σ_{dr} between the two frequencies. At 1.3 GHz σ_{dr} is roughly 15 dB higher than at 3.25 GHz. At this frequency large differences between wing positions are only found at front and rear aspects. These findings are consistent with the wings acting as Rayleigh scatterers. The dipole moment induced scattering effect is most prominent at frontal and rear aspect angles and at lower frequencies. This is fully in line with the assumptions made in Chapter 3.5.3.

4.3.3.2 Differential phase δ_{vh}

The idea behind using δ_{vh} is as discussed in Chapter 3.5.5 is best understood in the resonant and optics scattering region. According to high frequency theory, double bounce reflections from, for example, dihedrals are characterized with $\delta_{vh} = 180^\circ$ [127]. Such scattering is associated with the optics scattering region, and there is not expected to be major contributions from such in the case of birds in the relevant frequency bands. However, one exception could potentially be from a dihedral like corner formed at the wing root during certain phases of the wing beat sequence.

The hypothesis for using δ_{vh} in echoes from birds was introduced in Chapter 3.5.5 and is connected to the total phase being formed by the interaction between creeping waves traveling along different propagation paths and scaled by the relative contribution of any specular reflection. Predictions of δ_{vh} were made for different versions of the gannet model. Figure 4.14 shows δ_{vh} for both the gannet body without wings of different sizes and the gannet model scaled to 60% size with wings in three positions. The histograms show data from 40 frequencies ranging from 1.3 GHz to 3.25 GHz. Common to all figures is a predominance of slightly negative δ_{vh} values and a tendency towards lower δ_{vh} for lower size to wavelength ratios is observed.

Figures 4.14(a) and 4.14(b) cover the bird body of different sizes without wings for illumination angles in the interval $\theta \in [70^\circ, 110^\circ]$ and $\theta \in [0^\circ, 180^\circ]$ respectively. These figures are interesting to compare to the prolate spheroids covered in Figure 4.3(b). The values for the two largest models match the values of the prolate spheroids well. The two peaks in frequency for the smallest bird bodies shown by blue lines in subfigures 4.14(a) and 4.14(b), may be due to creeping waves traveling two times around the body.

Subfigures 4.14(c) and 4.14(d) show δ_{vh} for the gannet model scaled to 60% of full size with wings in three positions in two different illumination angle intervals. The variance in δ_{vh} values is the least at illumination $\pm 40^\circ$ around broadside seen in Figure 4.14(c), but even for the full azimuth interval in the lower right panel the a well defined peak around $\delta_{vh} = -40^\circ$ is observed. The wing orientation is not

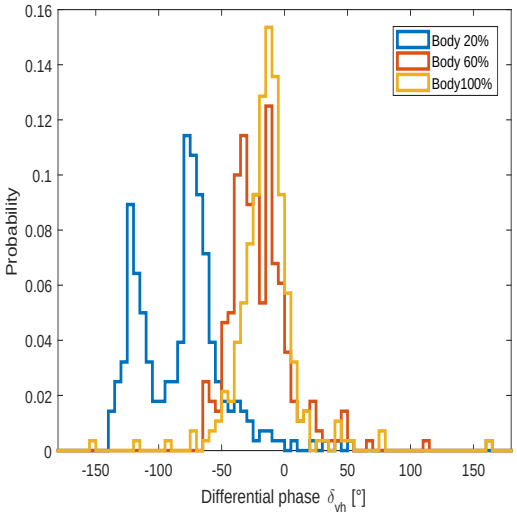

(a) Body without wings $70 \leq \theta \leq 110$

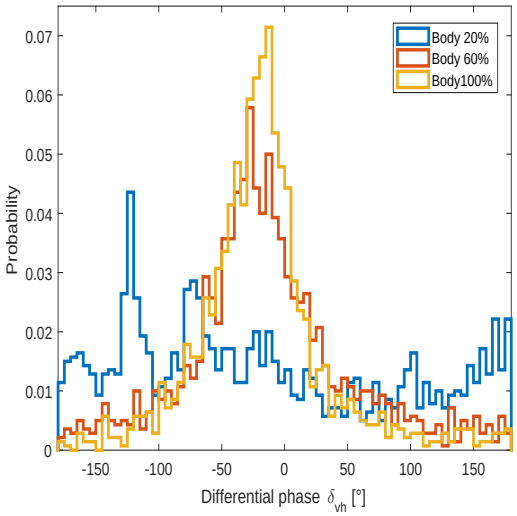

(b) Body without wings $0 \leq \theta \leq 180$

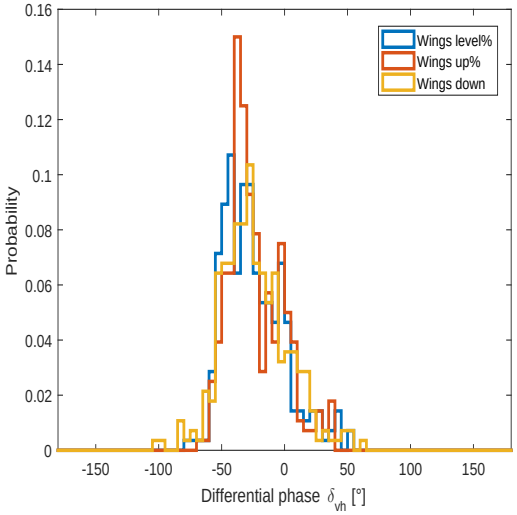

(c) Body with wings $70 \leq \theta \leq 110$

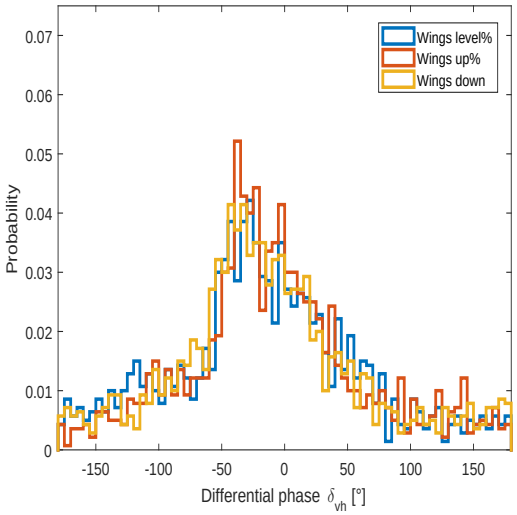

(d) Body with wings $0 \leq \theta \leq 180$

Figure 4.14: Differential phase δ_{vh} of gannet with wings and body alone of different sizes for frequencies $f_c \in [1.2, 3.4]$GHz. All results from predictions with the FDTD code

found to influence the predictions significantly.

The overall findings in the investigation of δ_{vh} on bird models is that its potential for use in classification is the best in a sector around broadside illumination. Here the theory of δ_{vh} of a prolate spheroid is applicable. From the front and rear more random values are found. At these illumination angles the influence from wings make the prolate spheroid more inaccurate as a bird model.

4.3.3.3 Amplitude modulations

Amplitude modulation (AM) on the backscattered E-field correlated with wing beats is covered in Chapter 2.1. Although Schaefer [33] claimed that bird wings do not contribute significantly to the overall bird RCS, simulations shown in this thesis show different results. At least this applies to birds in L-and S-band, for the wing oriented parallel to the applied E-field and at front and rear aspects.

Figure 4.15 shows the results of predictions of a gannet model with dielectric properties the same as those of human muscle with wings in different positions. These are referred to as upper, level and lower wing positions. The overall impression from this figure is that variations in RCS from wings being in the upper or lower position compared to in level position is small around broadside illumination. For illumination from the front and rear the variation is much larger. This indicates that reflections from wings may modulate the backscattered power the most from these two latter aspects. At broadside, the modulating effect of reflections from wings will be small. Here the reflection from the bird body totally dominates the reflections from wings. However, before prematurely concluding that wings are responsible for all modulation of the RCS, another possibility must be considered.

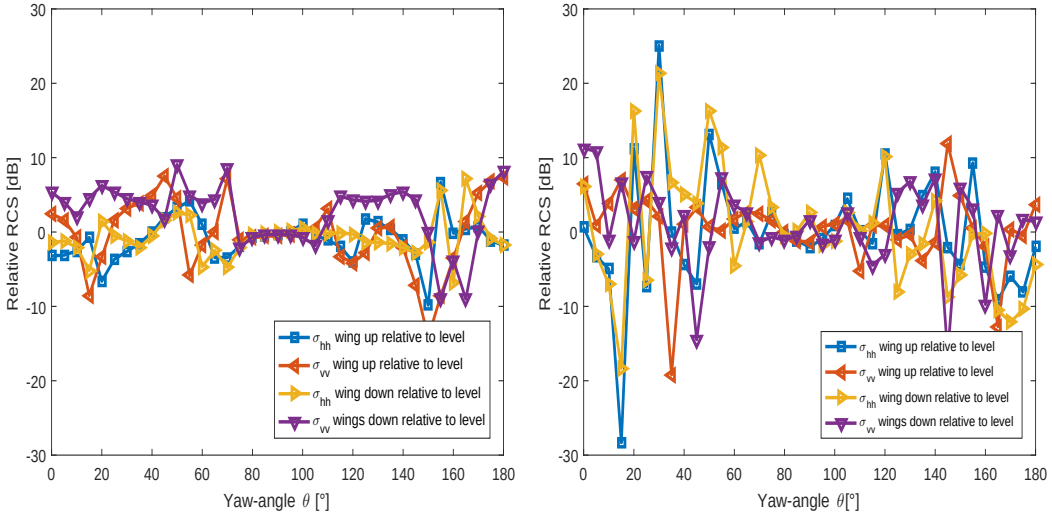

(a) Relative RCS levels in L-band (b) Relative RCS levels in S-band

Figure 4.15: Comparison of σ_{hh} and σ_{vv} for bird with wings 45° up and 45° down relative to model with horizontally oriented wings. Predictions from FDTD code

Since the RCS in the resonance region is defined by contributions from both

specular and surface wave effects, the possibility of changes in propagation paths of creeping waves has to be considered. Schaefer did not claim to understand the phenomena, but wondered if body shape changes was the major cause of the modulation. According to him the flexing and bending of the rib cage, and the probable enlarging of the abdominal volume during the flapping sequence might cause the RCS variations. The main idea is that the circumference would change and cause potential creeping waves to phase in and out at fixed frequencies.

If the bird for simplicity is first modeled as a prolate spheroid, and we let the potential enlargement of the bird body take place by keeping the semi-axis ratios m constant, the predictions for a prolate spheroid with axis $c = 18$ cm and $a = b = 5.14$ cm can be scaled by frequency. Figure 4.16 present σ_{hh} as function of wavelength to size ratio λ/b. Here the small effect of dispersivity in muscle tissue and the possibility of m not being constant in practical conditions is disregarded. Changes in size will affect the propagation path of creeping waves induced by both vertical and horizontal incident E-field. Figure 4.16 shows how σ_{hh} varies with λ/b for a selection of azimuth angles for a prolate sphere and the gannet bird body scaled to 60% of full size in the left and right panels respectively. Generally broadside illumination dominated by a large specular reflection results in large σ_{hh} compared to the two other illumination angles. One exception is as the 3D model is approaching the optics region for low values of λ/b in Figure 4.16(b). In both figures the sensitivity to variations in λ/b is found to be highest for lower values of λ/b and for illumination from the front marked by blue lines. From this aspect and for low values of λ/b, a change in a or b of roughly 2% or 1 mm can in extreme cases change σ_{hh} more than 10 dB. This illustrates the sensitivity to movements of the target body in the resonance region. From Figure 4.16 this sensitivity is seen to decrease with increasing wavelength or equivalently by decreasing bird size.

All in all there is indication of RCS modulations caused by both movements of the body caused by the flapping movement and the orientation of wings relative to the polarization of the incident wave. In a sector $\pm 60^\circ$ around frontal and rear aspects, reflection from wings alone can cause significant RCS modulations in both

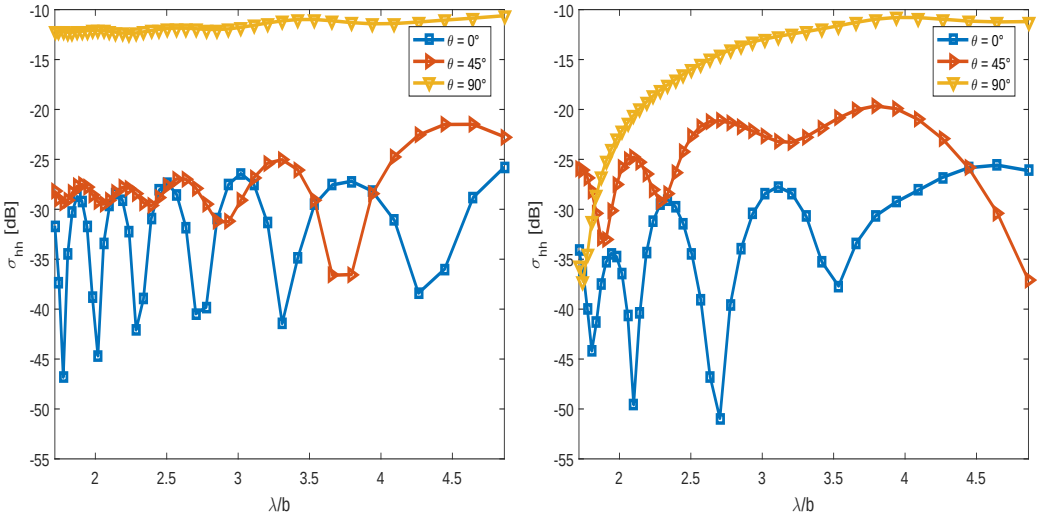

(a) Prolate spheroid. c=18 cm, a=b= 5.14 cm (b) Bird model 60% of full gannet size

Figure 4.16: Differential RCS σ_{dr} as function of wavelength to size ratio at selected illumination angles θ

frequency bands. In roughly the same sectors, body movements such as enlargement of the body cross section can lead to strong modulations as well. Broadside, there is no indication that significant modulation should occur.

4.4 Man-made aerial targets

The challenge of generally modeling bird sized man-made aerial targets is discussed in section 3.4.4. This section shows the results of EM-modeling of general scatterers such as conducting dihedrals and trihedrals as is believed to be more prominent for man-made targets compared to birds. However, the most important part of this section is the discussion of scattered fields from rotors and propellers. Key topics in this context material, size and polarization dependencies.

4.4.1 Dihedral, trihedral and wire scatterers

The dihedral and trihedral shown in Figure 4.17 were modeled with conductive material identical to aluminum. This was mainly done to illustrate how the size of corner reflectors affect the backscattered polarimetric phase. The reflectors covered here were made of flat plates measuring 10x10 cm each and are therefore considered to be in the resonant scattering region at typical long range air defence frequencies.

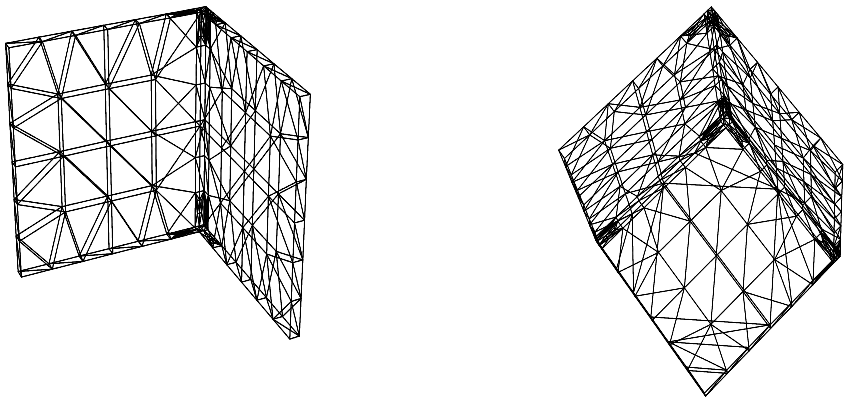

(a) Dihedral (b) Trihedral

Figure 4.17: Dihedral and trihedral. Each side 10 cm.

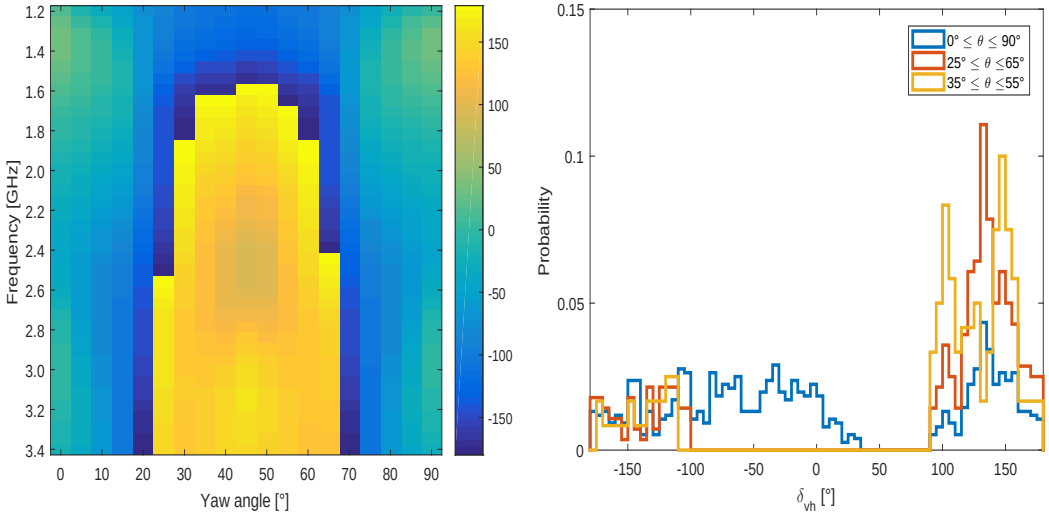

(a) δ_{vh} of aluminum dihedral (b) Histogram of δ_{vh}

Figure 4.18: Differential phase of dihedral corner reflector of 10x10 cm plates made in aluminum

Figure 4.18 presents the differential phase δ_{vh} and shows that the predicted values differ from $\delta_{vh} = -180°$ expected from classic high frequency theory. Similar results are found for the aluminum trihedral in Figure 4.19, where predicted values differ from the expected $\delta_{vh} = 0°$. These results indicate that the reflectors' size relative to the wavelength is important and that care must be taken when polarimetric responses from small targets are evaluated in the frequency bands investigated in

this thesis.

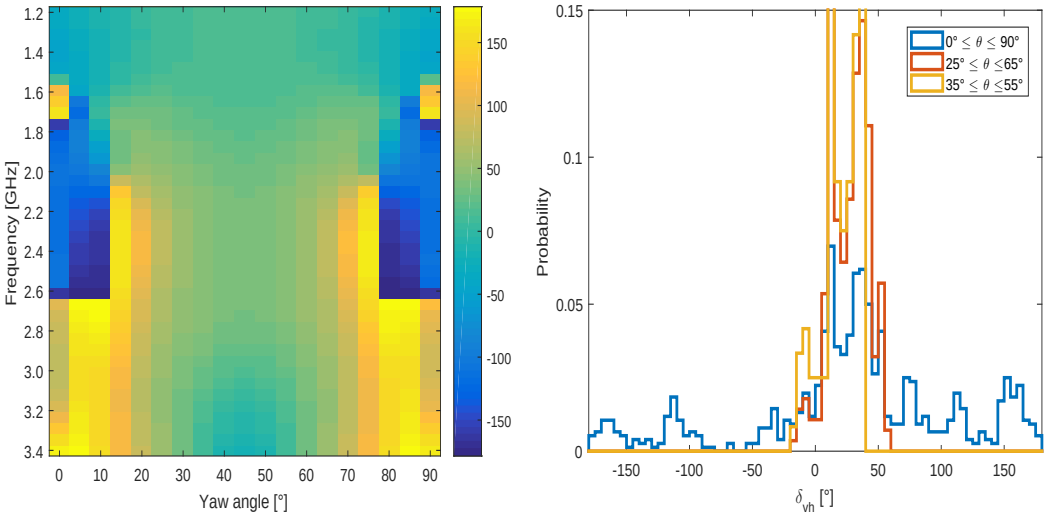

(a) δ_{vh} of aluminum trihedral (b) Histogram of δ_{vh}

Figure 4.19: Differential phase of trihedral corner reflector of 10x10 cm plates made in aluminum

As the fuselages of many small UAVs are rather transparent to radar pulses at the frequencies evaluated here, internal wires may be significant contributors to the total RCS. Many fixed wing models have wires inside the wings, that generally may contribute to σ_{hh}. The polarimetric scattering matrix for such a scatterer is given in Equation 3.13. The main difference separating the wings of an aircraft from that of a bird is the lack of potential micro-motion associated with them.

4.4.2 RCS prediction of rotors and propellers

In the same way that signatures of wings are considered key characteristics of flying birds, reflections from rotors and propellers of flying UAVs produce signatures unique to man-made objects. The question then is how the detectability of such rotors and propellers varies with size and material.

4.4.2.1 Micro-UAV rotor

The rotor of a DJI Phantom II [130], a quad copter type micro-UAV presented in Chapter 7, was modeled and its monostatic RCS was predicted. This is a 22.8 cm long rotor blade that comes in both carbon fiber and plastic variants. The longest

axis of the propeller coincides with the x-axis in the simulation and predictions were done with an aluminum and a plastic model with $\varepsilon_r = 2.2$.

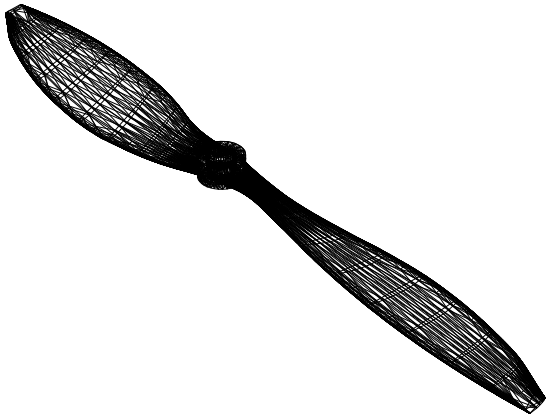

Figure 4.20: 3D model of DJI phantom II propeller. Maximum length 22.8 cm, width 2.4 cm and height 1.0 cm.

The results are found in Figure 4.21 and show RCS values sensitive to both polarization and material. Whereas plastic rotors tend to be virtually invisible to radar, carbon fiber blades of the same size and shape have significantly larger RCS [131]. Under the assumption that carbon fiber blades can be modeled as aluminum, this is confirmed in panel 4.21(a) and panel 4.21(c). Values as much as 30 dB lower are found for the plastic propeller. The differential RCS σ_{dr} in panels 4.21(b) and 4.21(d) indicate that σ_{vv} values are very low for both materials. The values of σ_{vv} in the plastic case are so low that the panel 4.21(d) must be interpreted with care due to the problem of finite numerical precision in the FDTD code.

4.4.2.2 Small helicopter UAV main rotor

RCS predictions with the FDTD code were made for a UAV helicopter main rotor blade model shown in Figure 4.22. This model is similar to the rotor blades found at the Kestrel 2000 UAV, presented in Chapter **??**. Predictions were done for the blade in full size ($79.0 \times 6.0 \times 0.7$ cm), and a version scaled to 20% of full size. For comparison predictions were also made for a rectangular box with sim-

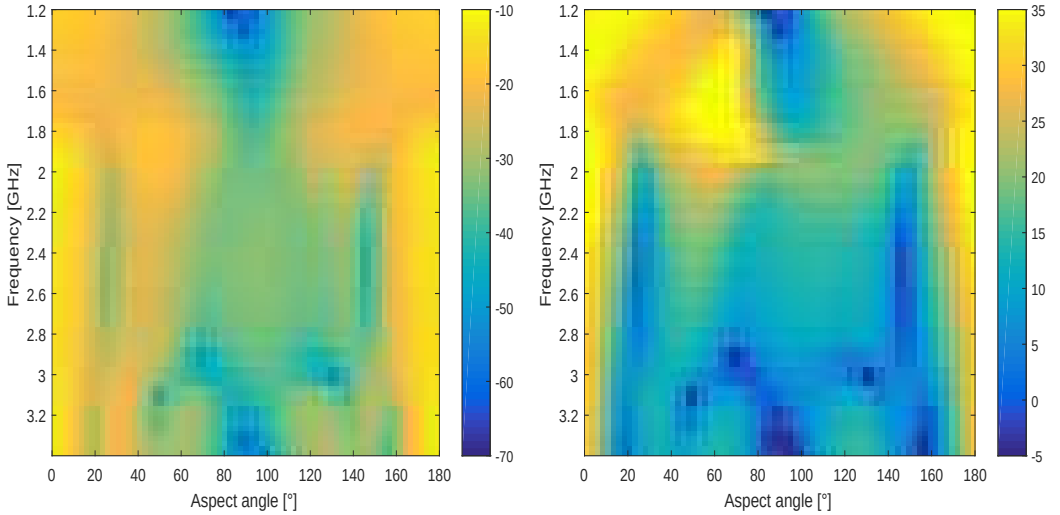

(a) σ_{hh} aluminum rotor (b) σ_{dr} aluminum rotor

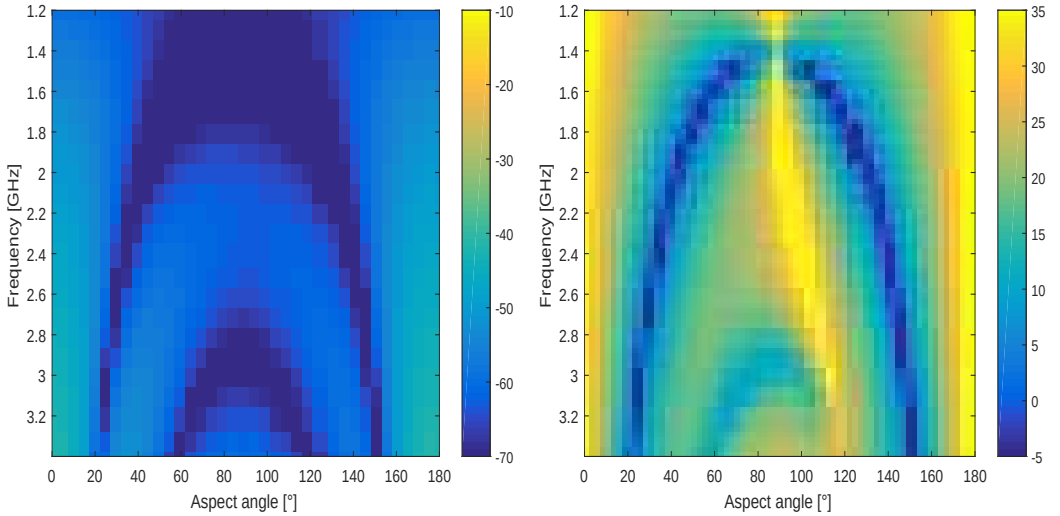

(c) σ_{hh} plastic rotor (d) σ_{dr} plastic rotor

Figure 4.21: Prediction of RCS [dBsm] of DJI phantom II 22.8 cm rotor blade. FDTD prediction code.

ilar dimensions as the full sized blade. The blade was oriented along the y-axis, such that a yaw-angle of 0° and 180° corresponds to front and rear view respectively. Predictions were made for aluminum material mimicking the carbon fiber blades. The results are presented in Figure 4.23. As expected increased RCS levels or flashes are observed at these illumination angles in both frequency bands in panels 4.23(a) and 4.23(b) and for both horizontal and vertical polarizations in panels 4.23(c) and 4.23(d) respectively. However, for the scaled down version flashes are not prominent at HH-polarization, and at VV-polarization the backscattered power

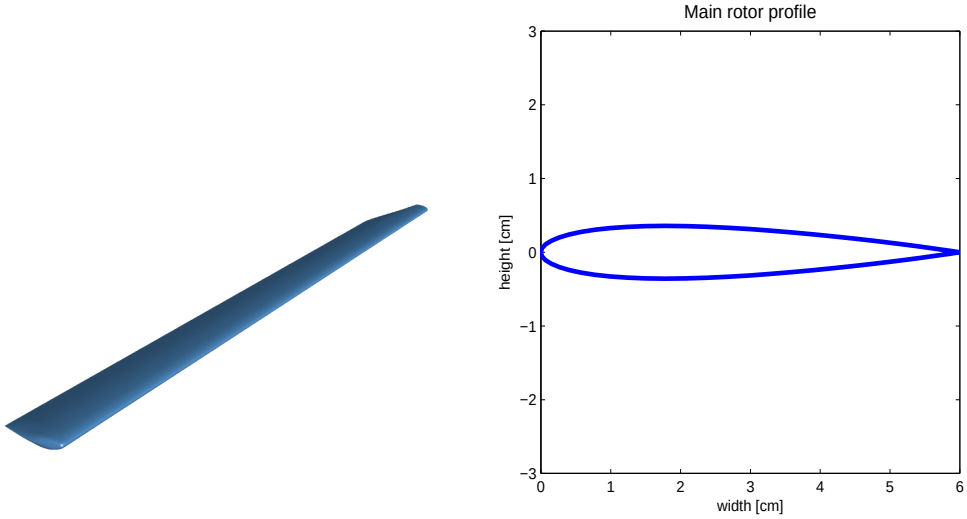

(a) Main rotor blade $79.0 \times 6.0 \times 0.7$ cm (b) Cross section of main rotor blade

Figure 4.22: Kestrel 2000 main rotor blade

is significantly lower than -70 dB and virtually not detectable. The rectangular box was included in the prediction to give an indication of how important the blade's curved geometry is at different frequencies. The hypothesis was that the shape of such small objects has little significance at the lowest frequencies and that the technique of distinguishing approaching and receding blades by RCS is useless under this conditions. The box model is seen to be a rather good approximation for both frequencies, however, the best match is found in L-band. This coincides well with σ_{hh} values seen from the front and the rear. The cursors show that in L-band the σ_{hh} is the same from both directions. In S-band the σ_{hh} from the front is roughly 2 dB higher than from the back. σ_{hh} in the flash of the scaled down version is significantly lower. The relatively high values around yaw-angles of 65° and 115° were not expected. σ_{vv} is generally much lower than σ_{hh} in all predictions.

4.4.3 Classification of UAVs as UAVs

Although only small UAVs are covered in this thesis, the variety of targets in the class is huge. Suggesting general classification techniques utilizing scattering from the aircraft body is difficult, as it is hard to find common characteristics. The use of different shapes and materials virtually transparent to radar is a huge challenge. As long as the task is as general as to classify a UAV as a man-made object, utiliza-

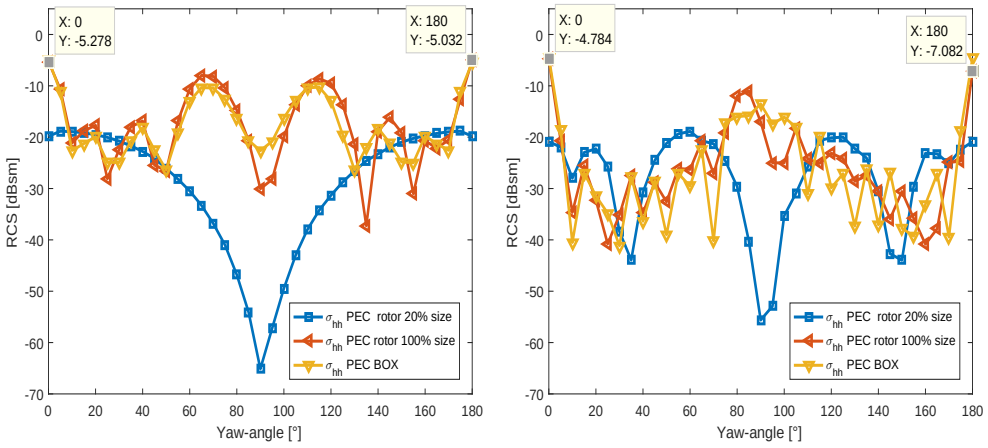

(a) σ_{hh} @1.3 GHz. Cursor is included for the full size rotor indicating RCS level from the front and rear

(b) σ_{hh} @ 3.25 GHz. Cursor is included for the full size rotor indicating RCS level from the front and rear

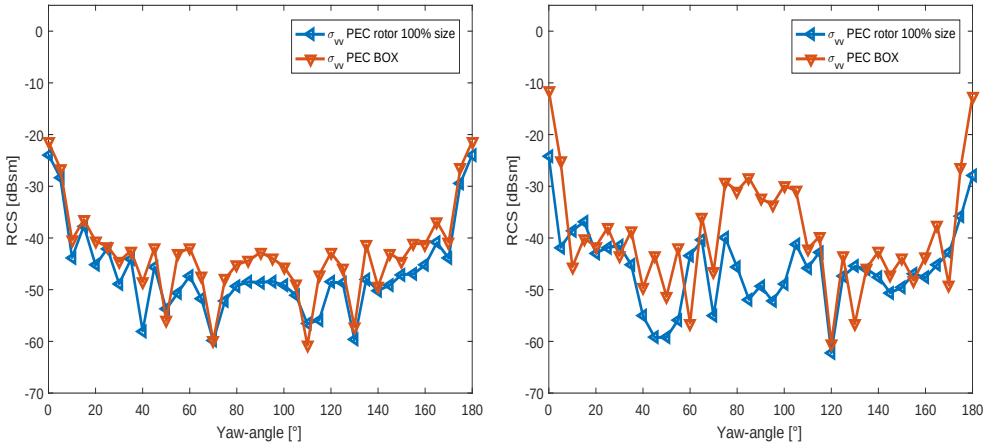

(c) σ_{vv} @1.3 GHz

(d) σ_{vv} @3.25 GHz

Figure 4.23: RCS of full size Kestrel 2000 main rotor blade, down scaled version to 20% of full size and full sized box model in L- and S-band at different polarizations

tion of characteristic signatures of propellers and rotors are suggested. Techniques connected to μ-Doppler signatures and RCS modulations are useful in this context. The EM modeling of rotors covered in previous section has revealed the low RCS of rotors and propellers made of plastic materials. This is challenging for extraction of robust signatures. In these situations the absence of bird characteristic features may be one possible approach.

4.5 Precision of electromagnetic predictions

This chapter has given an impression on how different target and target parts contribute to the total backscattered electric fields in terms of magnitude and phase. Uncertainties are connected to both the electromagnetic solver and the 3D models representing actual targets. Dealing with largely dielectric targets in the resonance region the FDTD method is considered a safe choice as it is a full wave method and easy to implement. Less time consumption and use of memory is achieved with alternative methods. The method has, as any numerical method, a finite precision depending on implementation. In the presented simulations low RCS values, roughly less than -60 dBsm, are associated with uncertainty due to lack of precision and should be considered with care.

The modeling of birds is simplified by representing all bird species by a model of a gannet with its wings in three different positions. Such an approach does not take variations in the bird's shape, orientation of head, tail and legs into account. On the other hand making models for more species and poses is tedious work, and most likely unnecessary due to the low requirement for target details in Rayleigh and resonant scattering regions. The choice of using a gannet model was due to measurements of this species in the initial part of the PhD work. However, the gannet is believed to be an excellent representative for most flying birds.

All models used are of homogeneous materials. For good conductors this is not a problem, since penetration into the target is impossible. However, for dielectrics, layers of materials with different impedance may contribute to the backscattered fields. In the case of birds, the attenuation is in Chapter 3.4.3 shown to attenuate internal reflections significantly and could generally be disregarded. The choice of using a dielectric constant equal to that of human muscle is in this context considered an insignificant source of error. Modeling of bird wings to only include the muscular parts is another uncertainty, however, it is considered significantly more accurate than including parts with mainly bones and feathers.

Despite all the uncertainty discussed here, the models presented are considered to be sufficiently accurate for the purpose of illustrating the general scattering

mechanisms for evaluation of classification methods and the best possible model taking the complexity and large processing load into account.

4.6 Summary

Electromagnetic modeling of target and target parts in the Rayleigh and resonance region has revealed both possibilities and challenges for classification. This chapter has investigated RCS at different polarizations of such targets and in particular focused on the detectability of bird wings, UAV rotors and propellers.

The prolate spheroid bird model covered in Chapter 3.4.1 is found to have some limitations for prediction of back-scattered fields. For a sector around broadside illumination the model is generally valid. However, for anterior and posterior illumination, the lack of wings makes the model inaccurate. 3D bird models are considered to be significantly better models for simulation of the scattered fields as the size to wavelength ratio increase.

The hypothesis that bird wings act as Rayleigh scatterers is strengthened throughout this chapter. This is reflected both in polarization dependencies and frequency dependent RCS. The smallest wings with a length of 9 cm is found to represent a small RCS in both L- and S-band. In particular broadside illumination results in insignificant RCS at all polarizations. Simulations show that the bird wing size should be at least two wavelengths long in order to ensure practical detectability at all aspect angles. As the wings enter the upper Rayleigh region a considerable contribution to the total RCS from these is found at illumination from the front and rear.

At these aspect angles, and due to the dipole moment induced scattering of elongated objects in the Rayleigh region, the differential RCS is based on simulations confirmed to hold information on the wing's apparent orientation around the radar's line of sight. The RCS of bird wings and UAV rotors and propellers are found to increase significantly when aligned with the polarization of the incident field. The use of σ_{dr} for classification relies on separating bird wings, propellers and rotors from the body/fuselage in velocity by spectral analysis. This is required

as more random values of σ_{dr} of larger scatterers are expected.

Predictions of the co-polar differential phase δ_{vh} of bird models shows a predominance of slightly negative values $-50^\circ \leq \delta_{vh} \leq 0^\circ$ dependent on its size to wavelength ratio. A general UAV model is unachievable, however, more random δ_{vh} values may be expected from man-made targets, potentially with a predominance of values around 0°and -180° due to single and double bounce scattering from curved surfaces, flat plates, trihedral or dihedral scatterers. However, simulations have shown that, as such scatterers get small compared to the wavelength, values of δ_{vh} associated with them may differ from values expected from high frequency theory.

The origin of potential amplitude modulations of bird echoes are investigated. In the case of birds illuminated from the front and back, both varying alignment of wings with the incident E-field and variations in body size and shape are found to have the potential of modulating the RCS significantly. At broadside illumination, the possibility for modulation is significantly less. As long the modulations are periodic and correlated with the wing beat frequency, this should be a strong feature for classification.

In the case of UAVs, both amplitude and phase modulations associated with reflections from propellers and rotors are expected to be useful features for classification. However, the RCS associated with such scatterers is found to be highly dependent on material and alignment with the incident polarization. As long as the object is conductive and reasonably well aligned with the E-field, characteristic flashes are expected as they rotate relative to the radar. As the rotor/propeller-length gets small compared to the wavelength, the flashes get less defined as the maximum power reflected decreases and the duration of the flash increases.

Regarding parameters for classification of birds, this chapter has shown that periodic amplitude modulation and differential RCS has the best potential for illumination in sectors around the front and rear. The differential phase δ_{vh} is complementary in that it is best predicted in a sector around broadside illumination. Although the simulation has revealed the potential for classification, uncertainty re-

garding the robustness still exists. In particular this applies to the detectability of bird wings and randomness of the differential phase. The practical limitations are best evaluated by relevant radar measurements.

Chapter 5

Initial measurements

This chapter presents measurements providing initial results and important understanding relevant to further development of hypotheses, algorithms and hardware. These studies formed a valuable basis for the preceding work, illustrate quite well the advantages of performing classification in higher frequency bands and are included for completeness. The covered work confirmed contributions to the total RCS of birds from wings and gave knowledge on how this varies with aspect angle. Moreover, the first studies of target part material properties and alignment with incident polarization were encouraging for the development of a dedicated measurement system.

5.1 Measurements

Prior to completion of the BirdRAD system, and as part of the the preparation for later measurements, a collection of measurements were done at various frequencies. These include data collection with a short range K-band CW radar, a network analyzer and the SAR sensor PicoSAR.

5.1.1 K-band

The very first radar experiments performed as part of the work described in this thesis were done with the low cost radar transceiver K-HC1 from RFbeam Microwave GmbH. Figure 5.1 shows the integration of the transceiver in a small suitcase. The carrier frequency of the unit is tunable between 23.5 and 24.5 GHz. The system is single polarized and the polarization is easily changed by changing the orientation

Figure 5.1: K-HC1 hardware

of the antenna. During the initial measurements only HH-polarized data were collected. The equivalent isotropically radiated power (EIRP) of the system is 20 dBm and detection ranges are consequently short. On the other hand the system is compact, light weight, affordable and consequently ideal for quick initial measurements.

The K-HC1 was used to record data of several targets, among them a mallard duck and the Kestrel 2000 UAV. The Kestrel is a helicopter type UAV, see Figure 5.2(b), with two carbon fiber main rotor blades of dimensions $79.0 \times 6.0 \times 0.7$ cm as was shown in Figure 4.22. The main objective of these measurements was to investigate μ-Doppler signatures of birds and man-made targets in spectrograms offering high time- and velocity-resolution. This gave valuable experience in analyzing such signatures as well as insight into what information may be extracted at higher frequencies. The duck data also forms the basis for the conference paper [38]. Keeping wild bird species in captivity is not allowed in Norway, and all data collections of birds presented in this thesis are collected of wild birds flying in their natural environment. This requires patience, and gathering data of ducks with a low power radar at ranges shorter than 50 meters is no exception.

5.1.2 Network analyzer at 1 GHz and 4 GHz

A different experiment was conducted at lower frequencies involving two rotary wing UAVs. These were the Kestrel 2000 UAV and the DJI Phantom II with rotor blades made of plastic and carbon fiber. Both targets are shown in Figure 5.2. This time a N5245A network analyzer from Agilent Technologies and a wideband dual polarized reflector antenna from Q-PAR Angus Ltd. were used. This gave the possibility to continuously measure the polarization scattering matrix **S** directly from the S-parameters available. Measurements were done at 1.0 GHz and 4.0 GHz, relatively close to L- and S-band respectively. The purpose of these measurements was to investigate how RCS of different rotor blades depend on carrier frequency, polarization and materials.

(a) DJI Phantom II with carbon fiber rotor blades on

(b) Kestrel 2000 rotary wing UAV

Figure 5.2: The two targets measured with network analyzer.

5.1.3 X-band

In November 2013, measurements of flying gannets were performed at the *Centro de experimentacin de El Arenosillo* (CEDEA) near Huelva in Spain. This data collection is described in the two conference papers [39] and [40], and was done as a private extension to the NATO RTO SET-180 measurement campaign UNDINE. The gannet is a large white sea bird recognized by its black wing tips and characteristic high velocity dives into the sea where they catch fish down to depths of 30 m. Radar data was collected in X-band with the SAR system PicoSAR made by Selex Galileo in Edinburgh. The polarization of this system is vertical, the center

frequency is 9.2 GHz and the instantaneous bandwidth is variable between 75 and 1500 MHz. The system makes use of the *deramp on receive* technique to limit the sampling frequency while still gathering high range resolution data within a limited collection window. In order to point the antenna and center this collection window at the target, an external tracking system was needed. This was provided by an optical tracker and a Ku-band tracking radar available at the test center.

Figure 5.3(a) shows one of the measured gannets through the optical tracking system provided, whereas Figure 5.3(b) shows a typical gannet track around five minutes long. Note the placement of PicoSAR marked RDR in the top right corner of the figure.

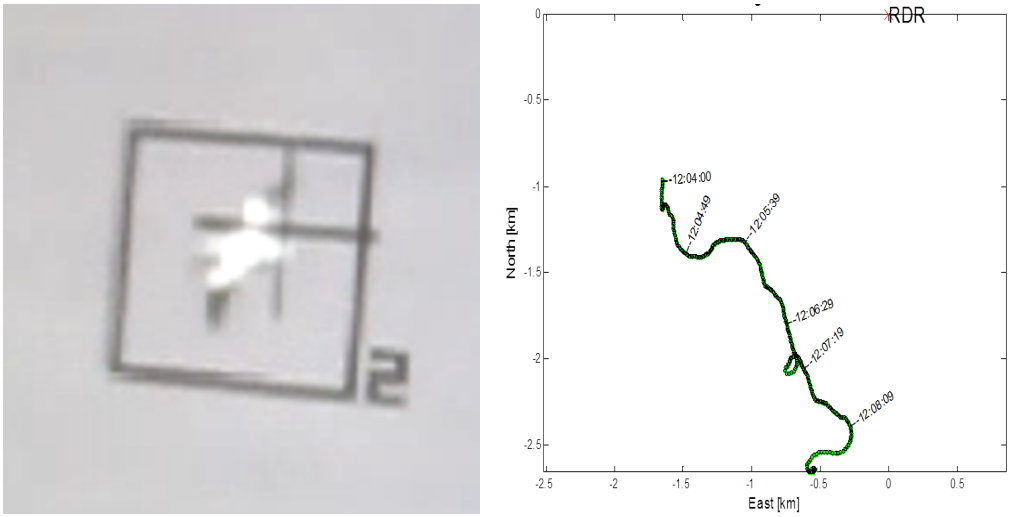

(a) Gannet seen in the optical tracking system

(b) Track of a flying gannet

Figure 5.3: The gannets were tracked by a Ku-band system and video well synchronized with the radar data was recorded.

Approximately five minutes of high quality data was collected this day. Generally high SNR was observed out to ranges of at least three kilometers. The correlated data and video made it possible to observe the effect of rotational wing movements in μ-Doppler signatures and identify intervals where the birds were soaring and flapping. However, a frame rate of 25 Hz is slightly low when sampling wing beat frequencies of around 4 Hz. During the campaign the bandwidth was set to 75 MHz and the PRF used was 3 kHz. The birds were probably looking for food during the collection, sometimes flying relatively straight legs and other times ma-

neuvering quite extensively. The track presented in Figure 5.3(b) is for example terminated by the gannet performing a characteristic dive into the sea from a height of around 30 meters.

5.2 Signal processing

Signal processing applied to data in this chapter is mainly connected to applying the translational movement compensation, spectral estimation and cepstral analysis. The processing relevant to these topics is similar to that applied to BirdRAD data covered in Chapter 8.3, Chapter 8.4 and Chapter 8.5.3 respectively.

5.3 Results

This section covers the results of the initial measurements presented so far. The focus is on evaluation of the contribution from rotating target parts, including Doppler shifts and RCS modulations from bird wings and UAV rotors. Results from the limited studies of polarization dependencies in relevant frequency bands are also included.

5.3.1 K-band measurements

Figure 5.4 shows the two very first datasets collected as part of the PhD-work. Figure 5.4(a) shows the spectrogram of a flying mallard duck with a CPI of 23 ms. At this carrier frequency the wing movement is well resolved in both time and velocity. In Figure 5.4(b) a similar spectrogram formed with a CPI of 4 ms shows the μ-Doppler signature of a Kestrel 2000 rotary wing UAV. The main rotor flashes, with rear rotor blade flashes in between are clearly visible.

To simplify the comparison of the two signatures, the translational velocity of both targets were compensated for as described in Chapter 8.3. Separating between the two signatures visually is easy. Note the significantly different scales on both time and velocity axes. However, the research questions to be answered in this thesis is what happens when the carrier frequency and available dwell time is reduced to that of an operational air defence radar system. These two measurements represents the starting point of this research, formed a basis for developing the signal

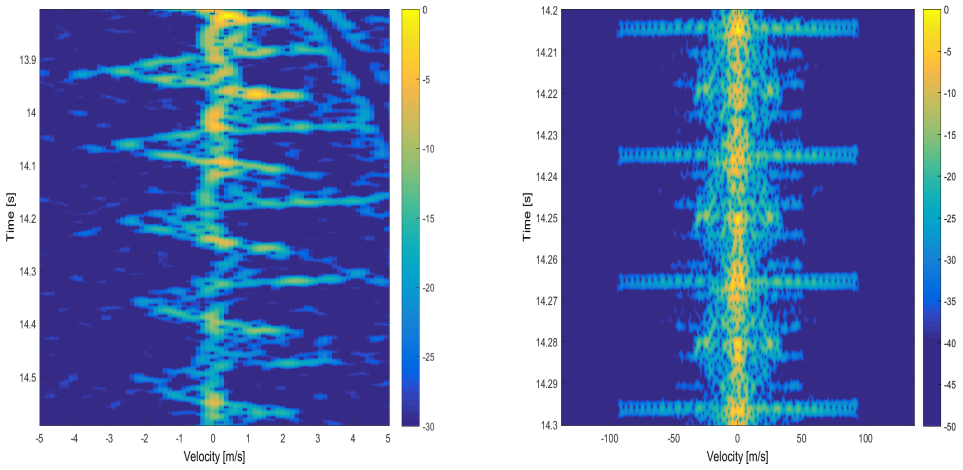

(a) Mallard duck. CPI=23ms (b) Kestrel UAV. CPI=4ms

Figure 5.4: Spectrogram of Mallard duck and Kestrel UAV measured in K-band

processing and gave valuable insight into the information available in μ-Doppler signatures at higher frequencies.

5.3.2 Network analyzer measurements at 1 and 4 GHz

This section presents the results of the network analyzer measurements of the Kestrel UAV, described in 5.1.2. Figure 5.5 shows the spectrogram of σ_{hh}, σ_{hv} and σ_{vv} at 1 GHz. At this frequency the most visible feature is from the main rotor blades measured at HH-polarization in the upper left panel. The short distinct flashes seen in Figure 5.4(b) are now replaced by flashes with longer duration. This can be explained by a high frequency approximation where the rotor blade acts as a re-radiating antenna with a beam width proportional to $\frac{\lambda}{L}$, where L is the blade length. The duration of the flash can be estimated from Equation 6.5. The directivity of the blade is less pronounced at lower frequencies.

At cross polarizations σ_{hv} and σ_{vh}, here identical due to reciprocity, the main rotor is not visible. This indicates that cross polarized reflection is at least -25 dB lower than σ_{hh}. In the lower left panel showing σ_{vv}, the main rotor blades can generally not be identified. This indicate a σ_{dr} of at least 25 dB as well. The rear rotor is, on the other hand, visible at a level 15 dB below σ_{hh}. This can be explained by a better alignment with the incident vertical E-field. The lower right panel shows

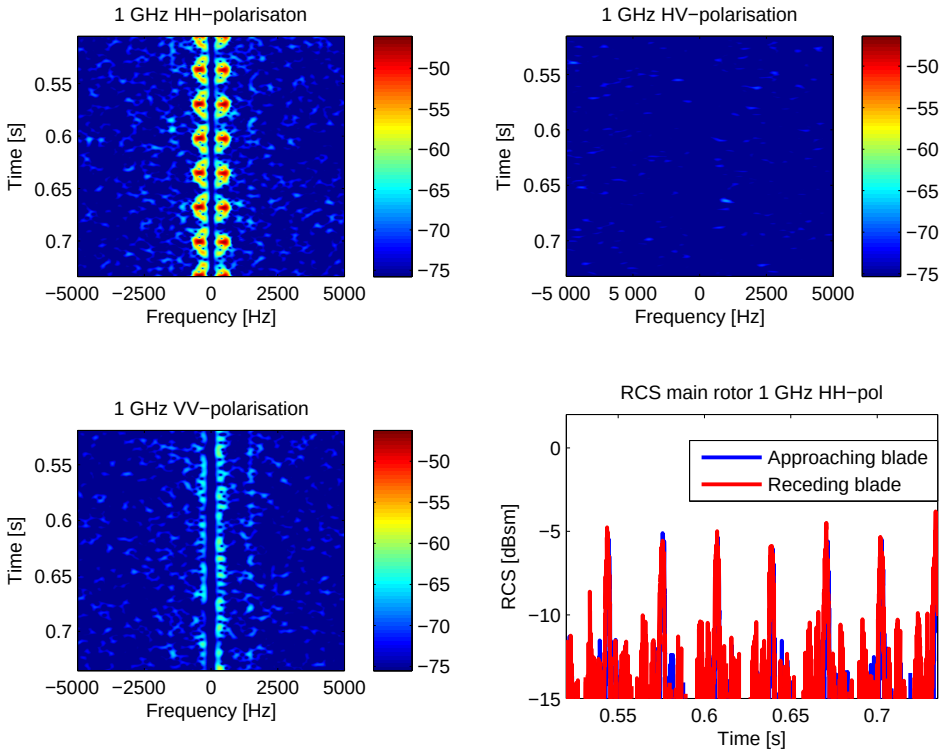

Figure 5.5: Measurements of UAV helicopter at 1 GHz with different polarizations.

calibrated σ_{hh} measurements for both approaching and receding blades in blue and red colours respectively. Note that the RCS of the main rotor is equal from the front and the back at this frequency. The absolute RCS is relatively constant at a level of -5 dBsm. This is the same value as predicted for L-band and shown in Figure 4.23, the same values for approaching and receding blades suggests that the shape of the rotor blade has no significance at this frequency.

Figure 5.6 shows the spectrogram of σ_{hh},σ_{hv} and σ_{vv} at 4 GHz. In the upper left panel showing σ_{hh}, the main rotor is again clearly visible. The same applies to the paddler, indicating that more details are detected compared to at 1 GHz. Now, the flashes have shorter duration compared to L-band. For the cross polarizations found in the upper right panel, there are some returns, from what is believed to be the paddler. The main rotor is not visible in this image, suggesting a σ_{hv} of at least -25 dB. For σ_{vv}, both the approaching and receding main rotor blades are clearly visible. A σ_{dr} of roughly 10 dB is observed in this case. This may be explained by the main rotor acting as a more pronounced Rayleigh scatterer in L-band. However,

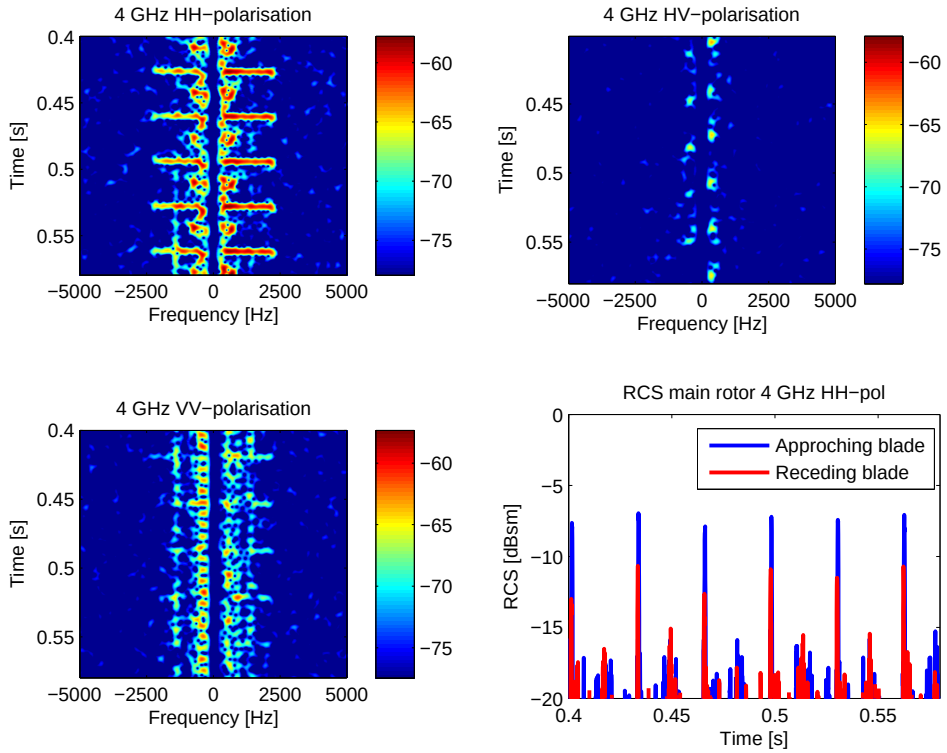

Figure 5.6: Measurements of UAV helicopter at 4 GHz with different polarisations.

still polarization is important at 4 GHz. The strongest reflections at σ_{vv} are seen from the rear rotor. This can be explained the same way as in the 1 GHz case. However, now the directivity of the rotor is much higher and the received echo power much larger. In the calibrated σ_{hh} plot in the lower right, the receding blades are seen to have lower RCS than the approaching ones. The measured difference is roughly 3 dBsm at 4 GHz, compared to a predicted difference of 2 dBsm at 3.2 GHz.

An indication of the difference between carbon fiber and plastic rotors as radar targets is found in Figure 5.7. A DJI Phantom II was successively equipped with plastic and carbon fiber rotors in two separate measurements. The rotors were run at approximately the same speed during the measurements. Although little power is visible in the spectrum of the plastic rotor in Figure 5.7(a), significantly more power over a much wider bandwidth is found in the case of carbon fiber rotors in Figure 5.7(b). The flash rate is indicated by the separation between harmonics in the spectra. These measurements were the first strong indication that there is significant

RCS differences between plastic and carbon fiber rotors and propellers.

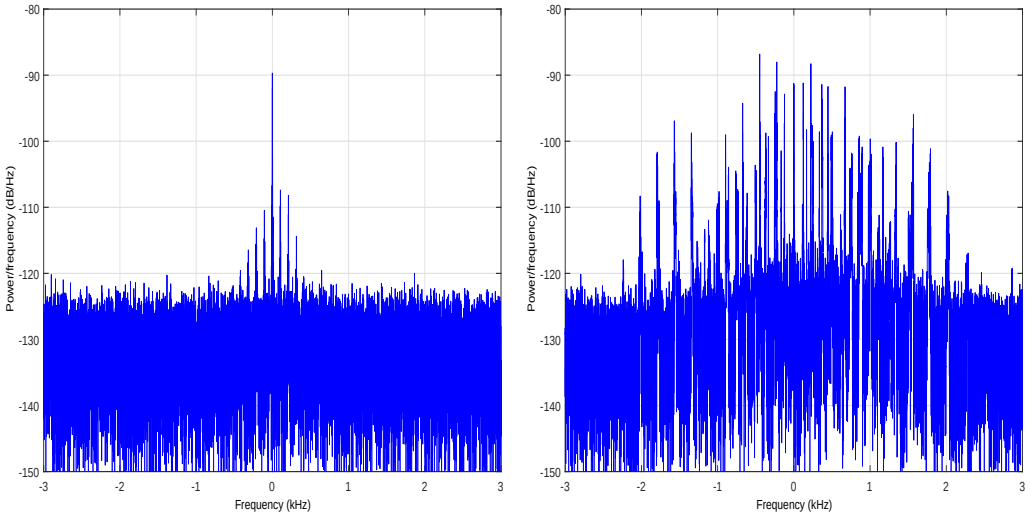

(a) Plastic rotors (b) Carbon fiber rotors

Figure 5.7: Power spectral density of returns from DJI Phantom II rotor blades of different materials at HH-polarization and $f_c = 4$ GHz.

The accuracy of this experiment is considered to be good. The main uncertainty is connected to the calibration sphere, which had to be attached to a nylon rope and moved back and forth to avoid the ground clutter. The measurements and predictions presented in Chapter 4.4.2.2 agree well and indicate that the accuracy for the RCS measurements is within 1 dBsm. This was the first experiment indicating that differential polarization may be a valuable feature for separation of target scatterers and target classification.

5.3.3 X-band measurements

The mallard duck spectrogram was the first indication that bird wings represents a considerable RCS, at least at selected aspect angles. New and more extensive measurements were done of gannets in X-band. The goal of this campaign was to establish whether bird wings actually contribute significantly to the overall RCS, and investigate if the wing orientation may be a source of the periodic RCS modulation at higher frequencies. Since this was done in X-band and the gannets are large birds, scattering is considered mainly to be found in the optics region. An advantage in this frequency band, compared to L- and S-band, is the improved velocity reso-

lution for fixed CPIs. This increased resolution enables better separation of wings and bird body, while still being able to resolve characteristic events in time.

The PicoSAR was not calibrated for absolute RCS measurements, however, the relative values are considered accurate. The external tracking system allowed for precise placement of the antenna beam and data collection window in range which resulted in high quality data.

5.3.3.1 Contribution from bird wings to overall RCS

The first aim was to quantify the contributions from wings to the overall RCS dependent on aspect angle. An automatic method, as described in Chapter 8.3, was used to compensate for the translational movement and identify the intervals with Doppler shifts from wings. After motion compensation, where the body's phase history is forced to be constant, any remaining phase shifts are considered to be caused by rotational movements of wings. The evaluation of RCS was in this case done in the time-domain after applying a band-pass filter around the expected wing Doppler response. Power at the output of this filter was considered originating from wings and the output of a similar low-pass filter was referred to as the body response. Due to the nature of the wing movement, only intervals with detected wing movement were evaluated. During intervals in between, wings and body are inseparable in Doppler due to the lack of velocity difference.

Figure 5.8(a) shows a μ-Doppler signature of a gannet flying towards the radar. The aspect angle was estimated to 0° in azimuth and 0° in elevation. Signatures of the wings are clearly visible during the entire interval. Maximal radial wing tip velocity is observed up to 4 m/s. This velocity is either caused by a component of the wing flapping movement, the sweeping movement of the wing or a combination of the two. The letters U (up), M (middle), D (down) in the figure indicate the position of the wings at the actual point in time. The wing position is estimated from the video.

Figure 5.8(b) shows a similar μ-Doppler signature of the same gannet flying perpendicular to the radar. The aspect angle is now estimated to 270° in azimuth and 0° in elevation and the video shows that the bird flaps its wings during the entire

interval. Contribution from wings is not as clearly seen, however, some movement is still detectable. The contribution from wings to the total RCS is visually determined to be less prominent at this aspect angle.

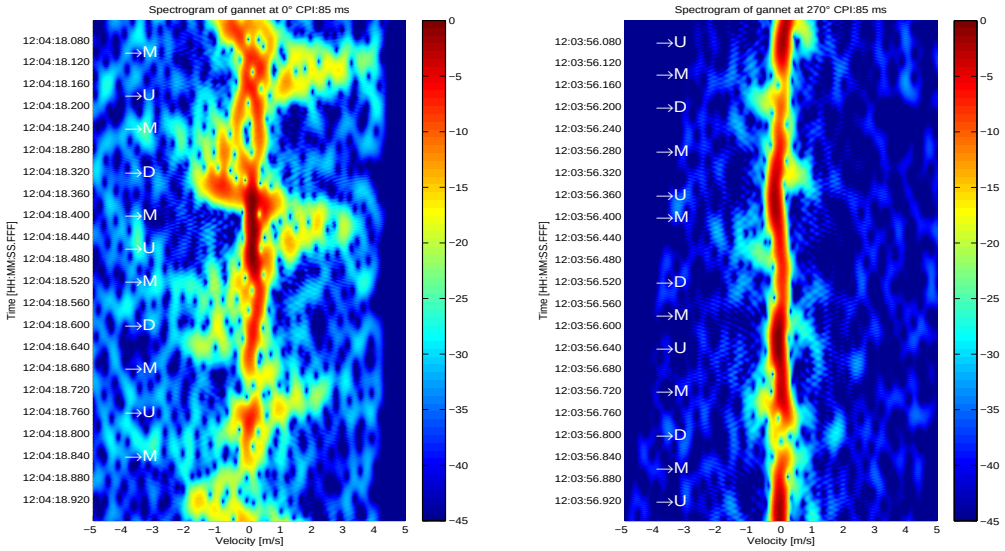

(a) Gannet observed from the front ©2014 IEEE (b) Gannet observed broad side ©2014 IEEE

Figure 5.8: Micro-Doppler signature of flying gannet at different aspect angles. Capital letters indicating position of wings (U=up, M=middle, D=down)

The examples showed in Figure 5.8 are typical for the signatures found in the data. However, to gather a broader statistical basis for evaluation of RCS from the entire bird and its body parts, 198 seconds of data from different azimuth angles were compared. The results are presented in Figure 5.9(a) and shows an interesting connection between RCS and azimuth angles. As seen in the upper panel of the figure, the total bird RCS, seen in green, is highest around broadside illumination. For the same azimuth angles the RCS of the wings, marked with red triangles, is at its lowest. The lower panel shows the ratio between RCS of wings and entire bird in green and wings and body only in blue. The findings are in accordance with X-band predictions presented in Figure 5.9(b). The upper panel shows the relative RCS of an entire bird with wings up in red and wings down in blue, compared to a model with level wings. The effect of wing position is observed to be most significant from the front and rear aspects. The RCS ratio between bird wings in three positions and

body is seen in the lower panel. It should be emphasized that RCS levels here are estimated from simulations of the RCS of body and wings made individually, which naturally excludes any potential interaction between wings and body. Still the figure shows a similar shape as found in the lower panel of Figure 5.9(a). Broadside the power of echoes from wings is found to be 20-25 dB lower than from the body, which is a significant difference. Illuminated from the front and rear the RCS is much more comparable. A difference of around -5 dB is observed here.

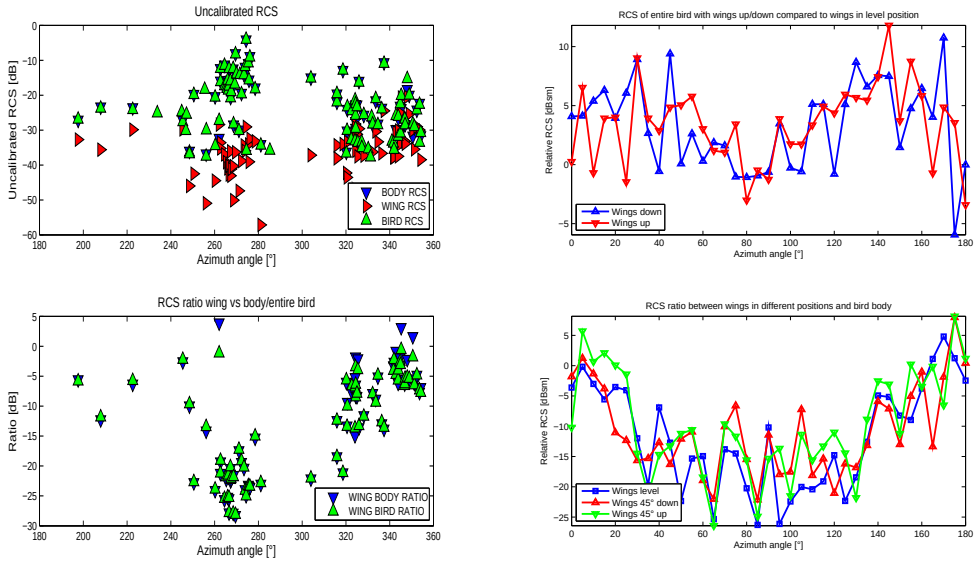

(a) Measured data ©2014 IEEE (b) Simulated data with FDTD code ©2014 IEEE

Figure 5.9: Upper left panel shows measured σ_{vv} of wings, body alone and entire bird as function of aspect angle. The lower left shows ratios between wings and body/entire bird. The upper right panel shows simulated σ_{vv} difference between bird with wings in upper and lower position compared to level wings. Lower right panel shows simulated ratios between σ_{vv} of wings and bird body. Dielectric parameters similar to human skin used in simulations.

The RCS values in Figure 5.9 are plotted against azimuth angles calculated from the track, adjusted for wind. Elevation angles are close to 0° One lesson learned from this campaign is that extracting accurate aspect angles of a maneuvering bird based on video recordings is surprisingly difficult. Therefore, the influence of the wind on the track was determined from the video, and used as basis for adjustment. This is believed to be more accurate than using visual aspect estimations

alone.

5.3.3.2 Periodic RCS modulations

The next question to be investigated was whether wing positioning may cause periodic RCS modulations. The upper panel of Fig. 5.9(b) shows as already discussed simulated differences in RCS between birds with wings in upper and lower positions, compared to a bird with level wings. The relative RCS values fluctuate considerably due to a de-correlation angle less than the azimuth step size of 5°, however, a distinct difference is observed as wings are either in upper or lower position. This is most prominent as the bird is observed from the front and the rear. At broadside illumination little influence from wing orientation is observed. An explanation to this can be found in the lower panel, where the relative contribution from wings to the overall RCS is found to be insignificant. Although large fluctuations are found in the simulations, the RCS is generally increased as wings are in upper and lower positions. These are positions were they are better aligned with the vertically polarized incident E-field. As the gannet wings may act as dipole scatterers even in X-band, this is believed to be a plausible explanation to any periodic RCS fluctuations in the data. In this case the modulations should be most prominent as the bird is illuminated from behind and front.

The gathered gannet measurements were divided into two groups based on the wing activity observed in the video. The first consisted of 168 intervals positively identified with periodic flapping movement, and the latter consisted of 30 intervals identified with irregular or no wing movement at all. In intervals with periodic flapping the WBF was visually estimated to 3-4 Hz. To resolve different WBFs with 1 Hz resolution an observation time of one second is required. This requirement is independent of carrier frequency.

The fluctuations observed in the first group soon proved to have more irregularities to them than data presented by Houghton and Blackwell [46]. The RCS distributions are generally exponential, which suggests contribution from several scatterers across the bird of which none is dominating the others. This indicates that irregular fluctuation due to decorrelation in the optics scattering region fre-

quently dominates any potential wing beat induced modulation. The contribution from several scattering centers does not seem to form a very robust periodic pattern related to the WBF.

Both spectral and cepstral analysis, as described in Chapter 8.4 and Chapter 8.5.3 respectively, were performed. The overall scores were disappointing with 53% and 34% correct WBF identification in the range 3-4 Hz respectively. More detailed results for the spectral analysis method as function of azimuth angle and SNR are found in Table 5.1. Here the number of samples in each segment is indicated in parentheses. Given SNR are mean levels for single pulses prior to filtering. Total score over SNR and azimuth angles is shown in the bottom row and rightmost column respectively. No significant increase in classification score is found with increasing SNR. The best score is found for illumination from the front (315 -360°). This is as predicted from Figure 5.9. However, the same increased score is not found for illumination from behind. This may be connected to the low number of samples at these angles.

SNR	*Azimuth angle [°]*				*Score*
[dB]	180-225°	225-270	270-315	315-360	[%] N
3-8	25% (4)	67% (6)	X / (0)	71% (14)	63% (24)
8-13	50% (2)	61% (18)	50% (4)	64% (33)	61% (57)
13-18	X (0)	26% (27)	27% (15)	67% (3)	29% (45)
18-23	X (0)	47% (17)	78% (9)	100% (1)	59% (27)
23 →	X (0)	83% (6)	56% (9)	X / (0)	67% (15)
Score	33% (6)	47% (74)	48% (37)	67% (51)	53% (168)

Table 5.1: WBF classification score as function of SNR and aspect angle ©2014 IEEE

The most disappointing discovery was that the overall WBF identification score for the control group with no or irregular wing movement was 43%, which is very close to the 53% achieved in the first group. This clearly shows that the applied processing does not manage to determine the correct WBF very well. The overall low score is believed to be connected to the interference between multiple scattering centers in the optics scattering region.

5.4 Summary

The described initial measurements formed the basis for further development of classification theory, signal processing and hardware development. μ-Doppler signatures collected at higher frequencies have the advantage of improved resolution in the time-frequency domain. This again allows for better analysis of target micro motion and enabled a rough quantification of the contribution of bird wings to the total bird RCS.

Although strictly valid only in the optics scattering region, the understanding of birds and bird parts as radar scatterers was significantly improved by conducting these experiments. Bird RCS are found to be largest at broadside illumination. This fits the prolate spheroid model. The contribution to σ_{vv} from wings are relatively independent of aspect angle. This leads to a relative RCS difference between wings and body of around 20-25 dB at these aspects. Illumination from the front and rear results in a much smaller difference of around 5 dB. All measurements are found to be in accordance with FDTD simulations presented. If detection of wing micro-motions are used for classification in a vertically polarized radar alone, these findings will result in a larger difference between detection range and classification range for illumination from broadside compared to that from the front and rear.

The potential for extracting WBF based on periodic RCS modulation was investigated. The correct WBF was only found in 53% of the data covering all aspect angles. Slightly better results were found at frontal illumination. The overall impression is that the observed RCS modulation is resulting from decorrelation effects of the target in the optics scattering region. Rapid aspect angle changes resulting from maneuvering and translational movement at short range is enough to cause modulations not correlated with the wing beating.

The measurements involving a dual polarized antenna and a two port network analyzer enabled high precision polarimetric measurement of a rotary wing UAV in controlled conditions. The measurements performed support the hypothesis that long and thin propellers acts as dipole scatterers at frequencies relevant for air defence radar systems. The hypothesis that plastic rotors are associated with signifi-

cantly lower RCS compared those made of carbon fiber was also strengthened.

Although these initial measurements gave relevant contributions, measurements in the relevant bands, by appropriate waveforms and of relevant targets are required to answer the research questions. For this purpose the BirdRAD system was developed and the remainder of this thesis is dedicated to results from this system.

Chapter 6

Hardware development of BirdRAD

Electromagnetic modeling may provide valuable contributions to improve the understanding of how radar interacts with any target. Being able to control material properties, target orientation and behavior, the absence of clutter and influence of radar hardware are all important strengths of simulation. However, in this thesis lack of accurate target models, material properties, and realistic movement lead to the desire for experimental results. Radar data of actual targets in relevant noise and clutter conditions are considered crucial in order to reveal practical problems and highlight the realistic capability of the suggested classification approach. This chapter provides a presentation of the hardware designed to investigate the research questions raised. Descriptions are kept at a high level as the hardware is considered more as a research tool than a novel contribution to the radar hardware literature. The design and implementation of the different parts of the system is, where not cited otherwise, done by the author.

6.1 Required capabilities

The lack of commercially available products capable of providing the data required led to the design of a new experimental radar system. This was the beginning of the BirdRAD system. The goal of its design was to collect data similar to those achievable in a classification mode of a future long range air defence radar. This did not demand a real-time system, however, a system providing high quality data for off line processing was required. As the primary task of long range radars is

Figure 6.1: BirdRAD antennas, pan-tilt device and video camera.

surveillance of large volumes, frequencies at L- and S-band are frequently used due to lower the propagation loss. To investigate and compare the performance of classification in these bands, the BirdRAD was designed with the opportunity to independently operate in both bands simultaneously.

Flexibility in terms of waveform and carrier frequency were important design requirements. Two arbitrary waveform generators (AWG) for waveform generation, a digitally controlled two channel RF-synthesizer used as local oscillators (LO), as well as linear power amplifiers (PA), gave the required flexibility to transmit practically any waveform within the Norwegian military air surveillance radar bands.

Sensitivity was another important factor in the system design. Large dynamic ranges in target signatures and generally small and slow targets lead to the desire for a sensitive receiver. The receiver noise figure was kept low, the LOs were selected based on their favorable phase noise characteristics, and a 16-bit resolution ADC combined with digital down conversion (DDC) was selected to provide high dynamic range and facilitate high fidelity echoes even in dense clutter scenarios.

In addition, to investigate the potential for classification based on system properties likely to be available in the near future, there was a desire to investigate

polarimetric features for the same purpose. Polarization has previously not been exploited for classification in long range air defence systems. In older systems with mechanically scanned antennas, polarization diversity has occasionally been used to increase the probability of detection. However, implementation in phased arrays, which is the dominating antenna technology in modern systems, leads to increased costs that have to be justified by a significant increase in performance. The research presented here should help to answer whether polarization is worth implementing in future systems.

The effects of polarization can be examined in terms of incoherent and coherent parameters, depending on whether amplitudes alone or both amplitudes and phases are utilized in the complex scattering matrix **S** respectively. The coherent representation demands significantly more of hardware and calibrations, however, the information extractable from a coherent description is substantially increased. A radar capable of collecting such data is often referred to as a quad polarization or polarimetric system. The decision was made to design BirdRAD with this capability.

Although much was done to facilitate imitation of a modern radar classification mode, there are two main hardware differences between the BirdRAD system and a long range radar. The first is the lack of beam-steering and the second is the significantly reduced detection range. These factors are not considered critical since the purpose of BirdRAD is to emulate a classification mode where detection range is of less importance and the antenna beam is fixed on the target for the required dwell time. BirdRAD continuously follows the targets of interest, one at the time, and the collected data can easily be divided into realistic dwell times for coherent off-line processing.

6.2 System specifications

System properties like carrier frequency, instantaneous bandwidth, oscillator stability, and waveform agility were carefully selected to meet the flexibility and quality requirements expected in modern or near future systems. Some important parame-

ters and related system requirements are discussed in the following paragraphs.

6.2.1 Bandwidth

As the primary task of long range ADRs traditionally has been detection at long distances, range resolution in the order of hundreds of meters is normally found sufficient. Although fine range resolution theoretically could help with classification of small targets, the total bandwidths available for radar at L- and S-band do not allow for resolving the small targets addressed in this thesis sufficiently in range. A range resolution fine enough to separate individual targets is on the other hand considered achievable and a realistic goal for BirdRAD. Typically this require a bandwidth of some tens of MHz for such targets. Each channel of the system was therefore designed with a minimum bandwidth of 125 MHz, limited by the analog to digital converter (ADC). Due to frequency allocation limitations in L-band, a decision was made to reduce the transmitted bandwidth in both bands to 50 MHz for all experiments covered in this thesis.

6.2.2 Detection range

The detection range of a mono-static radar system can be calculated from the radar range equation widely covered in almost any radar text book. According to [132] the maximal detection range for a pulse-Doppler radar may be written:

$$R_{max} = \sqrt[4]{\frac{P_{avg} G A_e \sigma \tau_d}{(4\pi)^2 S_{min}}} = \sqrt[4]{\frac{P_{avg} G^2 \lambda^2 \sigma \tau_d}{(4\pi)^3 S_{min}}} \tag{6.1}$$

where P_{avg} is the average RF output power, σ is the RCS, G is the antenna gain, A_e is the effective receive antenna area, λ is the wavelength, τ_d is the dwell time equal to the coherent processing interval CPI, and S_{min} defines the minimum signal power required for detection.

In terms of detection, the ultimate goal of BirdRAD is to gather back-scattered energy from the wings of birds. The RCS of these are expected to be small at L- and S-band, down towards -40 dBsm depending on the orientation. Movement during the wing beat cycle reduces the effective CPI providing integration gain. Wing beat

frequencies of birds are reported between 2-20 Hz mainly depending on the size of the bird. This equals wing beat periods ranging from 50 to 500 ms and a maximum CPI of 1/10 of this is considered sensible for coherent integration. Based on these assumptions the detection range of the system was estimated.

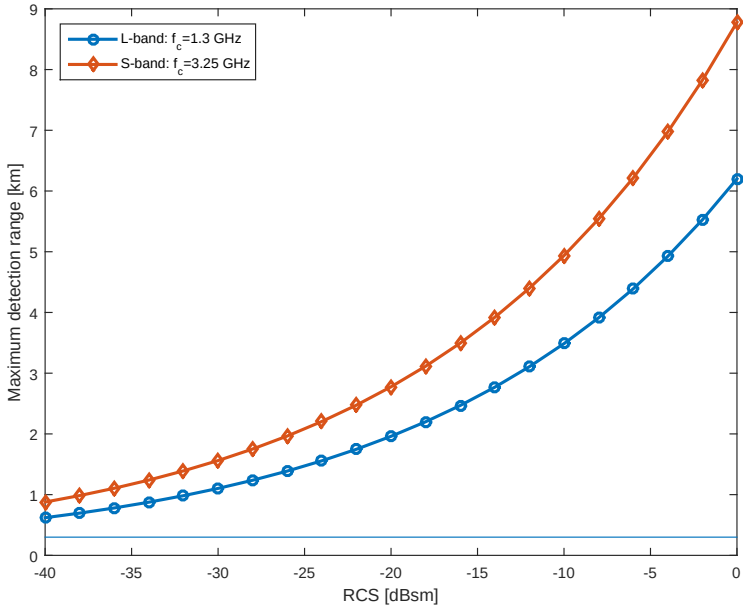

Figure 6.2: Calculated detection ranges for BirdRAD using parameters in Table 6.1.

Figure 6.2 shows the calculated detection range as function of RCS for both frequency bands. The waveform used in the calculation was the same as used in almost all experiments referred to in this thesis, the *50MHz2mu10kHz*. This is a waveform consisting of linear frequency modulated (LFM) pulses with parameters found in Table 6.1. This table also contains information on the interval of coherent integration, the transmitted power, noise factor and different losses taken into account in the calculation. The required SNR to declare detection was set to 13.6 dB, which equals the threshold for detection in Rayleigh distributed noise with a probability of false alarm P_{FA} of 10^{-6} [21].

The horizontal blue line indicates the inner blind range R_b of the system defined by the pulse length τ_p as

$$R_b = \frac{c\tau}{2} \tag{6.2}$$

This defines the minimum range at which a target can be detected, as the receiver

Parameter	*Description*	*Value*
B	Bandwidth	50 MHz
τ_p	Pulse length	$2\mu s$
PRF	Pulse repetition frequency	10 kHz
CPI	Coherent processing interval	20 ms
P_t	Peak power	200W
P_{avg}	Average power	4.0W
NF	Noise factor	2 dB
L_r	Receive loss	3 dB
L_t	Transmission loss	3 dB
L_{sp}	Signal processing loss	3 dB
SNR_{min}	Minimum signal to noise ratio	13.6 dB

Table 6.1: BirdRAD parameters used for detection range calculation.

in a pulse-Doppler radar normally is switched off during the transmission of the pulse. The BirdRAD is on the other hand operated with a separate receive antenna, and could in theory detect targets closer in. However, the direct signal between the antennas and close in echoes are believed to be so powerful that these ranges are gated out as a precaution.

The differences between the curves for L- and S-band, seen in Figure 6.2, are caused by the antenna providing less effective area A_e and gain G when operated in L-band. For a large bird or UAV with a total RCS of for example -10 dBsm, the orange and blue lines show that a detection range of more than 3 km can be expected in both frequency bands. A target part with a RCS of -30 dBsm can be detected out to ranges of around 1.1 km and 1.6 km at L- and S-band respectively. This is considered acceptable for practical data collection.

6.2.3 Pulse repetition frequency

The PRF of the system is of interest for several reasons. Pulse generation is, as covered in Chapter 6.3.1, taken care of by AWGs. For a classic pulse-Doppler waveform, one pulse form is uploaded to the memory and repeatedly played off at an arbitrary pulse repetition interval (PRI). In the following paragraphs requirements for the PRF are discussed.

6.2.3.1 Forming the scattering matrix from subsequent pulses

The system was designed to simultaneously collect coherent signatures on two orthogonal linear polarizations, horizontal H and vertical V. On transmission the polarization is alternated between the two from one pulse to the next. This is done under the assumption that the PRF is high compared to any change of target orientation. In this way the target can be treated as stationary between two subsequent pulses.

6.2.3.2 Pulse integration

In a low power and short range pulse-Doppler radar, the pulse length τ_p may be limited to minimize inner blind range. Consequently the compression gain is reduced and an increased need for pulse integration emerges to maintain the probability of detection. Increasing the PRF can be a solution to achieve the required SNR. However, increasing the PRF must be done with care as this defines the distance between ambiguities in range. As an example relevant to BirdRAD an unambiguous range of $R_u = 15$ km requires according to

$$PRF_{max} = \frac{c}{2R_u} \tag{6.3}$$

a maximum PRF of 10 kHz.

6.2.3.3 Sampling of periodic RCS modulations

Systematic variations of RCS may be used as feature for classification. One example is the periodic flashes back-scattered from rotational rotors of a rotary wing UAV. For a pulse based radar it is important that no blade flash is lost between two subsequent pulses, meaning that the sum of the pulse repetition interval τ_{PRI} and pulse duration τ_p must not exceed the duration of the blade flash τ_{bf}. The relation is according to Tait [23]

$$\tau_{bf} \geq \tau_{PRI} + \tau_p \tag{6.4}$$

Although the size to wavelength ratio might become small for the smallest UAVs, the rotor- or propeller-blades are here thought of as re-radiating antennas and the duration of this blade flash τ_{bf} is dependent on the wavelength λ, the length of the blade L, and its angular velocity ω as [23]

$$\tau_{bf} \approx \frac{\lambda}{L\,\omega} \tag{6.5}$$

This way the minimum PRF, PRF_{bf}, for UAV blade flash based classification can then be estimated as

$$PRF_{bf} \geq \frac{1}{T_{bf} - \tau_p} \tag{6.6}$$

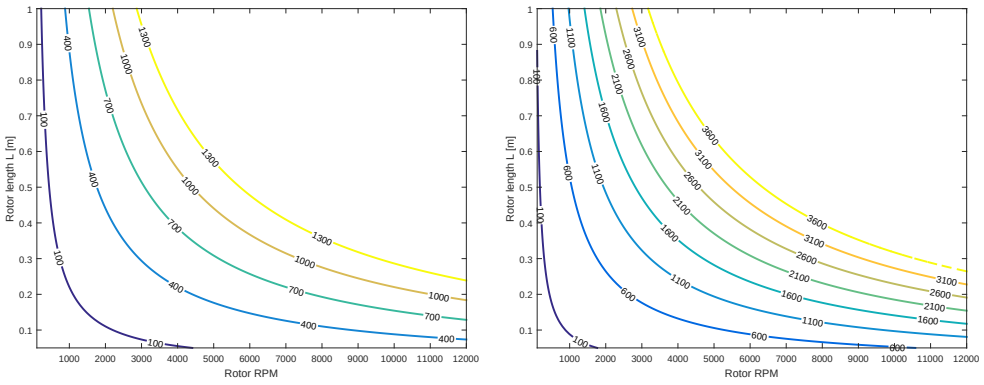

(a) L-band (b) S-band

Figure 6.3: PRF_{bf} [Hz] for sampling every blade flash as function of rotor/propeller blade length L and RPM.

Figure 6.3 shows curves of PRF_{bf} measured in Hz as function of L and RPM under the given assumptions. The angular velocity $\omega = \frac{v_t}{L}$ [rad/s] is here replaced by revolutions per minute RPM since this is a more frequently used measure in aviation. Increasing the blade length or frequency leads to a narrower flash beam width and thus a shorter duration. The sum of the UAVs translational velocity and blade tip velocity v_t will hardly ever exceed the speed of sound and no combination of RPM and L resulting in a velocity beyond this value is plotted.

Figure 6.3(a) reveals that PRF_{bf} of 1300 Hz is sufficient for any likely combination of rotor length and RPM at L-band (1.3 GHz). Similarly a PRF_{bf} of 3600 Hz is adequate in S-band (3.25 GHz). This proves not to be the toughest requirements

to PRF if the Doppler bandwidth Δf_d is to be sampled unambiguously.

6.2.3.4 Unambiguous sampling of velocity

The PRF also defines the maximum unambiguous velocity, and the maximum sum of translational and blade tip velocity v_t of the target relative to the radar sets a requirement on the minimum PRF, $PRF_{\Delta f_d}$, if ambiguities are to be avoided. During the design phase of BirdRAD, man-made targets with rotational parts like propellers and rotors were considered to constitute the toughest requirements in this context. The combined absolute velocity may in some rare cases approach to the speed of sound in air of 340 m/s, however, it rarely exceeds this. In comparison a bird wing's combined translational and blade tip velocity is assumed to stay below 25 m/s in most cases.

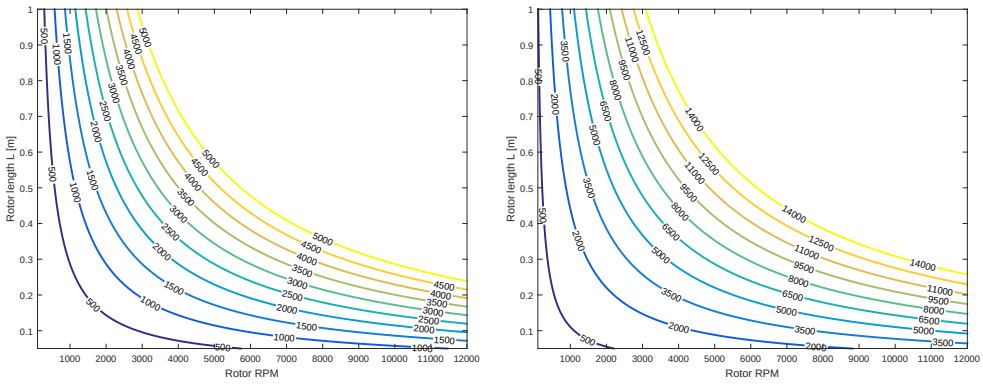

(a) L-band (b) S-band

Figure 6.4: $PRF_{\Delta f_d}$ [Hz] for sampling Doppler shift generated by blade tip velocity as function of rotor/propeller blade length L and RPM.

As it is the Doppler spectrum that is to be sampled unambiguously ($PRF_{\Delta f_d} \geq \Delta f_d$), different values apply to L- and S-band channels. Figure 6.4(a) shows that a $PRF_{\Delta f_d}$ approaching 5 kHz is required for some combinations of blade length and RPM at L-band. For S-band Figure 6.4(b) indicates that the same combinations require a $PRF_{\Delta f_d}$ up towards 14 kHz. This latter value is high and in practice all drone measurements presented in this thesis were unambiguously sampled at 10 kHz even in S-band.

6.3 Hardware implementation

The entire BirdRAD system was designed to fit in a 19-inch rack with a height of 120 cm. In addition the PAs were installed in two separate 19-inch racks with a height of 48 cm. The total weight is estimated to be around 150 kg and the total power requirement in field is covered by a petrol generator providing 1,5 kW. A photo of the system is found in Figure 6.5. The left part shows the two smallest racks on top of each other containing power amplifiers and the LNA unit. Figure 6.6 shows the hardware layout. Here blue symbols indicate components belonging to the L-band channels, whereas red indicate components in S-band channels. Green components are common to both bands. This sub chapter presents the hardware implementation and synchronization.

Figure 6.5: The BirdRAD system.

6.3.1 Pulse- and waveforms

Although frequency modulated continuous wave (FMCW) radars, due to no inner blind range, may provide better performance on short ranges, a pulse-Doppler design was chosen to better mimic an air defence radar.

The pulses are generated in two AFQ 100B arbitrary waveform generators

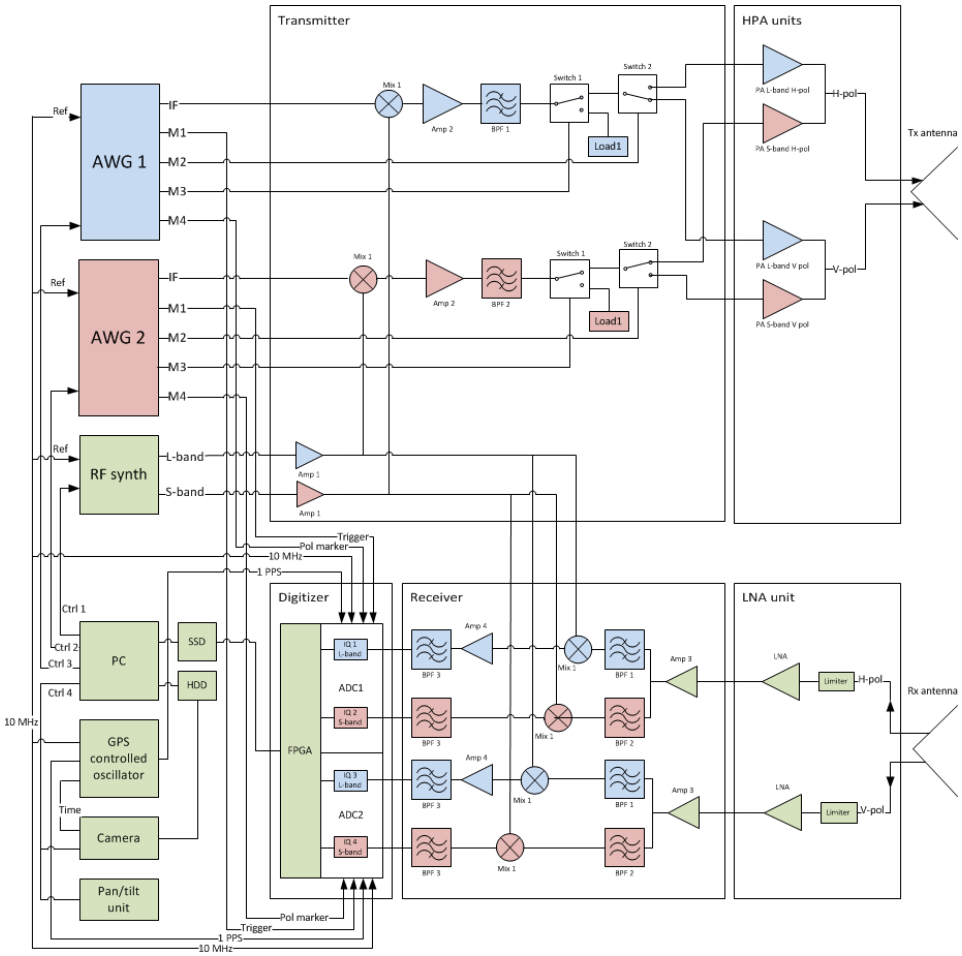

Figure 6.6: BirdRAD system hardware layout. Components in blue indicate L-band, red S-band and green components are common to both frequencies.

(AWG) from Rhode&Schwartz. These allow any time limited waveform with a bandwidth less than 528 MHz constructed in computer software to be uploaded to the memory of the device. The AWGs take care of the digital to analog conversion (DAC) of the signal and for the BirdRAD system pulses are generated at a IF-center frequency of 187.5 MHz.

Although an arbitrary waveform can be transmitted, all experiments covered in this thesis were pulse-Doppler waveforms based on LFM pulse-forms. A small library of waveforms, corresponding parameters and data volume generated can be found in Table 6.2. These waveforms were generated in Matlab and uploaded to the AWGs. In addition to generating IF-signals, the AWGs are used to control the timing of the system by its marker output channels. The column *Scene* in Table 6.2

shows the total sampled scene size in kilometers controlled by such markers. More details on this is found in Chapter 6.3.4.

Name	*B*	τ_p	*PRF*	P_{avg}	*Scene*	*Data volume*
50MHz2mu1kHz	50 MHz	2 μs	1 kHz	0.4 W	6 km	33 Mb/s/Ch
50MHz2mu2kHz	50 MHz	2 μs	2 kHz	0.8 W	10 km	67 Mb/s/Ch
50MHz2mu4kHz	50 MHz	2 μs	4 kHz	1.6 W	10 km	200 Mb/s/Ch
50MHz2mu10kHz	50 MHz	2 μs	10 kHz	4.0 W	6 km	200 Mb/s/Ch

Table 6.2: Predefined waveforms for the BirdRAD system.

6.3.2 Transmitter and Receiver

Although the hardware was tailored to collect experimental data needed to answer the research questions introduced in this thesis, the system is seen more as a research tool than a novel design. Therefore only a high level description of the system is provided. Tables listing all components used are found in Appendix A. Since practically no restrictions were put on weight, the radar transmitter and receiver were assembled by connectorized components. This also gave flexibility and made the mounting and testing easier. Both the transmitter and receiver were installed in separate aluminum boxes, each 19-inches wide and 4.5 inches (3 units) high.

The upper section of Figure 6.6 shows the local oscillator (LO), the transmitter, the power amplifiers (PA) and transmitter antenna, in addition to the waveform generators already covered. The LO frequencies for both L- and S-band channels are generated in a HS9002A RF synthesizer from Holtzworth. This device has two highly stable output channels covering the frequency range from 0.25 - 4 GHz. In the transmitter two mixers mix the LO frequencies for each channel with the corresponding waveforms, before amplification and band-pass filtering is performed. Two microwave switches marked *Switch 2* subsequently direct L-and S-band pulses to the vertical or horizontal feed of the antenna. The high PRF, required to justify forming the complex scattering matrix **S** from subsequent pulses, leads to an equally high switching rate between horizontally and vertically polarized pulses. Fast solid state RF-switches handling high power could not be found, and a solution with one PA for each polarization was chosen. Solid state switches specified for lower power

were then put in front of the PA in each transmitter channel. In total this required four PAs, two in each frequency band. These are all class AB amplifiers, linear up to more than 200W peak power and capable of supporting 100% duty cycle. This means they are continously amplifying whatever is on their input, no matter if this is signal or noise alone. To prevent transmitting the noise generated by the transmitter electronics between pulses, switches marked *Switch 1* were installed. These are designed to route the noise from components in front of it into 50Ω loads marked *Load1* when the channel is not active.

The antenna is a QSR700-OST dual polarized reflector antenna from Q-par Angus Ltd. Two such antennas, one for transmit and one for receive, covering 0.9-18 GHz were chosen for the flexibility of potentially doing bi-static measurements or using FMCW waveforms at a later time. Behind the receive antenna there is a LNA unit consisting of limiters and LNAs for each polarization. The LNA unit was placed together with the PAs as close as possible to the antennas. This was done to reduce losses in cables and thereby keep the receiver noise figure as low as possible and maximize the transmitted power respectively. During operation 2 meter long Sucoflex 100 RF-cables from Huber & Suhner connected the antennas to the PAs and LNA unit. The receiver noise figure for the current design is calculated to be 1.3 dB and 1.8 dB for L- and S-band respectively. Including an antenna noise temperature of 150 K results in an overall system noise figure more relevant for performance estimations of 1.8 dB for L-band and 2.0 dB for S-band.

The lower central part of Figure 6.6 shows the receiver. This consists of four channels, -one for each polarization at L-band and one for each in S-band. The signal in each channel is initially amplified and band-pass filtered before being downconverted by mixing the signal with the LO-frequencies back to the original IF-frequency of 187.5 MHz. This corresponds to the second Nyquist-zone of the digitizer and specially made 50 MHz wide IF-band-pass filters ensure sufficient attenuation outside this band before digitization.

6.3.3 Digitization

The NI 5762R (02) digitizer from National Instruments was selected for sampling. This comes without an anti-aliasing filter, which is a requirement for under sampling the IF signal in BirdRAD. This board has two input channels each and two boards are needed to sample two polarizations in two frequency bands. The sample rate of 250 Ms/s and 16-bits resolution in each channel makes the unit meet the specifications well. The card has a clock input for reference which is supplied with a 10 MHz signal from the GPS controlled oscillator. This common reference distributed over the entire system is key for synchronization. A trigger input is used to trigger the data collection. More on synchronization and system control can be found in Chapter 6.3.4.

On the back plane of each digitizer there is a NI PXI-7954R FlexRIO with a Virtex-5 field programmable gate array (FPGA) module. Although demodulation, decimation and pulse compression could be implemented in this FPGA, raw sampled data was streamed directly to the solid state hard disk. This requires more data storage, however, since BirdRAD is an off-line system being able to perform all steps of the digital processing in computer software, which gives better control for research purposes. The FPGA code and Labview software for writing data to disk was done by my colleague Idar Nordheim Næss. All other hardware design and implementation is done by myself.

6.3.4 System control

Figure 6.7 shows the distribution of reference clocks and control signals between units in the BirdRAD system. Keeping the different units synchronized is key when signals are to be recorded coherently. A 10 MHz reference clock signal is used for this purpose. This is a signal generated in the GPS controlled oscillator unit and distributed to the RF-synthesizer, digitizers and AWGs. The signal amplitude were adjusted either by splitting or attenuation to match the input requirements of each individual unit.

Other control signals like triggers and markers are distributed from the AWGs. The low voltage transistor-transistor logic (LVTTL) signal from these were used to

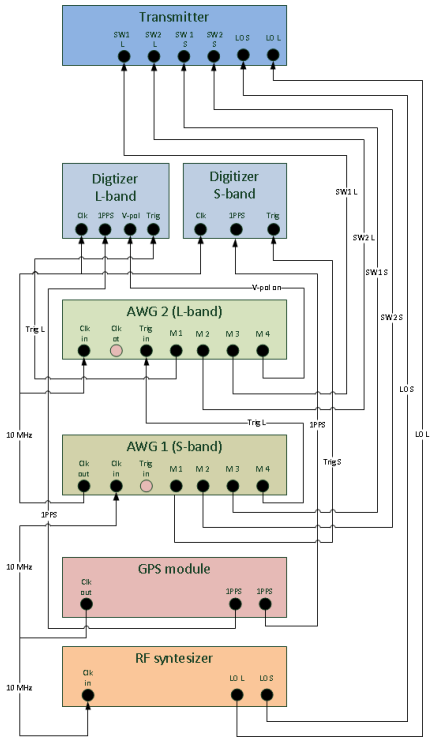

Figure 6.7: BirdRAD control signals.

trigger the digitizer, RF-switches (*SW1 & SW2*) and AWG. The *AWG1* was used as a master unit and one marker output on this (*M4*) was used to trigger *AWG2*. The corresponding *M4* on *AWG2* was fed to a digital input of the L-band digitizer. This signal marks whether V-polarization is transmitted. Since the system of polarization transmitted is deterministic, polarizations for all pulses can be determined from this. This association is done in the pre-processing steps covered in Chapter 8. An example showing the full sequence of transmitting one pulse at each polarization in each band is found in Appendix A.3.

6.4 Pan-tilt unit and camera

A low cost pan-tilt unit, PT-3002 from 2Bsecurity systems, was used to control the antennas. This is originally designed for security cameras, however, the weight and torque of the antennas are safely within the limits of the pedestal when mounted with the center of mass close to the rotation center. Software written in LabView was used to control the unit by serial communication (RS-485 Pelco-D protocol). Since the PT-3002 provides feedback on its current elevation and azimuth position,

a control loop was made to automatically follow a target broadcasting its position. Information on civilian aircraft position, heading, velocity and more is available via the automatic dependent surveillance system - broadcast (ADS-B). Such messages were decoded by a SBS-1 receiver from Kinetic Avionic Products Ltd. and was for example successfully used for collections presented in Figure 6.9. However, during the experiments presented in this thesis the antenna was controlled manually from the computer based on visual input from a video camera.

This video camera was, together with a zoom lens, mounted between the antennas, see Figure 6.1. This was used both for documentation and input for the manual optical tracking of targets. The camera was provided with accurate time from the GPS-clock making it possible to correlate video and data during analysis. One drawback of the video camera was the lack of auto focus. Both zoom and focus had to be manually controlled during data collection and required considerable attention from the operator.

6.5 System test and characterization

Lab tests of the full system were done by connecting the transmitter and receiver together with cables in the lab. This was done to test and characterize all the hardware as well as software for controlling the sampling, data handling and signal processing. A dedicated waveform with delayed LFM pulses was used to simulate point targets and attenuators with a total attenuation of 100 dB were put between the PAs and the LNA unit.

The frequency and impulse responses of the system were investigated. According to matched filter theory the filter that maximizes the detection of a point scatterer in white noise is the complex conjugate of the transmitted pulse [21]. Different point spread functions are observed when the matched filter is a theoretical representation of the transmitted pulse or a measured version of the actual generated pulse having passed through the transmitter and receiver channels. Pulse compression with the theoretical representation of the transmitted LFM pulse leads to sidebands in the impulse response, seen in blue in Figure 6.8. This is connected to

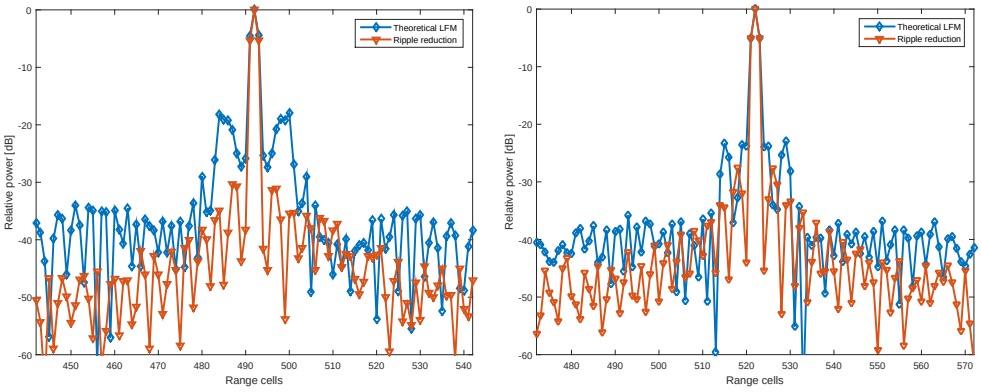

(a) L-band (b) S-band

Figure 6.8: HH-polarization impulse responses with pulse compression with theoretical LFM pulse in blue and measured frequency response with ripple compensation approach in red.

pass-band ripple observed in the system. Compression with a complex conjugated version of the measured frequency response corrects for unwanted phase shifts in the channel. Additional correction of the amplitude, from now on referred to as ripple reduction, proves to give a significantly improved impulse response. This is seen in orange in the same figure.

Although range resolution is of minor importance in the experiments documented in this thesis, the compensation was applied to all collected data as a part of the pre-processing step. The following example is included to emphasize the importance of compensating such channel distortion in situations were range resolution is critical, such as in ISAR-imaging.

6.5.1 Example: ISAR-imaging

One early test of the BirdRAD system was done by data collection of a Boeing 737-800 airliner in S-band passing FFI on the approach to Gardermoen airport. Figure 6.9(a) shows ISAR images formed over one second as the aircraft was 2.5 km out. At this range the translational velocity of the aircraft crossing the line of sight provided the aspect angle change required to resolve the aircraft in cross-range. Since there was no attempt to estimate accurate aspect angles during the collection, the cross-range resolution is unknown. This results in a range-Doppler image rather than a true ISAR image with unit meters on both axes.

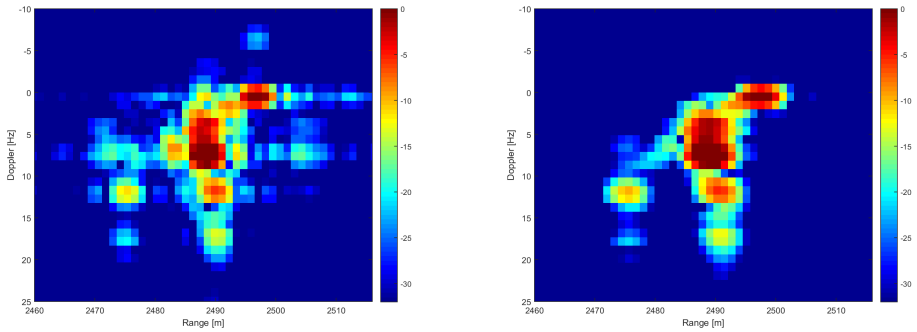

(a) No ripple reduction applied (b) Ripple reduction applied

Figure 6.9: ISAR images of a Boeing 737-800 formed from HH-channel in S-band with and without ripple reduction applied.

Figure 6.9(a) shows an image where the pulse compression is done with the theoretical LFM pulse. The artifacts in the range dimension complicate the analysis of the image and can easily be confused with real scatterers. Figure 6.9(b) on the other hand is formed on data pulse compressed with a measured impulse response and with corrected amplitude response. The result is a significantly improved image. The target is seen slightly from behind and the scatterers around 2475 meters are believed to be the tail, whereas the wing is seen at around 2490 meters. Being able to form well focused images such as the one seen in Figure 6.9(b) was taken as an early sign that the system was performing well.

6.5.2 Stability

Stability over time is another important quality of a polarimetric radar system. The differential power and phases between polarimetric channels were investigated in a cable loop-back test over 10 minutes. Figure 6.10(a) shows the results of the power difference between channels. Small absolute differences can be observed between channels, as all ideally should be 0 dB. However, the stability over time is good and the absolute differences are easily compensated for during calibration. Figure 6.10(b) shows the phase difference between the same channels. The findings here are similar. There are, as expected, some absolute phase differences between the channels, however, the stability is good and the phase differences are removed during calibration.

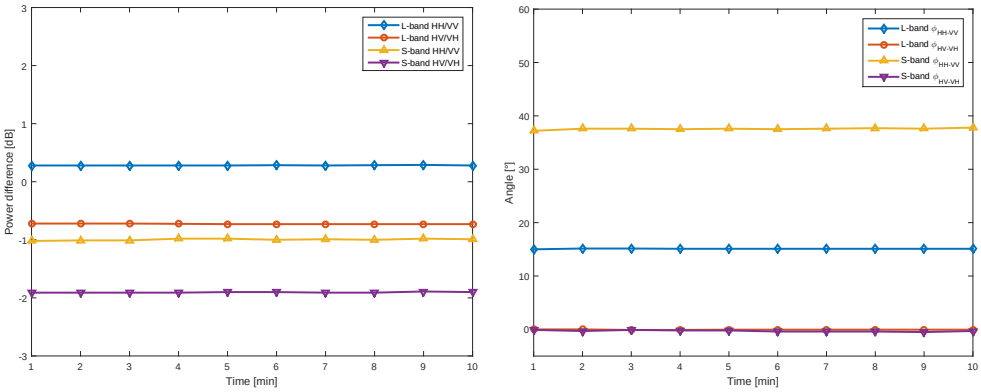

(a) Differential power (b) Differential phase

Figure 6.10: Stability measurements collected over 10 minutes.

6.6 System calibration

Calibration of the BirdRAD system prior to data collection has two main purposes. The most important is to ensure that the relative responses in the co- and cross-polarized channels are identical in terms of phase and amplitude. In addition to system characterization done in the lab as presented in the previous section, an in field calibration was performed prior to every data collection. Absolute RCS measurement is of secondary importance. However, calibration against an inflatable calibration balloon was done to enable estimation of absolute target RCS values.

6.6.1 Absolute RCS calibration

An inflatable sphere was filled with helium and used as a calibration sphere. The theoretical RCS of this was 0 dBsm. The diameter of 1,13 m ensured measurements in the optics region for both L - and S-band. Illumination of the sphere should theoretically ensure stable RCS values for all channels. However, the semi flexible surface may have contributed to fluctuations of more than 3 dB as the balloon was moved to separate it from ground clutter. Although this was a disappointment, it was considered good enough for rough calibration of absolute RCS. The positioning of the target within the antenna beam is probably a larger source of error. However, only data clearly visible in S-band was registered, which indicates that the targets were within the 3 dB beamwidth of both frequency bands. The accuracy of absolute RCS values are poor as variation of around 2 and 3 dB are found at L- and S-

band respectively. However, the precision or relative accuracy between channels are believed to be high due to good stability as shown in Chapter 6.5.2.

Figure 6.11: Calibration balloon with a diameter of 1.13 m.

6.6.2 Field calibration of polarimetric channels

To ensure coherent polarimetric data of high quality, calibrations of differential power and phases between co- and cross-polarized channels were performed prior to every experiment. Basically, this procedure is the same as used for characterization of the system. A special waveform for calibration with additional delayed pulses used as synthetic point scatter targets were transmitted. Data collection was done with all BirdRAD components including cables, however, with the two antennas replaced by two identical attenuators of 100 dB each attenuating the peak power of 200 W in each transmitter channel down to an acceptable level for the receiver channels. The procedure of calibration included collection of the digitized echoes of the transmitted pulses, first for co-polarized and then for cross-polarized channels. This way the system was regularly characterized prior to all data collections after powering up the system. As the pulse compression was done by post processing of the data, the four calibration waveforms (HH, HV, VH and VV) were associated with the correct data collection in both bands. As a part of this process the phases and amplitudes were equalized between all channels in both bands.

6.6.3 Characterization of antennas

The loop-back calibration process accounts for inaccuracies in the entire system except from the antennas. The phase differences in both Tx- and Rx-antennas are believed to be constant over time, but fundamentally unknown without proper characterization. The antennas were brought to the anechoic chamber belonging to the Norwegian Defence Logistics organization and measured in all relevant frequency bands. A portable Rhode & Schwartz FSH4 network analyzer was used in the process.

(a) Tx-antenna tilted 45° (b) BirdRAD antenna

Figure 6.12: Characterization of antenna in anechoic chamber

Figure 6.12(a) shows the antenna used for transmission during the measurements. This was a horn covering both L- and S-band and was tilted 45°relative to the horizontal plane to launch an E-field with equal horizontal and vertical components. Figure 6.12(b)shows the antenna under test. The phase of both the horizontal and vertical ports on the antenna under test was registered in both frequency bands, and the relative phase calculated from those measurements. Table 6.3 shows the

Band	Tx polarization	Rx polarization	Phase difference [°]
L	H	V	146
L	V	H	170
L	V	V	-24
S	H	V	-168
S	V	H	-160
S	V	V	-8

Table 6.3: Phase corrections.

results and phase corrections to be used in the final step of system calibration.

6.7 Summary

The BirdRAD system has been developed to collect data for off line verification of the electromagnetic modeling and the signal processing schemes suggested in this thesis. The hardware design is not claimed to be novel. However, fully polarimetric radars operating in both L-and S-band are not commercially available and needed to be developed specifically. Traditional pulse-Doppler waveforms are used to mimic a classification mode of a future long range air defence radar system.

Both flexibility and sensitivity were important factors in the system design. The use of arbitrary waveform generators and linear power amplifiers provide the ability to transmit practically any waveform within the air defence radar frequency bands. LOs with good phase noise characteristics and low noise factors in all receiver channels ensured sensitivity for detecting low flying, slow moving and low RCS targets.

In order to investigate the potential for using coherent polarimetric parameters for classification, the BirdRAD was designed as a fully polarimetric system. This complicated the design and increased the need for proper calibration. The system was characterized by loop-back measurements prior to every data collection, and equalization of all channels in terms of amplitude and phase was done by post processing. Calibration of absolute RCS has been of secondary interest, however, a helium filled calibration balloon specially designed for the purpose was used and enabled rough calibration.

Chapter 7

BirdRAD measurements

This chapter describes the most important radar measurements carried out during the project. These were done with the tailor-made BirdRAD system presented in Chapter 6. Focus is put on detailing relevant aspects of the campaigns such as measurement set up, targets involved and the outcome in terms of signatures added to the database.

7.1 Measurement overview

The BirdRAD measurements were done during two main campaigns. The first one were conducted in April 2015 at Smøla, a bird rich island in the north western part of Norway. The main objective of this campaign was collecting signatures of large sea birds. Around two minutes of high quality data of single sea eagles and black-backed gulls were collected during two days. As mentioned before, gathering data of wild birds require patience. The other campaign was carried out at Ydersboth south east of Oslo in mid April 2016. During these days collections of five UAVs and four new large bird species were added to the database.

Although the measurements were done one year apart, the system setup was very much the same. Except from an unfortunate error in the L-band power amplifier during the 2015 campaign, limiting results to S-band, the data is very similar and the campaigns are therefore covered jointly.

Figure 7.1: BirdRAD at Smøla April 2015.

7.2 Measurement setup

The system was installed in and operated from a van during both campaigns as illustrated in Figures 7.1 and 7.2. The antennas were installed together with a video camera on top of the pan-tilt device on a pedestal three meters away from the car.

Figure 7.2: BirdRAD at Ydersbotn April 2016.

Although having great flexibility in terms of pulse- and wave-forms, all the BirdRAD data used in final analysis was collected with the waveform named *50MHz2mu10kHz* in Table 6.2. This is composed of two millisecond long LFM-pulses transmitted at a repetition frequency of 10 kHz in each polarization channel. The high PRF is beneficial for pulse integration and minimizing the time between horizontal and vertical polarized pulses being transmitted. The time between alter-

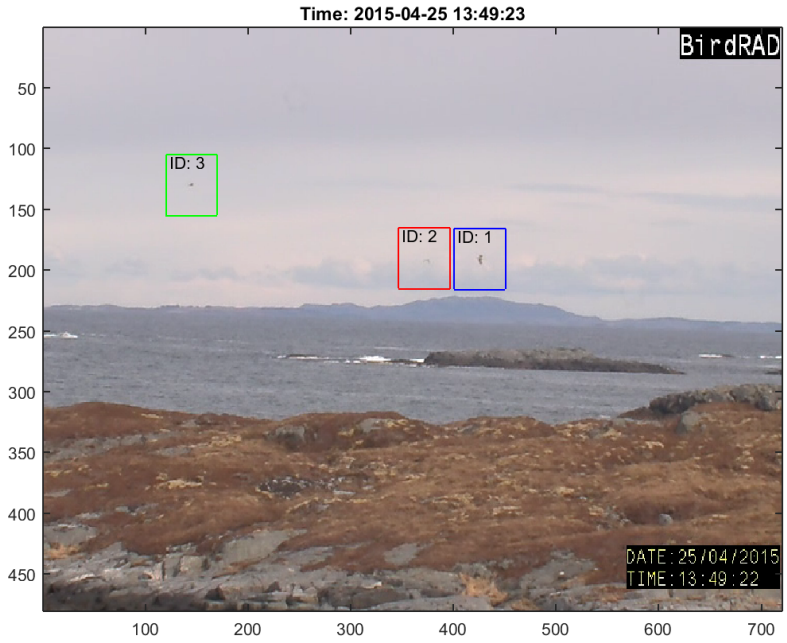

Figure 7.3: Three sea eagles during data collection.

nating pulses is in this way limited to only 50 μs. The resolution in range was 3 m and 8°in both azimuth- and elevation-angle during S-band operation. In L-band the range resolution was the same, but using the same antenna the azimuth and elevation-angle now increased to 15°. The data collections were done by tracking single targets manually in angle by use of the video camera aligned with the antenna. These targets were later isolated by signal processing in range and velocity for further analysis as presented in Chapter 8.

7.3 Targets

The targets covered by BirdRAD data collections consisted of both birds and small unmanned aircraft. Whereas collecting bird signatures is a highly time consuming activity, the challenge with UAV measurements was mainly connected to finding a relevant selection of models, and an authorized location and trained pilot to operate them. The final selection of birds and UAVs are considered to be relevant and suitable to illuminate the research questions.

7.3.1 Birds

The bird signatures originate from six large bird species, however, several individuals of the same kind are covered. These species include crows, mallard ducks, herring gulls, sea eagles and Canada geese. Detailed bird data can be found in [133]. The weight of a grown up crow (*Corvus cornix*) varies between 0.4-0.6 kg and its wingspan is normally in the range 85-100 cm. The mallard duck (*Anas platyrhynchos*) is not necessarily larger with its wing span of 81-98 cm, but heavier with a mass ranging from 0.7-1.6 kg. The herring gull (*Larus argentatus*) is even larger. Its wingspan can range from 125 to 155 cm, but the weight reaches only 0.7-1.5 kg. The sea eagle (*Haliaeetus albicilla*) has the largest wing span of the covered species with values typically between 180-244 cm, however, it is not the heaviest with masses ranging from 4-6.9 kg. The Canada goose is therefore normally slightly heavier with weights in the range 5-7 kg, however, their wing spans are normally not wider than 1.3-1.7 m.

7.3.2 UAVs

Among the aircraft, the quad-copter *DJI phantom II* [130] with 22.9 cm long carbon fiber rotor blades was the smallest of the man-made targets measured. A photo of this model is shown in Figure 5.2(a). The body of this drone is $35 \times 29 \times 21$ cm and the weight is 1.4 kg. The predicted and measured RCS of this drone is nicely presented in [134]. The second smallest quad-copter was the *3DR solo* [135]. This has 24 cm long plastic blades, measures roughly $46 \times 25 \times 25$ cm and has a mass of 1.5 kg. The data collected of these two drones form the basis for the journal paper [136]. Photos of this and UAVs discussed further is found in Figure 7.4. The largest quad-copter measured was the *Ravn*, which is built at FFI. This is heavier than the two others, $80 \times 80 \times 29$ cm large and is equipped with 40.0 cm long carbon fiber rotor blades.

Measurements were also made of two fixed wing aircraft. The smallest of these is the *Multiplex Easystar II* [137]. This is a model aircraft with a 18 cm long push-propeller made of plastic, wing span of 137 cm and a length of 97 cm. The weight is roughly 700 g. The actual model measured is modified by installation of

(a) 3DR solo UAV with black plastic rotors on

(b) Ravn quad-copter UAV

(c) Multiplex Easystar II fixed wing UAV

(d) Discovery model aircraft

Figure 7.4: Four of the man-made targets measured with BirdRAD.

an autopilot to make it fly like an UAV. The largest fixed wing model is the *STM Discovery Trainer* [138] model aircraft. This was controlled manually and has a 26.0 cm long propeller made of plastic material. This model weighs 1250 g and has a wing span and length of 146 cm and 122 cm respectively.

7.3.3 Bird measurements

Measurements of wild birds were gathered during the Smøla and Ydersbotn campaigns. The resulting data were grouped into two classes. One covering signatures from flapping birds, from now on referred to as class *A*. The other class contains measurements of soaring individuals and is defined as class *B*. This grouping was based on observation of the birds' activity in time synchronized video. A rough visual estimate of the aspect angle, as defined in Figure 7.5, was also recorded from the video. Each bird species is considered to cover most azimuth angles throughout the dataset, however, estimating the aspect angle to a small object at some range based on video is surprisingly difficult.

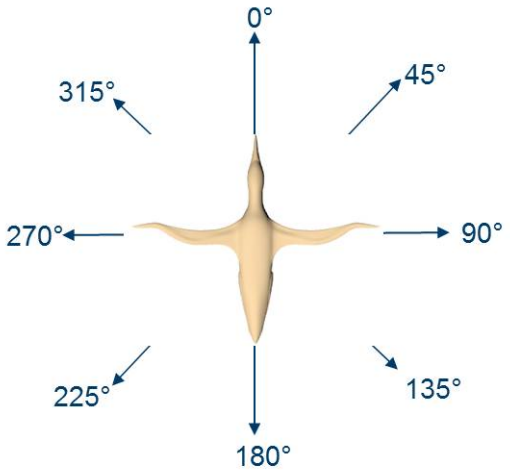

Figure 7.5: Bird aspect angles.

The visual difference between the classes is naturally connected to the presence of rotational wing movement. In terms of classification based on radar signatures, Doppler shifts from wings may be a distinctive feature for separating birds and man-made targets of similar size. In the case of a gliding bird without any rotational wing movement, the measurable Doppler bandwidth is expected to be insignificant in a practical air defence system. However, the lack of wing movement may have further consequences for classification. Potentially systematic RCS fluctuations suggested for classification may also be affected.

7.3.4 UAV measurements

The measured UAVs are divided into two classes. Class *C* includes UAVs with conductive rotors or propellers, whereas class *D* hold UAVs with non-conductive propellers or rotors.

The two platforms Ravn and the Multiplex Easystar II were equipped with inertial navigations systems (INS) and operated in an autonomous mode following predefined tracks. The actual trajectories flown in a north-east coordinate system with BirdRAD in the origin are seen in Figure 7.6. From the registered orientations of the UAVs in their local coordinate systems, the actual orientations relative to the radar were calculated. Figure 7.7 shows the results. In azimuth all angles are covered for both aircraft, although some angles are covered more frequently due to the

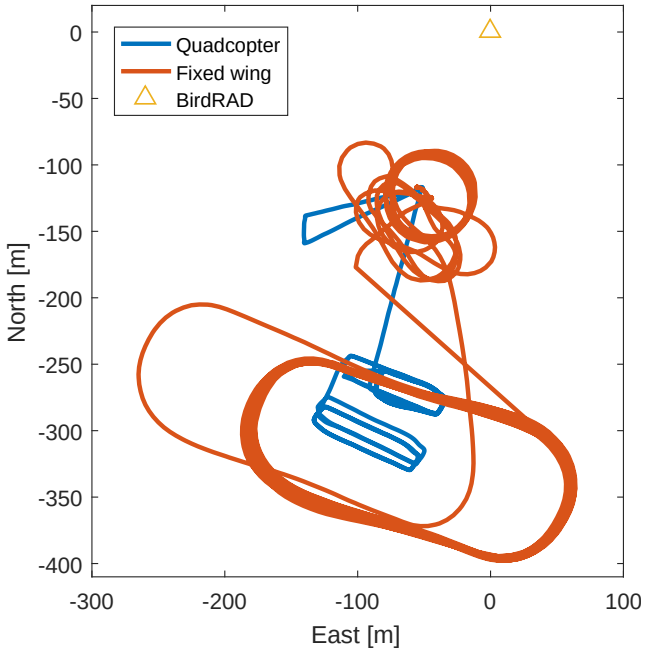

Figure 7.6: GPS tracks of quadcopter Ravn and fixed wing Multiplex Easystar II.

racetrack pattern flown. In elevation there is a predominance of negative angles due to the platforms being elevated around 80 m above the radar during collection. The span of values is seen to be different between UAVs, which is a result of the different flight dynamics between a quadcopter and a fixed wing aircraft. The orientations of the *STM Discovery trainer* were not recorded. However, the aircraft did maneuver quite heavily during data collection and at least all azimuth angles were covered.

7.4 Database

All collections done with the BirdRAD systems were organized in a database. This consists of three main tables. The first holding information on all radar settings and contextual information for all datasets. The second contains information about all detected targets within the data. This is data such as signal strength, range, estimated RCS, target id, aspect angle if determined etc. The last table contains the features extracted from target signatures. All tables are linked, such that all the information related to a signature can be easily extracted. This way of organizing data is key to keeping a record of large amounts of signatures, sorting them and quickly extracting data after certain criteria.

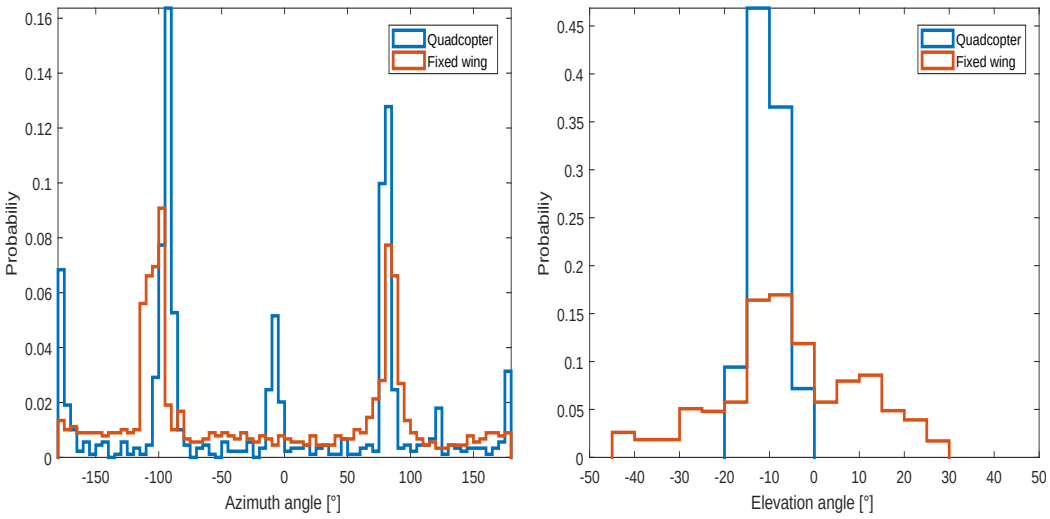

(a) Azimuth angles (b) Elevation angles

Figure 7.7: Distribution of orientation angles of UAVs relative to radar during data collection.

Class	Type	Frequency band	Duration [s]
A	Sea eagles	S	52
A	Black-backed gulls	S	63
A	Crows	L&S	29
A	Mallard ducks	L&S	27
A	Herring gulls	L&S	85
A	Canda geese	L&S	16
B	Sea eagles	S	26
C	DJI Phantom II	L&S	28
C	Ravn	L&S	43
D	3D solo	L&S	33
D	Multiplex Easystar 2	L&S	25
D	STM Discovery Trainer	L&S	72

Table 7.1: Duration of high quality signatures in the database.

The targets collected in the database are found in Table 7.1. This shows class membership, frequency bands covered and total duration of high quality signatures collected of each individual target. Figure 7.8 shows the distribution of velocities and ranges for birds and UAVs relative to the radar. The distribution of velocities are quite similar between the two classes although a slight predominance of birds flying away from the radar is observed. In range there are larger differences between the classes. The majority of UAVs measurements are made at short ranges less than

400 meters, whereas the distribution of bird measurements is more uniform out to 1200 meters.

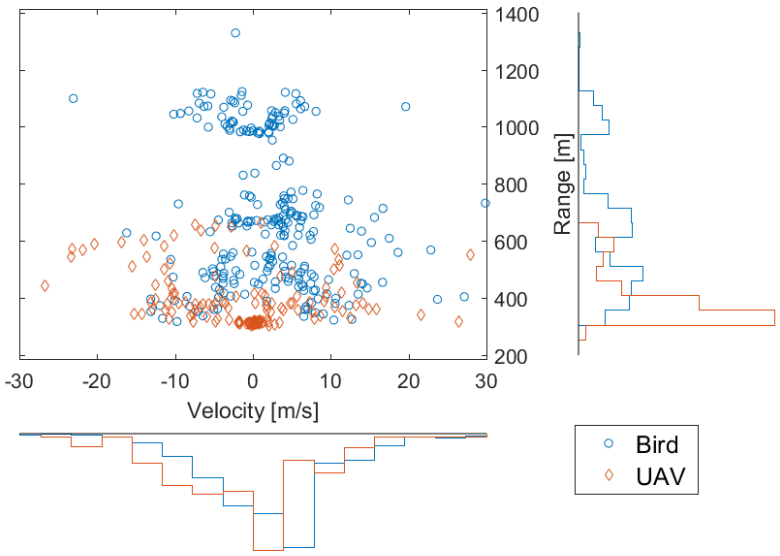

Figure 7.8: Range and velocities of targets covered in the database.

The targets are as presented divided into four classes depending on signature characteristics. One key difference between the all four classes is expected to be found in the Doppler spectra, as class *A* and *C* are associated with micro-motion measurable with radar under the right circumstances. Class *B* and *D* are not expected to have such rotational motion detectable by radar and are therefore believed to be the two classes most difficult to separate by more traditional means.

7.5 Summary

This chapter describes measurements carried out with the tailored BirdRAD system during the project. The data resulting from this is fully polarimetric and simultaneous L- and S-band measurements are considered useful for investigation of the research questions and hypotheses presented in this thesis. Features extracted from signatures of six birds species and six UAV targets were gathered and stored in a database for quick access and filtering on certain criteria. In total close to nine minutes of high quality small-target radar signatures were collected during two main

measurement campaigns.

Chapter 8

Signal processing

This chapter presents signal processing applied to BirdRAD recordings all the way from demodulation and compression, to signature analysis, feature extraction, and classification. Although the described approach is specifically described for BirdRAD data, the main processing steps applied to the initial measurements presented in Chapter 5 are identical. All major processing steps are covered for reproducibility, however, the focus is on methods being novel, adapted, or in any way non-standard.

8.1 Overview

All signal processing presented in this chapter is done by post processing in the commercial software package *Matlab* [139]. Several graphical user interfaces (GUI) have been developed to facilitate the processing at different stages. Figure 8.1 shows the four main packages and how they are connected to a database keeping track of measurements, targets and signatures. Data from BirdRAD is stored in a simple self defined binary data format, which for each transmitted pulse holds information about the number of range samples collected for that pulse, the actual raw digitized samples, time stamp from the GPS-receiver and the polarization of the transmitted pulse. The range samples are demodulated, compressed and merged with contextual information about the waveform used, sensor position and a description of the target and environment. The data resulting from this process is stored in a high level data format for efficient access. This process is done in the

BirdRADtransfer GUI, and is with the exception of typing in comments, fully automatic.

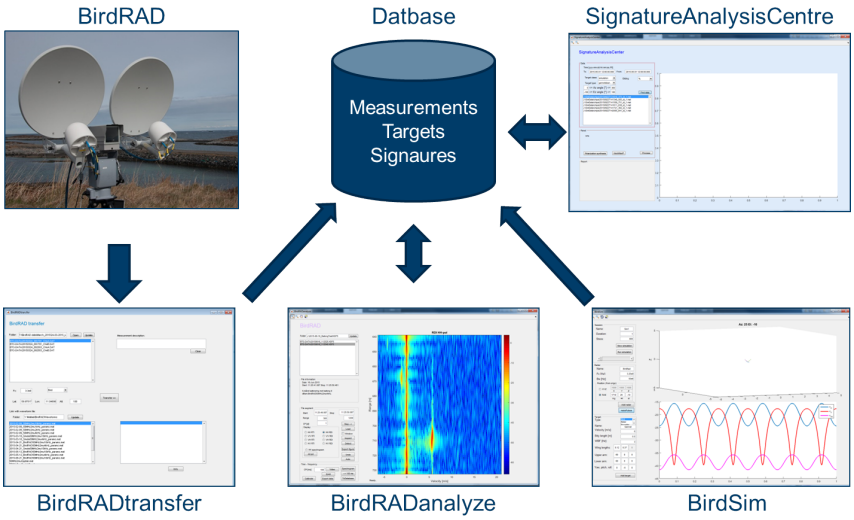

Figure 8.1: Software packages developed for processing of BirdRAD data. Both real and simulated data can be used as input to the processing chain.

The BirdSim GUI offers an alternative source of data. This is simulated data, stored in the BirdRAD high level data format, based on kinematic point scatterer models. Models available include one rotor/propeller model and a bird model with flapping, sweeping and twisting wing movements. Data resulting from these models was mainly used for testing of the processing chain and getting familiar with the nature of simple polarimetric μ-Doppler signatures from dynamic targets. This package is not used directly in the research and thus is not described further.

The next processing step is target detection and establishing signatures forming the basis for feature extraction. This is all done in the *BirdRADanalyze* GUI. Detection is done manually by a mouse click on the target in the range-Doppler image available. This step is followed by a reconstruction of the target's time domain signal, which is then compensated for translational movement and stored on a server in the Matlab *.mat* file format. Contextual information is uploaded to the database. The final steps of processing are done in *SignatureAnalysisCentre*, which is a GUI used for communication with the database, statistical analysis, feature extraction and classification.

8.2 Demodulation and compression

The transmitted signal during all measurements consisted of LFM pulses. These were generated in the AWGs at a center frequency f_{if}, with an amplitude A, and a chirp rate $\gamma_c = \frac{B}{\tau_p}$. Here B and τ_p are the modulation bandwidth and the pulse length respectively. The pulse repetition frequency is denoted f_{prf}. Such a signal can according to [140] be described as function of the fast time variable t_f and pulse number n as

$$s_{if}(n,t_f) = A\, rect(\frac{t_f - n/f_{prf}}{\tau}) e^{j(2\pi f_{if} t_f + \pi\gamma_c (t_f - n/f_{prf})^2)} \tag{8.1}$$

This signal s_{if} is common to all transmitted polarizations and carrier frequencies in the system. The pulse is then mixed up from the intermediate frequency f_{if} to the RF carrier frequency f_c to be used for that pulse, before being mixed down to f_{if} again in the relevant receiver channel by the stable LO described in Chapter 6.3.1.

The received and delayed version of s_{if} reflected from a point scatterer in the scene at range r_t can be written in the form

$$s_r(n,t_f) = a_t\, rect(\frac{t_f - n/f_{prf} - 2r_t/c}{\tau}) e^{j(2\pi f_{if} t - 2k r_t(n) + \pi\gamma_c (t_f - n/f_{prf})^2)} \tag{8.2}$$

where the wavenumber $k = \frac{\omega_c}{c}$, a_t is a variable proportional to the point scatterer's RCS σ_t and c is the speed of light in free space. At this stage $s_r(n,t_f)$ is digitized and the digital signal processing can begin.

8.2.1 Demodulation

As discussed in Chapter 6.3.3 the received signal is undersampled. This provides a direct IF to digital conversion, where the desired band limited spectrum folds into the baseband. This is an increasingly more common way of avoiding the traditional analog quadrature detector, and thereby reduce the number of hardware components and potential errors associated with amplitude and phase imbalance introduced by an extra mixer stage [141].

Although Equation 8.2 shows $s_r(n,t_f)$ as a complex exponential function, the digitized signal is actually real valued and the complex representation is accomplished in a demodulation stage. This basically includes three steps: *down conversion*, *low-pass filtering* and *decimation*. Multiplication with an exponential function mixes the signal to be centered at 0 Hz. Unwanted images are removed by a finite impulse response (FIR) band-pass filter and the sample rate is decimated by a factor four to reduce the amount of data. After forming a complex baseband representation, the received signal is ready for pulse compression.

8.2.2 Pulse compression

Although the pulse compression could be implemented in FPGA, BirdRAD is an offline system and the compression was done in *Matlab*. The reason for this is primarily the possibility of redoing the pulse compression with different matched filters after digitization. The downside is significantly increased time consumption. However, the demodulation and pulse compression were done in a separate processing step in the software *BirdRADtransfer*, from which the results were stored in the *HDF5* data format for efficient access. Subsequent processing was performed on range compressed data by efficiently looking up the subset of interest in the *.HDF5* file.

A classic implementation of the pulse compression of the received signal $s_r(n,t_f)$ can according to [142] be done as

$$G(n,\omega) = S_r(n,\omega)S_t^*(n,\omega) \tag{8.3}$$

Here $S_r(n,\omega)$ and $S_t(n,\omega)$ are the frequency domain representations of $s_r(n,t_f)$ and $s_t(n,t_f)$ respectively, and $G(n,\omega)$ is the compressed output. One specific advantage of the post processing approach is the possibility to adapt the matched filter to the system hardware channel by replacing $S_t(n,\omega)$ in Equation 8.3 with a measured spectrum $S_{ref}(n,\omega)$. This is described in Chapter 6.5. This small adaptation was done to the data based on recordings from the calibration routine. The data was then stored as complex range profiles calculated by an inverse fast Fourier transform

(IFFT) of $G(n, \omega)$ along the frequency dimension.

8.3 Target signature formation

Detection, signature and feature extraction were performed in the dedicated software package *BirdRADanalysis*. This has a graphical user interference and its purpose is to enable effective detection of targets, extract features needed for further classification and store these in the database. Examples of processing steps covered in this section are shown in Figure 8.2, and explained below.

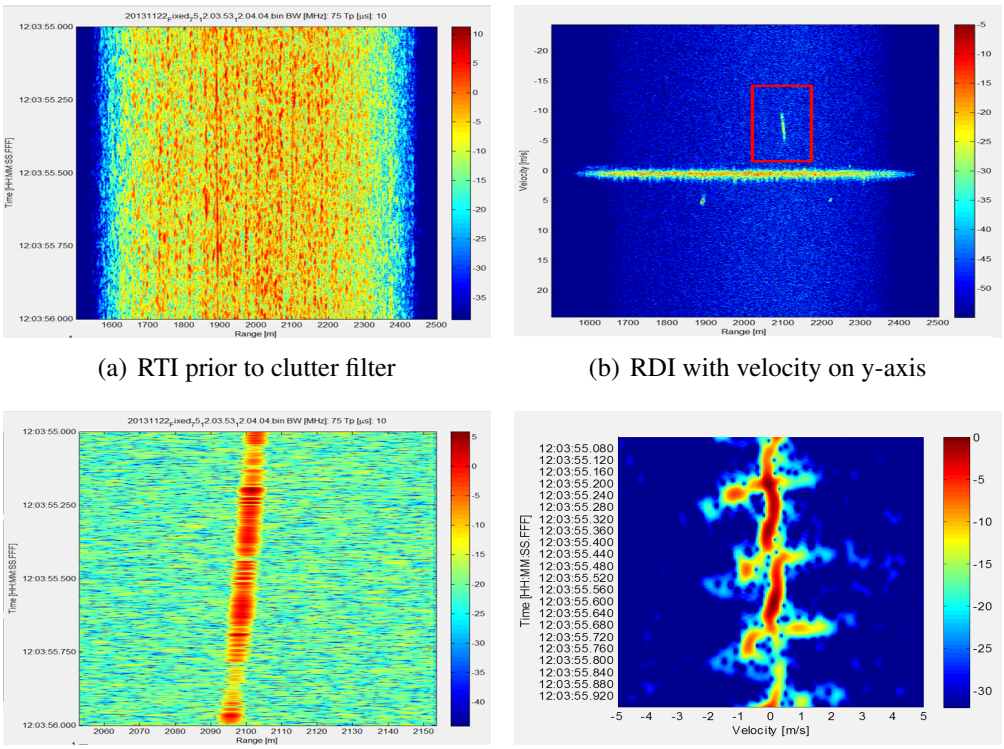

(a) RTI prior to clutter filter

(b) RDI with velocity on y-axis

(c) RTI after clutter filter

(d) Spectrogram

Figure 8.2: Different processing steps for signature extraction in the form of screenshots from the processing software. The target is a flapping gannet measured with PicoSAR in X-band.

8.3.1 Detection

Figure 8.2(a) shows range profiles for one second of data prior to any clutter filtering. In this case the birds present in the scene are buried in sea clutter. A FFT along the time dimension completely changes the detectability of the three birds, as can be seen in the range-Doppler intensity (RDI) image in Figure 8.2(b). An

automatic detection algorithm was implemented, however, in order to associate the correct echo with the target observed in the video, the detection was normally done manually.

8.3.2 Target time signal reconstruction

After selecting a target for further analysis in the range-Doppler domain, its time domain signal was automatically reconstructed. This could be done by isolating the target in range and Doppler with a small margin and performing an IFFT along the Doppler dimension to form a range time intensity (RTI) image. However, this approach was not used. The target was cut out with a couple of meters margin in range, but in Doppler only a high-pass ground clutter rejection filter was applied to the data prior to the IFFT. This provided equal noise bandwidth to all signatures in each band, ensuring the best comparison between signatures. This led to data containing several targets at the same range being excluded from further processing although being separable in velocity. The filter was implemented in the form of a FIR filter designed to suppress moving scatterers up to a velocity threshold $v_c =$ 1 m/s common to both L-and S-band. This required implementation of filters of different length in the two bands. However, the different delay resulting from this difference was compensated for.

Prior to transformation into the RTI domain, an interpolation along the range dimension was performed to reduce the effect of potential straddling loss and improve accuracy of range tracking introduced later in this chapter. Calibration coefficients were also applied at this stage to provide rough absolute RCS values. Similarly the phase correction coefficients provided in Table 6.3 were applied to enable measurement of meaningful δ_{vh} values and hence fully polarimetric exploitation of the data.

Figure 8.2(c) shows the target, inside the red box in Figure 8.2(b), after reconstruction in the RTI-image. The target is associated with translational velocity irrelevant for further feature extraction. This movement was compensated for in order to be left with the micro-Doppler signature from target parts like rotors, propellers and bird wings, and to better compare signatures at a later stage. The back-scattered

energy from the target body or fuselage will then be found in the DC-line of the RDI. The compensation of translational velocity was done in two steps.

The first step consisted of alignment of range profiles. As always one single target was isolated, the target is generally easy to track in the RTI-image. In data with several polarizations available, this tracking was carried out on the incoherent sum of data from all polarization channels. This counteracts the influence of fluctuation and improved tracking over single polarized data. The resulting range difference between subsequent pulses $\Delta(n)$ was described by a low order polynomial $p_t(n) \approx \Delta(n)$ and used to align the range profiles in a continuous manner by the Fourier transform shift property [143] as

$$\hat{g}(n,t) = \mathscr{F}^{-1}\left\{G(n,\omega)e^{-j\omega p_t(n)}\right\} \tag{8.4}$$

Here $\mathscr{F}^{-1}$ denotes the inverse Fourier transform and $\hat{g}(n,t)$ denotes the range aligned RTI-data. The isolated target time domain signal was now found in the aligned range samples as $s(n) = \hat{g}(n,t_t)$, where t_t corresponds to the target range.

The last step of the target time signal reconstruction was motion compensation to remove the Doppler shifts originating from translational velocity. This was done by tracking the body or fuselage component of the μ-Doppler signature in the joint time-frequency domain. The time-frequency representation selected was the *spectrogram*. This is a frequently used time-frequency transform revealing the instantaneous frequency content of a nonstationary signal such as $s(n)$. According to Chen [54] this can be formed as the square of the short time Fourier transform (STFT). The spectrogram was implemented as

$$S(m,\omega_d) = \mathscr{F}\left\{s(n)w(n-m)\right\} \tag{8.5}$$

where $S(m,\omega_d)$ is the spectrogram, $\mathscr{F}$ denotes the Fourier transform, ω_d is the Doppler shift and w is an analysis window centered at time m non-zero within its duration τ_w and zero elsewhere. In this thesis a *Hamming* window is used, providing a main lobe broadening factor of only 1.5, and yet a sidelobe level giving the

required dynamic range. The duration of this window τ_w is also later referred to as the coherent processing interval (CPI) or dwell time τ_d interchangeably. Note that the spectrogram has a time extent that is shorter than the original time signal, as this is truncated by half a window length in each end.

Several strategies for tracking the body components in $S(m, \omega_d)$ were tested. The final solution was to track the Doppler-cell with the highest intensity for each pulse to get $\omega_b(m)$ and assign a low order polynomial $p_b(m)$ to the resulting track to avoid abrupt Doppler frequency changes associated with rotational velocity. Subscript b here indicates *body*. This generally corresponded well with what was considered to be the translational velocity component. This polynomial was now used to compensate for the translational motion as of the time domain signal $s(m)$ as

$$s(m) = \hat{s}(m) e^{j \int_0^m p_b(k)\, dk} \tag{8.6}$$

$$\hat{s}(m) = s(m) e^{-j \int_0^m p_b(k)\, dk} \tag{8.7}$$

Here $\hat{s}(m)$ is the desired translational motion compensated time signal, and the phase of the correction signal is found as the cumulative integral of the estimated Doppler frequency represented by $p_b(m)$.

After application of calibration coefficients, this time signal is an estimate of the target RCS over time and $|\hat{s}(m)|^2 e^{j\phi(m)}$ is from now on referred to as $\sigma_{rt}(t)$, where subscript r and t denotes the polarization of received and transmitted signal respectively, t is the new slow time variable and $\phi(m)$ is the phase of $\hat{s}(m)$. The signal was at this processing stage saved to disk. Metadata such as target type, aspect angle, SNR, target behavior, velocity and acceleration were stored in the database. Identical processing was applied to all polarizations available. This ensured that no mutual differences in terms of amplitude or phase were applied to the different channels.

8.4 Spectral estimation

The motivation for introducing spectral estimation is linked to the wish of detecting micro-motion in the form of frequency shifted echoes from rotating target parts. These are referred to as micro-Doppler signatures. In this thesis the spectral content is estimated by use of the FFT, which is a classic approach to spectral analysis. This is used to both form periodograms for evaluation of the power spectral density (PSD) as already shown for calculation of the spectrogram.

8.4.1 The periodogram

The PSD can according to [144] be calculated in form of a periodogram as

$$\phi_{rt}(\omega_d) = \lim_{N\to\infty} E\left\{ \frac{1}{N} \left| \sum_{t=1}^{N} \sqrt{\sigma_{rt}}(t) e^{-j\omega_d t} \right|^2 \right\} \tag{8.8}$$

This definition shows that the PSD is calculated as the DFT of the signal. However, an unlimited number of samples is strictly required in order to calculate the PSD. This is naturally unachievable in a practical scenario, however, an estimate $\hat{\phi}_{rt}(\omega_d)$ can still be made for limited numbers of N. One consequence of limiting N is the limited spectral resolution associated with the DFT, which according to [144] equals $\Delta\hat{f} = 1/N$ measured in normalized frequency [cycles/sample]. As $f = \hat{f} f_s$, the frequency resolution measured in Hz is given as

$$\Delta f = \frac{f_s}{N} = \frac{1}{\tau_d} \tag{8.9}$$

where τ_d is the observation or dwell time in seconds. This is an important observation with practical consequences as τ_d is always limited in a radar system and determines the minimum frequency difference two scatterers with identical RCS must have in order to be resolved in frequency. As the periodogram is generally applied to non-stationary signals throughout this thesis, the output is interpreted more as a time averaged power spectrum or energy spectral density than a true power spectral density.

8.4.2 Velocity resolution

If Equation 8.9 is combined with an expression for the Doppler frequency shift from a scatterer moving radially at velocity v, the velocity resolution measured in m/s can be derived as

$$\Delta v = \frac{\lambda \Delta f_d}{2} = \frac{\lambda}{2\tau_d} \tag{8.10}$$

This reveals that the velocity resolution is dependent both on the wavelength λ and the observation time τ_d. If the length of the periodogram or window length τ_w in the spectrogram is equally long in L- and S-band, this will lead to different velocity resolution achieved in the two bands. Figure 8.3 illustrates the achievable resolution as function of eight dwell times τ_d investigated throughout this thesis.

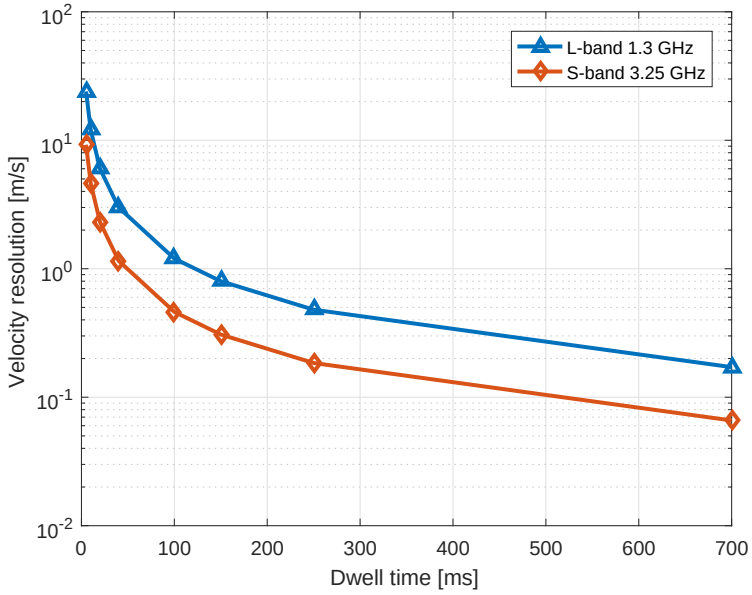

Figure 8.3: Velocity resolution for selected dwell times τ_d of 5, 10, 20, 40, 100, 150, 250 and 700 ms.

The achieved resolution in S-band, shown by the red line, is found to be significantly better than in L-band indicated by the blue line. Note that the y-axis is logarithmic in order to handle the great span in values.

8.4.3 Extraction of measures associated with micro-motion

Such velocity resolution is utilized to investigate several parameters associated with rotational parts such as bird wings, UAV propellers and rotors, in the form of peri-

dograms and spectrograms of the reconstructed time signal compensated for translational movement. Features used in the automatic classification approach implemented to address research question number one in Chapter 1.5 are resolved in either time or velocity. The velocity resolution is achieved by applying the periodogram over τ_d. For $\tau_d \leq 250$ ms, the translational velocity shift is compensated for by a linear phase shift only, as no trustworthy higher order velocity estimates can be made on such short signals. The spectrograms are formed to visualize the joint-time frequency distribution of different non-polarimetric and polarimetric parameters, as well as to investigate distributions of such between the target body/fuselage and rotational parts. This is done to highlight what information is available in target signatures formed over longer observation times, and hence addressing research question number two.

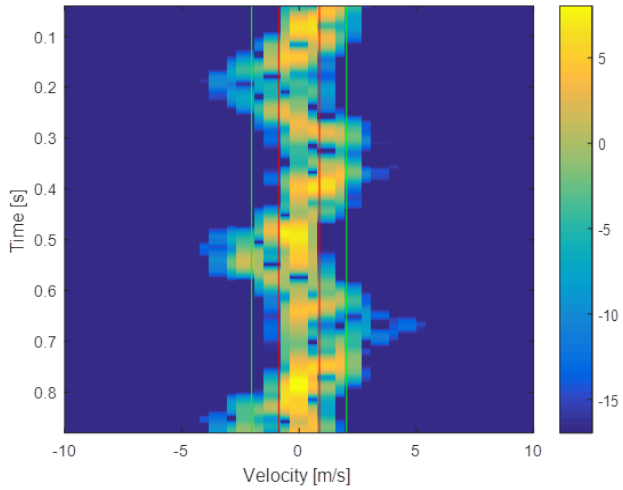

Figure 8.4: Spectrogram of flapping sea eagle. σ_{hh} in S-band. τ_d=150 ms. Colours indicate uncalibrated power values. Epoch: 2015-04-25 14:00:44.000.

Figure 8.4 shows an example of a spectrogram based on σ_{hh} of a flapping sea eagle. Such a spectrogram has been used to estimate the parameters associated with different target parts. By setting a velocity threshold like the red or green vertical lines, and identifying the intervals of the sequence where bird wings or rotors/propellers are resolved in velocity, an estimation of the energy associated with such target parts can be made. Power from velocities below the threshold is considered to originate from the body or fuselage, whereas power from micro-

motion above the thresholds on each side is associated with rotational target parts. A time-domain reconstruction after detection in the joint time-frequency domain can be done in the form of an inverse spectrogram, as described in [145]. However, the selected approach was based on summing up the power in the desired regions directly.

8.5 Extraction of features for classification

As already introduced, a selection of features for automatic separation between birds and UAVs were extracted from signatures provided by methods presented in previous sections. These were all based either on time- or velocity-resolved signatures. Joint time-frequency representations may hold useful information, but as the focus is on short dwell times such representations are used for visualization only.

8.5.1 Spectral features

In total 11 features were extracted from the Doppler spectrum $\hat{\phi}_{rt}(\omega_d)$ compensated for translational velocity. These include eight spectral moments, four based on HH-measurements and four on VV. In addition the power associated with the target body was compared to the total target power in a parameter referred to as *body to total power ratio*. This was calculated for HH-, VV- and σ_{dr}-data in the form of B_{hh}, B_{vv} and B_{dr} respectively.

8.5.1.1 Spectral moments

Spectral moments provide valuable parameters for characterization of the compensated Doppler spectrum $\hat{\phi}_{rt}(\omega_d)$. The first and higher order moments are calculated according to [146] as

$$m_1 = \frac{1}{m_0} \int_{\omega_1}^{\omega_2} \omega \, \hat{\phi}_{rt}(\omega) \, d\omega \tag{8.11}$$

$$m_n = \frac{1}{m_0} \int_{\omega_1}^{\omega_2} (\omega - m_1)^n \hat{\phi}_{rt}(\omega) \, d\omega \tag{8.12}$$

Here the second and higher order moments are seen to be the central moments around the first spectral moment m_1 which is the mean frequency. m_0 is the total power in the signal, and ω_1 and ω_2 are the lowest and highest frequency component detected respectively. The second to fourth order spectral moments can be interpreted as the *variance*, *skewness* and *kurtosis* of the spectrum. Of particular interest is the mean frequency and variance, as these give information of spectral center of gravity and spectral width which is believed to be different, for example, between flapping bird wings and rotating UAV rotors.

8.5.1.2 Body to total power ratio

The *body to total power ratio B* is a parameter calculated as

$$B_{rt} = \frac{\int_{-2\Delta_{\omega_d}}^{2\Delta_{\omega_d}} \hat{\phi}_{rt}(\omega)\, d\omega}{\int_{\omega_1}^{\omega_2} \hat{\phi}_{rt}(\omega)\, d\omega} \tag{8.13}$$

Here Δ_{ω_d} is the Doppler frequency resolution given by τ_d. The idea behind this parameter is that the portion of power back-scattered from a target's body or fuselage can vary between classes. Short dwell times and low carrier frequencies will naturally limit the usefulness of this feature as the resolution may not always be high enough.

8.5.1.3 Periodic RCS modulations

In an attempt to reveal periodicity associated with RCS modulations in the time domain, a periodogram was formed of $|\sigma_{rt}(t)|$. The first method applied to detect potential periodicity was based on identification of any fundamental frequency f_{0rt} as

$$f_{0rt} = \underset{f_{0rt}>0}{\operatorname{argmax}}(\mathscr{F}\{|\sigma_{rt}(t)|\}) \tag{8.14}$$

As long as f_{0rt} is above a certain threshold, a periodicity is identified. This method does not utilize potentially higher order harmonics in the spectrum. This is done by the methods based on cepstral analysis suggested in Chapter 8.5.3.

8.5.2 Time domain features

The only non-polarimetric feature extracted from the time domain data directly was the ratio between the maximum and mean value of the time series $\sigma_{rt}(t)$ in the interval defined by τ_d.

8.5.2.1 Maximum to mean RCS ratio

The *maximum to mean RCS ratio* is defined as

$$M = \frac{max(|\sigma_{rt}(t)|)}{\overline{|\sigma_{rt}(t)|}} \tag{8.15}$$

Here $\overline{|\sigma_{rt}(t)|}$ denotes the time average of the RCS values. M was calculated for horizontal and vertically co-polarized data in the form of M_{hh} and M_{vv} respectively. This parameter estimates the RCS variability. Typically flashes from rotating propellers or rotors may result in large M, which thus is a characteristic of man-made targets.

8.5.3 Quefrency domain features

Cepstral analysis [147] was also used to determine periodicity. This was inspired by methods covered in Chapter 2.1.8 on classification of μ-Doppler signals. The cepstrum was calculated of both the magnitude and real part of $\sigma_{rt}(t)$.

8.5.3.1 Periodic RCS modulations

Periodic variation in RCS may be a strong feature for classification. The cepstrum of the signal $|\sigma_{rt}(t)|$ was calculated to identify the fundamental rahmonic q_0 connected to the *flash rate* as $\frac{1}{q_0}$[s]. The cepstrum was calculated according to [79] and q_0 identified as the maximum quefrency component as

$$q_0 = \text{argmax}(\mathscr{F}^{-1}\{\log(\mathscr{F}\{|\sigma_{rt}(t)|\})\}) \tag{8.16}$$

8.5.3.2 Periodic modulations of RCS and phase

In addition to calculating the flash rate q_0 from the cepstrum of the magnitude of the time signal $\sigma_{rt}(t)$, q_{0r} based on the cepstrum of the real value of the signal was

also calculated.

$$q_{0r} = \text{argmax}(\mathscr{F}^{-1}\{\log(\mathscr{F}\{\Re(\sigma_{rt}(t))\})\}) \tag{8.17}$$

This measure is strictly not only related to the periodicity of RCS variation, as periodicity in the form of phase modulations contribute as well. This feature is not found to contribute much in the case of birds, however, from the much larger Doppler-shifts associated with rotating UAV parts the feature may be valuable.

8.5.4 Polarimetric processing

The BirdRAD system is capable of measuring the scattering matrix **S** at time t with elements of $\sqrt{|\sigma_{rt}(t)|}e^{j\phi_{rt}}$, from which $\mathbf{S}_{rel}$ can be derived as covered in Chapter 3.5.1. Although **S** is formed by use of two successive pulses, and strictly is a *pseudo scattering matrix*, a short time between successive pulses Δt improves the situation. From Equation 8.2, the phase difference $\Delta\phi$ induced can be found as

$$\Delta\psi = 2k(r_2 - r_1) = \frac{4\pi f_c v \Delta t}{c} \tag{8.18}$$

Here r_1 and r_2 are the distance to the target at a time of receiving echoes from the two successive pulses. With a PRF of 10 kHz in each channel, the time between two subsequent pulses is $\Delta t = \frac{1}{20kHz} = 50\mu$s. Assuming a maximum velocity of $v = 25$ m/s, the polarimetric phase error $\Delta\psi$ then becomes at most 4° in L-band and maximum 10° in S-band. Normally the radial velocity and thus phase error is far less. Although possible, this error was not compensated for in the subsequent processing.

In the further work of describing small targets by $\mathbf{S}_{rel}$, the focus will be on the three magnitudes $|S_{hh}|$,$|S_{hv}|$,$|S_{vv}|$ and the relative phase term $e^{j(\phi_{vv}-\phi_{hh})}$. In order to make all features for classification independent of range and RCS, only differential variables have been suggested. The derivation and physical origin for some of these, like the incoherent differential RCS and linear depolarization ratio, and the coherent differential phase and polarimetric correlation coefficients have already been covered in Chapter 3.5. An explanation of the concepts of polarization

synthesis and polarimetric decomposition is now provided.

8.5.4.1 Polarization synthesis

Access to the complex $\mathbf{S}_{rel}$ enables the possibility to synthesize an arbitrary polarization of both the transmitting and the receiving antenna by post-processing. This technique was here implemented under the limitation of allowing only for co- and cross-polar polarization in the synthesis. This corresponds to the limitations found in the frequently used *polarimetric signature* graphs. According to Boerner et al. [148] polarization synthesis can be calculated as

$$P_{\psi\chi} = S_R K S_T \tag{8.19}$$

where K is the measured Kennaugh matrix as found at page 339 in [148], S_R and S_T are the Stokes matrices $S_{T,R} = [1 \;\; \cos(2\psi)\cos(2\chi) \;\; \sin(2\psi)\cos(2\chi) \;\; \sin(2\chi)]^T$ for the receive and transmit antenna respectively. ψ and χ denotes the inclination and ellipticity angle of the polarization ellipse. Corresponding to this definition, χ ranges from -45° and right hand circular polarization, through 0° and linear polarization to 45° and left hand circular polarization. If χ is kept at 0°, $\psi = 0°$corresponds to linear horizontal polarization and $\psi = 90°$ is associated with vertical polarization.

The polarimetric signature resulting from synthesis with co-oriented transmit and receive antennas was used to investigate if bird wing orientation could be estimated. If bird wings act like dipole scatterers in the Rayleigh region, increased received power will be expected when ψ coincides with the apparent orientation of the wings. Only linear polarizations were studied ($\chi = 0°$). The value of ψ maximizing the received power for all relevant pixels in the spectrogram was calculated. Performing this in a joint time-frequency representation is essential as a pure wing signature with little influence from the bird body can be isolated, at least through parts of the wing beat period.

8.5.4.2 Polarimetric decomposition

Polarimetric decomposition seeks to find a dominant scattering mechanism of a target associated with additive noise and speckle. The returns are in this case not necessarily fully polarized and the decomposition aims at expressing an average scattering mechanism as a sum of independent contributions, which are in turn associated with physical scattering mechanisms. The first target decomposition theorem was formalized by Huynen in [91]. Since then many alternative decomposition techniques have been proposed based on the dichotomy of the Kennaugh matrix, the covariance matrix, the coherency matrix and the scattering matrix directly. In this thesis only the $H/A/\bar{\alpha}$ technique by Cloude and Pottier [149] is investigated. This approach is frequently used in remote sensing, and selected here as it provides parameters independent of dielectric properties and target orientation about the radar line of sight [128].

This method was developed for use in SAR-systems, and application in NCTR of air targets in BirdRAD requires a small adaptation. The theory makes use of the average coherency matrix formed by spatial averages of several pixels in the image to reduce the impact of speckle. As small targets generally occupy one range resolution cell, and no cross-range resolution is present, a spatial average is impossible. However, a dynamic target like a bird or small UAV is subject to temporal variations. Although not equally susceptible to speckle as SAR images, the backscattered signal may still be associated with interference between several scattering mechanisms despite the low size to wave length ratio. This leads to the concept of *distributed targets* discussed by Huynen [91] and thus partially polarized returns. Extraction of the dominating scattering mechanism of a small, potentially distributed target in an air defence radar is suggested to be done by replacing the spatial ensemble average by a time average over the dwell time τ_d. Using the time averaged coherence/covariance matrices is described for meteorological radar in Chapter 3 of [150]. The key idea is that multiple samples of the same process are obtained. This requires stationarity during the observation, which again requires the averaging period τ_d of a bird or UAV to be smaller than any major changes in orientation or pose. Averaging over

dwell times exceeding this may result in extracting an average scattering mechanism not necessarily of value for classification.

The $H/A/\bar{\alpha}$ approach is based on analysis of the the coherency matrix T according to [151] formed as

$$T = \left\langle KK^{*T} \right\rangle \tag{8.20}$$

where K is the *3-D k-target vector* $K = \frac{1}{\sqrt{2}}[S_{hh} + S_{vv} \quad S_{hh} - S_{vv} \quad 2S_{hv}]^T$ and $\langle \ldots \rangle$ originally denotes spatial ensemble average over pixels in the polarimetric SAR image. As mentioned above, this is here suggested to be replaced with a temporal average.

This coherency matrix can according to [149] be parameterized as

$$T = U_3 \begin{bmatrix} \lambda_1 & 0 & 0 \\ 0 & \lambda_2 & 0 \\ 0 & 0 & \lambda_3 \end{bmatrix} U_3^T \tag{8.21}$$

$$U_3 = \begin{bmatrix} \cos\alpha_1 & \cos\alpha_2 & \cos\alpha_3 \\ \sin\alpha_1\cos\beta_1 e^{j\delta_1} & \sin\alpha_2\cos\beta_2 e^{j\delta_2} & \sin\alpha_3\cos\beta_3 e^{j\delta_3} \\ \sin\alpha_1\sin\beta_1 e^{j\delta_1} & \sin\alpha_2\sin\beta_2 e^{j\gamma_2} & \sin\alpha_3\sin\beta_3 e^{j\gamma_3} \end{bmatrix} \tag{8.22}$$

Here U_3 is a unitary matrix with three unit orthogonal eigenvectors and λ denotes the eigenvalues. Three variables resulting from this method are used in the further work. These are the entropy H and anisotropy A, both derived from the eigenvalues, and $\bar{\alpha}$ derived from the eigenvectors, and described below.

The entropy H is a parameter describing the statistical disorder of the polarimetric scattering and can in the mono-static case according to [149] be defined as

$$H = -\sum_{k=1}^{3} P_k \log_3(P_k) \tag{8.23}$$

Here P_k is defined as the pseudo-probability $P_k = \frac{\lambda_k}{\sum_{k=1}^{3} \lambda_k}$. H may have values between 0 and 1. One extreme is the fully polarized returns unambiguously defined by **S**,

resulting in only one nonzero eigenvalue. This corresponds to $H = 0$. The other extreme is a non-polarized echo, resulting in nonzero, identical eigenvalues and $H = 1$. For low entropy values, $H < 0.3$, the dominant scattering mechanism can according to [127] be described by $\mathbf{S}$, as only one eigenvalue really contributes in these cases. In these cases coherent decomposition methods should be applicable. Particularly in the case of class C, UAV targets with short prominent rotor flashes, the entropy is found to be high and decomposition from $\mathbf{S}$ directly is not possible.

The anisotropy value A is complementary to H and describes the relative importance of the second least important and the least important eigenvalue as

$$A = \frac{\lambda_2 - \lambda_3}{\lambda_2 + \lambda_3} \tag{8.24}$$

where $\lambda_1 > \lambda_2 > \lambda_3$. Naturally, the relevance of A increases with increasing H as λ_2 and λ_3 are dominated by noise as long as entropy is low [127].

The last parameter suggested for classification from this decomposition method is $\bar{\alpha}$. This is in [127] defined as

$$\bar{\alpha} = \sum_{k=1}^{3} P_k \alpha_k \tag{8.25}$$

where α_k is derived from the eigenvectors in Equation 8.22. This parameter is independent of the target orientation like A and H and is claimed to be related to the physics of the scattering process. According to Fig 1.12 in [128] α is an element of a spherical triangle on the Poincare sphere, and thus related to the inclination and ellipticity angles ψ and χ covered in Chapter 8.5.4.1. Values of $\bar{\alpha}$ close to 0° indicate surface scattering or specular scattering where the differential phase $\delta_{vh} \neq 180^\circ$ [127]. This includes spheres, flat plates and trihedrals as covered in Chapter 4. $\bar{\alpha}$ close to 45° is associated with dipole scattering, whereas larger values can be related to double bounce scattering such as, for example, echoes from dihedrals.

8.5.4.3 Differential RCS

The concept of differential RCS was discussed in 3.5.3, here defined as

$$\sigma_{dr} = \frac{\langle |S_{vv}|^2 \rangle}{\langle |S_{hh}|^2 \rangle} \tag{8.26}$$

This parameter is independent of phase and may therefore be referred to as an incoherent parameter. A consequence is that a fully polarimetric system as described in Chapter 6 is not required for calculation of this feature.

8.5.4.4 Linear depolarization ratio

The linear depolarization ratio was discussed in Chapter 3.5.4, and is defined as

$$\delta = \frac{\langle |S_{vh}|^2 \rangle}{\langle |S_{hh}|^2 \rangle} \tag{8.27}$$

This variable is like σ_{dr} incoherent and does not require fully polarimetric measurements to be calculated.

8.5.4.5 Polarimetric correlation coefficients

Coherency between polarimetric channels is considered to hold information useful for classification. The magnitudes of this generally complex measure are here referred to as the polarimetric correlation coefficients and are treated in this section. The argument is also known as polarimetric phase difference and is covered in the next section.

The co-polarized and two cross-polarized correlation coefficients can according to [127] be expressed as

$$|\rho| = \frac{|\langle S_{hh} S_{vv}^* \rangle|}{\sqrt{(\langle |S_{hh}|^2 \rangle \langle |S_{vv}|^2 \rangle|}} \tag{8.28}$$

$$|\beta| = \frac{|\langle S_{hh} S_{hv}^* \rangle|}{\sqrt{\langle |S_{hh}|^2 \rangle \langle |S_{hv}|^2 \rangle|}} \tag{8.29}$$

$$|\varepsilon| = \frac{|\langle S_{hv} S_{vv}^* \rangle|}{\sqrt{\langle |S_{hv}|^2 \rangle \langle |S_{vv}|^2 \rangle|}} \tag{8.30}$$

8.5.4.6 Polarimetric phase differences

The topic of polarimetric phase difference was discussed in Chapter 3.5.5. These measures are calculated as the argument of the polarimetric coherence. The actual implementation of the co-polarized and two cross-polarized phase differences can according to [127] be done as

$$\delta_{vh} = \angle\langle S_{hh}\, S_{vv}^{*}\rangle \tag{8.31}$$

$$\angle\beta = \angle\langle S_{hh}\, S_{hv}^{*}\rangle \tag{8.32}$$

$$\angle\varepsilon = \angle\langle S_{hv}\, S_{vv}^{*}\rangle \tag{8.33}$$

Here $\angle$ denotes the angle between the components and $\langle\ldots\rangle$ now denotes time average over τ_d. The averaging is as for the correlation coefficients done over τ_d

8.5.5 Feature extraction recap

A total number of 32 features are in the previous sections suggested for classification. The selection includes parameters that are as general as possible, and measures such as absolute velocity and RCS were deliberately not included.

All features were extracted in the GUI *SignatureAnalysisCenter* for eight selected dwell times τ_d between 5 and 700 ms. Figure 8.5 gives an overview of the feature extraction process. The reconstructed time domain signal $\sigma_{rt}(t)$ is split into four parallel processing chains providing cepstral-, spectral-, time-domain-, and time-frequency-analysis. The last branch based on time-frequency analysis seen in the lower part of the figure is not included in the automatic classification at this stage. This is only used to visualize how different features can be used to identify target behaviour when long coherent data collections are available. The remaining three branches extract signatures for classification. The spectral analysis branch, indicated by the *periodogram* box is split into two for extraction of polarimetric and non-polarimetric parameters. The same applies for the reconstructed time signal. The last processing chain takes care of the cepstral analysis. This is performed for single polarized data only, here defined as parameters collected either at HH- or

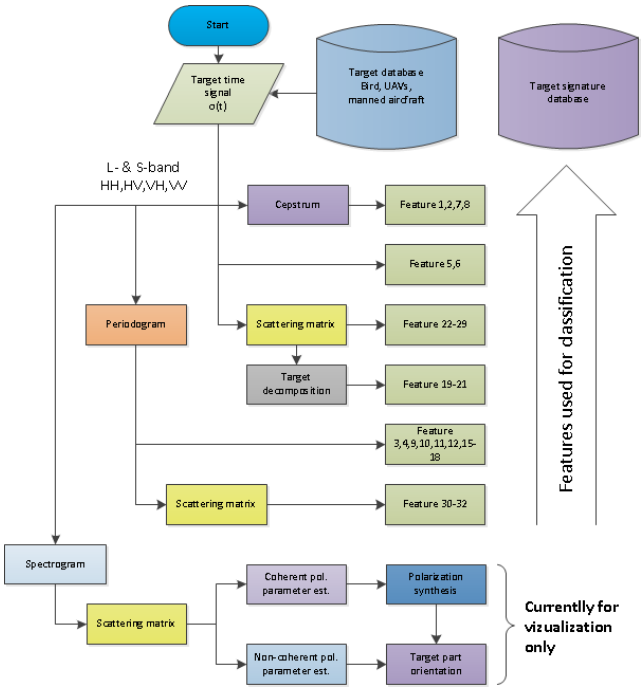

Figure 8.5: Feature extraction from time domain signal $\sigma(t)$.

VV-polarization.

Id	Name	Description	Equation
1	q_{0hh}	Flash rate extracted from cepstral analysis of $\|\sigma\|$	8.16
2	q_{0vv}	Flash rate extracted from cepstral analysis of $\|\sigma\|$	8.16
3	f_{0hh}	Fundamental frequency from spectral analysis of $\|\sigma\|$	8.14
4	f_{0vv}	Fundamental frequency from spectral analysis of $\|\sigma\|$	8.14
5	M_{hh}	Maximum to mean RCS ratio	8.15
6	M_{vv}	Maximum to mean RCS ratio	8.15
7	q_{0rhh}	Flash rate extracted from cepstral analysis of $\Re(\sigma)$	8.17
8	q_{0rvv}	Flash rate extracted from cepstral analysis of $\Re(\sigma)$	8.17
9	Δv_{hh}	Velocity span corresponding to m_2	8.12
10	Δv_{vv}	Velocity span corresponding to m_2	8.12
11	B_{hh}	Body to total power ratio	8.13
12	B_{vv}	Body to total power ratio	8.13
13	S_{hh}	Mean frequency corresponding to m_1	8.11
14	S_{vv}	Mean frequency corresponding to m_1	8.11
15	$m3_{hh}$	Spectral moment of third order - skewness.	8.12
16	$m3_{vv}$	Spectral moment of third order - skewness	8.12
17	$m4_{hh}$	Spectral moment of fourth order - kurtosis	8.12
18	$m4_{vv}$	Spectral moment of fourth order - kurtosis	8.12

Table 8.1: Non-polarimetric features tested for classification.

In the remainder of this thesis the features are grouped into non-polarimetric and polarimetric parameters in order to investigate any benefit from including polarimetric measurement in future systems. The 18 non-polarimetric parameters hold information on time domain periodicities, fluctuation and spectral shape. Table 8.1 gives an overview and reference to the equation used for processing.

A similar overview of the 14 polarimetric features is given in Table 8.2. Parameters found here span from variables holding information on scattering mechanisms and degree of polarization to coherence between polarimetric channels and incoherent ratios between elements in the scattering matrix.

Id	Name	Description	Equation
19	A	Anisotropy	8.24
20	H	Entropy	8.23
21	$\bar{\alpha}$	Polarimetric eigenvector parameter	8.25
22	$\lvert\rho\rvert$	Co-polarized correlation coefficient	8.28
23	δ_{vh}	Co-polarized phase difference	8.31
24	$\lvert\beta\rvert$	Cross-polarized correlation coefficient	8.29
25	$\angle\beta$	Cross-polarized phase difference	8.32
26	$\lvert\varepsilon\rvert$	Cross-polarized correlation coefficient	8.30
27	$\angle\varepsilon$	Cross-polarized phase difference	8.33
28	δ	Linear depolarization ratio	8.27
29	σ_{dr}	Differential polarization ratio	8.26
30	S_{dr}	Mean frequency of σ_{dr} corresponding to m_1	8.11
31	S_δ	Depolarization mean frequency measure	8.11
32	B_{dr}	Differential body to total power ratio	8.11

Table 8.2: Polarimetric features tested for classification.

8.6 Feature selection

The next major step is to evaluate the usefulness of the suggested features for classification. The ultimate goal is to identify those that can provide separation between birds and UAVs. In particular, will polarimetric measurements be worth the increased expense?

Depending on the number of parameters to choose from, different approaches for feature selection can be used. PCA and SVD are well-known methods for reduction of dimensionality in classification problems. These transform the data into

a new feature space with reduced dimensionality. The classification is then carried out in this new space. In order to easily link the classification performance to physical parameters, all classification presented in this thesis is done in the original feature space with no transformation applied. Instead feature selection was applied to the extracted features directly. Some alternative approaches were evaluated.

8.6.1 Exhaustive search

The intuitive way ahead would be to check how all combinations of available features perform in a classifier. Figure 8.6 shows the challenge with this approach as the number of features increases. The numbers in the figure are based on all of the data available in the data base and implementation of a simple classifier in Matlab running on a standard modern desktop computer. The problem is that adding one parameter doubles the processing time. A maximum number of 17 parameters is considered to be the practical limit as the process is repeated for each dwell time τ_d and frequency band evaluated. This is still high as the total time consumption in this case would be roughly one week for eight dwell times and two frequency bands.

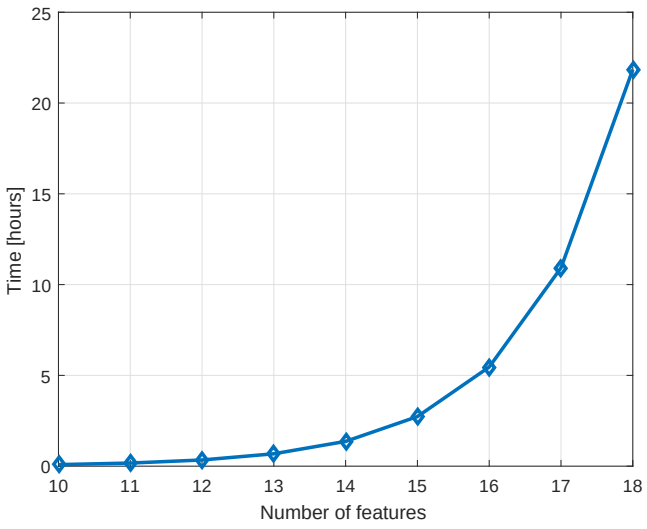

Figure 8.6: Time consumption for exhaustive search with increasing number of features included.

8.6.2 Sequential search

Performing sequential searches through the parameters is, although suboptimal, a possible way of finding suitable features. This is done by evaluating the perfor-

mance of a classifier after sequentially adding the best feature according to a selected criterium, one by one until the improvement in classification is insignificant. This means that for each round of evaluation the feature providing the largest improvement is identified and excluded from the next round of evaluation. Alternatively, the method can be done backwards starting with all features and then removing the worst one by one until there is no improvement of the classification result. In both cases, the problem is that a sequential search only tests the impact of one feature at a time. This way such a search will terminate when no single feature will improve the score. However, in many cases a combination of several features could improve the performance considerably.

8.6.3 Selected approach

One central aspect of performing feature selection here is to quantify the impact of polarimetric features on classification performance. In this thesis the total number of 32 features is simply too high for one exhaustive search, as by extrapolation of the curve in Figure 8.6 it would require 41 years. The chosen solution is to perform exhaustive searches in two steps. This is suboptimal in the sense that not all possible combinations are tested for finding the feature set providing the best overall classification among all available features. On the other hand the approach is found to achieve better classification results than the alternative sequential search.

The selected procedure was as follows. Features extracted from single polarization time and frequency domain data, listed in Table 8.1, and polarimetric variables found in Table 8.2, were initially evaluated separately. This resulted in three sets of features denoted *A*-*C* in Figure 8.7. Subsequently the selected features for each polarization of the non-polarimetric parameters were merged with the polarimetric parameters and a new exhaustive search were done among these. The results are two feature selections named *D* and *E* in Figure 8.7. This approach gives the opportunity to investigate how a classifier performs based on HH- and VV-polarization alone, and compare this to the classification score when polarimetric features are included. Investigating the performance for different dwell times τ_d and frequency bands gives a broader picture providing insight into which features

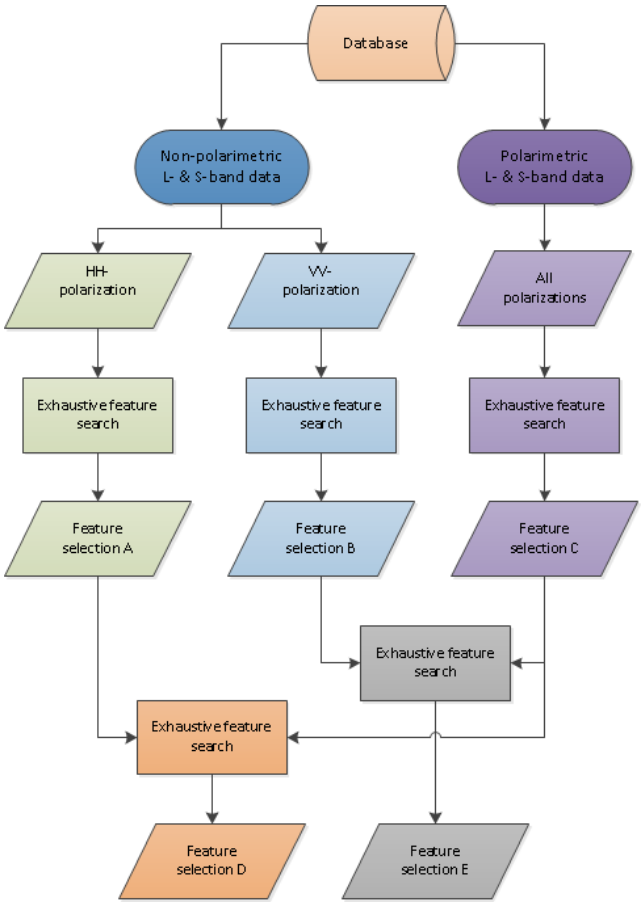

Figure 8.7: Feature selection procedure

contribute to classification of small and slow targets in modern air defence radar.

Comparison of classifier performance should generally be done with care in order to make the basis for comparison fair. Particularly in operational systems, an *unknown*-class should be included to avoid forced decisions and factors such as probability of false alarm (P_{FA}) and probability of declaration (P_d) should be evaluated carefully [152]. P_{FA} is defined as the ratio between the sum of false declarations and all declarations made. P_d is similarly defined as the ratio between the sum of all targets not labeled *unknown* and all declarations. These factors are taken into consideration in the final evaluation of the classification performance. However, in the feature selection process, potentially forced decisions and a single measure for comparison is accepted for simplicity. This measure was the probability of correct classification (P_{cc}), here defined as the ratio between the sum of correct declarations and all declarations made.

8.7 Classification

The motivation for applying classification routines to the data in this thesis is mainly connected to the need for ranking the performance of different feature sets. The choice of classifier was therefore made based on simplicity of implementation. This coincides with the advice given by Schiller and Rosenbach in Chapter 6 of [7]. Here they claim that selection of robust and discriminative features is far more important than choosing the optimum classifier.

8.7.1 Classifier

The choice fell on a Nearest Neighbour classifier. In the final code an implementation available in the *Matlab statistics and machine learning toolbox* was used. This classifier operates by identifying the feature vector in the training set that is closest to the feature vector under test. This evaluation is done in the feature space. To mitigate the effect of selecting an outlier from a wrong class, the k nearest neighbours in the training set are included and the most frequent class label among these is selected [7]. An evaluation among the 10 nearest neighbours was selected in this thesis.

The nearest neighbour classifier is discrete in the sense that it provides a class label and normally no associated measure of the probability of the classification being correct. However, the Matlab implementation provides a validation score based on the distance to other classes in the feature space. This way a confidence in the classification can be calculated. This is important for the inclusion of an *unknown*-class in the classification problem. Not including an unknown target class may yield over optimistic classification results as the target is forced to make a decision between the included classes. In this context the confidence measure was used to calculate a threshold for declaring targets *unknown*.

8.7.2 Cross validation

An important principle in classification is testing and training a classifier on different data. One way of still exploiting all measured data for both purposes is by applying cross validation. A five fold cross validation was applied to all data prior

to evaluation of all classification performances presented. In practice this means that the data used to train the classifier were randomly divided into five equally large sets. One portion at a time was then used to evaluate the performance of the classifier trained by the remaining four subsets.

As the division of the total dataset into subsets is random, running evaluation of the classifier on identical feature sets may result in slightly different results. This may also potentially result in a feature with marginal contribution to the classification being included in the selected feature set at one run and being excluded in the next. However, this is considered to have no real implication on the final results and the variance of classification scores is in practice found to be insignificant.

8.8 Summary

The signal processing of BirdRAD includes demodulation and compression, signature formation, feature extraction and classification. All this is done in the form of post processing in the commercially available software package *Matlab* and the most important steps are discussed in this chapter. Features suggested for classification are extracted from time domain-, frequency domain- and polarimetric-signatures. In total 32 parameters are evaluated. A special focus in this thesis is put on the evaluation of contribution from polarimetric measurements in terms of classification. 14 polarimetric features including incoherent and coherent differential measures, correlation coefficients and three target decomposition parameters, are compared to features extracted from single polarized measurements.

Evaluating the usefulness of extracted features is central in this thesis. The chosen approach for feature selection was based on finding the optimal combination among non-polarimetric and polarimetric variables separately. The performance of these two groups is then compared and the total classification score is found by selecting the optimal combination of features in the two categories.

Chapter 9

BirdRAD measurement results

This chapter presents key results of radar measurements carried out with the BirdRAD system described in Chapter 7. The content is subdivided into three main sections. The first part presents examples of bird and UAV signatures in the time and joint time-frequency domains. The aim of this section is to visualize selected characteristic features that can be extracted within the frames of processing suggested in Chapter 8. One representative target for each class *A*-*D* is selected and used as an example throughout this first part of the chapter. Part two covers feature statistics. A selection of signature properties is chosen to show potential differences among classes. The last part presents the classification process, first by explaining the process of selecting good features and then by showing the results of classification based on these. Classification performances are then compared on the basis of carrier frequency, dwell time and polarization.

9.1 Target class characteristics

This section aims at identifying characteristic features in each target class. Signatures are investigated in both the time- and joint time- and frequency-domain, and as a function of carrier frequency and polarization. Four targets, one representative in each class *A*-*D*, are selected for visualization of characteristics of that class. The targets are found in Table 9.1.

Class	*Type*	*Azimuth angle*	*Epoch*
A	Crow	140°	2016-04-13 12:43:07.658
B	Sea eagle	270°	2015-04-25 14:00:04.000
C	Ravn	-2°	2016-04-13 08:11:59.583
D	Multiplex Easystar	-105°	2016-04-13 08:36:34.718

Table 9.1: Targets selected for visualization of target characteristics.

9.1.1 Time domain characteristics

Periodic RCS fluctuations, or similarly amplitude modulations, have as presented in Chapter 2 been suggested for classification of both birds and UAVs. The following paragraphs give an idea of how time domain characteristics may separate the target classes. Signatures presented here result from the processing covered in Chapter 8.3.2.

9.1.1.1 Class A - Flapping birds

Figure 9.1 shows how the RCS of a crow, seen slightly from behind ($\theta \approx 140°$), varies with time at different linear polarizations. The results are given in the form of σ_{hh}, σ_{hv} and σ_{vv} in L- and S-band, shown in Figures 9.1(a) and 9.1(b) respectively. The crow was flapping its wings with a frequency visually determined to be 4-5 Hz from the synchronized video. Some factors observed are considered general and important.

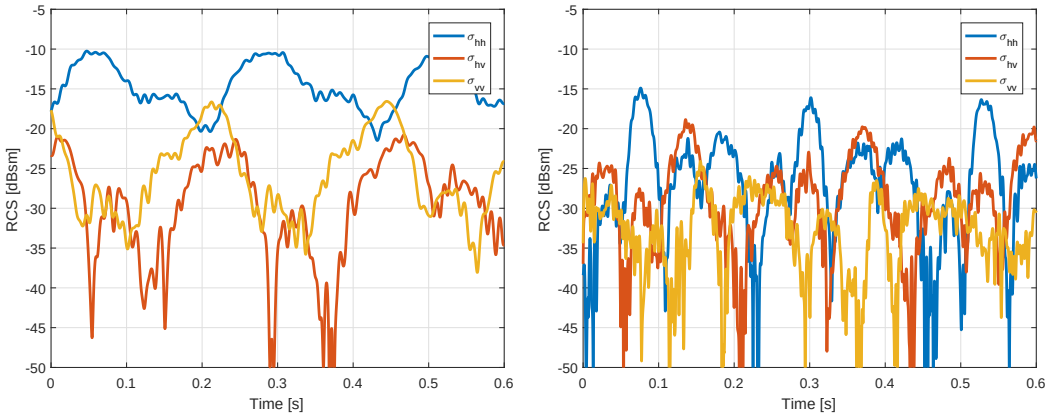

(a) L-band @ 1.3 GHz (b) S-band @ 3.25 GHz

Figure 9.1: RCS of crow with flapping wings illuminated at $\theta \approx 140°$. Epoch: 2016-04-13 12:43:07.658.

L-band RCS values generally show less fluctuation compared to S-band data. This agrees well with simulations presented in Chapter 4.3. Larger wavelength to target size ratio, gives less room for phase change over the target and thus less fluctuation. A crow is not a large bird, however, it cannot be considered a Rayleigh scatterer. This means that contributions potentially from creeping waves or more local scattering from wings and body may add up in phase constructively or destructively, and thereby modulate the scattered field considerably.

The close to three full wing beat cycles occurring during the interval is easily recognized by eye in both Figure 9.1(a) and Figure 9.1(b). The origin of such modulations is still an open question. The fluctuations in terms of RCS are large, as variations exceeding 10 dB are found at all polarizations. As was discussed in Chapter 4.3.3.3, such modulations may be caused by changes of the volume of the bird, orientation of the wings or fluctuations caused by interaction between multiple scatterers.

In this particular case values of σ_{hh} and σ_{vv} are out of phase, which may be associated with wing orientation. In addition major peaks in the time series coincide in time in the two frequency bands, indicating non-resonant scattering. Assuming that wings act as Rayleigh scatterers, wings in the upper or lower positions align better with the vertical incident E-field than level wings. Likewise, the horizontally oriented wings reflects the most when parallel to a horizontally polarized E-field. If the modulations were to be caused by orientation of the wings alone, $\sigma_{hh} + \sigma_{vv}$ should be constant through the wing beat sequence. This test shows different results between the bands. Whereas this sum in L-band result in variation less than 5 dB, fluctuations exceeding 15 dB are still found in the S-band data. This indicates that the hypothesis of wings being capable of modulating the echo on a single polarization holds far better when the size to wavelength ratio is small. This is also observed by the many less prominent peaks in the S-band data that cannot be explained by wing positions. Contribution from several scattering mechanisms is likely in both bands, the effects of interference between local scattering centers is reduced in L-band.

Recognizing the physical origin of RCS modulations is generally difficult for targets in the resonance scattering region. Many degrees of freedom make a general interpretation valid for all aspect angles unachievable. Still, as long as the aspect angle is constant, repetitive bird movements may cause periodic modulations extractable by signal processing. However, measurements of non-migrating birds observed at short range reveal rapid aspect angle changes and not necessarily a strong periodicity of wing beats.

9.1.1.2 Class B - soaring birds

Figure 9.2 shows a soaring sea eagle illuminated broadside in S-band. Only S-band data is available of soaring birds. A bird of this size, falling in the upper resonance region in S-band, makes the back-scattered power level sensitive to aspect angle changes. The soaring sea eagles observed this day were maneuvering significantly while gliding, -sometimes circling, sometimes rapidly changing direction of flight made by small corrections in wing orientation. The power levels observed in Figure 9.2 indicate that such small changes in the bird's posture may modulate back-scattered fields on any polarization.

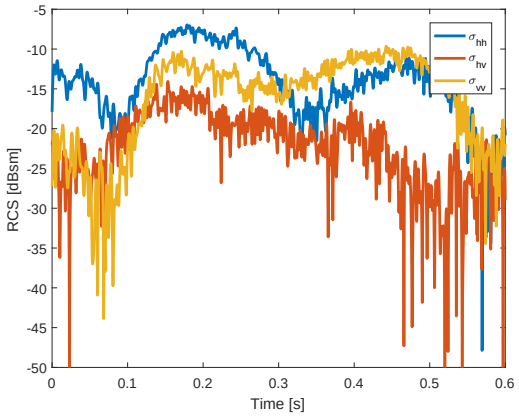

Figure 9.2: RCS in S-band of soaring sea eagle seen broadside ($\theta \approx 270°$). Epoch 2015-04-25 14:00:04.000.

The sea eagle is a large bird, and in S-band contribution from several local scattering centers like on the wings and body is probably contributing to the modulation. A rough high frequency estimation of the de-correlation angle as $\Delta\theta = \frac{\lambda}{2L}$ from [21], where L is the target length, indicates de-correlation of a few degrees for

a target like the sea eagle in S-band. The circling movements are believed to cause aspect angle changes of several degrees per second, and may therefore be a major cause of the modulation.

9.1.1.3 Class C - UAVs with conductive propellers and rotors

The quad-copter Ravn was chosen to represent class *C*. This drone has carbon fiber rotor blades and should according to simulations presented in Chapter 4.4.2 produce easily recognizable RCS modulations.

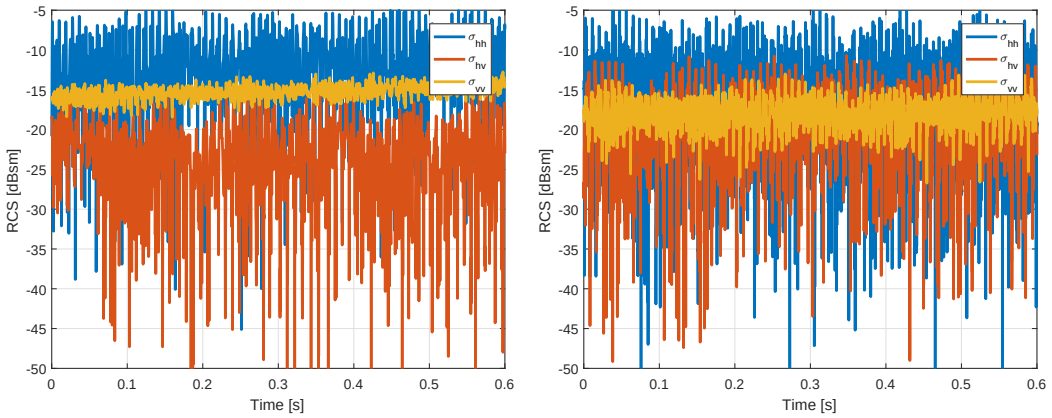

(a) L-band (b) S-band

Figure 9.3: RCS of Ravn UAV flying towards the radar ($\theta = -2°$). All relevant polarizations and both frequency bands. Epoch: 2016-04-13 08:11:59.583.

Figure 9.3 shows the fluctuations in both bands for linear co- and cross-polarizations. Compared to birds observed in Figure 9.1 and Figure 9.2 the long term fluctuations are far less prominent, whereas the rapid changes in back-scattered power are significant in both bands. Differences between polarizations are observed and explained by the alignment of the rotors with the incident E-field, as discussed in Chapter 4.4.2. The drone was observed from the front and slightly from below, with an azimuth angle $\theta = -2°$ and elevation angle $\phi = -5°$. The rotors are therefore only 5° out of the horizontal plane in the antenna centered coordinate system. They thus align largely better with the horizontally polarized E-field and a considerably larger RCS is found at HH-polarization.

9.1.1.4 Class D - UAVs with non-conductive propellers and rotors

The representative from class D is the Multiplex Easystar model aircraft. This target is according to its size expected to potentially contribute with both resonant and high frequency scattering effects. Figure 9.4 shows how RCS measured at different polarizations varies over time in L- and S-band. No prominent RCS modulation originating from the propeller is observed, nor are any significant long term variations present. This is rather typical for observations made of targets in this class. However, as the aspect angle changes, due to translational movement, turbulence or maneuvering, significant fluctuations are observed in both frequency bands also for targets in this class.

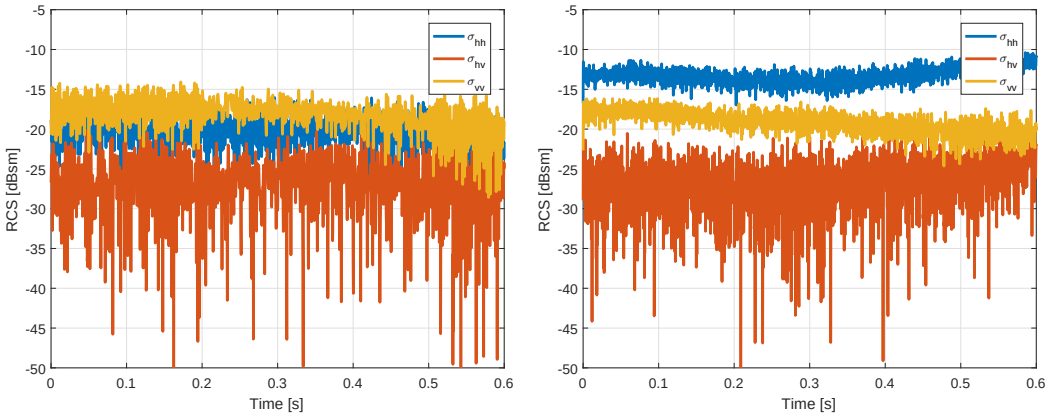

(a) L-band @ 1.3 GHz (b) S-band @ 3.25 GHz

Figure 9.4: RCS of Multiplex EasyStar flying towards the radar ($\theta = -105°$). Epoch: 2016-04-13 08:36:34.718.

Due to the high SNR associated with the BirdRAD measurements in this class, rotational propeller motion is occasionally detected at power levels less than 30 dB lower than the main target reflection. Such signatures are not considered useful for classification in an operational air defense scenario where the SNR may be far less.

9.1.2 Non-polarimetric μ-Doppler features

Joint time-frequency representations formed over long coherent data collections may be informative to the human eye. Although all features suggested for classification in this thesis are extracted either in the time- or frequency-domain, spectrograms are here used for visualization of features and the basis for the suggested

classification process. In addition to present an informative picture, this method is, due to its relationship to the DFT-based periodogram, useful for explaining the effects of the applied processing. The presented figures in this section are based on a standard STFT and processing described in Chapter 8.3. The CPI in the following examples, also referred to as dwell time τ_d, was set to 150 ms to provide a reasonable balance between velocity and time resolution, yet ensuring the necessary degree of spectral stationarity. A threshold of 13.8 dB was applied to extract target signatures from white Gaussian noise with a probability of false alarm $P_{FA} = 10^{-6}$.

9.1.2.1 Class A - Flapping birds

Figure 9.5 shows spectrograms of σ_{hh} of the already introduced flapping crow in L-and S-band. Almost three complete wing beat cycles are observed, resulting in reflectivity variations along both the time and velocity axes.

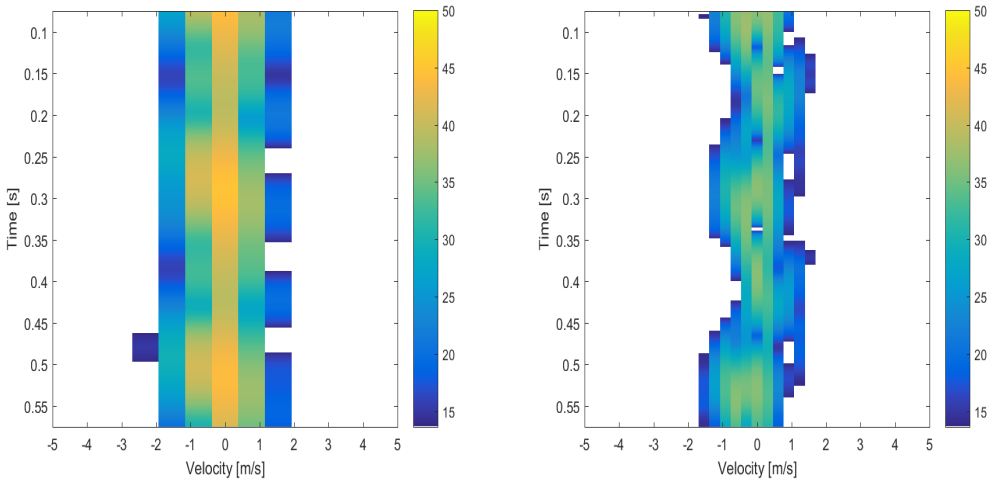

(a) σ_{hh} @ 1.3 GHz (b) σ_{hh} @ 3.25 GHz

Figure 9.5: Simultaneous μ-Doppler signatures of flapping crow in L- and S-band. The colour indicates SNR. A threshold of 13.8 dB is applied. CPI τ_d=150 ms. Epoch: 2016-04-13 12:43:07.658.

As frequently observed in spectrograms of flapping birds, rotational movement from wings are visible $\pm$1.5 m/s around the body centered in the figure. The resolution provided by a given CPI is different in the two frequency bands. Compared to the spectrograms presented for K- and X-band in Chapter 5.3, the velocity resolution is observed to be poor even for τ_d=150 ms. For longer dwell times the time

resolution is poor and the non-stationary wing Doppler spectrum will result in significant smearing along the velocity axis. The achievable velocity resolution can be observed from the pixel size along the velocity axis as no interpolation is applied. The ability to resolve wing movement in velocity is clearly limited in L-band compared to S-band. The Hamming tapering window applied as part of the time-frequency transform reduces the actual resolution by 30% and care must be taken so that smearing of the body response is not mistaken for wing movement. On the other hand a proper window function is required to reduce leakage of power from the body into sidelobes with the potential of masking wing micro-motion.

Potential influence from amplitude modulations on the μ-signature, as covered in Chapter 3.6.3, should also be kept in mind. Significant amplitude modulations are frequently associated with bird data collected in L- and S-band. As was shown in Figure 9.1, significant impulse like modulations are found in both bands. The duration of these is longer in L- band, and measured in velocity the theoretical broadening of the spectrum is roughly ± 1 m/s in both bands. By forming spectrograms of the phase only, an image of the frequency content caused by phase modulations can be investigated and a comparison to the original spectrogram can be made. Although, the influence from amplitude modulations is present, the shifts due to phase modulation seems to dominate. This is also indicated by the non-symmetric frequency content observed in Figure 9.5.

The crow selected to represent class *A*, is associated with limited micro-motion detectable by radar. Relative rotational velocities exceeding ± 3 m/s are occasionally observed in μ-Doppler signatures of larger birds. Still spectrograms of birds in L-band generally offer limited information on wing movement. S-band signatures are found to be more useful due to the improved velocity resolution. This is in accordance with predictions shown in Figure 3.9.

9.1.2.2 Class B - soaring birds

Figure 9.6 shows a similar spectrogram of a soaring sea eagle. Regrettably, only S-band measurements are available for soaring birds. However, since this μ-Doppler signature does not reveal any significant micro-motion, the result in L-band is easily

imaginable. In comparison signatures of flapping eagles frequently show relative wing movements of up towards ± 3 m/s. Generally signatures of soaring birds show little detectable micro-motion beyond the velocity resolution.

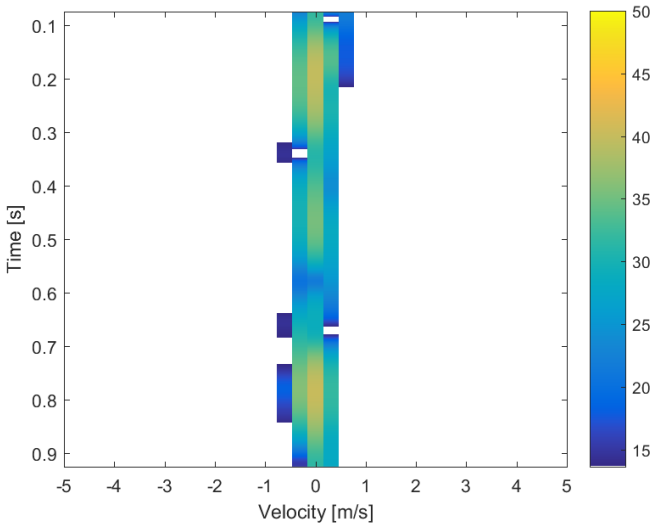

Figure 9.6: σ_{hh} time-frequency signature of soaring sea eagle in S-band. The colour indicates SNR. A threshold of 13.8 dB is applied. CPI τ_d=150 ms. Epoch: 2015-04-25 14:00:04.000.

9.1.2.3 Class C - UAVs with conductive propellers and rotors

Time-frequency signatures of targets in this class frequently show characteristics useful for classification. Figure 9.7 show spectrograms based on σ_{hh} in L- and S-band of the quad-copter UAV Ravn observed from the front ($\theta = -2^\circ$). Since the CPI is kept at 150 ms as for the other classes, the rotor blades have time to rotate many times during the observation time. The process is non-stationary and the periodicity in time results in harmonics in the spectrum. Dependent on the shape and duration of these flashes, the amplitude variation itself may cause double sided frequency responses independent of carrier frequencies as discussed in 3.6.3. In the case of L-band shown in Figure 9.7(a) this frequency response is very similar to the expected double sided Doppler response of the symmetric rotors. For long dwell times this flash induced spectrum tends to dominate over the Doppler spectrum. The width of the spectrum seen in Figure 9.7(a) is thus dependent on the flash duration and the spacing between harmonics dependent on the flash rate.

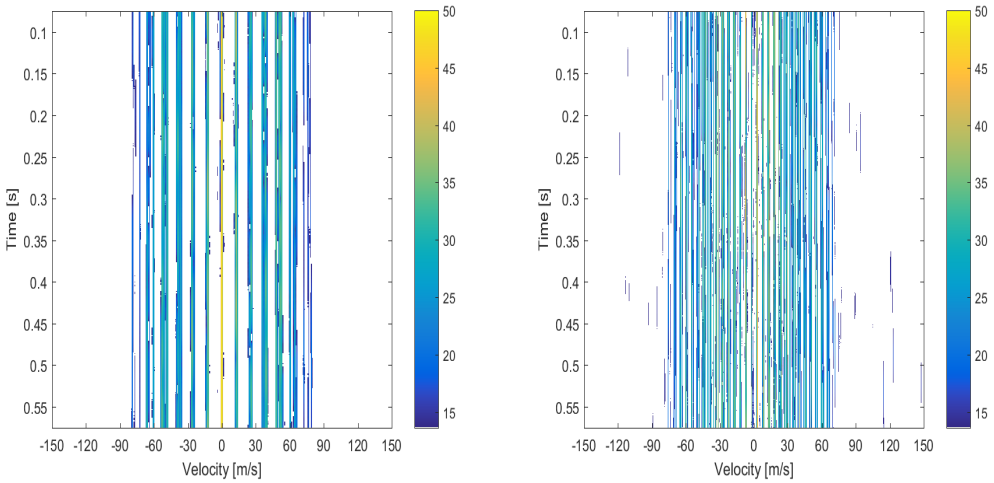

(a) σ_{hh} @ 1.3 GHz (b) σ_{hh} @ 3.25 GHz

Figure 9.7: Spectrogram of Ravn UAV in L- and S-band. The colour indicates SNR. A threshold of 13.8 dB is applied. CPI τ_d=150 ms. Note that the velocity axis differ from the other figures. Epoch: 2016-04-13 08:11:59.583.

As discussed in Chapter 6.2.3.3, the flash duration may in S-band be somewhat shorter, leading to a wider spectrum. However, the flash rate will be the same. To be in accordance with the previous figures the spectrograms here are shown as a function of velocity. This leads to the harmonics appearing closer together in S-band although, in terms of frequency, they are not. The total velocity span observed in the two bands are equal. This is believed to be caused by the Doppler shifts from rotors exceeding the amplitude modulation induced spectrum in S-band. This illustrates that the physical origin of rather similar characteristics might be different in the two bands. The further use of terms like *Doppler bandwidth* and *velocity span* might in light of this be imprecise as the spectral broadening is not always induced by relative velocity and phase modulations.

Anyway, independent of the physical origin, the characteristic spectra shown in Figure 9.7 can only stem from man-made targets and the detection of such is a strong feature in the two-class classification problem. For a quad-copter like UAV the detectability of rotor blades is found to be rather independent of aspect angle. However, for fixed wing UAV with conductive propellers, shadowing from the target body is expected to lower detectability at certain aspect angles.

9.1.2.4 Class D - UAVs with non-conductive propellers and rotors

Figure 9.8 shows spectrograms of the fixed wing Multiplex Easystar model aircraft in L- and S-band. No rotational movement is detected in either band as no additional frequency components associated with micro-motion is observed (the velocity axis in the figure is kept identical to the bird examples and no harmonics are present outside the ±5m/s span showed here). In this specific case little variation in power over time is observed in both bands.

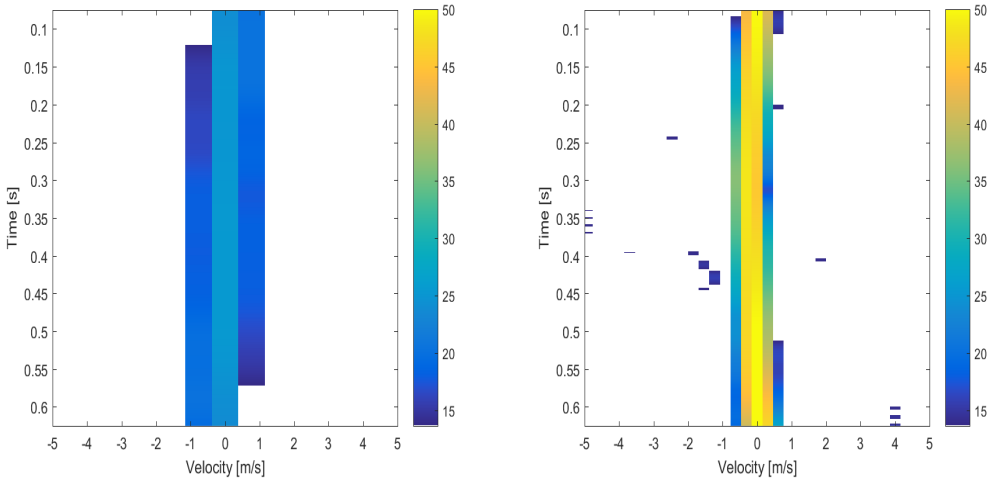

(a) σ_{hh} @ 1.3 GHz (b) σ_{hh} @ 3.25 GHz

Figure 9.8: Spectrogram of Multiplex Easystar model aircraft in L- and S-band. The colour indicates SNR. A threshold of 13.8 dB is applied. CPI τ_d=150 ms. Epoch: 2016-04-13 08:36:34.718.

9.1.3 Polarimetric μ-Doppler features

Polarimetric data was in Chapter 1 introduced as a potential source of information for classification when the available spatial and velocity resolution is limited. Polarimetric features are in this context derived from the target scattering matrix **S** and shown in the form of spectrograms. This is done to visualize the behavior of polarimetric parameters as function of time and velocity, and to couple this to target behavior. All figures show signatures of targets and intervals introduced in Table 9.1 and already covered in non-polarimetric examples.

9.1.3.1 Class A - Flapping birds

Polarimetric signatures of the flapping crow are shown for L-band and S-band in the following figures. These are shown in the form of spectrograms obtained by comparison of two non-polarimetric spectrograms. The polarimetric parameter is calculated for all pixels where power is detected in one of the compared channels. If such a detection is done only for one polarization, the noise value in the other is used. The only exception is for the differential phases, where power must be detected in both compared channels for the phase to be calculated. This is done to prevent random phase values in the signature.

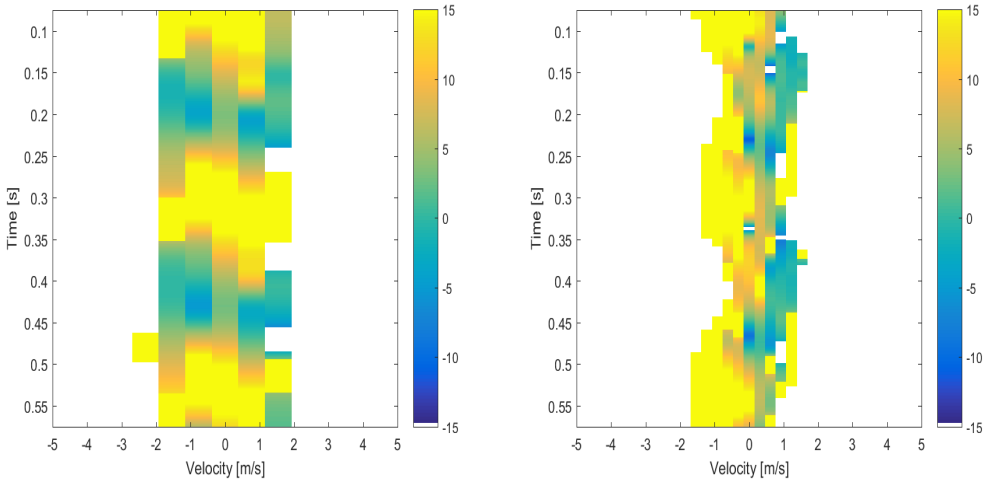

(a) σ_{dr} @ 1.3 GHz (b) σ_{dr} @ 3.25 GHz

Figure 9.9: Spectrogram of differential RCS σ_{dr} for flapping crow. $\tau_d = 150$ *ms*. Epoch: 2016-04-13 12:43:07.658

Figure 9.9(a) and 9.9(b) show the differential RCS σ_{dr} in L- and S-band respectively. Significant periodicity is found in both figures. The parameter σ_{dr} is, for dipole like scatterers like wings in the Rayleigh, region believed to hold information on apparent wing orientation about the radar line of sight. High levels in yellow are associated with wings in a level position. The higher degree of symmetry in the L-band signature is believed to be caused by more equal contribution from both wings in this case.

The linear depolarization ratio δ is shown in Figure 9.10. This parameter is believed to have large values as the wings are in upper or lower positions, 0 dB

at $\pm 45^{\circ}$and very low values when the wings are horizontally aligned. The L-band signature in Figure 9.10(a) match this theory very well. The S-band data in Figure 9.10(b) partially fits the hypothesis, but some areas of high values that can not be described as the result of an oriented dipole scatterer alone indicate more complex scattering mechanisms present in the S-band case.

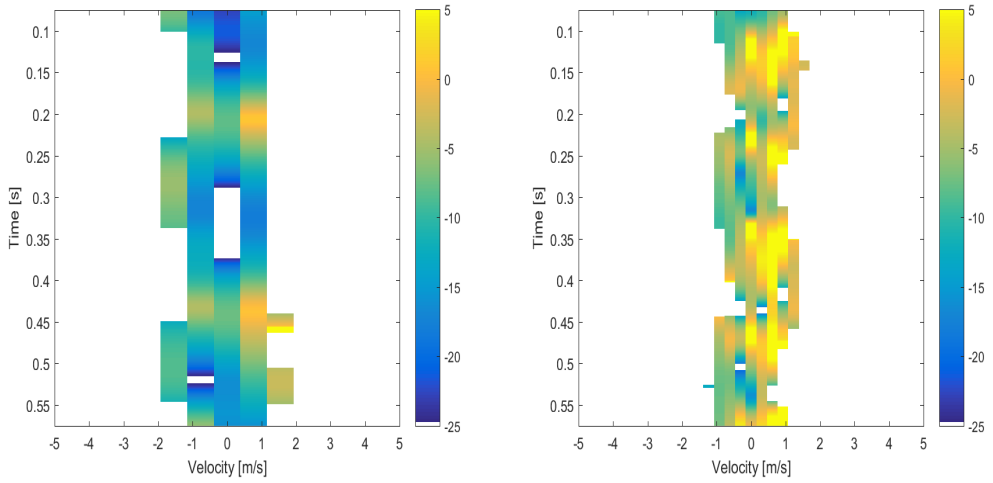

(a) δ @ 1.3 GHz (b) δ @ 3.25 GHz

Figure 9.10: Spectrogram of linear polarization ratio δ for flapping crow. $\tau_d = 150$ *ms*. Epoch: 2016-04-13 12:43:07.658.

Spectrograms showing the co-polarized phase difference δ_{vh} are found in Figure 9.11. The results for L- and S-band shown in Figure 9.11(a) and Figure 9.11(b) respectively, are not expected to be identical. Still the signature have certain similarities. As was discussed in Chapter 4.3 the value of δ_{vh} of a bird body at an azimuth angle of $140^{\circ}$is difficult to predict. In the L-band signature in the left panel, the values are slightly positive, whereas in the S-band figure they are somewhat more negative. The high degree of periodicity and large areas of relatively constant values yet suggests that δ_{vh} holds useful information about the scattering mechanisms.

Polarization synthesis can, as discussed in Chapter 8.5.4.1, be done as long as the complex $\mathbf{S}$ is available. Figure 9.12 shows the maximum co-polarized inclination angle ψ. Based on the hypothesis of bird wings acting as dipole scatterers in the Rayleigh scattering region, the idea is that the value of ψ maximizing the received power coincides with the apparent orientation of the wings along the line

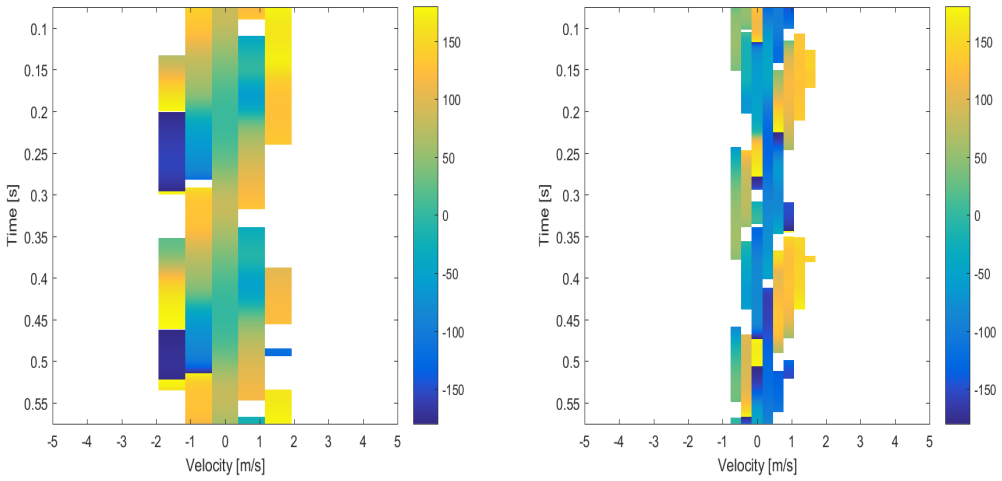

(a) δ_{vh} @ 1.3 GHz (b) δ_{vh} @ 3.25 GHz

Figure 9.11: Spectrogram of co-polarized phase difference δ_{vh}. for flapping crow. $\tau_d = 150\ ms$. Epoch: 2016-04-13 12:43:07.658.

of sight. For L-band in Figure 9.12(a), two distinctive sections of the signature stand out with high values. This would according to the theory correspond to the wings in either upper or lower position. In time this agrees well with the anticipated wing orientation estimated from the other parameters presented. The S-band results found in Figure 9.12(b) are more inconclusive. High ψ values are found in roughly the same intervals, however, generally lower values are found compared to L-band. The accuracy of the polarization synthesis is dependent on calibration of both magnitudes and phases in $\mathbf{S}$. The calibration of the BirdRAD system is described in Chapter 6.6 and inaccuracies are naturally possible. On the other hand, the scattering mechanisms are not necessarily identical in the two bands. It is reasonable to believe that bird wings are better modeled as dipole scatterers in L-band compared to in S-band due to the smaller size to wavelength ratio in this band. Results from polarization synthesis are not included in the final automatic classification routine, but included here to show that it is an interesting technique to use for extracting more detailed information of targets applicable to research question number two. The Cloude-Pottier $H/A/\bar{\alpha}$ decomposition approach covered in this thesis, takes the polarization synthesis concept further by providing parameters independent of target orientation around the line of sight. Such parameters are included in the au-

tomatic classification.

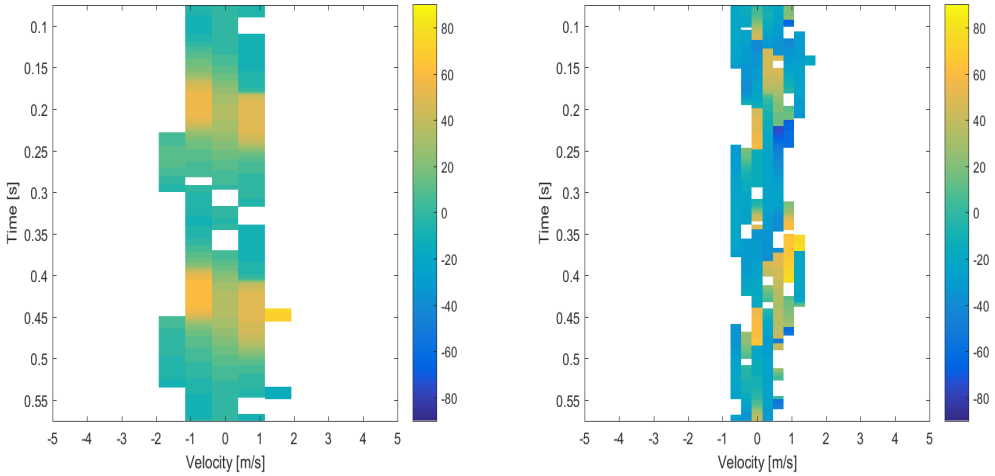

(a) Polarization synthesis @ 1.3 GHz (b) Polarization synthesis @ 3.25 GHz

Figure 9.12: Spectrogram of maximum ψ [°] in polarization synthesis for flapping crow. $\tau_d = 150\ ms$. Epoch: 2016-04-13 12:43:07.658.

9.1.3.2 Class B - soaring birds

Spectrograms of selected parameters are in this section shown for the soaring sea eagle. Figure 9.13(a) and Figure 9.13(b) show σ_{dr} and δ respectively. The characteristic periodicity observed in the flapping bird case is not present here. σ_{dr} values around 0 dB, predominantly slightly positive, is as expected for a bird body illuminated broadside. Although soaring, the eagle is constantly adjusting its bearing and the high values associated with the highest relative velocities are believed to be caused by wings co-oriented with the horizontal axis of the antenna centered coordinate system. The values of δ are generally low around -10 dB, with some exceptions believed to be associated with the apparent orientation of wings along the line of sight.

Figure 9.14(a) and Figure 9.14(b) show the co-polarized differential phase δ_{vh} and maximum ψ from polarization synthesis respectively. Relatively constant values of δ_{vh} around -50° at broad side illumination corresponds rather well with the theory introduced in Chapter 3.5.5 and predictions presented in Figure 4.14. The results of polarization synthesis shows that the inclination angle ψ that maximizes

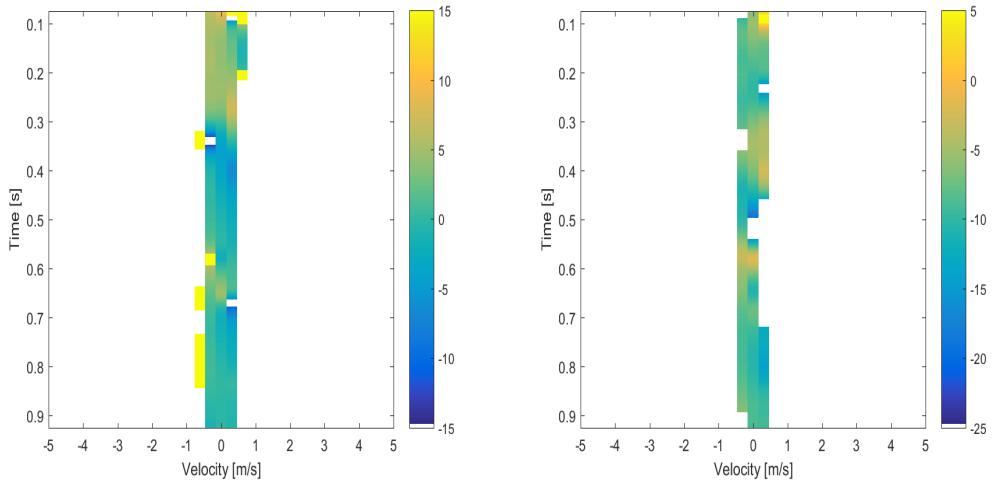

(a) σ_{dr} @ 3.25 GHz (b) δ @ 3.25 GHz

Figure 9.13: Spectrogram of linear depolarization ratio δ and differential co-polarization ratio σ_{dr} for soaring sea eagle in S-band. $\tau_d = 150$ *ms*. Epoch 2015-04-25 14:00:04.000.

the received power changes slightly during the total observation time. At broadside illumination contributions from wings are negligible when not resolved in velocity. The assumption forming the basis for estimating a scatterer's orientation by polarization synthesis is an elongated shape and size small relative to the wavelength along the relevant dimensions. A sea eagle is considered to be too large, and the values are thus difficult to interpret.

9.1.3.3 Class C - UAVs with conductive propellers and rotors

The Ravn UAV representing class *C* is a quad-copter type with rotor blades mainly rotating in the horizontal plane. The hypothesis is that such blades will act as dipole scatterers in both L- and S-band, and that σ_{dr} holds information about their orientation in the antenna oriented coordinate system. Figure 9.15 shows spectrograms based on this parameter in L- and S-band. These are formed with significantly shorter dwell time (τ_d =3 ms) compared to that used in Figure 9.7 in order to resolve flashes in time and prevent harmonics. The short τ_d results in poor velocity resolution, especially in L-band. However, echoes from the rotor blades are resolved in both bands and high values of σ_{dr} strongly indicate close to horizontal orientation of these.

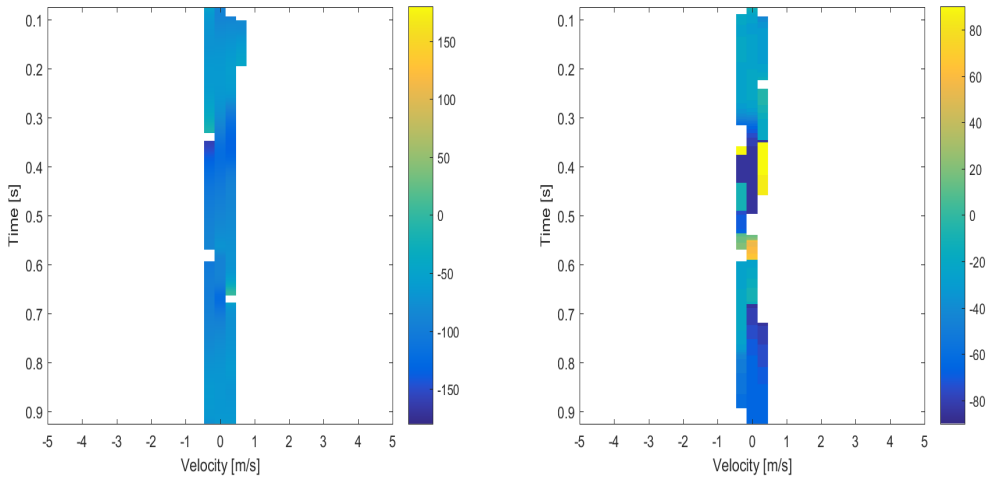

(a) δ_{vh} @ 3.25 GHz (b) Polarization synthesis

Figure 9.14: Spectrogram of maximum δ and σ_{dr} for soaring sea eagle $\tau_d = 150\,ms$. Epoch 2015-04-25 14:00:04.000.

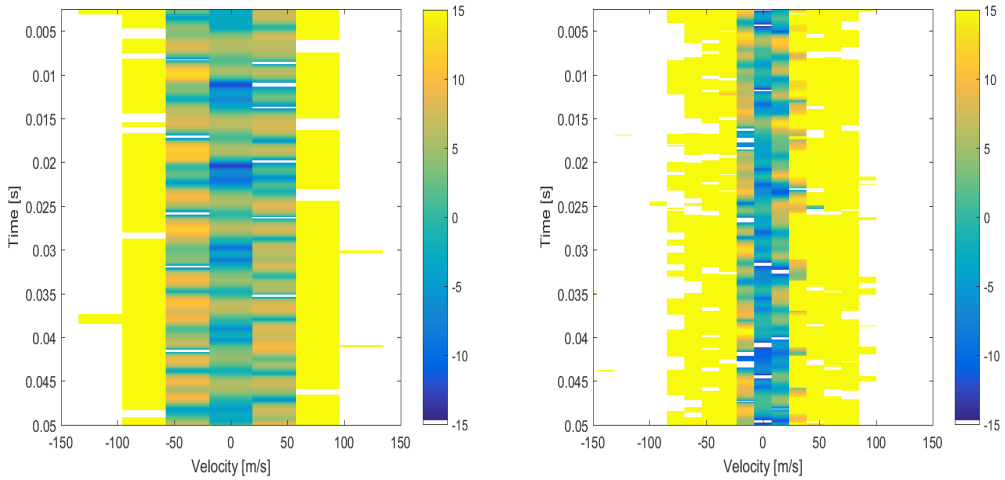

(a) σ_{dr} @ 1.3 GHz (b) σ_{dr} @ 3.25 GHz

Figure 9.15: Spectrogram of σ_{dr} Ravn UAV with dwell time $\tau_d = 3$ ms. Epoch: 2016-04-13 08:11:59.583.

9.1.3.4 Class D - UAVs with non-conductive propellers and rotors

Spectrograms showing σ_{dr} of the Multiplex Easystar is found in Figure 9.19. The target is not resolved in velocity and the response of the total target is thus found at 0 m/s for both L- and S-band in the left and right panels respectively. This model is too large to be considered as a Rayleigh scatterer, which is a prerequisite for

extraction of its orientation. Contribution from several scattering mechanisms may occur across the target and can explain to the different values in L- and S-band. Nearly constant values are found in L-band, whereas more fluctuation is observed in the more aspect angle sensitive S-band.

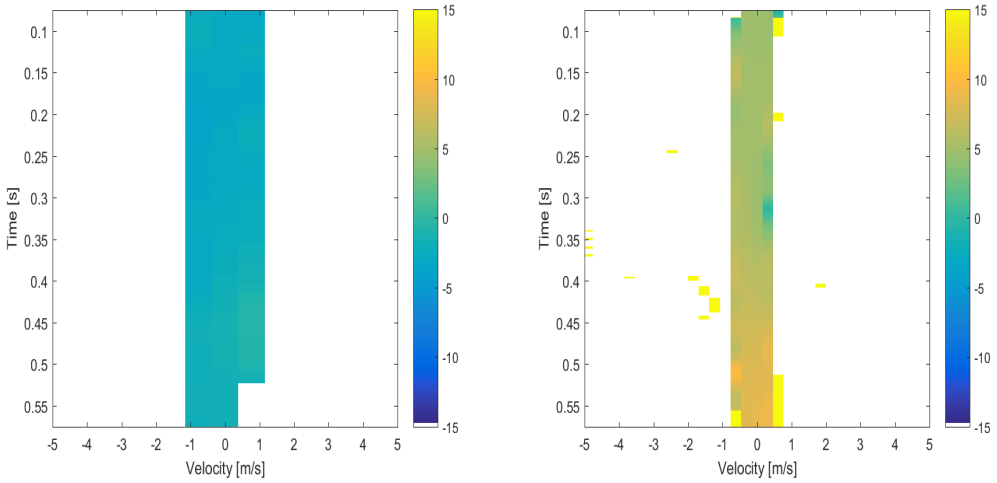

(a) σ_{dr} @ 1.3 GHz (b) σ_{dr} @ 3.25 GHz

Figure 9.16: Spectrogram of σ_{dr} Multiplex Easystar UAV with dwell time $\tau_d = 150ms$. Epoch: 2016-04-13 08:36:34.718.

Figure 9.17 shows the co-polarized phase difference δ_{vh} of the Multiplex Easystar in both frequency bands. The model is illuminated close to broadside and the scattering can be interpreted to be dominated by odd bounce scattering due to values close to 0° in both bands.

9.1.4 Target characteristics summarized

Joint time-frequency representations of polarimetric features are truly interesting and to my knowledge not presented before. Information available may for example be used to understand how the orientation of bird wings vary with time during the flapping period and provide classification at the more detailed levels in the classification tree presented in Table 1.1. In particular such presentation is informative to the human eye. However, forming μ-Doppler signatures of this type requires long coherent dwell times. This is time an air defence radar normally only can afford to spend once in a while, due to higher prioritized tasks. Typically, this could be

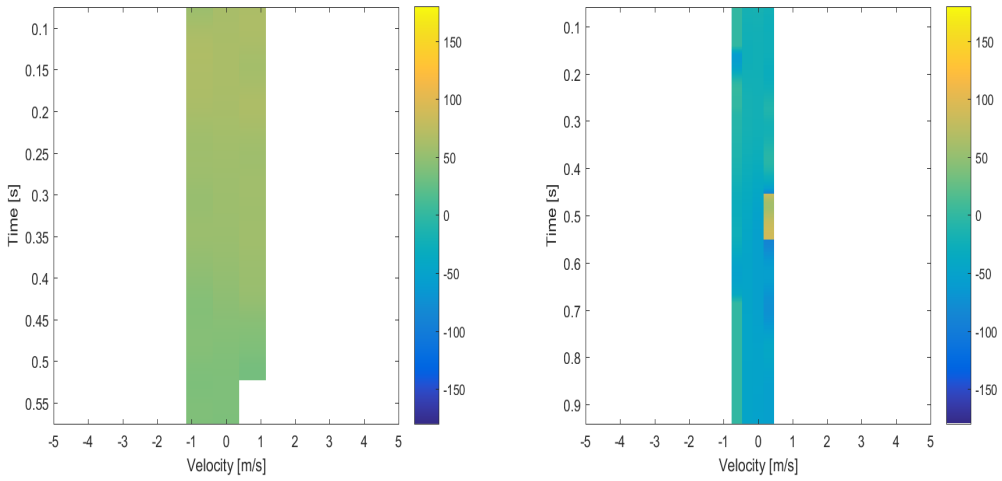

(a) δ_{vh} @ 1.3 GHz (b) δ_{vh} @ 3.25 GHz

Figure 9.17: Spectrogram of co-polarimetric phase difference δ_{vh}. Multiplex Easystar UAV with dwell time $\tau_d = 150$ ms. Epoch: 2016-04-13 08:36:34.718.

done in an intelligence mode where extracting information about the target is highly important. Results presented so far are therefore mainly considered to shed light on research question number two formulated in Chapter 1.5. In radar systems where search of vast volumes is prioritized, the classification should be done in much shorter time, ideally by utilizing existing search pulses without requiring any extra time on target. This forms the basis for investigation of research question number one.

9.2 Feature statistics

In order to give a wider picture of the distribution of extracted feature values among different target classes, statistics of selected parameters are provided. The combination of many features are suggested for classification and providing an adequate basis for evaluation of the usefulness of features in the form of two or three dimensional plots is considered impossible. A small selection of features is therefore presented here.

9.2.1 Non-polarimetric features

Figure 9.18 shows the distribution of the velocity span Δv_{hh} and the body to total power ratio B_{hh}, extracted at HH-polarization and with dwell time $\tau_d = 150$ ms. Histograms for each individual feature is shown together with the two dimensional scatter plot in both panels. From this figure it is evident that class *C* stands out from the other classes in both dimensions. Most pronounced is this along the Δv-axis, where the width of the occupied frequency spectrum is significantly wider for class *C* than for the other classes due to reflections from the conductive propellers. Along the *y*-axis, B_{hh} is found which shows the distribution of power originating from the body or fuselage compared to the total back-scattered power. At higher values a greater portion of the echo originates from the body. Soaring birds, only measured in S-band, is for example found in the upper left corner of the scatter plot. Class *C* is on the other hand generally associated with lower values of B_{hh} than the other classes, indicating that most of the scattered power originates from the propellers. The remaining classes are more challenging to separate, at least by use of a few non-polarimetric features.

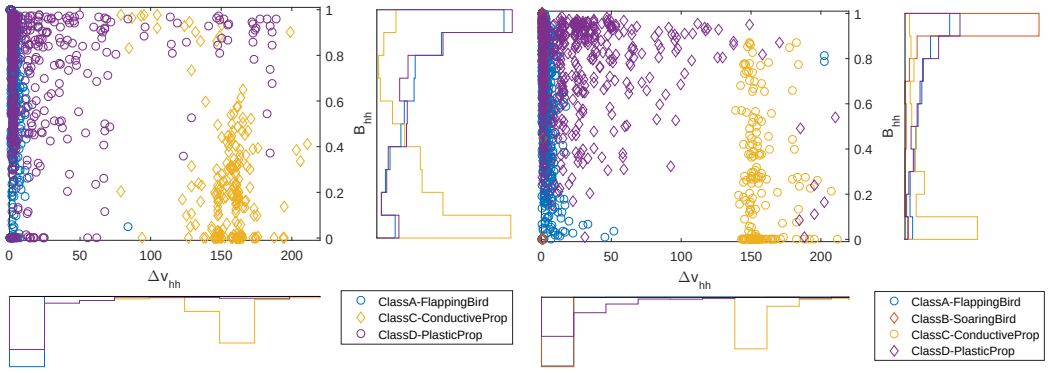

(a) L-band @ 1.3 GHz (b) S-band @ 3.25 GHz

Figure 9.18: B_{hh} shown as function of Δv_{hh} for all classes available in each band. Data from all BirdRAD collections in the database. Dwell time $\tau_d = 150$ ms.

9.2.2 Polarimetric features

Polarimetric features have been given considerable attention throughout this thesis. One of the parameters investigated thoroughly in the initial chapters was the differential RCS σ_{dr}. This is assumed to hold information on the apparent orientation

of bird wings and UAV propellers or rotors around the radar line of sight. Figure 9.19 shows the σ_{dr} extracted from measurements of the Multiplex Easystar in Figure 9.19(a) and a flying seagull in Figure 9.19(b). The figures both show values associated with micro-motion of such target parts as well as the bird body and UAV fuselage. These were extracted as described in Chapter 8.4.3.

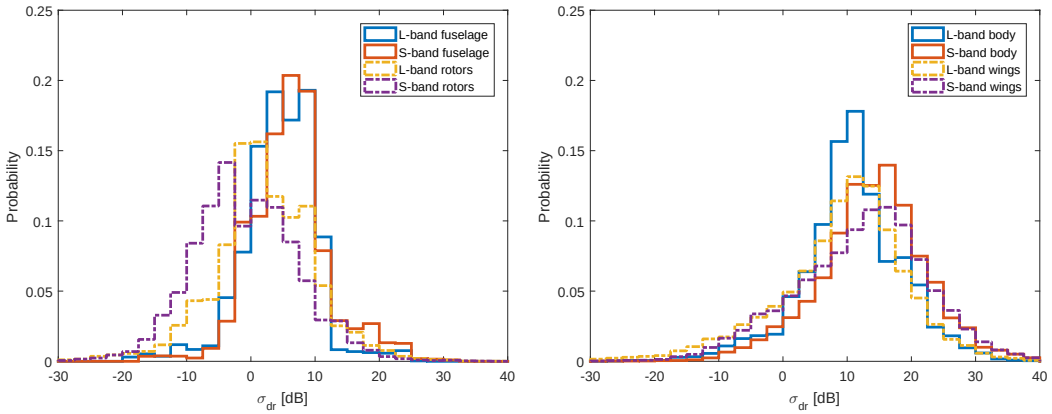

(a) Multiplex Easystar UAV (b) Seagull

Figure 9.19: σ_{dr} based on BirdRAD measurements of fixed wing UAV and flapping seagull. Body/fuselage and rotational parts in solid and dashed lines respectively. Values calculated from spectrograms formed with dwell time $\tau_d = 150$ ms.

Figure 9.19(a) shows σ_{dr} of all data available of the Multiplex Easystar. Dashed yellow and purple lines indicate echoes associated with the propeller in L- and S-band respectively. Although rotor detections are present in only 1% of the dataset, the ones made show distributions with significant elements of both negative and positive σ_{dr}. Since the propeller of this model rotates in the vertical plane, its apparent orientation with the radar antenna coordinate system when flashes occur is dependent on the orientation of the model. The solid red and blue lines show values of σ_{dr} in L- and S-band associated with reflections from the fuselage. This fuselage is too large to be considered as a Rayleigh scatterer, and its orientation is therefore not estimated. The distributions in both bands show very comparable values, with a predominance of positive values likely to be caused by contributions from horizontally oriented structures like wires in wings etc.

Similarly σ_{dr} values of all data available of a flapping seagull are presented in Figure 9.19(b). Dashed lines indicate bird wings, with similar distributions in

L- and S-band. A predominance of positive values is explained by the fact that the wings must form an angle with the horizontal plane in the antenna centered coordinate system exceeding $\pm 45^\circ$ in order to generate negative values. At such angular excursions the relative velocity of the wings is normally so small that the power reflected off the wings is easily associated with the body. Red and blue solid lines indicate L- and S-band values associated with the bird body. This is, as in the case of the UAV, considered to be too large to act as a Rayleigh scatterer and therefore not expected to hold information on the bird's orientation. σ_{dr} of simple bird bodies were in Figure 4.3 found to vary with orientation and model size to wavelength ratio. The observed predominance of positive values in both bands are slightly more positive than expected for a uniform illumination at all aspect angles. However, the distribution of aspect angles is not uniform, and a predominance of oblique illumination can explain the high values.

Another feature investigated in the initial chapters was the co-polar differential phase δ_{vh}. Figure 9.20 shows this parameter extracted from bird bodies in the left panel and fixed wing UAVs in the right. In the case of the birds, δ_{vh} was calculated for all birds in the database independent of aspect angle. Blue line denotes L-band, whereas red indicate S-band measurements. The two curves have some similarities. The most prominent is the peak at around $\delta_{vh} = -60^\circ$. In Figure 4.14 in Chapter 4, δ_{vh} was simulated for a wide range of aspect angles and frequencies. A significant predominance around $\delta_{vh} = -40^\circ$ is found in that figure. The deviation between measurements and simulation may be attributed to phase calibration error. However, the uncertainties connected to the bird size and body shape in the measurements are large. The phase differences measured in S-band have a much more random nature than observed in L-band. This can be understood by the increased significance of target details in higher bands. The scattering mechanisms are simply believed to be more predictable in L-band. However, there is one significant deviation from the predictions found for L-band. That is the significant peak found around $\delta_{vh} = 50^\circ$. The origin of this is not understood.

The measured values of δ_{vh} for all fixed wing UAVs in the database are found

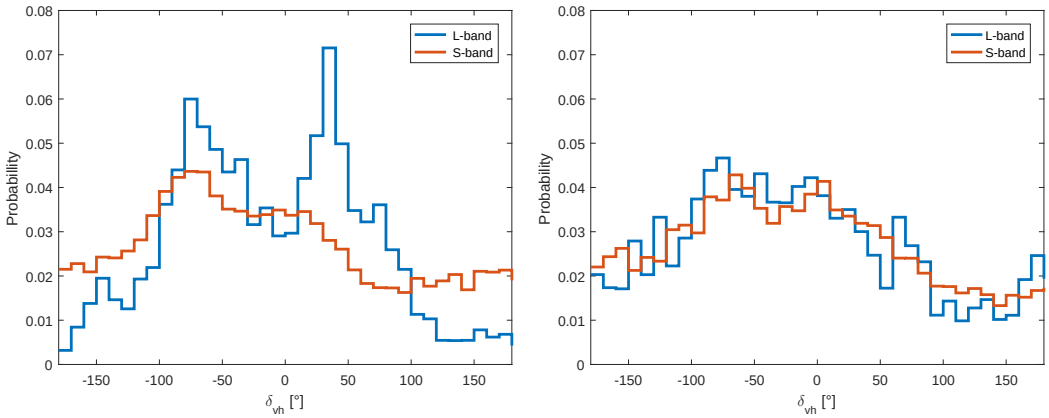

(a) Bird body δ_{vh} (b) UAV δ_{vh}

Figure 9.20: δ_{vh} for all bird bodies and fixed wing UAVs in the database. Dwell time $\tau_d =$ 150 ms.

in Figure 9.20(b). These models are the Multiplex Easystar and Discovery, and the values are calculated for all available aspect angles. The blue and red curves denotes L- and S-band respectively and show a more random nature than the corresponding values for birds. The correspondence between the curves is very high, and significantly different from the situation with birds.

Figure 9.21 show the results of Cloude-Pottier decomposition of polarimetric time-domain signals. L- and S-band data is found in Figure 9.21(a) and Figure 9.21(b) respectively. The parameters shown are the entropy H and $\bar{\alpha}$ holding information on the dominating scattering mechanism. Both variables are calculated over a dwell time $\tau_d = 5$ ms. Values for both bands are shown in the form of scatter plots and associated histograms for each parameter. The most prominent observation is that the entropy associated with class C is generally higher than found for the other classes. This is probably connected to the high degree of disorder in scattering dominated by both blade flashes in short periods and by the fuselage in intervals in between. The other classes are not well separated on the basis of these two parameters. However, some differences are found in the generally overlapping distributions of $\bar{\alpha}$. From the histograms of this parameter in both bands, a predominance of values around 45° is found for classes A and B, whereas values of around 60°are the most frequent for class D. Values of $\bar{\alpha}$ around 45° are, as covered

in Chapter 8.5.4.2, associated with dipole scattering, whereas higher values may indicate a higher degree of double bounce scattering.

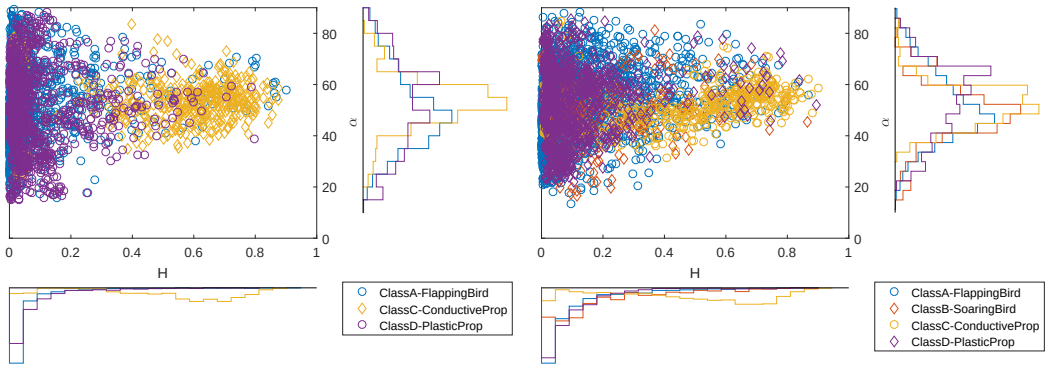

(a) L-band @ 1.3 GHz (b) S-band @ 3.25 GHz

Figure 9.21: BirdRAD measurements. H vs. $\bar{\alpha}$ for all classes. Dwell time $\tau_d = 5$ ms.

The entropy is observed to be higher in S-band than in L-band. This is explained by more distributed scattering as smaller target details are expected to contribute in this band. However, according to [127] $H < 0.3$ is considered to be associated with more highly polarized returns and thus scattering mechanisms that could be decomposed by coherent methods.

This section has provided a glimpse of selected features' ability to separate between target classes. Limited separation between target classes in the overall probability distribution along one or two dimensions alone does not necessarily result in poor classification results, as the combination of many features often is the key to precise classification. A more systematic evaluation of each feature's suitability for classification as function of dwell time and frequency band is required. Instead of evaluating each feature individually, investigation of classification performance utilizing different combinations of features is needed.

9.3 Feature selection

This section presents the results of feature selection based on the procedure presented in Figure 8.7. The classification performance of the Nearest Neighbour classifier described in Chapter 8.7.1 was evaluated for eight selected dwell times and for all the data available in the database. At this point the classifier was trained to

distinguish between the two classes *Bird* and *UAV* only. The feature sets resulting from this selection process form the basis for further evaluation of classification performance presented in Chapter 9.4.

9.3.1 Single polarized features

The first step was finding optimal combinations of single polarized parameters. The 18 features in Table 8.1 were divided into two groups: one with nine horizontally and the other with nine vertically co-polarized features. Due to these low numbers, an exhaustive search among all possible combinations was performed in each group.

The optimal feature combinations and classification scores achieved at different dwell times τ_d and polarizations are found in Table 9.2 and Table 9.3. The ordering of the features is indifferent. In the rightmost column the classification score is shown in the form of P_{cc}. This is defined as the ratio between the number of correctly classified signatures and declarations made, which in the forced decision environment is identical to the term accuracy discussed in [153].

$\tau_d[ms]$	*Band*	*Features included*			$P_{cc}[\%]$
5	L	Δv_{hh}	B_{hh}		59.7
	S	S_{hh}	Δv_{hh}	B_{hh}	67.8
10	L	Δv_{hh}	B_{hh}		57.9
	S	S_{hh}	Δv_{hh}		70.0
20	L	Δv_{hh}	B_{hh}		61.7
	S	Δv_{hh}			72.3
40	L	Δv_{hh}			65.3
	S	Δv_{hh}			76.5
100	L	Δv_{hh}			70.2
	S	Δv_{hh}			84.0
150	L	Δv_{hh}			72.6
	S	Δv_{hh}			86.1
250	L	Δv_{hh}			74.6
	S	Δv_{hh}			89.1
700	L	Δv_{hh}	B_{hh}		78.2
	S	S_{hh}	Δv_{hh}		91.0

Table 9.2: Selected horizontal co-polarized features among candidates found in Table 8.1. Feature selection A according to Figure 8.7.

The selected features and associated scores for HH-polarization is found in Table 9.2. Out of nine available features, the selection process reduced this number

down to the total of three across all investigated dwell times and frequency bands. Not surprisingly the velocity span Δv contributes across all observation times. However, the velocity resolution is reduced with decreasing observation time and frequency. This leads to a limited classification performance at the shortest dwell times and generally poorer performance in L-band compared to S-band. For targets in class *C* associated with amplitude modulations, here referred to as blade flashes, a significant contribution to the spectral broadening originates from such modulations for reasons described in Chapter 3.6.3. This broadening is not dependent on carrier frequency, but dwell time is still an important factor defining the ability to resolve spectral components by DFT-based spectral estimation techniques.

$\tau_d[ms]$	*Band*	*Features included*			$P_{cc}[\%]$
5	L	S_{vv}	B_{vv}		46.8
	S	S_{vv}	B_{vv}		52.8
10	L	S_{vv}	B_{vv}		52.3
	S	S_{vv}	Δv_{vv}	B_{vv}	58.3
20	L	S_{vv}	Δv_{vv}	B_{vv}	58.6
	S	S_{vv}	Δv_{vv}	B_{vv}	66.4
40	L	S_{vv}	Δv_{vv}	B_{vv}	65.1
	S	S_{vv}	Δv_{vv}	B_{vv}	71.5
100	L	Δv_{vv}	B_{vv}		68.0
	S	Δv_{vv}			78.5
150	L	S_{vv}	Δv_{vv}	B_{vv}	68.5
	S	Δv_{vv}			82.2
250	L	S_{vv}	Δv_{vv}		69.2
	S	Δv_{vv}			84.3
700	L	Δv_{vv}	B_{vv}		76.4
	S	Δv_{vv}			90.4

Table 9.3: Selected vertical co-polarized features among candidates found in Table 8.1. Feature selection B according to Figure 8.7.

The two other parameters found to contribute are the first order spectral moment *S*, interpreted as a measure of mean frequency, and the target body to total RCS ratio *B*. More surprising is the low contribution from features connected to RCS modulations. Neither flash rate estimation based on spectral nor cepstral analysis contributes significantly to the classification. Both these methods do to some extent individually show ability to recognize periodicity originating from rotating

conductive blades. However, the parameter Δv in the actual data shows even better ability to separate between classes and the contributions from periodicity related features seems redundant.

Table 9.3 shows similar results for vertical polarized features. The probability of correct classification associated with the selected feature combinations are significantly lower at this polarization compared to horizontal. Figure 9.22 shows the comparison across dwell times on a logarithmic scale for the two frequency bands and polarizations. Here the results for HH-polarization are shown in dotted blue and red lines for L- and S-band respectively. Similarly the results of VV-polarization are found in solid yellow and purple lines indicating L- and S-band respectively. The considerably poorer score at VV-polarization is believed to be caused by the limited ability to extract strong features associated with the horizontally oriented quad-copter rotors at this polarization. The difference between frequency bands is considered to be associated with the different velocity resolutions in the two bands.

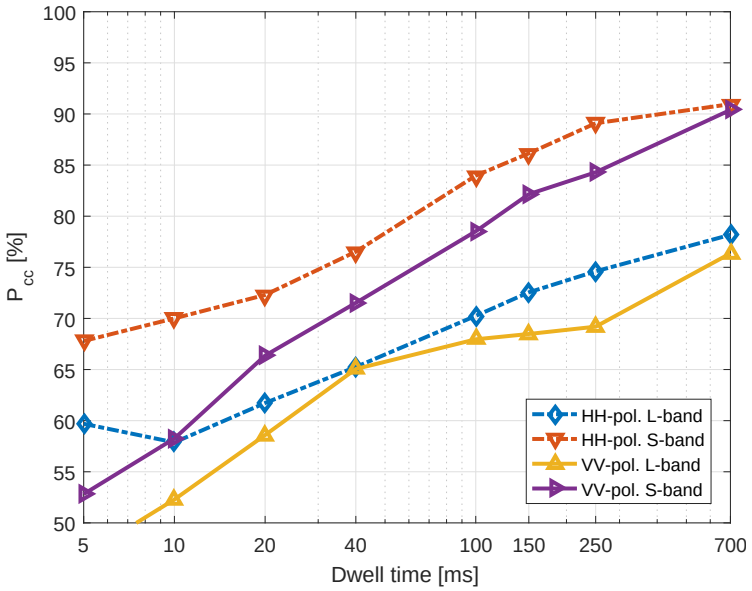

Figure 9.22: Comparison of classification performance based on single polarized features at two polarizations and in two frequency bands.

9.3.2 Polarimetric features

The results of an exhaustive feature search among the 13 polarimetric variables in Table 8.2 are found in Table 9.4. The resulting classification scores differs from

the single polarized variables in one important way, -the best results are found for the shortest dwell times. This is promising as being able to do necessary classification at short dwell times would save time for other important tasks in the radar system and is considered to be one of the main objectives of this work. Figure 9.23 visualizes the scores for the two frequency bands as function of dwell time. The blue line with diamond markers indicates results for L-band, whereas the red line with triangles indicates S-band. Generally the performance is found to be independent of the observation time, however, at the longest intervals the score drops in L-band. Except at the these longest dwell times, there is no significant difference in classification performance as function of frequency. These two findings support the initial assumption presented in Chapter 1.4 that the ability of polarimetric features to discriminate between targets is not reduced with decreasing dwell time or carrier frequency such as many traditional features relying on spatial or velocity resolution.

$\tau_d[ms]$	*Band*	*Features included*											$P_{cc}[\%]$
5	L	A	H	$\bar{\alpha}$	$\lvert\rho\rvert$	δ_{vh}	$\lvert\beta\rvert$	$\angle\varepsilon$	δ	σ_{dr}	S_{dr}	S_δ	85.0
	S	A	H	$\bar{\alpha}$	$\lvert\rho\rvert$	δ_{vh}	$\lvert\beta\rvert$	$\angle\beta$	$\lvert\varepsilon\rvert$	$\angle\varepsilon$	δ	S_{dr}	84.6
10	L	A	H	$\bar{\alpha}$	$\lvert\rho\rvert$	δ_{vh}	$\lvert\varepsilon\rvert$	$\angle\varepsilon$	δ	σ_{dr}	S_{dr}		83.9
	S	A	H	$\bar{\alpha}$	δ_{vh}	$\lvert\beta\rvert$	$\angle\beta$	$\lvert\varepsilon\rvert$	$\angle\varepsilon$	δ	S_{dr}	S_δ	84.3
20	L	A	H	$\bar{\alpha}$	$\lvert\rho\rvert$	$\angle\beta$	$\lvert\varepsilon\rvert$	$\angle\varepsilon$	δ	σ_{dr}	S_{dr}	S_δ	82.5
	S	A	H	$\bar{\alpha}$	$\lvert\rho\rvert$	δ_{vh}	$\lvert\beta\rvert$	$\angle\varepsilon$	δ	S_{dr}	S_δ		82.8
40	L	A	H	$\bar{\alpha}$	$\lvert\rho\rvert$	δ_{vh}	$\lvert\varepsilon\rvert$	$\angle\varepsilon$	δ	σ_{dr}	S_{dr}	S_δ	80.8
	S	A	H	$\bar{\alpha}$	$\lvert\rho\rvert$	δ_{vh}	$\lvert\beta\rvert$	$\angle\varepsilon$	δ	σ_{dr}	S_{dr}	S_δ	80.3
100	L	A	H	$\bar{\alpha}$	$\lvert\rho\rvert$	$\lvert\beta\rvert$	$\lvert\varepsilon\rvert$	σ_{dr}	S_{dr}	S_δ			80.9
	S	A	H	$\lvert\rho\rvert$	δ_{vh}	$\lvert\beta\rvert$	$\angle\beta$	$\lvert\varepsilon\rvert$	δ	σ_{dr}	S_{dr}	S_δ	81.9
150	L	A	H	$\bar{\alpha}$	$\lvert\rho\rvert$	δ_{vh}	$\lvert\beta\rvert$	$\lvert\varepsilon\rvert$	δ	B_{dr}			81.8
	S	H	δ_{vh}	$\lvert\beta\rvert$	$\lvert\varepsilon\rvert$	δ	σ_{dr}	S_{dr}	S_δ				82.3
250	L	A	H	$\bar{\alpha}$	$\lvert\rho\rvert$	$\lvert\beta\rvert$	$\lvert\varepsilon\rvert$	δ	B_{dr}				80.7
	S	A	H	$\bar{\alpha}$	$\lvert\rho\rvert$	$\lvert\beta\rvert$	δ	S_δ					82.5
700	L	$\lvert\beta\rvert$	$\angle\beta$	$\lvert\varepsilon\rvert$	σ_{dr}	B_{dr}							76.1
	S	A	$\lvert\rho\rvert$	δ	σ_{dr}	S_{dr}							81.9

Table 9.4: Selected polarimetric features among candidates found in Table 8.2. Feature selection C according to Figure 8.7.

Generally many polarimetric features contribute to the classification, especially at shorter dwell times. Out of 14 variables available, 11 are frequently included in the optimal combination for shorter dwell times. However, the number of features contributing positively to the result is decreasing with increasing observa-

tion time. Although, some polarimetric features are parts of the optimum combination at most dwell times and in both bands, the impression is that many individually less strong features contribute to an overall improved result. A similar situation is not found for single polarized features, where the inclusion of many weak features have shown to reduce the classification score significantly.

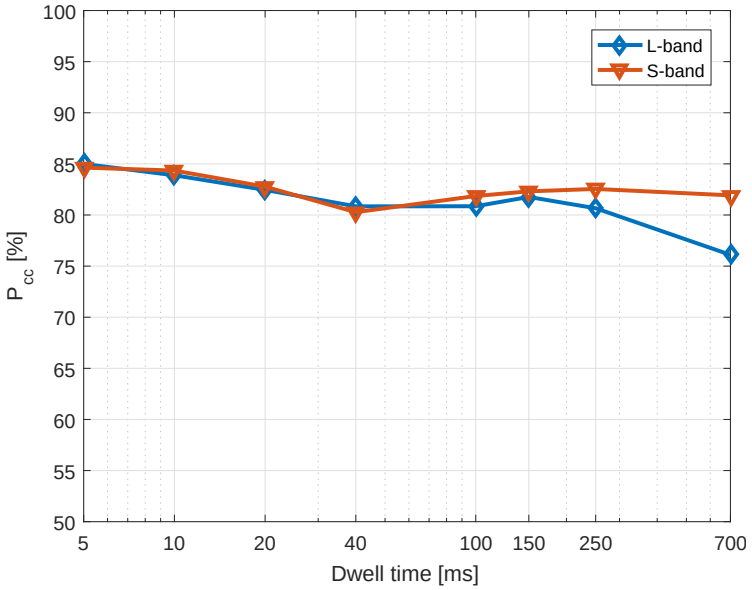

Figure 9.23: Comparison of classification performance based on polarimetric features alone extracted from L- and S-band.

The relative significance of features could be investigated by the sequential search algorithm presented in Chapter 8.6.2. This method evaluates the contribution to classification of each feature individually, thus combinations of new features are not investigated. This is considered to be a limitation of the method. Figure 9.24 shows the results of a forward sequential search among the polarimetric features of all the data in the database. Only the three shortest dwell times, 5 ms in blue, 10 ms in red and 40 ms in yellow, are included for clarity. The classifier used was identical to the one used in the exhaustive searches. This figure shows the mentioned limitation of a sequential search quite well. The methods stops before reaching the optimal combination found in Figure 9.23. The figure supports the impression that no polarimetric feature evaluated individually is significantly better than the others, however, S and A are found to be the parameters individually providing the best classification score.

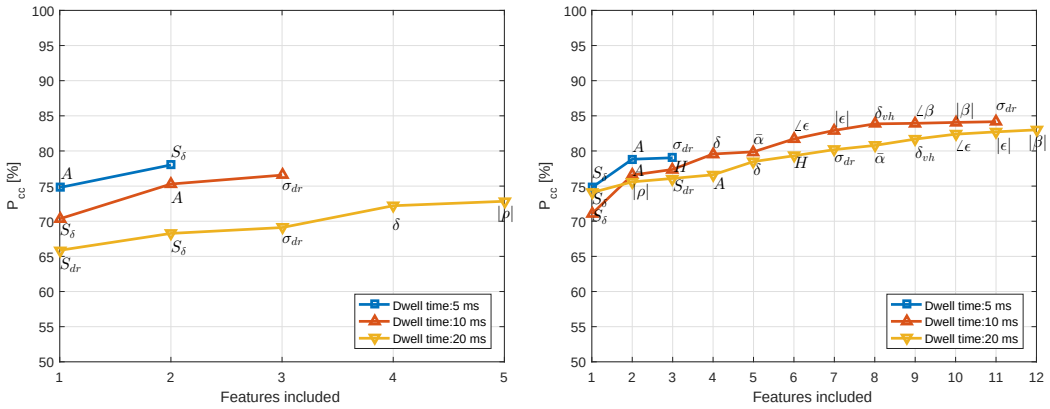

(a) L-band (b) S-band

Figure 9.24: Results of forward sequential search among polarimetric features in Table 8.2.

9.3.3 Combination of all available features

After finding optimal combinations of available single polarized and polarimetric features separately, the resulting parameters were combined and a new exhaustive search was performed among these for each dwell time. The results are presented in Table 9.5 and Table 9.6 for horizontal and vertical polarizations respectively.

$\tau_d[ms]$	*Band*	*Features included*											$P_{cc}[\%]$
5	L	A	H	$\bar{\alpha}$	δ_{vh}	$\lvert\beta\rvert$	$\angle\varepsilon$	δ	σ_{dr}	S_{dr}			84.8
	S	Δv_{hh}	B_{hh}	A	H	$\bar{\alpha}$	$\lvert\rho\rvert$	δ_{vh}	$\lvert\varepsilon\rvert$	$\angle\varepsilon$	δ		88.8
10	L	A	H	$\bar{\alpha}$	$\lvert\rho\rvert$	δ_{vh}	$\angle\varepsilon$						83.4
	S	Δv_{hh}	A	H	$\bar{\alpha}$	δ_{vh}	$\lvert\beta\rvert$	$\lvert\varepsilon\rvert$	$\angle\varepsilon$				87.5
20	L	A	H	$\bar{\alpha}$	$\lvert\rho\rvert$	$\angle\beta$	$\lvert\varepsilon\rvert$	$\angle\varepsilon$	σ_{dr}	S_δ			80.6
	S	Δv_{hh}	A	H	$\bar{\alpha}$	$\lvert\rho\rvert$	δ_{vh}	$\lvert\beta\rvert$	$\angle\varepsilon$	δ	S_{dr}	S_δ	86.1
40	L	A	H	$\bar{\alpha}$	$\lvert\rho\rvert$	δ_{vh}	$\lvert\varepsilon\rvert$	$\angle\varepsilon$	δ	S_{dr}	S_δ		80.1
	S	Δv_{hh}	H	δ_{vh}	δ	σ_{dr}							85.3
100	L	Δv_{hh}	A	$\lvert\rho\rvert$	$\lvert\beta\rvert$	$\lvert\varepsilon\rvert$	σ_{dr}	S_{dr}					79.8
	S	Δv_{hh}	H	δ									90.0
150	L	Δv_{hh}	$\lvert\beta\rvert$	δ									84.8
	S	Δv_{hh}	H	δ									89.8
250	L	Δv_{hh}	$\lvert\beta\rvert$	δ									81.3
	S	Δv_{hh}	H	δ	S_δ								90.7
700	L	Δv_{hh}	σ_{dr}										81.5
	S	S_{hh}	Δv_{hh}										91.0

Table 9.5: Final selection of features for classification. Combination of polarimetric and HH-polarized features. Feature selection D according to Figure 8.7.

According to Table 9.5, the best classification in L-band and at short dwell times is done based purely on polarimetric features. This is expected as the per-

formance of single polarized features is poor at short observation times. For $\tau_d \geq 100$ ms the velocity span Δv contribute to classification. All the polarimetric variables available are included in the optimum combination for at least one dwell time in L-band. The contribution from these are found to be of less importance to the total classification performance at the longest dwell times. However, there still is a contribution here as well.

In S-band the performance of single polarized features is better and contribution to classification is found at all investigated dwell times. In total the three parameters Δv, B and S are included. For $\tau_d \geq 250$ this contribution is substantial and the polarimetric features are found to be less important. In this frequency band 12 of 13 available polarimetric features are included at least once. Only $\angle\beta$, one of the cross-polarized phase difference measures, is excluded.

$\tau_d[ms]$	*Band*	*Features included*										$P_{cc}[\%]$
5	L	A	H	$\bar{\alpha}$	$\lvert\rho\rvert$	δ_{vh}	$\lvert\beta\rvert$	$\angle\varepsilon$	δ			85.0
	S	B_{vv}	A	H	$\bar{\alpha}$	δ_{vh}	$\angle\varepsilon$	δ	S_{dr}			90.2
10	L	A	H	$\bar{\alpha}$	$\lvert\rho\rvert$	δ_{vh}	$\angle\varepsilon$	δ	S_{dr}			83.7
	S	Δv_{vv}	B_{vv}	A	H	$\bar{\alpha}$	δ_{vh}	$\lvert\beta\rvert$	$\lvert\varepsilon\rvert$	$\angle\varepsilon$	δ	S_{dr}	89.8
20	L	A	H	$\bar{\alpha}$	$\lvert\rho\rvert$	$\angle\beta$	$\lvert\varepsilon\rvert$	$\angle\varepsilon$	S_{dr}	S_δ			80.2
	S	Δv_{vv}	B_{vv}	A	H	$\bar{\alpha}$	δ_{vh}	$\angle\varepsilon$	S_δ				87.4
40	L	A	H	$\bar{\alpha}$	$\lvert\rho\rvert$	δ_{vh}	$\lvert\varepsilon\rvert$	$\angle\varepsilon$	δ	σ_{dr}	S_{dr}	S_δ	79.9
	S	S_{vv}	Δv_{vv}	B_{vv}	A	$\bar{\alpha}$	$\lvert\rho\rvert$	δ_{vh}	$\lvert\beta\rvert$	δ	σ_{dr}	S_δ	85.8
100	L	$\lvert\beta\rvert$	σ_{dr}	S_{dr}	S_δ								79.6
	S	Δv_{vv}	H	δ									88.5
150	L	S_{vv}	Δv_{vv}	$\lvert\rho\rvert$	δ								82.4
	S	Δv_{vv}	H	δ									89.5
250	L	Δv_{vv}	$\lvert\beta\rvert$	δ									77.0
	S	Δv_{vv}	H	δ									89.0
700	L	Δv_{vv}	σ_{dr}										78.5
	S	Δv_{vv}	S_{dr}										91.8

Table 9.6: Final selection of features for classification. Combination of polarimetric and VV-polarized features. Feature selection E according to Figure 8.7.

The corresponding best combinations of VV single polarized and polarimetric features are shown in Table 9.6. The same features contributing to classification involving HH single polarized parameters contribute here. This means that one single polarized and 13 polarimetric features contribute in L-band, whereas three non-polarimetric and all but $\angle\beta$ contribute in S-band. Only minor differences in

the distribution of features in the two tables are found. In L-band the influence of Δv is for example only seen for $\tau_d \geq 150$ ms, which is slightly longer compared to the results including HH single polarized features. Generally there is not much difference in the classification performance between contribution from HH- and VV- single polarized features. The most significant difference is found in L-band at the two longest dwell times, where the performance is 3-4 percentage points lower when involving VV-polarization.

9.3.4 Impact of introducing polarimetric features

Now it is possible to evaluate the impact of including polarimetric measurements on classification performance. Figure 9.25 shows a comparison of the performance of the single polarized features indicated by dotted lines and the combination of the selected non-polarimetric and polarimetric features by solid ones.

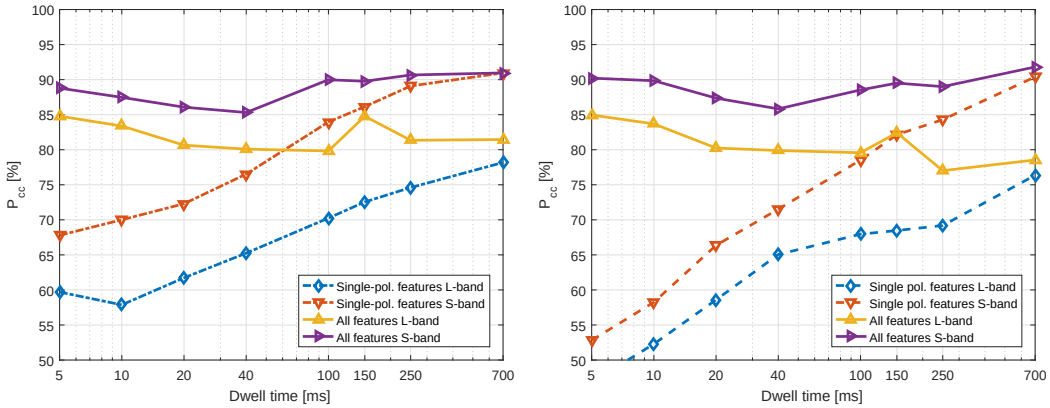

(a) Polarimetric and HH-polarized features (b) Polarimetric and VV-polarized features

Figure 9.25: Comparison of classification performance based on single polarized parameters along and combination of single polarized and polarimetric features.

In the case where the single polarization is HH, Figure 9.25(a) shows that the difference is large at short dwell times. At $\tau_d = 5$ ms the inclusion of polarimetric features improve classification by 25.1 and 21.0 percentage points in L-and S-band respectively. The difference gradually decrease with increasing dwell times until $\tau_d = 700$ ms, where the difference is more marginal with 3.3 and 0.0 percent points in the two frequency bands respectively.

For combinations involving single VV-polarized features, Figure 9.25(b)

presents similar results as in the horizontal polarization case. Since the performance of VV-polarized features alone is poorer than HH-features at short dwell time, the improvement of adding polarimetric measurements is even greater. The difference between the two approaches at $\tau_d = 5$ ms is now 38.2 percentage points and 37.4 percentage points in L- and S-band respectively. As in the previous example this difference decreases gradually down to 2.1 and 1.4 percentage points in L-and S-band at $\tau_d = 700$ ms.

This is a new and interesting result. The initial results from the described feature selection approach indicate that polarimetric measurements help out with separation between birds and man-made targets when the time available is limited. This is central to air defence radar systems where time is a highly limited resource. In a tracking radar with more time available, polarimetric parameters are not that important.

The absolute values of P_{cc} resulting from the selection process presented in this section must be treated with some care due to the potential of forced decisions in the two-class problem. The scores as presented so far do not provide information about the confidence in labeling a target correctly. For the feature selection process treated so far, this is not considered important as the aim of the comparison is to make a relative ranking of feature sets under identical conditions. However, for an operational classifier it is crucial to have information on how certain the classification is. A more thorough investigation of the achieved classification performance is discussed next.

9.4 Classification results

This section focuses on the classification performance of the Nearest Neighbour classifier making use of the selected features presented in the previous section. In order to pursue these findings of the significant contribution from polarimetric features, the focus is short dwell times only from now on. The confidence in classification is taken into account, the most challenging classes to separate (*A*-*D*) are identified, and the value of combining features from two frequency bands is inves-

tigated.

9.4.1 Two classes: *Bird* or *UAV*

ROC curves are frequently used to illustrate the trade offs between true positive and false positive rates for a binary classifier. Here the true positive rate is defined as the ratio between correctly labeled instances of the positive class and the total number of instances of that class. Likewise the false negative rate is the ratio between the number of instances of the negative class misclassified as positive and the total number of negative instances. A confusion matrix shows the results of one threshold setting and thus one point at the ROC curve only [153]. The ROC curve is obtained by adjusting the threshold between class distributions as indicated by the position of the solid black line in Figure 9.26. The actual implementation is done by use of the *perfcurve* function available in the Matlab statistics and machine learning toolbox.

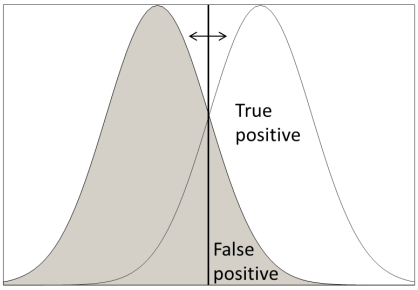

Figure 9.26: True positives and false positives in binary classification problem. By adjusting the threshold indicated by the solid black line, the true positive and false negative rate change.

Figure 9.27 shows ROC curves for the classifier using optimum features with UAV as the positive class for three selected short dwell times. Solid lines indicate utilization of all selected features, whereas dotted lines denote HH-polarized features alone. The grey diagonal lines indicate the performance of random classification. An ideal classifier would separate between the classes perfectly and give a true positive rate equal one for all false positive values down to zero. How fast the curve rises and how close it gets to the upper left corner of the figure is therefore an indication of the performance. In both L- and S- band, shown in Figure 9.27(a) and Figure 9.27(b) respectively, the inclusion of polarimetric features results in solid

curves significantly closer to the upper left corner than the HH-polarized features. Another measure linked to this performance is the area under each of the curves AUC. The AUC is a measure of the average performance of the classifier and performs well as a general measure of classification performance [153].

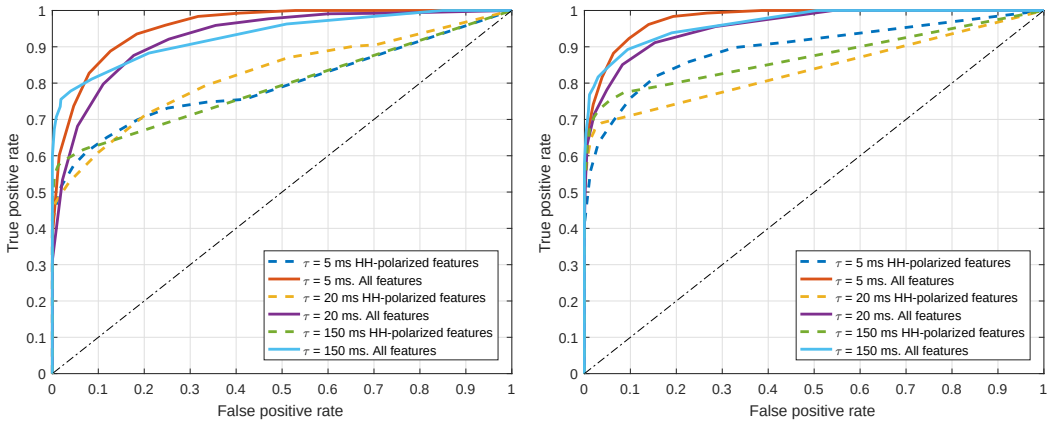

(a) L-band (b) S-band

Figure 9.27: ROC curves for UAV as positive class in the two-class problem.

The AUC associated with each curve in Figure 9.27 is found in Table 9.7. Significantly higher values are found for both frequency bands when polarimetric features are included in the classification. The improved performance in S-band compared to L-band observed earlier in the chapter is confirmed. So is the result of best performance at the shortest dwell times as long polarimetric features are exploited. From this table the conclusion is that the combination of single polarized features and polarimetric features outperform single polarized features alone at all practical thresholds.

	AUC L-band		*AUC S-band*	
$\tau_d[ms]$	*Single polarization*	*All selected*	*Single polarization*	*All selected*
5	0.795	0.956	0.895	0.977
20	0.822	0.927	0.833	0.961
150	0.793	0.932	0.872	0.966

Table 9.7: AUC for two-class problem in L- and S-band. Areas are presented for HH-single polarized features and the combination of all selected HH-single polarized and polarimetric features at three dwell times τ_d.

9.4.2 Three classes: *Bird*, *UAV* or *Unknown*

One way of revealing the confidence in the labeling process is by including an *unknown*-class. Now the targets associated with low confidence are no longer forced into one of the classes present in the reference data, but labeled *unknown*. The same will ideally happen to targets of classes not included in the reference data in the first place. By adjusting the confidence level, a threshold can be found that gives a predefined probability of declaring a class rather than labeling the target *unknown* denoted P_d, as defined in [152].

The Nearest Neighbour classifier is discrete in the sense that it only returns class affiliation. The target under test is labeled with the class label of the nearest target, or as in this specific case the most frequent label among the ten closest targets, in the feature space. However, a confidence measure can be calculated based on the distances to neighbouring targets in the same space. If the difference in Euclidean distance between the test sample and any instance belonging to a class not selected is small, the confidence in the classification is low. On the other hand, if the test target is close to a group of targets from one class and well separated from instances of any other class, the confidence is high.

An alternative ROC curve expressing the trade off between P_d and P_{cc} is covered in [152]. Figure 9.28 shows ROC curves for the classifier with an *unknown*-class included. The upper bound of P_{cc} is the P_d and is indicated by grey diagonal lines. The plots then gives an impression of how large portion of the targets associated with an actual class are correctly labeled for each feature set. If the probability of declaring a class is one, the situation is identical to the forced decision case discussed until now. Reducing P_d, meaning being more restrictive in labeling a class, hence the portion of correctly labeled targets will increase. As a consequence the number of targets classified *unknown* will naturally also increase.

The best performing feature sets are found closest to the optimum gray diagonal line. In both Figure 9.28(a) and Figure 9.28(b) the solid lines representing results from including polarimetric features are found closest to this line at all three investigated dwell times. This is a new indication of the value of including polari-

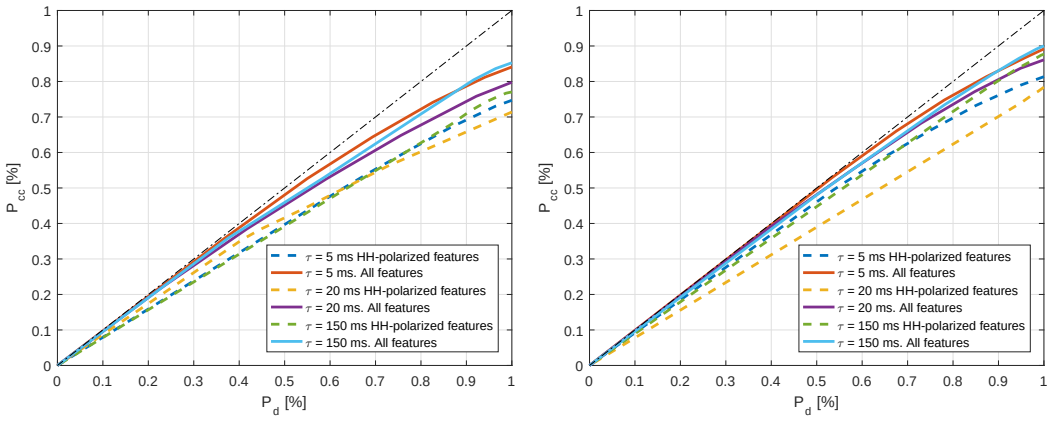

(a) L-band (b) S-band

Figure 9.28: Alternative ROC curve indicating performance of classifier as function of the probability of declaring a class rather than labeling the target *unknown*.

metric features in classification at these dwell times.

9.4.3 Four classes: *A-D*

So far only the problem of separating between birds and UAVs has been covered. By subdividing each class into two, thus introducing a four-class classification problem, an investigation of where the challenges of classification hide can be done. The four classes *A-D* are introduced in Chapter 7. For simplicity we use the same feature sets optimized for the two-class problem, although these features are not necessarily optimum for solving this problem. Two main challenges are identified by investigation of confusion matrices for the three shortest dwell times, $\tau_d = 5$ ms, $\tau_d = 20$ ms and $\tau_d = 150$ ms, with and without use of polarimetric features. The first is separation between soaring and flapping birds, and the next is separation between UAVs with non-conductive propellers/rotors and birds. The first challenge is not particularly interesting to the research problem as birds are birds if they are flapping or not, however, the last one is more critical. An investigation of how well targets of classes *C* and *D* are separated from birds by use of non-polarimetric and polarimetric features is required.

Figure 9.29 shows ROC curves indicating the classification performance for the UAV classes *C* and *D* in the four-class case in L-band. In Figure 9.29(a) the performance of the classification of UAVs with conductive propellers/rotors is shown.

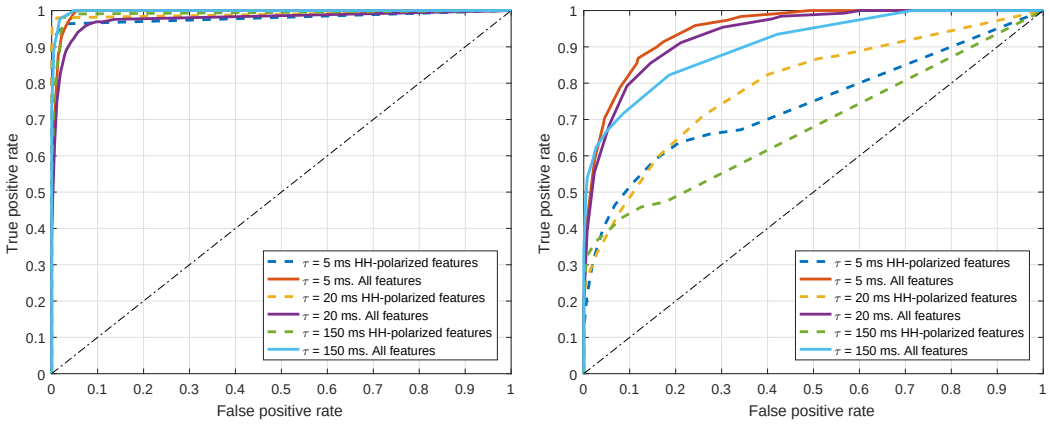

(a) Positive class *C* (b) Positive class *D*

Figure 9.29: Classification performance in four-class problem in L-band.

Dotted curves indicate single-polarized features alone, whereas solid lines still indicate inclusion of polarimetric features. The classification of targets of this class is observed to not be a problem in L-band. The classification performance is not increased by inclusion of polarimetric features. This is likely due to the characteristic wide Doppler spectrum returned from targets of this class. Figure 9.29(b) shows the classification of UAVs in class *D*. Here the broadening of the spectrum is generally minimal, and the single polarized features represented by dotted lines do not perform particularly well. However, the inclusion of polarimetric parameters result in significantly improved classification performance.

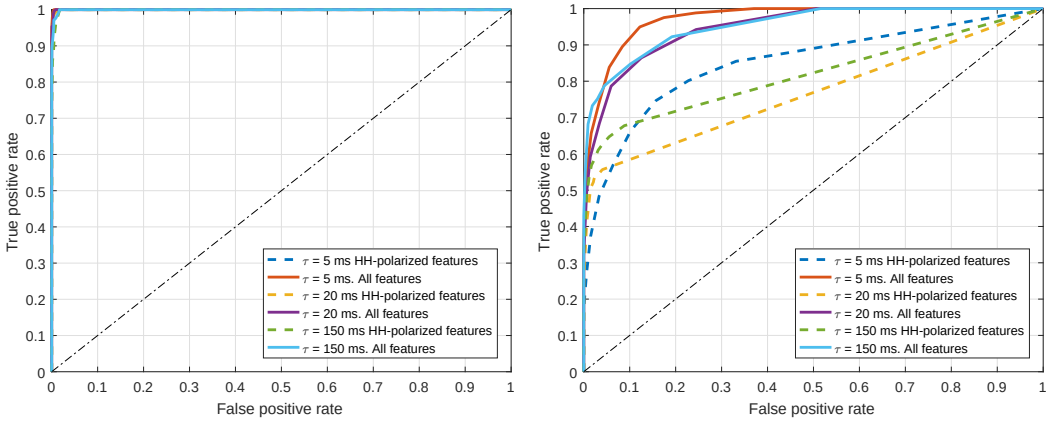

(a) Positive class C (b) Positive class D

Figure 9.30: Classification performance in four-class problem in S-band.

In S-band the curves of 9.30(a) indicate that the classification of targets in

class C is close to perfect both with and without help from polarimetric measurements. However, as in L-band the story is quite different for targets in class D. Figure 9.30(b) shows that the performance of HH-polarized features is generally poor. Again introducing polarimetric features helps significantly.

9.4.4 Comparison of frequency bands

So far L- and S-band have been treated individually. Since simultaneous data has been collected of all classes except for class B, a comparison between classification in the bands separately and in both combined can be made for classes A, C and D. In the previous examples all available data in the database has been used. To make the comparison fair, only multi-band data is included. All L-band data has an S-band counterpart. However, as the L-band power amplifier failed during the Smøla campaign, there exist data only available in S-band. This is easily filtered out in the database query being a part of the classification process.

	L-band		*S-band*		*L- and S-band*	
$\tau_d[ms]$	HH-pol.	All selected	HH-pol.	All selected	HH-pol.	All selected
5	0.795	0.956	0.887	0.972	0.902	0.986
20	0.822	0.927	0.834	0.971	0.856	0.979
150	0.793	0.932	0.861	0.965	0.959	0.982

Table 9.8: AUC for the two-class problem based on individual L- and S-band measurement and both combined. Areas are presented for HH single polarized features and combination of all selected HH single polarized and polarimetric features at three dwell times τ_d.

Table 9.8 shows the AUC results obtained by the same approach as used to form Table 9.7. The results for L-band alone are found in column number two and three and are identical in the two tables. For S-band the results are calculated on a subset of the data used in Table 9.7, and the results in Table 9.8 are therefore marginally different. The two rightmost columns hold results from combining simultaneous measurements in L- and S-band. These show that combining the two bands provides better classification performance at all selected dwell times compared to applying the same approach to any of the two bands individually. This applies both to single polarized HH-measurements and the selection of non-polarimetric and polarimetric features resulting from the previously described

feature selection process. Although the AUC is claimed to be a good measure of the average classification of a classifier [153], a practical example is included to give an idea of how the performance is affected in practice.

		Declared class								
		L-band			*S-band*			*L&S-band*		
		Bird	UAV	Unknown	Bird	UAV	Unknown	Bird	UAV	Unknown
True class	BIRD	0.0%	0.0%	100.0%	59.3%	4.6%	36.1%	64.7%	3.1%	32.2%
	UAV	0.0%	0.0%	100.0%	14.5%	54.4%	31.1%	13.1%	57.1%	29.8%

Table 9.9: Confusion matrix of true positive rates for separation between birds and UAVs based on both HH single polarized features alone with $P_m < 0.1$ and $\tau_d = 5$ *ms*.

To avoid a high degree of forced decisions, the probability of misclassification P_m is now required to stay below $P_m < 0.1$. This means that the classifier labels the target *unknown* when the confidence in the classification is low. P_m is here defined as the ratio between the number of incorrectly labeled signatures and all declarations made. Table 9.9 shows the confusion matrices with declaration results per true class for L-band alone, S-band alone and the combination of L- and S-band. Only the shortest dwell time of $\tau_d = 5$ ms and single polarized HH-features are included in this example. The requirement of a false alarm rate less than 10% leads to all targets being classified as *unknown* in the L-band alone case. Naturally this results in a probability of correct classification of $P_{cc} = 0\%$. A significant improvement is found in S-band where the P_{cc} is increased to 56.5%. The combination of L- and S-band is the best with a P_{cc} of 60.3%.

The results of a similar example involving polarimetric parameters are shown in Table 9.10. Still $P_m < 0.1$ is required and the dwell time investigated is $\tau_d = 5$ ms. Including polarimetric features helps significantly in terms of the classification score. The L-band performance is now increased to $P_{cc} = 73.1\%$, which is significantly better than the combination of L- and S-band using single polarized features. S-band is even better with a $P_{cc} = 79.6\%$. The combination of L- and S-band again gives the best results with $P_{cc} = 82.6\%$.

		Declared class								
		L-band			*S-band*			*L&S-band*		
		Bird	UAV	Unknown	Bird	UAV	Unknown	Bird	UAV	Unknown
True class	BIRD	72.5%	10.1%	17.4%	77.4%	9.0%	13.7%	80.0%	6.8%	13.2%
	UAV	6.7%	75.0%	13.3%	5.2%	81.0%	13.9%	2.9%	84.0%	13.1%

Table 9.10: Confusion matrix of true positive rates for separation between birds and UAVs based on both HH single polarized and polarimetric features with $P_m < 0.1$. $\tau_d = 5$ *ms*.

9.4.5 Inclusion of radial velocity

Radial velocity has so far been kept out of the classification process for fear of introducing a measure that is dependent on the measurement scenario. For example if one UAV class is flown at a higher velocity radially towards the radar than all other classes, this would be a strong characteristic in the specific data set, but not a strong feature in general. However, the radial velocity of a target may indirectly hold information on target aspect angle, which may be useful for resolving otherwise overlapping distributions. A plot containing all radial velocities for birds and UAVs was shown in Figure 7.8, and the distribution of velocities is quite similar for all classes. An example showing the result of introducing this parameter is included to show the best classification results achieved.

		Declared class								
		L-band			*S-band*			*L&S-band*		
		Bird	UAV	Unknown	Bird	UAV	Unknown	Bird	UAV	Unknown
True class	BIRD	82.2%	12.6%	5.1%	86.9%	13.1%	0.0%	91.0%	9.0%	0.0%
	UAV	7.0%	89.0%	4.0%	6.9%	93.1%	0.0%	5.5%	94.5%	0.0%

Table 9.11: Confusion matrix of true positive rates for separation between birds and UAVs based on radial velocity in addition to automatic selected features with $P_m < 0.1$ and $\tau_d = 5$ *ms*.

Table 9.11 shows the confusion matrices as radial velocity information is added to the automatically selected features shown in Table 9.5, still with $P_m < 0.1$ and $\tau_d = 5$ ms. Similarly to the previous two tables this presents, L-band alone, S-

band alone and the combination of L - and S-band. The results of L-band alone with radial velocity information included are better than those already presented for combined L- and S-band classification. The achieved probability of correct classification achieved in L-band alone is now $P_{cc} = 86.3\%$. S-band alone and the combination of L- and S-band with velocity information included show even better results with P_{cc} of 90.1% and 93.4% respectively.

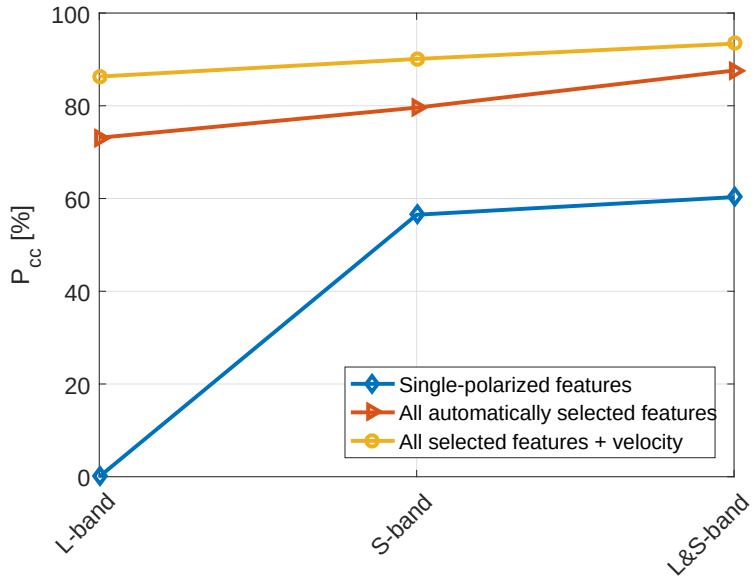

Figure 9.31: P_{cc} for classification with $P_m < 0.1$ and $\tau_d = 5$ ms in different frequency bands. Blue line denote HH-features alone, red shows the combination of HH-features and polarimetric parameters and yellow show the performance where radial velocity is included in addition.

Figure 9.31 provides a summary of the presented findings in the examples with $P_m < 0.1$ and $\tau_d = 5$ ms. A general finding is that S-band provides better classification performance than L-band. However, the best score is found by combining L- and S-band measurements. Non-polarimetric features, shown in the blue solid line, provide poor classification scores at such short dwell times. Adding polarimetric parameters significantly improves the situation, as shown by the red line. Furthermore, including information on radial velocity provides the best overall classification performance, as shown by the yellow line.

9.5 Potential sources of error

Measurements are naturally connected with uncertainties, and BirdRAD measurements are no exception. Absolute RCS accuracy has already been presented as not being high. The calibration of this measure involved an inflatable helium sphere. RCS fluctuation was observed exceeding 2 dB in L-band and up towards 3 dB in S-band with the balloon centered in the antenna beam. The largest uncertainty of absolute RCS measurements is still connected to target position in the beam. Absolute RCS values are not considered important in this thesis. Differential measures between polarizations are on the other hand central. As long as the target is kept within the 3 dB beamwidth in each band, the antenna beam pattern at vertical and horizontal polarization introduce insignificant differences. After calibration, the accuracy of differential magnitudes is expected to better than 1 dB. The differential phase is more uncertain. The accurate phase calibration done on a frequent basis excluded the use of antennas. These were measured separately in an anechoic chamber. The fact that $\mathbf{S}$ strictly is a pseudo scattering matrix introduces a target velocity dependent error not compensated for. In total the accuracy in differential phase measurements is expected to be $\pm 10^{\circ}$. Phase measurements are dependent on SNR, and all signatures were extracted from targets detected with SNR above 25 dB.

This high SNR led to occasional detections of non-conductive propellers in class *D* around 30 dB lower than the fuselage (in about 1% of the data). This is caused by the short range to targets during measurements. The distance to the UAVs were generally shorter than the range to all birds during measurements. This is not considered to have affected the classification results significantly. The main classification goal has been to separate UAVs and birds, and the distribution between members of these classes in the database is roughly equal. In the four class case *A*-*D* the distribution is more uneven. Especially the number of members in the soaring class is significantly lower than the other classes, and performance of separation between flapping and soaring birds is not included. All in all the sources of error are considered to be small and the results valid as a basis for drawing conclusions.

9.6 Summary

This chapter has presented target signatures in both the time- and joint time-frequency domain. Some classes provide characteristic non-polarimetric features, whereas other are better described by polarimetric ones. Spectrograms providing such information are found to be informative to the human eye as long as the observation time is long enough. Such representations are believed to hold information useful for classification at a more detailed level than aimed for in this thesis, and are considered valuable in a dedicated classification mode of a modern air defence radar system.

Parameters suggested for classification are extracted either from the time- or Doppler frequency-domain. Statistics of selected examples of such parameters are presented. Target classes *C*, consisting of UAVs with conductive propellers, is found to be well separated from the other classes based both on single polarized and polarimetric data. More challenging is the separation between flapping and soaring birds in class *A* and *B* respectively, and between birds and class *D* consisting of UAVs with non-conductive propellers and rotors. Polarimetric features are found to be of great value for separation between the latter.

Results of automatic feature selection are presented for both single polarized and polarimetric features. The wish to evaluate physical properties for classification directly excluded methods for dimensionality reduction introducing non-physical features. The high number of features to be evaluated makes exhaustive searches too time consuming, and optimal combinations of feature subsets were used in the selection process. This enabled comparison of the classification performance based on non-polarimetric and polarimetric features as function of dwell time. This comparison clearly shows that polarimetric parameters contribute significantly at the shortest dwell times. At longer observation times single polarized features do a better job, and the contribution from polarimetry is far less.

The last part of the chapter has focused on classification performance. The selected feature sets are compared in the two-class problem of separating between birds and UAVs, in the three class case including an *unknown*-class and finally in

the four class problem where a special focus is put on separation achieved between birds and class *C* and *D*. The main focus in this thesis is on separation between birds and UAVs and by including the *unknown*-class the classifier performance is evaluated in a more operational context. In this case the confidence in classification is important and classification performance as function of probability of class declaration is presented. The results from all comparisons show that inclusion of polarimetric measurements significantly improves classification at the shorter dwell times investigated (5, 20 and 150 ms).

A comparison of classification in L- and S-band has been made, and the benefit of combining features from both bands has been investigated. L-band features alone provide the poorest results, S-band is better, and the best results are found as measurements in both bands are combined. This is valid both for single polarized features and combination of non-polarimetric and polarimetric parameters. Classification is exclusively based on features considered independent of the measurement scenario. Therefore absolute RCS measures and velocities are deliberately excluded from the classification process. However, as the radial velocity is considered to be a strong feature due to its relation to the target aspect angle, measurements with and without velocity information were compared. The best classification results were achieved when the radial velocity was included in the classification process.

Chapter 10

Conclusions and future work

Modern air defence radars are military ground based systems responsible for detecting targets associated with low RCS at long ranges. As a result of an increased presence of UAVs or drones in civilian and military airspace, the demand for detection of small and slow moving targets has emerged. The consequence is frequent detections of birds associated with comparable RCS and behaviour.

This thesis addresses the problem of unwanted bird detections and separation between small man-made targets and birds within limitations commonly found in this radar class. This is done through electromagnetic simulations, measurements, extraction of target signatures and identification of features suitable for classification.

10.1 Summary of scope

The primary task for this class of radar is searching a vast volume at high update rates, providing early warning of enemy aircraft in sufficient time to respond with the appropriate means. Historically this has led to limited illumination time on each target and operation in L- or S-band to reduce the attenuation through atmosphere and precipitation. These factors do not form a good basis for traditional NCTR approaches making use of range or velocity resolution for classification. The advent of agile beam steering also in air defence systems, may enable longer dwell times. However, time is still a highly critical resource in these system. Prioritization of specific targets will eventually affect the quality of other prioritized tasks. One

goal of the study presented in this thesis has been to investigate the potential for classification of birds and UAVs of comparable size in such a classification mode allowing for increased time on target. However, the main objective has been to find methods capable of separating the classes in less time, ideally utilizing search pulses already used for detection.

The problem of separating between birds and UAVs in air defence radar has not been previously covered specifically in the literature. The vast majority of publications in the field of NCTR cover implementation in tracking radars, providing high carrier frequency and wide bandwidths. The problem addressed in this thesis is clearly different. Birds and UAVs of similar size are considered too small to be resolved in range by the bandwidths available in any of the relevant frequency bands, and the combination of short dwell times and low carrier frequency result in poor velocity resolution. The small size also makes these targets normally fall in the resonance scattering region and the dominating high frequency scattering models must be put aside. In addition, the range of materials of these targets further complicates the understanding of the contributing scattering mechanisms. The key to success in this challenging situation is considered to focus on potential advantages associated with scattering in this region, such as reduced significance of target details and signatures being dominated by the overall target shape.

Polarimetric methods are in this context considered to take advantage of scattering in low frequency regions, as interpretation of polarimetric features may be easier here. Exploitation of periodic RCS modulations on echoes from birds and UAVs are a different approach for extracting information about a target independent of spatial or velocity resolution. Both these two approaches are in addition to μ-Doppler signature based methods investigated in the form of simulations and measurements. As polarimetric measurements require additional hardware and increased costs, one of the goals was to quantify the potential benefit of including such capability in future systems. The methods were therefore grouped into non-polarimetric and polarimetric methods to enable such a comparison.

10.2 Summary of findings

Investigation of radar signatures in the form of simulations and measurements has increased the understanding of the dominating scattering mechanisms present on small targets in several frequency bands. Studies of RCS as function of incident polarization, the target's electrical size and material, as well as the contribution from bird wings and UAV rotors or propellers, has been central in this study. In L- and S-band, bird bodies are found to be well modeled as prolate spheroids with semi-major- to semi-minor-axis ratio around 3.5. The RCS at broadside illumination is then found to be 15-30 dB higher compared to at frontal and rear view aspects. This ratio varies as birds roughly heavier than 5 g in S- and 50 g in L-band fall in the resonance scattering region. However, the presence of bird wings makes the prolate spheroid model imprecise at frontal and rear views. At these aspect angles the RCS of wings is found comparable to that of the body. Bird wings are generally found to fall in the Rayleigh region, and thus act as dipole scatterers associated with RCS highly dependent on their alignment with the incident polarization.

Similar observations are made of UAV propellers and rotors. As long as the RCS is significantly large, their shape and size to wavelength ratio result in a distinct dipole like polarimetric signature. Target material is found to be important in this context. The smallest UAVs are frequently equipped with rotors and propellers of plastic material. Generally, these are associated with a very small RCS compared to those made of, for example, carbon fibers. As long as back-scattered power from rotating target parts of man-made targets is high enough, the effect of this rotation is easily separable from that of biological scatterers in the form of amplitude- or phase-modulations.

In the case of long coherent observations, characteristic non-polarimetric and polarimetric parameters have been presented in the form of joint time-frequency representations. This is found to be particularly useful to the human eye. Such μ-Doppler signatures are found to hold valuable information on target activity by revealing variable bird wing orientation or indicating orientation of rotating propellers and rotors.

The research questions raised in this thesis differentiate between classification in search mode without much prioritization of resources, and in a classification mode offered more time. This is addressed by evaluation of features as a function of dwell times in eight steps ranging from 5 to 700 ms. Features for classification were extracted from measurements of birds and small-UAVs made with the specially designed BirdRAD system. This is a fully polarimetric radar providing simultaneous data in L- and S-band. Selection among these features was done automatically based on a Nearest Neighbour classifier and exhaustive searches in subsets of horizontally polarized features, vertically polarized features, polarimetric parameters, as well as combinations of non-polarimetric and polarimetric features.

The classification performance based on non-polarimetric parameters alone is dependent on polarization, carrier frequency and dwell time. Parameters collected at horizontal polarization is generally found to provide a better basis for classification compared to vertically polarized parameters. This is connected to the improved detection of horizontally oriented rotors of quad-copter UAVs. In terms of frequency, L-band is found to provide less accurate classification compared to S-band. This is caused by the reduced velocity resolution in this band. The greatest impact on classification using non-polarimetric parameters is still found to be dwell time. The performance increases significantly with increased observation time in both bands and at both polarizations. This is connected to the increased frequency resolution provided by longer dwells.

In total 14 polarimetric features were evaluated. The classification performance is not found to differ significantly between the frequency bands. The best performance are for these parameters found at the shortest dwell times, where the scores are significantly better than the non-polarimetric features can provide. The performance is in general found to be independent of dwell time. However, some decrease in performance is observed with increasing dwell times. This may be caused by the averaging applied to parameters over the entire dwell time, thus forming an average parameter. This is done to better extract the dominating scattering mechanism in potentially distributed targets. However, for the longest dwell times,

the underlying scattering mechanisms may change and the averaging may at long dwell times do more harm than good.

The value of polarimetric parameters is evaluated. A considerable improvement in classification was found at short dwell times by including polarimetric measurements in both bands and for both polarizations. For $\tau_d = 5$ ms, an increase in probability of correct classification of 25.1 and 21.0 percentage points was found in L- and S-band respectively. At longer dwell times, the contribution from polarimetric measurements are insignificant. At $\tau_d = 700$ ms the difference is reduced to 3.3 and 0.0 percentage points in the two bands. In summary, this indicates that polarimetric parameters are of great value in the search mode scenario, whereas they are not required in the case of a classification mode which is assigned more time.

A closer investigation of which target classes are the most challenging to separate revealed that birds and UAVs with non-conductive propellers or rotors are the most difficult. In this case the advantage of including polarimetric parameters is significant. Targets with conductive propellers and rotors are, on the other hand, reasonably well recognizable by use of non-polarimetric measurements even at short dwell times. This is mainly due to the characteristic wide frequency spectrum caused by amplitude or phase modulations from such fast rotating target parts.

The results of comparing classification performance in different frequency bands at the shortest dwell time of 5 ms, highly relevant in air defence search radar, shows that classification in L-band achieves the poorest score, S-band is better, but the best results are found when combining the two bands. This result applies both as non-polarimetric, and polarimetric features are included. This shows that the best classification performance in modern air defence radar systems are found when including polarimetric measurements and operation in both frequency bands, however, the best single measure is to include polarimetric parameters.

10.3 Summary of achievements

The work presented in this thesis has resulted in several novel contributions highlighted in Chapter 1.6. However, the main result of this work is considered to be the

identification of features capable of supporting separation between birds and UAVs of comparable size within the limitations of air defence radars. This requires the introduction of polarimetric capability not yet commonly seen in modern systems. Such a capability is expected to increase the price, however, in return this study indicates that good separation between the target classes can be achieved within dwell times of around 5 ms. Such illumination times are normally available during a normal air defence radar scan and is in the context of NCTR extremely short.

10.4 Further work

This thesis has resulted in some key achievements summarized in the previous section. However, it has also opened up many possibilities for further work and improvements.

The use of joint time-frequency representations is in this thesis limited to visualization of signatures only. Such representations based on polarimetric measurements are informative to human interpretation, and classification utilizing joint time-frequency information should be investigated further. The limited velocity resolution, especially associated with bird signatures in L-band, calls for alternatives to the STFT-based spectrogram. Introduction of methods providing higher time-frequency resolution like Cohen's class time-frequency representations are suggested for further studies.

A total of 32 features are tested for classification in this study. Several polarimetric parameters based on alternative decomposition techniques should be tested. Studies of more optimal use of averaging applied prior to extraction of polarimetric parameters are also recommended. In this study potentially suboptimal averaging over the entire dwell time was performed. Only class *C* is in this study wasb found to be associated with high levels of entropy. Further studies of the degree of polarization to be expected and the potential use of coherent decomposition techniques is suggested. Further investigation of using polarization synthesis to enhance detection of wanted targets and decrease detectability of unwanted targets and clutter is interesting.

One of the findings in this thesis is that classification can be done with reasonable accuracy by using short dwell times. Combining several independent classification results in time is considered to be an interesting approach. The reason is that the prominence of characteristic features may vary during the wing flapping sequence. Some intervals in time are simply better for classification than others. By combining classification results from for example scan to scan, the performance may be increased to a higher level still without significantly influencing the time budget in the resource manager.

Experiments can always be improved. In addition to more targets, improved video recording with frame rates higher than 25 frames per second is desirable to better correlate video and radar signatures. Integration in more powerful systems, increasing the detection range would be beneficial in order to reduce aspect angle changes induced by translational velocity. Studies of migrating birds under such conditions may reveal periodicity useful for classification despite scattering close to the optics region. If useful signatures are found, studies of lowering the revisit rate to each bird is suggested. A revisit rate around 20 Hz should theoretically be sufficient to extract the wing beat frequency of most large birds unambiguously.

The work so far has focused on signatures of single birds and UAVs, whereas bird flocks and UAV swarms are topics to be investigated. Man-made targets flying like birds with mechanical wings, referred to as ornithopters, are reported. An example is the SmartBird [154]. So far the payload of such vehicles is low, and the threat in an air defence scenario is limited. However, this may change and such a target constitutes an interesting challenge in terms of classification.

Ground- and sea-clutter are factors limiting the detectability of the targets classes presented in this thesis. The theory is presented for classification of already detected targets, however, a thorough study of its operational usefulness is required. The influence of clutter is dependent on the environment of the target, its position, RCS and radial velocity, the radar's spatial resolution and velocity resolution achieved as function of carrier frequency and dwell time. Evaluation of combined detection and classification performance is suggested. In cases where

the radial velocity is low, the dwell time required to separate the target from, for example, ground clutter may be longer than the time needed to do classification.

This study has addressed the problem of separating birds and UAVs by use of radar signatures alone, although information on radial velocity was included in the last example of classification. However, combining signatures from radar data and track is potentially a good strategy to achieve the best results. An investigation of classification performance based on the combination of radar track, non-polarimetric and polarimetric signatures would require a full size experimental radar system significantly more complex than BirdRAD. However, such a comprehensive experiment should be conducted in order to confirm the advantage of polarimetric measurements in an operational scenario.

Appendix A

BirdRAD hardware

This appendix lists the components used in the design of the BirdRAD system and provides an example of the timings of one full PRI for all four channels.

A.1 Transmitter

Table A.1 contains the components in the L-band transmitter indicated by blue symbols in Figure 6.6. Similarly components of the S-band channels marked with red symbols in the same figure are shown in Table A.2.

#	*Reference*	*Name*	*Function*	*Manufacturer*
1	Amp 1	AMF-4F-00450380	Amplifier	Miteq
1		ZA3PD-2-S+	Splitter	Mini-Circuits
1	Mix 1	ZX05-C42-S+	Mixer	Mini-Circuits
1	Amp 2	ZJL-4HG+	Amplifier	Mini-Circuits
1	BPF 1	10LB40-187.5/T50-0/0	Filter	K&L
1	Switch1	ZFSWA2-63DR+	Switch	Mini-Circuits
1	Switch2	ZFSWA2-63DR+	Switch	Mini-Circuits
1	Load1	MCL STRM-50	Load	Mini-Circuits
2	PA L-band	AM10-1.2-1.4-53-53R	Power amplifier	Microwave Amplifiers Ltd

Table A.1: Components in L-band transmitter

#	*Reference*	*Name*	*Function*	*Manufacturer*
1	Amp 1	AMF-4F-00450380	Amplifier	Miteq
1		ZN3PD-622W-S+	Splitter	Mini-Circuits
1	Mix 1	ZX05-C42-S+	Mixer	Mini-Circuits
1	Amp 2	ZJL-4HG+	Amplifier	Mini-Circuits
1	BPF 2	16FV50-1300/T100-0/0	Filter	K&L
1	Switch1	ZFSWA2-63DR+	Switch	Mini-Circuits
1	Switch2	ZFSWA2-63DR+	Switch	Mini-Circuits
1	Load1	MCL STRM-50	Load	Mini-Circuits
2	PA S-band	AM83-3.1-3.3-53-53R	Power amplifier	Microwave Amplifiers Ltd

Table A.2: Components in S-band transmitter

A.2 Receiver

The components used in the receiver are similarly listed in Table A.3 and Table A.5 for L- and S-band respectively.

#	*Reference*	*Name*	*Function*	*Manufacturer*
1	Limiter	VLM-63-2W-S+	Limiter	Mini-Circuits
1	LNA	PSA4-5043+	Low noise amplifier	Mini-Circuits
1	Amp 3	ZX60-V62+	Amplifier	Mini-Circuits
1		ZFRSC-42-S+	Splitter	Mini-Circuits
2	BPF 2	16FV50-1300/T100-0/0	Filter	K&L
2	Mix 1	ZX05-C42-S+	Mixer	Mini-Circuits
2	Amp 4	ZFL-2AD+	Amplifier	Mini-Circuits
2	BPF 3	10LB40-187.5/T50-0/0	Filter	K&L
1	ADC 1	NI 5762R (2)	Digitizer	National Instruments
1	FPGA	NI PXI-7954R FlexRIO	FPGA module	National Instruments

Table A.3: Components in L-band receiver channels

The components of the LNA unit are found in Table A.4.

#	*Reference*	*Name*	*Function*	*Manufacturer*
2	Limiter	VLM-63-2W-S+	Limiter	Mini-Circuits
2	LNA	PSA4-5043+	Low noise amplifier	Mini-Circuits

Table A.4: Components in LNA unit

#	*Reference*	*Name*	*Function*	*Manufacturer*
1	Amp 3	ZX60-V62+	Amplifier	Mini-Circuits
1		ZFRSC-42-S+	Splitter	Mini-Circuits
2	BPF 1	10CS19-3250/E102.1-0/0	Filter	K&L
2	Mix 1	ZX05-C42-S+	Mixer	Mini-Circuits
2	BPF 3	10LB40-187.5/T50-0/0	Filter	K&L
1	ADC 2	NI 5762R (2)	Digitizer	National Instruments
1	FPGA	NI PXI-7954R FlexRIO	FPGA module	National Instruments

Table A.5: Components in S-band receiver channels

Other central components being part of the BirdRAD system are listed in Table A.6.

#	*Reference*	*Name*	*Function*	*Manufacturer*
1	AWG 1	AFQ100B	Arbitrary waveform generator	Rohde & Schwartz
1	AWG 2	AFQ100B	Arbitrary waveform generator	Rohde & Schwartz
1	RF synth	HS9002A	Local oscillator	Holzworth
1	GPS unit	XLi	GPS time & frequency	Symmetricom
1	Tx antenna	WBHDP0.9-18S	Antenna feed	Q-par Angus Ltd
1	Rx antenna	WBHDP0.9-18S	Antenna feed	Q-par Angus Ltd
1	Tx antenna	QSR700-OST	Antenna reflector	Q-par Angus Ltd
1	Rx antenna	QSR700-OST	Antenna reflector	Q-par Angus Ltd
1	Pan/tilt unit	PT-3002	Az/El control	2B security
1	Camera	BKC-IP-21	Video camera	2B security
4		Sucoflex 100	2m RF cable	Huber+Suhner
2		Sucoflex 100	3m RF cable	Huber+Suhner
2		Model 2382-2	L-&S-band power combiner	Narda

Table A.6: Other central BirdRAD components

A.3 Signal timing

This example shows the full sequence of transmitting one pulse at each polarization in each band according to timings in Figure A.1. The waveform used is the *50MHz2mu10kHz* found in Table 6.2. The polarization is as usual alternated between horizontal and vertical from one pulse to the next. The cycle can be summarized as:

1. Transmission of S-band pulse with horizontal polarization
    - $t = 0 \rightarrow 2\mu s$: *AWG1* generates a pulse at IF
    - $t = 0 \rightarrow 2\mu s$: *M3* on *AWG1* is set high to turn *Switch 1* in the S-band transmitter on. This passes the generated RF pulse in the transmitter on to the designated PA.
    - $t = 2\mu s \rightarrow$: *M1* on AWG1 is set high. This triggers the S-band digitizer to sample N samples in the horizontal and vertical polarized channels. The number of samples N can be chosen in the software controlling the digitization process.
2. Transmission of L-band pulse with horizontal polarization
    - $t = 25 \rightarrow 67\mu s$: *M4* on *AWG1* is set high to trigger *AWG2*
    - $t = 25\mu s \rightarrow 27\mu s$: *AWG2* generates a pulse at IF
    - $t = 25 \rightarrow 27\mu s$: Marker 3 on AW2 is set high to turn Switch 1 in the L-band transmitter on. This passes the generated RF pulse in the transmitter on to the PA.
    - $t = 27\mu s \rightarrow$: *M1* on *AWG2* is set high. This triggers the L-band digitizer to sample N samples in the horizontal and vertical polarized channels.
3. Transmission of S-band pulse with vertical polarization
    - $t = 34 \rightarrow 67\mu s$: *M2* on *AWG1* is set high to turn on Switch 2 in S-band transmitter. This routes the transmitted pulse to the vertical polarized antenna port.

- $t = 50 \rightarrow 52\mu s$: *AWG1* generates a pulse at IF
- $t = 50 \rightarrow 52\mu s$: *M3* on *AWG1* is set high to turn *Switch 1* in the S-band transmitter on. This passes the generated RF pulse in the transmitter on to the PA.
- $t = 52\mu s \rightarrow$: *M1* on *AWG1* is set high. This triggers the S-band digitizer to sample N samples in the horizontal and vertical polarized channels.

4. Transmission of L-band pulse with vertical polarization

- $t = 75 \rightarrow 93\mu s$: *M4* on *AWG2* is set high to mark transmitted pulse as vertical in the digitizer.
- $t = 59 \rightarrow 93\mu s$: *M2* on *AWG2* is set high to turn on *Switch 2* in L-band transmitter. This routes the transmitted pulse to the vertical polarized antenna port.
- $t = 75 \rightarrow 77\mu s$: *AWG2* generates a pulse at IF
- $t = 75 \rightarrow 77\mu s$: *M3* on *AWG1* is set high to turn *Switch 1* in the L-band transmitter on. This passes the generated RF pulse in the transmitter on to the PA.
- $t = 77\mu s \rightarrow$: *M1* on *AWG2* is set high. This triggers the L-band digitizer to sample N samples in the horizontal and vertical polarized channels.

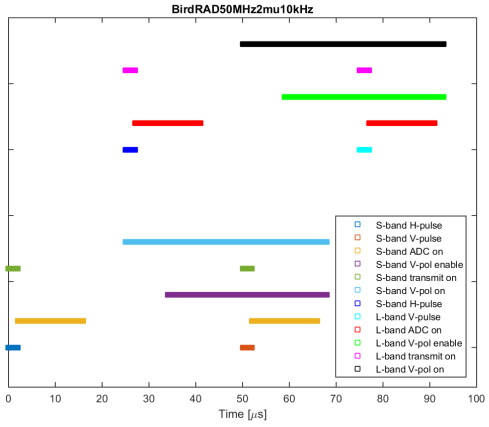

Figure A.1: Timings of BirdRAD during one full PRI for all four channels

Appendix B

New prolate spheriod model

This section shows the calculation of the semi-major to semi-minor axes ratio under the assumption of a prolate spheroid bird model. The semi-minor axes are found from the measurements of circumference in the literature. From this the semi-major axis that forms a volume identical to that of the bird is found.

Measurements of total length L_{tot}, tail length L_{tail}, circumference C_p, mass W_p and density $\overline{\rho}_p$ of 12 plucked bird species are presented in [122]. Values for plucked birds is relevant since the dielectric properties of feathers are close to that of air, as presented in Chapter 2.1.3. The semi-minor axes $a = b$ were estimated from $C_p = 2\pi b^2$, and the body length was found as $L_{body} = L_{tot} - L_{tail}$. Using these values to estimate the semi-axis ratio gives $m = \frac{L_{body}}{2b}$. This measure includes the head and neck.

The percent of body mass represented by feather is in [122] found to vary between species. However, based on average values of the data the relationship between total weight W_t and weight of plucked birds W_p can be expressed as $W_p = 0.937\, W_t$. For a prolate spheroid model of a plucked bird where $a = b$ and $\overline{\rho}_p$ denotes the average density of plucked birds, the weight can then be estimated from its volume V_p as

$$V = \frac{4}{3}\pi\, a\, b\, c \tag{B.1}$$

$$V_p = \frac{4}{3}\pi\, c\, a^2 \tag{B.2}$$

$$W_p = V_p\, \overline{\rho_p} = 1.25\, \pi\, m\, a^3 \tag{B.3}$$

Bibliography

[1] C. R. Vaughn, "Birds and insects as radar targets: A review," *Proceedings of the IEEE*, vol. 73, pp. 205–227, Feb 1985.

[2] E. F. Knott, J. F. Shaeffer, and M. T. Tuley, *Radar Cross Section*. Artech House, 1993.

[3] G. W. Schaefer, "The study of bird echoes using a tracking radar," in *Proceedings of the 14th International Ornithological Congress*, 1966.

[4] C. Gabriel, "http://niremf.ifac.cnr.it/tissprop/."

[5] D. Moffatt, "The echo area of a perfectly conducting prolate spheroid," *IEEE Transactions on Antennas and Propagation*, vol. 17, no. 3, pp. 299–307, 1969.

[6] R. modeling tool for designers, "http://www.rhino3d.com/."

[7] D. Blacknell and H. D. Griffiths, *Radar Automatic Target Recognition (ATR) and Non-Cooperative Target Recognition (NCTR)*. Institution of Engineering and Technology, 2013.

[8] NATO, *AAP-06 Edition 2013. NATO Glossary of Terms and Definitions (English and French)*, 2013.

[9] J. W. Wilson, T. M. Weckwerth, J. Vivekanandan, R. M. Wakimoto, and R. W. Russell, "Boundary layer clear-air radar echoes: Origin of echoes and accuracy of derived winds," *Journal of Atmospheric and Oceanic Technology*, vol. 11, no. 5, pp. 1184–1206, 1994.

[10] D. S. Zrnic and A. V. Ryzhkov, "Polarimetry for weather surveillance radars," *Bulletin of the American Meteorological Society*, vol. 80, no. 3, pp. 389–406, 1999.

[11] V. M. Melnikov, R. R. Lee, and N. J. Langlieb, "Resonance effects within S-band in echoes from birds," *IEEE, Geoscience and Remote Sensing Letters*, vol. 9, no. 3, pp. 413–416, 2012.

[12] S. Bachmann and D. S. Zrnic, "Spectral density of polarimetric variables separating biological scatterers in the VAD display," *Journal of Atmospheric and Oceanic Technology*, vol. 24, pp. 1186–1198, July 2007.

[13] P. Zhang, A. V. Ryzhkov, and D. S. Zrnic, "Detection of birds and insects using polarimetric radar observation," in *Preprints, 11th Conference on Aviation, Range, and Aerospace Meteorology*, vol. 5, (Hyannis, MA), 2004.

[14] D. S. Zrnic and A. V. Ryzhkov, "Observations of insects and birds with a polarimetric radar," *IEEE Transactions on Geoscience and Remote Sensing*, vol. 36, no. 2, pp. 661–668, 1998.

[15] S. Haykin, "Cognitive radar: a way of the future," *IEEE Signal Processing Magazine*, vol. 23, no. January, pp. 30–40, 2006.

[16] J. R. Moon, "Effects of birds on radar tracking systems," in *Proceedings of IEE Radar 2002*, (Edinburgh), pp. 300–304, October 2002.

[17] D. J. Rabideau and P. Parker, "Ubiquitous MIMO multifunction digital array radar," in *Conference Record of the Thirty-Seventh Asilomar Conference on Signals, Systems and Computers, 2004*, vol. 1, (Pacific grove, California), pp. 1057–1064 Vol.1, 2003.

[18] B. Dawber and B. Wallace, "The advanced radar technology integrated system testbed (ARTIST) and the need for cognitive radar management and control." Defence applications of signal procesessing. Workshop, Queensland, July 2011.

[19] W. L. Flock, "Radar echoes from birds and their effects on radar performance," in *Atmospheric Effects on Radar Target Identification and Imaging*, vol. 27 of *NATO Advanced Study Institutes Series*, pp. 425–435, Springer Netherlands, 1976.

[20] D. Mackenzie, "A flapping of wings," *Science*, vol. 335, no. 6075, pp. 1430–1433, 2012.

[21] M. A. Richards, J. A. Scheer, and W. A. Holm, eds., *Principles of Modern Radar: Basic Principles*. SciTech Publishing, 2010.

[22] S. Moore, "Review of the state of the art of UK AESA technology and the future challenges faced," in *2007 IET International Conference on Radar Systems*, (Edinburgh), pp. 1–7, IET, 2007.

[23] P. Tait, *Introduction to Radar Target Recognition*. IEE radar, sonar, navigation, and avionics series, Institution of Engineering and Technology, 2005.

[24] V. C. Chen, D. Tahmoush, and W. J. Miceli, *Radar Micro-Doppler Signatures: Processing and Applications*. Electromagnetics and Radar Series, Institution of Engineering and Technology, 2014.

[25] W. L. Flock and J. L. Green, "The detection and identification of birds in flight, using coherent and noncoherent radars," *Proceedings of the IEEE*, vol. 62, pp. 745 – 753, june 1974.

[26] L. L. Bonham and L. L. Blake, "Radar echoes from birds and insects," *Scientific Monthly*, vol. 82, pp. 204–209, 1956.

[27] M. Brooks, "Electronics as a possible aid in the study of bird flight and migration," *Science*, vol. 101, p. 329, 1945.

[28] D. Lack and G. C. Varley, "Detection of birds by radar," *Nature*, vol. 156, p. 446, 1945.

[29] M. I. Skolnik, *Radar Handbook*. Electronic engineering series, McGraw-Hill, 1990.

[30] E. Eastwood, *Radar Ornithology*. Methuen & Co, Ltd., 1967.

[31] P. B. Chilson, K. Bolognini, B. L. Cheong, and J. Kelly, "Using a dual-polarimetric weather radar simulator to investigate microwave backscatter from birds," in *34 th Conference on Radar Meteorology, AMS*, (Williamsburg, VA), pp. 5–9, 2009.

[32] J. Lemieux, *One Bird Strike and You're Out!: Solutions to Prevent Bird Strikes*. Trafford Publishing, 2009.

[33] G. W. Schaefer, "Bird recognition by radar a study in quantitative radar ornithology," in *The problem of birds as pests*, (London), pp. 53–56, 1968.

[34] J. Edwards and E. W. Houghton, "Radar echoing area polar diagrams of birds," *Nature*, vol. 184, p. 1059, 1959.

[35] J. Blacksmith, P. and R. B. Mack, "On measuring the radar cross sections of ducks and chickens," *Proceedings of the IEEE*, vol. 53, p. 1125, aug. 1965.

[36] J. Green and B. B. Balsley, "Identification of flying birds using a Doppler radar," in *A conference on the biological aspects of the bird/aircraft collision problem*, (Clemson, South Carolina), pp. 491–508, February 1974.

[37] C. M. Alabaster, E. J. Hughes, and D. W. Forman, "Is it a bird or is it a plane?," in *Proc. IEEE 6th International Conference on Waveform Diversity and Design*, (Lihue, HI), 2012.

[38] B. Torvik, K. E. Olsen, and H. D. Griffiths, "K-band radar signature analysis of a flying mallard duck," in *Proc. 14 th International Radar Symposium (IRS), 2013*, vol. 2, (Dresden, Germany), pp. 584–591, 2013.

[39] B. Torvik, A. Knapskog, O. Lie-Svendsen, K. E. Olsen, and H. D. Griffiths, "Amplitude modulation on echoes from large birds," in *Proceedings of the*

11th European Radar Conference (EuRAD), 2014, (Rome, Italy), pp. 177–180, Oct 2014.

[40] B. Torvik, K. E. Olsen, and H. D. Griffiths, "X-band measurements of radar signatures of large sea birds," in *International Radar Conference, 2014*, (Lille, France), pp. 1–6, Oct 2014.

[41] R. B. Mack, P. Blacksmith, and O. E. Kerr, "Measured L-band radar cross sections of ducks and geese," tech. rep., Defense Technical Information Center document, 1979.

[42] S. Emlen, "Problems in identifying bird species by radar signature analyses: intra-specific variability," in *A conference on the biological aspects of the bird/aircraft collision problem*, (Clemson, South Carolina), pp. 509–524, February 1974.

[43] J. R. Moon, "A survey of bird flight data relevant to radar tracking systems," in *Proceedings of the IEE Radar 2002*, (Edinburgh), pp. 80–84, October 2002.

[44] N. Mohajerin, J. Histon, R. Dizaji, and S. L. Waslander, "Feature extraction and radar track classification for detecting UAVs in civillian airspace," in *2014 IEEE Radar Conference*, (Cincinatti, USA), pp. 0674–0679, May 2014.

[45] A. H. LaGrone, A. P. Deam, and G. B. Walker, "Angels, insects, and weather," *Radio Science Journal of Research NBS/USNC-URSI*, vol. 68, no. 8, pp. 895–901, 1964.

[46] E. W. Houghton and F. Blackwell, "Use of bird activity modulation waveforms in radar identification," tech. rep., Bird strike committee Europe Vojens, Denmark, 1972.

[47] C. H. Greenewalt, "The wings of insects and birds as mechanical oscillators," *Proceedings of the American Philosophical Society*, vol. 104, pp. 605–611, 1960.

[48] B. Parslew and W. J. Crowther, "Simulating avian wingbeat kinematics," *Journal of Biomechanics*, vol. 43, no. 16, pp. 3191–3198, 2010.

[49] M. E. Griffiths, "The variation in the wingbeat pattern of the starling (sturnus vulgaris) and the wood-pigeon (columba palumbus)," tech. rep., Biophysics Research Unit, Univeristy of Technology, Loughborough, 1969.

[50] M. E. Griffiths, "Wingbeat frequencies and flight patterns of the more common migrant birds of the British Isles and Europe," tech. rep., Biophysics research unit, University of Technology, Loughborough, 1970.

[51] W. L. Flock, "The identification of birds by radar," in *A conference on the biological aspects of the bird/aircraft collision problem*, (Clemson, South-Carolina), pp. 429–442, February 1974.

[52] B. Bruderer, B. Jaquat, and U. Brückner, "Zur bestimmung von flügelschlagfrequenzen tag-und nachtziehender vogelarten mit radar," *Ornithologishe Beobachter*, vol. 69, pp. 189–206, 1972.

[53] L. C. Ireland and T. C. Williams, "Radar observations of bird migration over Bermuda," in *A conference on the biological aspects of the bird/aircraft collision problem* (S. G. Jr., ed.), (Clemson, South Carolina), pp. 383–408, May 1974.

[54] V. C. Chen, *The Micro-Doppler Effect in Radar*. Artech House Remote Sensing Library, Artech House, 2011.

[55] L. W. Martinson, "A preliminary investigation of bird classification by Doppler radar," tech. rep., RCA Government and Commerical Systems, Missile and Surface Radar Division, 1973.

[56] J. L. Green and W. Flock, "Characteristics of radar echoes from birds in flight." Presented at UNSC-URSI Spring meeting, Washington D.C., April 1972.

[57] A. G. Stove, "A Doppler-based target classifier using linear discriminants and principal components," in *The Institution of Engineering and Technology Seminar on High Resolution Imaging and Target Classification.*, pp. 107–125, IET, November 2006.

[58] S. A. Gauthreaux, J. W. Livingston, and C. G. Belser, "Detection and discrimination of fauna in the aerosphere using Doppler weather surveillance radar," *Integrative and Comparative Biology*, vol. 48, no. 1, pp. 12–23, 2008.

[59] N. F. Troje, "Decomposing biological motion: A framework for analysis and synthesis of human gait patterns," *Journal of Vision*, vol. 2, no. 5, p. 2, 2002.

[60] J. de Wit, R. Harmanny, and P. Molchanov, "Radar Micro-Doppler feature extraction using the singular value decomposition," (Lille, France), pp. 1–6, Oct 2014.

[61] R. G. Raj, V. C. Chen, and R. Lipps, "Analysis of radar human gait signatures," *IET Signal Processing*, vol. 4, pp. 234–244, June 2010.

[62] A. Balleri, K. Chetty, and K. Woodbridge, "Classification of personnel targets by acoustic micro-Doppler signatures," *IET radar, sonar & navigation*, vol. 5, no. 9, pp. 943–951, 2011.

[63] E. A. Mueller, "Differential reflectivity of birds and insects," in *Proceedings of 21st Conference on Radar Meteorology*, (Edmonton, Canada), pp. 465–466, September 1983.

[64] E. A. Mueller and R. P. Larkin, "Insects observed using dual-polarization radar," *Journal of Atmospheric and Oceanic Technology*, vol. 2, no. 1, pp. 49–54, 1985.

[65] T. J. Lang, S. A. Rutledge, and J. L. Stith, "Observations of quasi-symmetric echo patterns in clear air with the CSU-CHILL polarimetric radar," *Journal of Atmospheric and Oceanic Technology*, vol. 21, no. 8, pp. 1182–1189, 2004.

[66] S. M. Bachmann and D. Zrnic, "Spectral polarimetry for identifying and separating mixed biological scatterers," in *Proceedings of the 32nd International Conference on Radar Meteorology*, (Albuquerque, New Mexico), October 2005.

[67] T. Schuur, A. Ryzhkov, P. Heinselman, D. Zrnic, D. Burgess, and K. Scharfenberg, "Observations and classification of echoes with the polarimetric WSR-88D radar," *Report of the National Severe Storms Laboratory, Norman, OK*, vol. 73069, p. 46, 2003.

[68] D. Tahmoush and J. Silvious, "Human polarimetric micro-Doppler," in *SPIE Defense, Security, and Sensing*, (Orland, Florida), pp. 802106–802106, International Society for Optics and Photonics, April 2011.

[69] D. Tahmoush and J. Silvious, "Radar polarimetry for security applications," in *European Radar Conference (EuRAD)*, (Paris), pp. 471–474, Sept 2010.

[70] J. Park, J. T. Johnson, N. Majurec, M. Frankford, K. Stewart, G. E. Smith, and L. Westbrook, "Simulation and analysis of polarimetric radar signatures of human gaits," *IEEE Transactions on Aerospace and Electronic Systems*, vol. 50, pp. 2164–2175, July 2014.

[71] F. Fioranelli, M. Ritchie, H. Griffiths, and A. Balleri, "Analysis of multiband monostatic and bistatic radar signatures of wind turbines," in *2015 IEEE Radar Conference*, (Johannesburgh), pp. 277–282, Oct 2015.

[72] O. A. Krasnov and A. G. Yarovoy, "Polarimetric micro-Doppler characterization of wind turbines," in *10th European Conference on Antennas and Propagation (EuCAP)*, (Davos, Switzerland), pp. 1–5, April 2016.

[73] S. Giangrande and T. U. of Oklahoma. School of Meteorology, *Investigation of Polarimetric Measurements of Rainfall at Close and Distant Ranges*. University of Oklahoma, 2007.

[74] S. Zaugg, G. Saporta, E. Van Loon, H. Schmaljohann, and F. Liechti, "Automatic identification of bird targets with radar via patterns produced by wing flapping," *Journal of the Royal Society interface*, vol. 5, no. 26, pp. 1041–1053, 2008.

[75] F. Zhu, Y. Feng, Y. Luo, and Z. Qun, "A novel method of identifying moving status of bird based on waveform entropy variance," in *International Conference on Communications, Circuits and Systems, 2008.*, (Hong Kong), pp. 922–926, IEEE, 2008.

[76] F. Zhu, Y. Luo, Q. Zhang, Y.-Q. Feng, and Y.-Q. Bai, "ISAR imaging for avian species identification with frequency-stepped chirp signals," *IEEE, Geoscience and Remote Sensing Letters*, vol. 7, no. 1, pp. 151–155, 2010.

[77] M. Arjomandi, S. Agostino, M. Mammone, M. Nelson, and T. Zhou, "Classification of unmanned aerial vehicles," tech. rep., The University of Adelaide, 2007.

[78] J. J. M. de Wit, R. I. A. Harmanny, and G. Prmel-Cabic, "Micro-Doppler analysis of small UAVs," in *9th European Radar Conference (EuRAD)*, (Amsterdam, Netherlands), pp. 210–213, 2012.

[79] R. I. A. Harmanny, J. J. M. de Wit, and G. P. Cabic, "Radar micro-Doppler feature extraction using the spectrogram and the cepstrogram," in *Proceedings of the 11th European Radar Conference (EuRAD), Rome*, pp. 165–168, 2014.

[80] P. Molchanov, R. I. Harmanny, J. J. de Wit, K. Egiazarian, and J. Astola, "Classification of small uavs and birds by micro-doppler signatures," *International Journal of Microwave and Wireless Technologies*, vol. 6, no. 3-4, pp. 435–444, 2014.

[81] C. E. Rotander and H. Von Sydow, "Classification of helicopters by the L/N-quoutient," in *Proceedings IET Radar 97*, (Edinburgh, UK), pp. 629–633, Oct 1997.

[82] S.-H. Yoon, B. Kim, and Y.-S. Kim, "Helicopter classification using time-frequency analysis," *Electronics Letters*, vol. 36, no. 22, pp. 1871–1872, 2000.

[83] A. Cilliers and W. Nel, "Helicopter parameter extraction using joint time-frequency and tomographic techniques," in *2008 International Conference on Radar*, (Adelaide), pp. 598–603, IEEE, September 2008.

[84] A. French, *Target recognition techniques for multifunction phased array radar*. PhD thesis, UCL (University College London), 2010.

[85] V. C. Chen, W. J. Miceli, and B. Himed, "Micro-doppler analysis in ISAR-review and perspectives," in *International Radar Conference "Surveillance for a Safer World"*, (Bordeauc, France), pp. 1–6, IEEE, October 2009.

[86] V. Chen, "Analysis of radar micro-Doppler with time-frequency transform," in *Proceedings of the 10h IEEE Workshop on Statistical Signal and Array Processing*, (Pennsylvania, USA), pp. 463–466, August 2000.

[87] C. Clemente, A. Balleri, K. Woodbridge, and J. J. Soraghan, "Developments in target micro-Doppler signatures analysis: radar imaging, ultrasound and through-the-wall radar," *EURASIP Journal on Advances in Signal Processing*, vol. 2013, no. 1, pp. 1–18, 2013.

[88] T. Sparr and B. Krane, "Micro-Doppler analysis of vibrating targets in SAR," *IEE Proceedings-Radar, Sonar and Navigation*, vol. 150, no. 4, pp. 277–283, 2003.

[89] W.-M. Boerner, "Recent advances in extra-wide-band polarimetry, interferometry and polarimetric interferometry in synthetic aperture remote sensing and its applications," *IEE Proceedings -Radar, Sonar and Navigation*, vol. 150, pp. 113–124, June 2003.

[90] D. Giuli, "Polarization diversity in radars," *Proceedings of the IEEE*, vol. 74, pp. 245–269, Feb 1986.

[91] J. R. Huynen, *Phenomenological theory of radar targets*. PhD thesis, TU Delft, Delft University of Technology, 1970.

[92] E. Johnson, W. Petersen, and C. Schultz, "Dual-polarimetric radar." http://www.nwas.org/committees/rs/Dual_Polarimetric_Radar_ Newsletter_Article_Oct07.pdf, October 2007.

[93] A. V. Ryzhkov and D. Zrnic, "Discrimination between rain and snow with a polarimetric NEXRAD radar," in *Preprints, 31st International Conference on Radar Meteorology*, (Seattle), August 2003.

[94] M. Skolnik, *Introduction to Radar Systems*. McGraw-Hill, 2001.

[95] A. J. Poelman, "Virtual polarisation adaptation a method of increasing the detection capability of a radar system through polarisation-vector processing," *Communications, Radar and Signal Processing, IEE Proceedings F*, vol. 128, pp. 261–270, October 1981.

[96] F. Sadjadi, "Improved target classification using optimum polarimetric SAR signatures," *IEEE Transactions on Aerospace and Electronic Systems*, vol. 38, no. 1, pp. 38–49, 2002.

[97] L. M. Novak, S. D. Halversen, G. J. Owirka, and M. Hiett, "Effects of polarization and resolution on sar atr," *IEEE Transactions on Aerospace and Electronic Systems*, vol. 33, no. 1, pp. 102–116, 1997.

[98] "Introduction to polarization." https://www.nrcan.gc.ca/earth-sciences/geomatics/satellite-imagery-air-photos/satellite-imagery-products/educational-resources/9275, October 2013.

[99] C. Lardeux, P.-L. Frison, C. Tison, J.-C. Souyris, B. Stoll, B. Fruneau, and J.-P. Rudant, "Classification of tropical vegetation using multifrequency partial SAR polarimetry," *IEEE Geoscience and Remote Sensing Letters*, vol. 8, no. 1, pp. 133–137, 2011.

[100] O. A. Krasnov, Z. Wang, R. F. Tigrek, and P. van Genderen, "OFDM waveforms for a fully polarimetric weather radar," in *Tyrrhenian International Workshop on Digital Communications-Enhanced Surveillance of Aircraft and Vehicles (TIWDC/ESAV)*, (Capri, Italy), pp. 69–72, IEEE, September 2011.

[101] W. M. Boerner, *Direct and inverse methods in radar polarimetry 2*. Kluwer Academic Publishers, 1992.

[102] N. E. Chamberlain, E. K. Walton, and F. D. Garber, "Radar target identification of aircraft using polarization-diverse features," *IEEE Transactions on Aerospace and Electronic Systems*, vol. 27, pp. 58–67, Jan 1991.

[103] M. Martorella, F. Berizzi, R. Soleti, L. Cantini, A. Corucci, B. Haywood, and J. Palmer, "Target classification by means of fully polarimetric isar images," in *2006 IEEE International Symposium on Geoscience and Remote Sensing*, (Denver, Colorado), pp. 141–144, August 2006.

[104] M. Martorella, E. Giusti, A. Capria, F. Berizzi, and B. Bates, "Automatic target recognition by means of polarimetric ISAR images and neural networks," *IEEE Transactions on Geoscience and Remote Sensing*, vol. 47, pp. 3786–3794, Nov 2009.

[105] M. Martorella, A. Cacciamano, E. Giusti, F. Berizzi, B. Haywood, and B. Bates, "CLEAN technique for polarimetric ISAR," *International Journal of Navigation and Observation*, vol. 2008, 2008.

[106] H. Mott, *Remote Sensing with Polarimetric Radar*. John Wiley & Sons, Inc., Publication, Wiley, 2007.

[107] S. R. Cloude and E. Pottier, "A review of target decomposition theorems in radar polarimetry," *IEEE Transactions on Geoscience and Remote Sensing*, vol. 34, pp. 498–518, Mar 1996.

[108] M. Martorella, E. Giusti, L. Demi, Z. Zhou, A. Cacciamano, F. Berizzi, and B. Bates, "Target recognition by means of polarimetric isar images," *Aerospace and Electronic Systems, IEEE Transactions on*, vol. 47, pp. 225–239, January 2011.

[109] A. Ksienski, Y. Lin, and L. White, "Low-frequency approach to target identification," *Proceedings of the IEEE*, vol. 63, pp. 1651–1660, Dec 1975.

[110] H. Lin and A. Ksienski, "Optimum frequencies for aircraft classification," *IEEE Transactions on Aerospace and Electronic System*, vol. 17, pp. 656–665, Sept 1981.

[111] C. W. Chuang and D. Moffatt, "Natural resonances of radar targets via Prony's method and target discrimination," *IEEE Transactions on Aerospace and Electronic Systems*, vol. 12, pp. 583–589, Sept 1976.

[112] D. L. Moffatt and R. Mains, "Detection and discrimination of radar targets," *IEEE Transactions on Antennas and Propagation*, vol. 23, pp. 358–367, May 1975.

[113] M. Morgan, "Singularity expansion representations of fields and currents in transient scattering," *IEEE Transactions on Antennas and Propagation*, vol. 32, pp. 466–473, May 1984.

[114] D. Dudley, "Progress in identification of electromagnetic systems," *Antennas and Propagation Society Newsletter, IEEE*, vol. 30, pp. 5–11, August 1988.

[115] G. A. Lazarakos, "Radar target identification by natural resonances: Evaluation of signal processing algorithms," Master's thesis, Monterey, California. Naval Postgraduate School, 1991.

[116] F. Fok and D. L. Moffatt, "The K-pulse and E-pulse," *IEEE transactions on antennas and propagation*, vol. 35, no. 11, pp. 1325–1326, 1987.

[117] D. Gjessing, *Target adaptive matched illumination radar: principles & applications*. IEE electromagnetic waves series, Institution of Electrical Engineers, 1986.

[118] D. Gjessing, J. Saebboe, and O. Helleren, "Recognition of targets by linear and non-linear (Delta K) processing of multi frequency data," in *NATO-RTO-MP-SET-080*, (Oslo, Norway), October 2004.

[119] D. M. Pozar, *Microwave engineering*. Wiley, 1997.

[120] F. T. Ulaby, D. G. Long, W. J. Blackwell, C. Elachi, A. K. Fung, C. Ruf, K. Sarabandi, H. A. Zebker, and J. Van Zyl, *Microwave radar and radiometric remote sensing*. University of Michigan Press Ann Arbor, 2014.

[121] A. Vander Vorst, A. Rosen, and Y. Kotsuka, *RF/Microwave Interaction with Biological Tissues*. Wiley Series in Microwave and Optical Engineering, Wiley, 2006.

[122] D. M. Hamershock, T. W. Seamans, and G. E. Bernhardt, "Determination of body density for twelve bird species," tech. rep., Wright Lab Wright-Patterson AFB OH, 1993.

[123] C. Gabriel, S. Gabriel, and E. Corthout, "The dielectric properties of biological tissues: I. Literature survey," *Physics in medicine and biology*, vol. 41, p. 2231, 1996.

[124] S. Gabriel, R. Lau, and C. Gabriel, "The dielectric properties of biological tissues: II. Measurements in the frequency range 10 Hz to 20 GHz," *Physics in medicine and biology*, vol. 41, p. 2251, 1996.

[125] S. Gabriel, R. Lau, and C. Gabriel, "The dielectric properties of biological tissues: III. Parametric models for the dielectric spectrum of tissues," *Physics in medicine and biology*, vol. 41, no. 11, p. 2271, 1996.

[126] E. J. Riley, E. H. Lenzing, and R. M. Narayanan in *SPIE Defense+ Security*, (Baltimore), pp. 946103–1–946103–8, International Society for Optics and Photonics, April 2015.

[127] J. S. Lee and E. Pottier, *Polarimetric Radar Imaging: From Basics to Applications*. CRC Press, 2009.

[128] S. Cloude, *Polarisation: Applications in Remote Sensing*. OUP Oxford, 2010.

[129] A. Taflove and S. C. Hagness, *Computational Electrodynamics - The Finite-Difference Time-Domain Method*. Boston: Artech House, third ed., 2005.

[130] http://www.dji.com/.

[131] M. Ritchie, F. Fioranelli, H. D. Griffiths, and B. Torvik, "Micro-drone RCS analysis," in *IEEE Radar Conference*, (Johannesburgh, South Africa), pp. 452–456, 2015.

[132] G. W. Stimson, H. D. Griffiths, C. J. Baker, and D. Adamy, *Stimson's Introduction to airborne radar. Third edition.* SciTech Publishing, 2014.

[133] T. Fonstad, B. Gensbl, and M. Gunther, *Aschehougs fuglebok*. Aschehoug forlag, 2008.

[134] A. Schroder, M. Renker, U. Aulenbacher, A. Murk, U. Boniger, R. Oechslin, and P. Wellig, "Numerical and experimental radar cross section analysis of the quadrocopter DJI Phantom 2," in *2015 IEEE Radar Conference*, (Johannesburgh, South-Africa), pp. 463–468, Oct 2015.

[135] https://3dr.com/.

[136] B. Torvik, K. E. Olsen, and H. D. Griffiths, "Classification of birds and uavs based on radar polarimetry," *IEEE Geoscience and Remote Sensing Letters*, vol. 13, pp. 1305–1309, Sept 2016.

[137] http://www.multiplex-rc.de/en/products/categories/products/details/productgroup/rc-accessories/productcategory/elapor-models-1/product/kit-easystar-ii.html.

[138] http://elefun.no/p/prod.aspx?v=19939.

[139] www.mathworks.com/.

[140] W. Carrara, R. Goodman, and R. Majewski, *Spotlight Synthetic Aperture Radar: Signal Processing Algorithms*. The Artech House Remote Sensing Library, Artech House, 1995.

[141] R. Mitchell, "Creating complex signal samples from a band-limited real signal," *IEEE Transactions on Aerospace and Electronic Systems*, vol. 25, no. 3, pp. 425–427, 1989.

[142] C. Alabaster, *Pulse Doppler radar: principles, technology, applications*, vol. 2. IET, 2012.

[143] K. Rottmann, *Matematisk formelsamling*. Spektrum forlag, 2001.

[144] P. Stoica and R. L. Moses, *Introduction to spectral analysis*, vol. 1. Prentice hall Upper Saddle River, 1997.

[145] J. B. Allen and L. R. Rabiner, "A unified approach to short-time Fourier analysis and synthesis," *Proceedings of the IEEE*, vol. 65, pp. 1558–1564, Nov 1977.

[146] F. Vogel, S. Holm, and O. C. Lingjærde, "Spectral moments and time domain representation of photoacoustic signals used for detection of crude oil in produced water," in *Proceedings on Nordic Symposium on Physical Acoustics*, (Ustaoset, Norway), January 2001.

[147] B. P. Bogert, M. J. Healy, and J. W. Tukey, "The quefrency alanysis of time series for echoes: Cepstrum, pseudo-autocovariance, cross-cepstrum and saphe cracking," in *Proceedings of the symposium on time series analysis*, vol. 15, pp. 209–243, chapter, 1963.

[148] F. Henderson, R. Ryerson, A. Lewis, A. S. for Photogrammetry, and R. Sensing, *Principles and applications of imaging radar*. No. v. 5 in Manual of remote sensing / ed. by Robert A. Ryerson. Publ. in cooperation with the American Society for Photogrammetry and Remote Sensing, Wiley, 1998.

[149] S. R. Cloude and E. Pottier, "An entropy based classification scheme for land applications of polarimetric SAR," *IEEE Transactions on Geoscience and Remote Sensing*, vol. 35, pp. 68–78, Jan 1997.

[150] V. Bringi and V. Chandrasekar, *Polarimetric Doppler Weather Radar: Principles and Applications*. Cambridge University Press, 2001.

[151] M. Ouarzeddineuarzeddine, B. Souissi, and A. Belhadj-Aissa, "Target detection and characterization using H/alpha decomposition and polarimetric signatures," in *2nd International Conference on Information Communication Technologies*, vol. 1, (Damascus), pp. 395–400, April 2006.

[152] G. E. Smith, M. Vespe, K. Woodbridge, and C. J. Baker, "Radar classification evaluation," in *2008 IEEE Radar Conference*, (Rome, Italy), pp. 1–6, May 2008.

[153] T. Fawcett, "An introduction to ROC analysis," *Pattern Recognition Letters*, vol. 27, no. 8, pp. 861–874, 2006.

[154] https://www.festo.com/net/SupportPortal/Files/46270/Brosch_SmartBird_en_8s_RZ_110311_lo.pdf.